

Structure Sensitivity of Manganese-Promoted Cobalt Fischer-Tropsch Synthesis Catalysts

Citation for published version (APA):

Kimpel, T. F. (2023). *Structure Sensitivity of Manganese-Promoted Cobalt Fischer-Tropsch Synthesis Catalysts*. [Phd Thesis 1 (Research TU/e / Graduation TU/e), Chemical Engineering and Chemistry]. Eindhoven University of Technology.

Document status and date:

Published: 09/11/2023

Document Version:

Publisher's PDF, also known as Version of Record (includes final page, issue and volume numbers)

Please check the document version of this publication:

- A submitted manuscript is the version of the article upon submission and before peer-review. There can be important differences between the submitted version and the official published version of record. People interested in the research are advised to contact the author for the final version of the publication, or visit the DOI to the publisher's website.
- The final author version and the galley proof are versions of the publication after peer review.
- The final published version features the final layout of the paper including the volume, issue and page numbers.

[Link to publication](#)

General rights

Copyright and moral rights for the publications made accessible in the public portal are retained by the authors and/or other copyright owners and it is a condition of accessing publications that users recognise and abide by the legal requirements associated with these rights.

- Users may download and print one copy of any publication from the public portal for the purpose of private study or research.
- You may not further distribute the material or use it for any profit-making activity or commercial gain
- You may freely distribute the URL identifying the publication in the public portal.

If the publication is distributed under the terms of Article 25fa of the Dutch Copyright Act, indicated by the "Taverne" license above, please follow below link for the End User Agreement:

www.tue.nl/taverne

Take down policy

If you believe that this document breaches copyright please contact us at:

openaccess@tue.nl

providing details and we will investigate your claim.

Structure Sensitivity of Manganese-Promoted Cobalt Fischer-Tropsch Synthesis Catalysts

PROEFSCHRIFT

ter verkrijging van de graad van doctor aan de Technische Universiteit Eindhoven, op gezag van de rector magnificus prof.dr. S. K. Lenearts, voor een commissie aangewezen door het College voor Promoties, in het openbaar te verdedigen op donderdag 9 november 2023 om 11:00 uur

door

Tobias F. Kimpel

geboren te Eberbach, Duitsland

Dit proefschrift is goedgekeurd door de promotoren en de samenstelling van de promotiecommissie is als volgt:

voorzitter:	prof. dr.ir. D.C. Nijmeijer
1 ^e promotor:	prof.dr.ir. E.J.M. Hensen
copromotor:	dr. R. Pestman
leden:	prof.dr.ir. J. van der Schaaf prof.dr. F. Gallucci prof.dr. G. Rothenberg (Universiteit van Amsterdam) dr.ir. L.M.T. Somers
adviseur:	dr.ir. I.A.W. Filot

Het onderzoek of ontwerp dat in dit proefschrift wordt beschreven is uitgevoerd in overeenstemming met de TU/e Gedragscode Wetenschapsbeoefening.

To my family

„God made the bulk; the surface was invented by the devil“

Wolfgang Pauli

Tobias F. Kimpel

Structure Sensitivity of Manganese-Promoted Cobalt Fischer-Tropsch Synthesis Catalysts

A catalogue record is available from the Eindhoven University of Technology Library

ISBN: 978-90-386-5865-0

Copyright © 2023 by Tobias F. Kimpel



The work described in this thesis has been carried out at the Inorganic materials & Catalysis group at the Eindhoven University of Technology.



This research was supported by NWO

Cover design: Ferdinand F.E. Kohle

Printed by: Gildeprint – The Netherlands

Table of Contents

Content	Page
Chapter 1: Introduction	1
Chapter 2: Fundamentals of Mn promotion of Co-based Fischer-Tropsch catalysts	17
Appendix A	48
Chapter 3: The influence of Co reduction degree on the particle size dependence of CoMn/TiO ₂ Fischer-Tropsch catalysts	61
Appendix B	94
Chapter 4: Highly active and selective Co(Mn)/TiO ₂ catalysts prepared by precipitation: on the impact of reduction temperature	98
Appendix C	127
Summary	133
Acknowledgements	136
List of publications	137
Curriculum Vitae	138

Chapter 1: Introduction

1.1 Catalysis

Controlling chemical reactions has been a pivotal aspect of the development of the human species, starting from a simple camp fire to the sophisticated petrochemical industry of today which forms the foundation of our modern life. At the beginning of the 20th century, revolutionary processes were developed that enabled large scale production of ammonia (the Haber-Bosch process) and hydrocarbons (the Fischer-Tropsch process) from coal-derived feedstocks. These processes enabled the production of targeted products by the use of catalysis, a phenomenon first mentioned by Berzelius as early as 1835 and described in a more scientific way by Ostwald in 1895¹ as:

“a catalyst accelerates a chemical reaction without affecting the position of the equilibrium”.

For instance, ammonia synthesis initially required harsh conditions like high pressure and temperatures to obtain adequate reaction rates, which led to high energy consumption and wear and corrosion of process equipment. The use of catalysts provided the necessary breakthroughs to operate reactions under milder conditions, which in the case of exothermic ammonia synthesis also allowed higher equilibrium yields. In addition to that, many reactions were nonselective, resulting in formation of many undesired byproducts. The main goal of present-day catalysis research is aimed at increasing the selectivity towards the desired product so that separation costs can be minimized and the use of milder reaction conditions improving both raw material and energy consumption.

During catalysis the overall energy barriers (activation energy E_a) are lowered compared to the uncatalyzed reaction, by stabilizing the transition state of a reaction. According to the Arrhenius equation, this leads to a higher reaction rate. In addition to that, catalysis can help improving the product distribution of a chemical reaction by selectively facilitating the formation of the desired product. The concept is very general and is not restricted to a certain mechanism nor whether chemical catalysts or enzymes, i.e., Nature's catalysts, are employed. Heterogenous catalysis can be characterized as a surface phenomenon where reactants and catalyst are in different aggregate states. A typical catalytic reaction path is depicted in Fig. 1.1 The whole process is cyclic, restoring the catalyst surface after the reaction has ended.^{2,3}

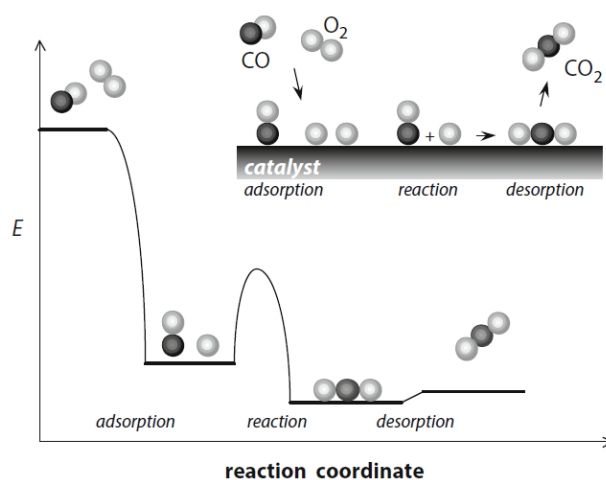


Figure 1.1. Energy diagram of a heterogeneous reaction depicting elementary steps involved in the catalytic cycle of a CO oxidation reaction. Adapted from [2]

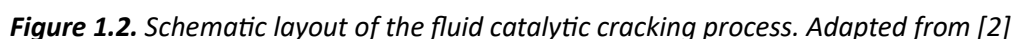
The fundamental reaction steps involved in a heterogeneous reaction over a supported catalyst, can be described as follows:

- 1) Diffusion of reactants through the boundary layer to the catalyst surface
- 2) Diffusion of reactants into the pores (pore diffusion)
- 3) Adsorption of the reactants on the catalyst surface and surface diffusion of adsorbates to each other
- 4) Chemical reaction on the catalyst surface
- 5) Desorption of the products from the catalyst surface
- 6) Diffusion of the products out of the pores
- 7) Diffusion of the products through the boundary layer and into the gas or liquid phase

1.2 Catalysis in energy and environmental applications

By definition, catalysis is inevitably interconnected with the use of energy in our daily life, not only as a tool to facilitate chemical reactions by reducing E_a but also as an enabler for a more efficient use of energy sources^{3,4}. In the case of crude oil which is currently the most important source of energy carriers, catalysis plays a pivotal role during its refining where the complex mixture of hydrocarbons with varying properties is converted into transportation fuels, next to other valuable chemicals⁴. An example of the numerous chemical reactions conducted in a refinery is hydrotreating^{5,6}, in which hydrogen is used in combination with a catalyst containing Ni/Co and WS_2/MoS_2 supported on Al_2O_3 to remove heteroatoms like sulfur, nitrogen and oxygen, improving the fuel quality and significantly reducing the emission of pollutants during combustion. Another example is the conversion of heavy residues from vacuum distillation (boiling point of $\geq 340^\circ C$), which are of little use, into more favorable short-chain hydrocarbons using a process called fluid catalytic cracking (FCC)⁷, which comprises a riser reactor for cracking and a fluidized-bed reactor for regeneration of the catalyst in air. Since, after a contact time of only a few seconds in the cracking section, the cracking catalyst is largely deactivated by carbonaceous deposits, the catalyst is transferred to a regenerator, where the coke is burned

Another major application of catalysis concerns exhaust gas treatment of combustion processes, especially in mobility (passenger cars, trucks). Modern fuels contain only minor sulfur levels (~ 10 ppm in Europe) due to the aforementioned hydrotreating process, leading to low SO_x emissions. Nevertheless, combustion leads to the formation of pollutants like CO, NO_x and soot, the latter in particular for diesel-fueled engines. As a result, sophisticated catalytic converters have been developed to eliminate such pollutants for example by the so-called three-way catalyst (TWC) technology for gasoline engines introduced in 1979^{8,9}. The catalytic converter consists of platinum group metal (PGM) particles supported on a ceramic monolith. The name TWC refers to the simultaneous reduction NO_x and oxidation of CO and hydrocarbons. To achieve high rates of all these three reactions is challenging, since at elevated oxygen content the CO consumption would be too high, depleting the reductant for the converting NO to N_2 . If the oxygen content is too low, all NO can be converted by CO, but hydrocarbons and CO are not fully oxidized. TWC technology makes use of catalysts that when operated under a properly adjusted air-to-fuel ratio of 14.7, controlled by using an oxygen sensor, can achieve high conversion degrees of all three pollutants. Catalytic exhaust gas treatment has contributed to a significant improvement of air quality and is with an estimated market size of 43 billion US\$ an economically important market.



However, since the combustion of fossil fuels is becoming increasingly undesirable due to global warming caused by increasing atmospheric CO₂ concentrations, alternative environmentally benign energy carriers are sought after. A major challenge of using sustainable energy sources is energy storage, which is needed due to the mismatch in time between production and consumption of renewable energy. Here, a promising solution for a sustainable and CO₂ neutral society is the idea of a hydrogen-based economy provided that the electricity for water splitting is derived from renewable sources like wind and solar^{10,11}. Despite the possibility to feed H₂ directly into fuel cells or even combustion engines, it is also attractive to convert it with CO_x or nitrogen into gaseous and liquid hydrogen carriers like hydrocarbons, methanol or ammonia. It has been shown that ammonia can be easily decomposed into hydrogen and N₂ using, for instance, heterogenous Ru catalysts^{12,13}. This would enable facile storage and transport of hydrogen by production of NH₃ in places with plenty of carbon neutral energy and a subsequent shipping to countries with a high energy demand where hydrogen can be recovered by ammonia splitting¹⁴. Converting carbonaceous molecules with hydrogen to energy carriers like methane or methanol is not only an approach to re-use CO_x from the atmosphere or industrial exhaust streams thus alleviating global warming, but also an opportunity to use them as circular feedstock for the chemical industry. As methanation and methanol manufacture are established processes in the chemical industry, existing infrastructure does not need to be adjusted and proven catalysts (e.g., Ni for methanation and Cu/Zn for methanol) are readily available. Additional upgrading steps for methanol like the methanol-to-olefins (MTO) process are currently under investigation and give access to a range of chemicals to replace fossil-based ones. Related to this, CO₂-neutral gasoline is available via the methanol-to-gasoline process (MTG) using ZSM-5 catalysts. This process was initially developed by Mobil in the 1970s. Another process, which circumvents the intermediate formation of methanol, directly converts a mixture of hydrogen and CO_x into fuels. Fischer-Tropsch synthesis (FTS) is currently practically used to convert synthesis gas (syngas) derived from methane or coal into mainly long-chain hydrocarbons and chemicals¹⁵.

1.3 Fischer-Tropsch Synthesis - A historical overview

The Fischer-Tropsch (FT) synthesis is a surface polymerization reaction converting synthesis gas (a mixture of H₂ and CO) into a range of mainly linear paraffins, which can be used for the production of high-quality diesel fuel, gasoline and linear chemicals. The foundation was laid by Sabatier¹⁶ who reported methane formation when synthesis gas (syngas, a mixture of CO and H₂) was passed over a Ni catalyst. The process was further developed for the production of higher hydrocarbons by Franz Fischer and Hans Tropsch at the Kaiser-Wilhelm-Institut für Kohlenforschung in Mülheim an der Ruhr, who published their famous work in 1926 using alkalized Fe as well as Co catalysts^{17,18}. By 1938, 9 FT plants were operated in Germany using synthesis gas derived from coal gasification and Co-based catalysts at about 0.1 MPa, whose total capacity was about 0.66 million tons per year. FT plants were also briefly operated in other places like Japan, Manchuria and France, but were shut down after the Second World War as they were uneconomic^{19,20}. During the period of 1955–1970, the world energy market was governed by cheap oil. As a result, major developments and research in FT synthesis were

mainly restricted to politically isolated South Africa where Sasol had been operating commercial FT plants since 1955. Not only the energy crises of the 1970s but also increasing demand for liquid fuels and the possibility to use abundant natural gas resources caused renewed interest in Fischer-Tropsch synthesis. An overview of currently operated FT plants is given in Table 1.1.

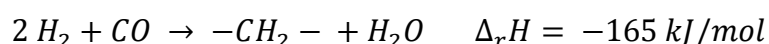
Table 1.1: Overview of commercial FTS plants worldwide.

<i>Company</i>	<i>Country</i>	<i>Time of operation</i>	<i>Capacity (in 10⁶ t/a) (oil equivalent)</i>	<i>Feedstock</i>
<i>Ruhrchemie</i>	Germany	1935-1945	0.5	Coal
<i>SASOL</i>	South Africa	1955 1980 1982	7	Coal/Natural gas
<i>Mossgas</i>	South Africa	1992	1.1	Natural gas
<i>Shell</i>	Malaysia	1993	0.7	Natural gas
<i>SASOL</i>	Qatar	2006	1.7	Natural gas
<i>Shell</i>	Qatar	2011	6.9	Natural gas
<i>Chevron</i>	Nigeria	2014	1.7	Natural gas
<i>Nigeria/SASOL</i>	China	2016/2017	4	Coal
<i>Synfuels China</i>				
<i>Sasol/Petronas/Uzbekneftegaz</i>	Uzbekistan	2021	1.3	Natural gas

Today almost 100 years after the initial discovery by Fischer and Tropsch the reaction is still subject to research as it represents a universal reaction that converts nearly all carbon sources (coal, natural gas, biomass and CO₂), via syngas, into a large range of organic compounds. Recently, FT has received growing attention due to the possibility to produce climate neutral eFuels from H₂ and CO obtained from CO₂ by reverse water-gas shift reaction.

1.4 FT Process

The conversion of syngas, a mixture of H₂ and CO to paraffins is a highly exothermic surface polymerization process.



Even though the underlying mechanism is still not completely understood (see section 1.4 below) it can be divided into four steps:

initiation: dissociation of CO/H₂ and formation of CH_x species

propagation: chain growth by coupling of CH_x species

termination: hydrogenation of the carbon chain (paraffins) or β hydrogen abstraction (olefins) and subsequent desorption from the catalyst surface

secondary reactions: primary hydrocarbon products react further e.g., by olefin readsorption followed by hydrogenation or chain growth reinitiation.

The main products of FT synthesis are linear paraffins and alpha olefins, whereas only minor amounts of branched molecules as well as oxygenates are formed. The product selectivity can be approximated by the Anderson-Schulz-Flory (ASF) distribution, which introduces the chain-growth probability α as a single parameter independent of the chain length to describe the product distribution. This parameter α is defined as the ratio of the rate of propagation k_g to the overall reaction rate being the sum of the growth k_g and termination rate k_t :

$$\alpha = \frac{k_g}{k_g + k_t} \quad (1.1)$$

α is considered one of the most relevant performance indicators of FT catalysts and in general, a high α value is desired to achieve the most efficient utilization of syngas²¹. For a given value of α the fraction of a product molecule with chain length n , C_n , can be calculated via equation 2:²²

$$C_n = (1 - \alpha)\alpha^{n-1} \quad (1.2)$$

However, the simplified approach assumes a carbon-chain-independent growth probability and underestimates methane formation in cases the rate of methane formation is higher than of termination of a single specific chain-length as it is mostly the case for Co-based FT catalysts. For very low α values (e.g. Fe-based FTS to oxygenates), methane formation would be overestimated.

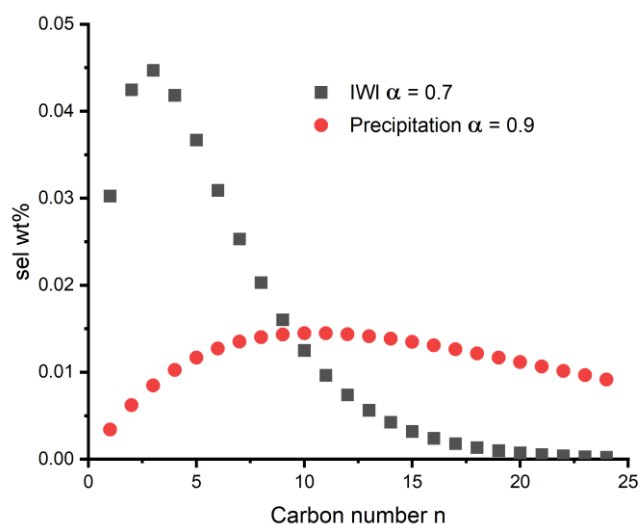


Figure 1.3. Experimental values of the product distribution for Co based catalysts prepared by incipient wetness impregnation (IWI) and precipitation exhibiting different chain growth probabilities α .

Already in 1926 Fischer and Tropsch pointed out that Fe, Ni and Co are active metals for FT synthesis. Ru has been found to be the most active metal, yet due to pricing Fe and Co are the

only metals in use in commercial FT plants²¹. In general, the highest α values, beneficial for high wax yields, are obtained during low-temperature FT synthesis at 200–240°C and 10–40 bar using Co-based catalysts. Fe is much cheaper than Co but has a considerable water–gas shift activity leading to a high CO₂ selectivity. This is advantageous when syngas with a low H₂/CO ratio (<2) is used as a feedstock. Another drawback of Fe-based low-temperature FT synthesis is the relatively low α value, leading to a relatively high fraction of short-chain hydrocarbon. In the case of high-temperature FTS (300–350°C, 10–40 bar), mostly Fe is applied leading to gasoline product, oxygenates and short-chain olefins.

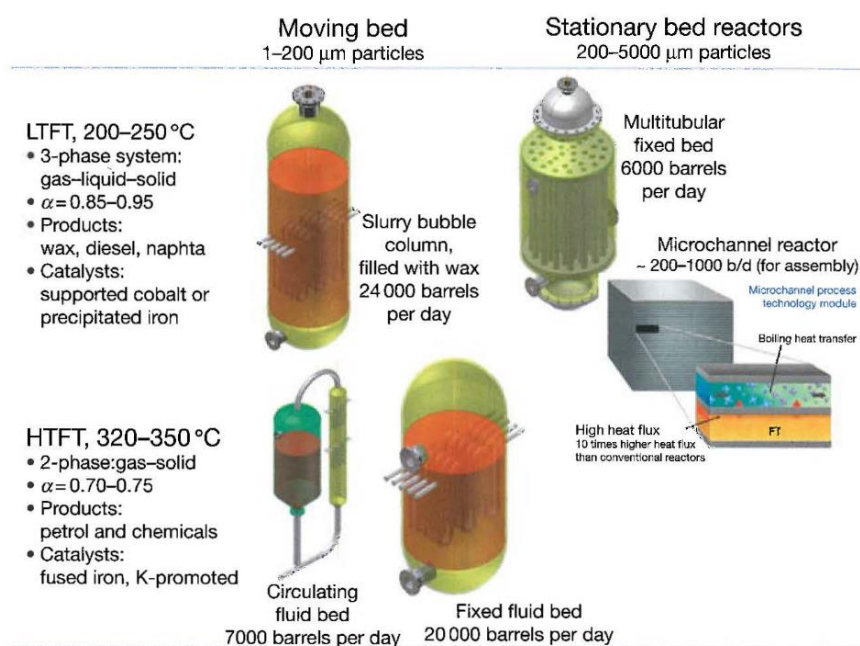


Figure 1.4. Overview of the typical reactor technology and reaction conditions used in FT synthesis. Adapter from [25]

One of the most challenging aspects designing a FT reactor is the handling of the high exothermicity of the reaction in combination with a strong temperature dependency of product selectivity^{23,24}. If the temperature increases, methane formation and termination by hydrogenation is favored decreasing the chain growth rate and lowering the α value. Hence, the reactor must allow efficient heat removal. Four reactor types are used commercially today. For low-temperature synthesis (<250 °C), multi-tubular fixed bed or slurry bubble column reactors are used. For high temperature ($T > 300$ °C), circulating fluidized bed or bubbling fluid bed reactors are used.

1.5 Mechanism and catalyst

Since the discovery of the FTS reaction, a lively discussion about the mechanistic foundations has developed. Nowadays two competing mechanisms are considered relevant, which are the carbide (Fig. 1.5 a) and the CO insertion mechanism²⁶ (Fig. 1.5 b). The former one assumes dissociation of CO and the subsequent formation of CH_x species, which are able to form C-C bonds among each other. The other mechanism explains the chain growth by insertion of a CO molecule into a growing chain (or coupling with a CH_x molecule) forming oxygenates, which is followed by dissociation of the C-O bond. Chain growth thus occurs by repeated insertion of CO followed by CO scission in this mechanism. In order to form long-chain products the carbide

mechanism requires the rate of CO dissociation to be fast compared to the rate of methane formation, which is needed to provide sufficient CH_x intermediates to maintain a high rate of chain growth²⁶. Also, the formation of long-chain products requires the rate of termination to be slow compared to the rate of chain growth. This implies that in the carbide mechanism an increased rate of chain termination by CO insertion or through hydrogen transfer reactions would decrease chain growth, and accordingly the chain-growth probability.

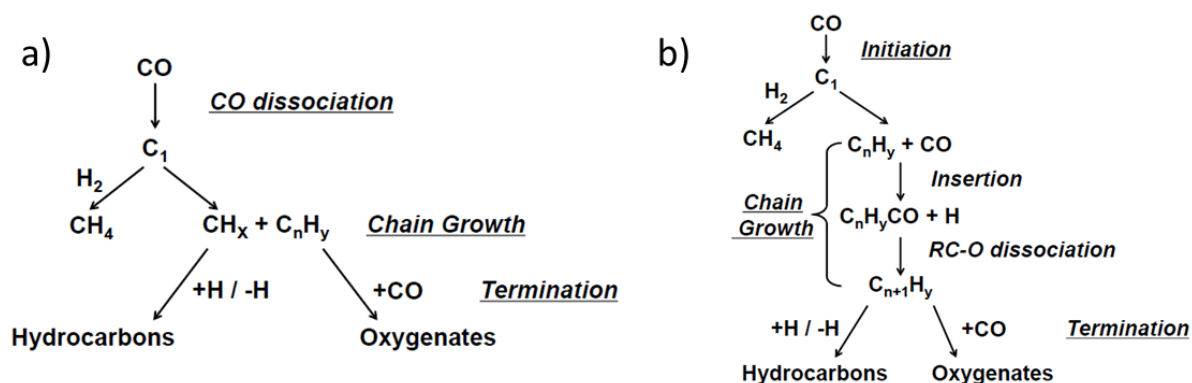


Figure 1.5. Depiction of the most prominent reaction mechanisms for FT synthesis: a) carbide mechanism and b) CO insertion mechanism.

A plethora of kinetic studies and reviews is available discussing the arguments for and against each particular mechanism^{26,27,21}. Since CO dissociation is a pivotal step during FTS independently from the mechanism as in both CH_x species initiate the chain growth, plenty of work has been devoted to the study its exact mechanism. Surface science studies have shown that CO adsorbs molecularly on a flat Co(0001) surface and, in line with this, density functional theory (DFT) calculations predict high activation energies for CO dissociation on this surface^{28,29}. However, single crystal experiments are idealizations as Co nanoparticles can exist of fcc and hcp structures exhibiting different surface terminations as well as defect sites exposing highly reactive undersaturated metal atoms. Actually, experimental³⁰ and theoretical studies³¹ indicate a high activity of certain surface structures for CO dissociation like hcp (11-21) and (10-11), which expose very favorable step sites combining square and triangular geometry on a step (B_5 sites)³¹.

1.6 Promoters

The catalytic performance of FT synthesis catalysts strongly depends on the methods of catalyst preparation as well as choice of support and admixed elements. Already in the fundamental work of Fischer and Tropsch, promoters were used to improve and steer catalytic properties like number of metal sites, resistance to impurities and other characteristics^{32,33}. They can be distinguished by their desired function. Structural promoters influence the formation and stability of the active phase, whereas electronic promoters affect the elementary steps involved in the chemical reaction which takes place on the catalyst. They do so by influencing the electronic structure of an active metal by adding or withdrawing electron density near the Fermi level in the valence band of the metal. As a consequence, the chemisorption properties of the active metal are changed which consequently influences the

catalytic reaction. In addition to the previous mentioned groups synergistic promoters which actively become part of the catalytic cycle are also known.

The main functions of structural promoters are to modify the Co dispersion by modifying the Co-support interactions. A high Co dispersion is desired as it results in a large active Co metal surface area and increases metal usage, for which Pt, Ru and Re can be applied. Structural promotion may lead to an increased catalyst activity and stability but does not influence the product selectivity since it only increases the number of active sites in a catalyst material. This increase is achieved by preventing the formation of metal-support compounds or agglomeration and sintering of Co particles under FT synthesis conditions. Another function of structural promoters is the stabilization of the oxidic support like in the case of TiO_2 , which can be stabilized by adding Zr or Ta³⁴

Electronic effects of promotion can be understood as changing the surrounding (electronic) environment of an active Co site. Electronic promotion can only occur when there is a direct chemical interaction between the promoter element and the cobalt active surface. Which is achieved by either covering the Co particles (in the case of MnO_x ³⁵) or alloying as in the case of noble metals like Pt, Re and Ru.

1.7 Catalyst support

During preparation, the active phase is spread onto a porous support to obtain a highly dispersed phase allowing maximum metal usage. However, in the case of oxidic supports like Al_2O_3 and TiO_2 interactions with oxidic catalyst precursors like Co_3O_4 are inevitable. These so-called metal-support interaction (SMSI) are even more prominent with reducible supports (TiO_2 ^{36,37}, Nb_2O_5 and CeO_2 ³⁸) especially after high temperature activation in hydrogen atmosphere. Several studies have observed an overgrowth of support material covering the metallic nanoparticles. As a consequence, H_2 and CO adsorption can be hampered significantly changing catalytic performance. In the recent years, tuning strong metal-support interactions (SMSI) has led to significant improvements for example by a reduction-oxidation-reduction (ROR) treatment as described in literature^{39,40}. Most likely highly active CoO_x -support compounds are formed which help catalyzing the rate limiting steps during hydrogenation.

1.8 Structure sensitivity in catalysis

Since heterogeneous catalysis is a surface phenomenon only the outermost atomic layer of metal particles is involved in the chemical reaction while the majority of “bulk” atoms remain inaccessible. The most common approach to increase the efficiency of a catalyst is to decrease the number of these bulk atoms by decreasing the particle size of the catalytically active phase thus increasing the surface to volume ratio and consequently exposing more atoms. In the most extreme case, only a single atom would be used for the catalytic reaction which has been recently proven to be feasible in particular cases⁴¹. However, decreasing the particle size of metal particles might alter its properties. For example, although bulk cobalt crystallizes in a hcp crystal system, shrinking Co particles below 20 nm results in predominance of the fcc

phase⁴². Furthermore, the amount and structure of active surface sites with a low coordination number such as edges and corners, defects, or kinks and steps changes when changing the particle size, thus altering the catalytic properties of the catalyst.

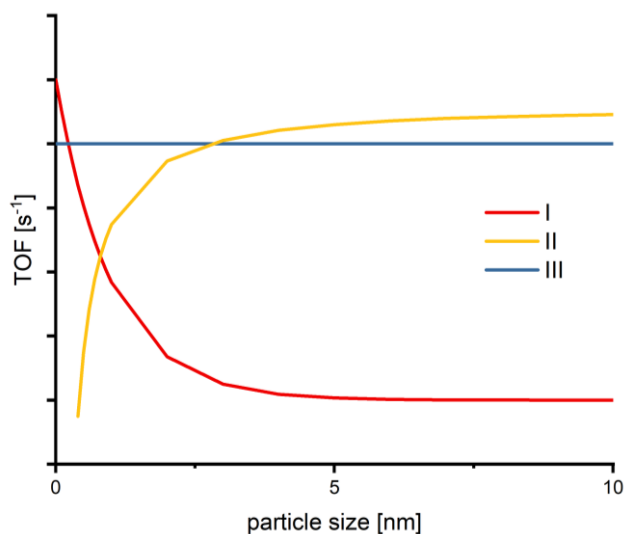


Figure 1.6. Possible scenarios of size-activity relationships as a function of particle size. Type I increasing TOF with decreasing particle size, type II decreasing TOF with decreasing particle size, type III particle size independent TOF.

If the catalytic performance of a reaction depends on the particle size the reaction is classified as structure sensitive, while otherwise it is considered structure insensitive. Based on the understanding of structure sensitivity/in-sensitive-reactivity, reactions can be categorized into three different types, where rate normalized per exposed metal surface atom, (i) decreases, (ii) increases or (iii) remained constant with increasing particle size⁴³.

Structure sensitivity depends strongly on the type of bonds involved in the reaction. Since π and σ bonds have different symmetries, their activation by occupation of antibonding molecular orbitals requires different surface geometries. Some examples of structure insensitive reactions (type III on Fig. 1.1) are benzene hydrogenation on Pt/Al₂O₃⁴⁴ and CO oxidation on Ru catalysts⁴⁵. Also industrially relevant reactions, such as FT synthesis⁴⁶, CO₂ methanation⁴⁷, and methanol synthesis⁴⁸ exhibit type II structure sensitivity. Consequently, surface normalized rate decreases with increasing particle dispersion. In some examples the activity passes a maximum before further decrease as in the case of FT synthesis. In general, type I structure sensitivity results in suboptimal use of the active metal.

Several hypotheses have been developed to explain the structure sensitivity of the FTS reaction. As mentioned above specific atomic configurations on stepped surfaces (B₅ sites) exhibit a favorably low CO activation energy³¹. Since the cleavage of the CO bond is important independent from the preferred mechanism, influencing this reaction step will impact the overall reaction rate. As the amount of irreversibly adsorbed CO increases with sinking particle size^{49,50} B₅ sites will be poisoned preferably due to their high affinity towards CO and its dissociation products. Thus, leaving crystallographic phases unaffected which exhibit a

relatively high activation energy for CO bond cleavage. Consequently, leading to a deterioration of the reaction rate. Another hypothesis is concerned with the amount of B₅ sites on metallic particles which decreases with Co particle size⁵⁰. Literature results point towards a minimum Co particle size necessary to stabilize B₅ sites⁵¹. Below the critical particle size of around 6 nm the fraction of B₅ sites decreases drastically leading to a degradation of the catalytic activity.

1.9 Scope of the thesis

FT synthesis represents a key technology for the conversion of carbonaceous materials to mainly linear alkanes and olefins via synthesis gas (a mixture of H₂ and CO). Despite decades long research devoted to the FT reaction, there is still room for improvements in performance of the catalysts, which can be guided by better understanding of the working mechanism of the FT reaction. As the need for Co is rising due to a high demand for energy applications (e.g., in batteries), a more efficient use of this scarce metal is desirable. The aim of this thesis is to provide a detailed study to optimize Co catalysts with respect to particle size and the use of an Mn promoter. Despite the widespread use of Mn as a cheap promoter in the FT synthesis reaction and many research works on its role, often contradicting results have been reported. Especially at low pressure a strong effect of Mn promotion has been reported, whereas the effect of Mn during high-pressure FT seems to be much smaller. In addition to that, Mn has received increased attention during the last few years for obtaining unprecedented results such as the formation of cobalt carbide, leading to a shift in the product distribution to alcohols or non-ASF type behavior with respect to light olefins. Studying Mn promotion is not only relevant to improve the performance but also to gain a more detailed understanding about the mechanism of the FT reaction, which could clarify the apparently contradicting results in the literature.

To better understand the role of Mn promotion on Co, Co/SiO₂ catalysts promoted by increasing amounts of Mn are studied in **Chapter 2**. SiO₂ is chosen as a support that has relatively weak interactions with these metals. The materials are characterized in detail to develop an understanding of the role of Mn promoter on the structure of the catalysts. The catalysts are evaluated for their performance in the FT reaction in a range of H₂/CO ratios as well as pressures ranging from 1 bar to 20 bar, the higher pressures reflecting industrially relevant conditions. These catalytic tests are complemented by *in situ* IR spectroscopy to characterize the catalyst during CO hydrogenation, providing insight into the reaction mechanism and the role of Mn on Co. A density functional theory study helps rationalize the promotional effect of Mn.

Chapter 3 investigates the effect of the Co particle size on the FTS performance. In order to obtain a set of well-defined catalysts, a new precursor deposition method is applied to obtain TiO₂-supported Co particles with a size smaller than 6 nm. TiO₂ was chosen as a support relevant to commercial practice with stronger Co-support interactions than with SiO₂. The effect of particle size on the catalytic performance at low and high reaction pressure is investigated, confirming a loss of activity and increased methane selectivity as the cobalt particle size falls below 6 nm. Characterization with X-ray absorption spectroscopy and

Mössbauer spectroscopy clarifies the structure and oxidation state of Co particles under working conditions. The differences in the degree of reduction of cobalt can explain the differences in the catalytic activity, where Mn contributes significantly to these differences. By decreasing the reduction temperature from 450 °C, where complete reduction of Co is achieved, to 280 °C, the catalytic performance could be improved significantly with a relatively strong increase of the performance of small Co particles (< 6 nm) in terms of activity and C₅₊ selectivity, especially when promoted by Mn.

In **Chapter 4**, the insights from the previous chapters are used to prepare small (<6 nm) Co particles on TiO₂ with improved catalytic performance compared to their large counterparts (>6 nm). By applying a precipitation method, a narrow particle size distribution for small (<6 nm) and large particles (>6 nm) is obtained at a relatively high Co loading of 10 wt% on TiO₂. *Quasi in situ* XPS is used to determine the oxidation state of the Co catalysts after reduction at 280 °C and 450 °C. As Co reduction degrees are low after reduction at 280 °C, the influence of the FT reaction on the degree of reduction was also studied. XAS is performed to investigate structural differences between particles of similar size derived by impregnation and precipitation. The benefit of combining Co metal with Co- and Mn-oxide obtained by low-temperature reduction in the FT reaction is demonstrated.

Finally, the main findings of this work are summarized in **Chapter 5** and a brief outlook on possible future research directions is presented.

References

- (1) Wisniak, J. The History of Catalysis. From the Beginning to Nobel Prizes. *Educ. Quim.* **2010**, *21* (1), 60–69. [https://doi.org/10.1016/S0187-893X\(18\)30074-0](https://doi.org/10.1016/S0187-893X(18)30074-0).
- (2) Chorkendorff, I.; Niemantsverdriet, J. W. *Concepts of Modern Catalysis and Kinetics*; WILEY-VCH Verlag GmbH & Co. KGaA, 2017.
- (3) Schlögl, R. Heterogeneous Catalysis. *Angew. Chemie - Int. Ed.* **2015**, *54* (11), 3465–3520. <https://doi.org/10.1002/anie.201410738>.
- (4) Rostrup-Nielsen, J. R. Fuels and Energy for the Future: The Role of Catalysis. *Catal. Rev. - Sci. Eng.* **2004**, *46* (3–4), 247–270. <https://doi.org/10.1081/CR-200036716>.
- (5) Mochida, I.; Choi, K. H. An Overview of Hydrodesulfurization and Hydrodenitrogenation. *J. Japan Pet. Inst.* **2004**, *47* (3), 145–163. <https://doi.org/10.1627/jpi.47.145>.
- (6) Sun, M.; Adjaye, J.; Nelson, A. E. Theoretical Investigations of the Structures and Properties of Molybdenum-Based Sulfide Catalysts. *Appl. Catal. A Gen.* **2004**, *263* (2), 131–143. <https://doi.org/10.1016/j.apcata.2003.12.011>.
- (7) Vogt, E. T. C.; Weckhuysen, B. M. Fluid Catalytic Cracking: Recent Developments on the Grand Old Lady of Zeolite Catalysis. *Chem. Soc. Rev.* **2015**, *44* (20), 7342–7370. <https://doi.org/10.1039/c5cs00376h>.
- (8) Dey, S.; Mehta, N. S. Automobile Pollution Control Using Catalysis. *Resour. Environ. Sustain.* **2020**, *2* (September), 100006. <https://doi.org/10.1016/j.resenv.2020.100006>.
- (9) Wang, J.; Chen, H.; Hu, Z.; Yao, M.; Li, Y. A Review on the Pd-Based Three-Way Catalyst. *Catal. Rev. - Sci. Eng.* **2015**, *57* (1), 79–144. <https://doi.org/10.1080/01614940.2014.977059>.
- (10) van der Spek, M.; Banet, C.; Bauer, C.; Gabrielli, P.; Goldthorpe, W.; Mazzotti, M.; Munkejord, S. T.; Røkke, N. A.; Shah, N.; Sunny, N.; Sutter, D.; Trusler, J. M.; Gazzani, M. Perspective on the Hydrogen Economy as a Pathway to Reach Net-Zero CO₂ Emissions in Europe†. *Energy Environ. Sci.* **2022**, *15* (3), 1034–1077. <https://doi.org/10.1039/d1ee02118d>.
- (11) Abe, J. O.; Popoola, A. P. I.; Ajenifuja, E.; Popoola, O. M. Hydrogen Energy, Economy and Storage: Review and Recommendation. *Int. J. Hydrogen Energy* **2019**, *44* (29), 15072–15086. <https://doi.org/10.1016/j.ijhydene.2019.04.068>.
- (12) Szmigiel, D.; Raróg-Pilecka, W.; Miśkiewicz, E.; Kaszkur, Z.; Kowalczyk, Z. Ammonia Decomposition over the Ruthenium Catalysts Deposited on Magnesium-Aluminum Spinel. *Appl. Catal. A Gen.* **2004**, *264* (1), 59–63. <https://doi.org/10.1016/j.apcata.2003.12.038>.
- (13) Wang, Z.; Cai, Z.; Wei, Z. Highly Active Ruthenium Catalyst Supported on Barium Hexaaluminate for Ammonia Decomposition to CO_x-Free Hydrogen. *ACS Sustain. Chem. Eng.* **2019**, *7* (9), 8226–8235. <https://doi.org/10.1021/acssuschemeng.8b06308>.
- (14) Wang, M.; Khan, M. A.; Mohsin, I.; Wicks, J.; Ip, A. H.; Sumon, K. Z.; Dinh, C. T.; Sargent, E. H.; Gates, I. D.; Kibria, M. G. Can Sustainable Ammonia Synthesis Pathways Compete with Fossil-Fuel Based Haber-Bosch Processes? *Energy Environ. Sci.* **2021**, *14* (5), 2535–2548. <https://doi.org/10.1039/d0ee03808c>.

- (15) Dieterich, V.; Buttler, A.; Hanel, A.; Spliethoff, H.; Fendt, S. Power-to-Liquid via Synthesis of Methanol, DME or Fischer–Tropsch-Fuels: A Review. *Energy Environ. Sci.* **2020**, *13* (10), 3207–3252. <https://doi.org/10.1039/d0ee01187h>.
- (16) Sabatier, P. Hydrogenations et Dehydrogenations Par Catalyse. *Berichte der Dtsch. Chem. Gesellschaft* **1911**, 1984.
- (17) Fischer, F.; Tropsch, H. Über Die Direkte Synthese von Erdöl-Kohlenwasserstoffen Bei Gewöhnlichem Druck. **1926**, No. November 1925, 830–831.
- (18) Fischer, F.; Tropsch, H. Über Die Synthese Hochmolekularer Paraffin-Kohlenwasserstoffe Aus Kohlenoxyd. *Berichte der Dtsch. Chem. Gesellschaft* **1927**, 2–6.
- (19) Schulz, H. Short History and Present Trends of Fischer–Tropsch Synthesis. *Appl. Catal. A Gen.* **1999**, *186* (1–2), 3–12. [https://doi.org/10.1016/S0926-860X\(99\)00160-X](https://doi.org/10.1016/S0926-860X(99)00160-X).
- (20) Introduction, G. *Promotion Effects in Co-Based Fischer–Tropsch Catalysis*; 2007; Vol. 19. <https://doi.org/10.1039/9781847555229-00001>.
- (21) Van der Laan, G. P.; Beenackers, A. A. C. M. Kinetics and Selectivity of the Fischer–Tropsch Synthesis: A Literature Review. *Catal. Rev.* **1999**, *41* (3–4), 255–318. <https://doi.org/10.1081/CR-100101170>.
- (22) Weststrate, C. J.; van Helden, P.; Niemantsverdriet, J. W. Reflections on the Fischer-Tropsch Synthesis: Mechanistic Issues from a Surface Science Perspective. *Catal. Today* **2016**, *275*, 100–110. <https://doi.org/10.1016/j.cattod.2016.04.004>.
- (23) Méndez, C. I.; Ancheyta, J.; Trejo, F. Modeling of Catalytic Fixed-Bed Reactors for Fuels Production by Fischer-Tropsch Synthesis. *Energy and Fuels* **2017**, *31* (12), 13011–13042. <https://doi.org/10.1021/acs.energyfuels.7b01431>.
- (24) Dry, M. E. The Fischer-Tropsch Process: 1950-2000. *Catal. Today* **2002**, *71* (3–4), 227–241. [https://doi.org/10.1016/S0920-5861\(01\)00453-9](https://doi.org/10.1016/S0920-5861(01)00453-9).
- (25) Van de Loosdrecht, J.; Botes, F. G.; Ciobica, I. M.; Ferreira, A.; Gibson, P.; Moodley, D. J.; Saib, A. M.; Visagie, J. L.; Weststrate, C. J.; Niemantsverdriet, J. W. *Fischer-Tropsch Synthesis: Catalysts and Chemistry*; 2013; Vol. 7. <https://doi.org/10.1016/B978-0-08-097774-4.00729-4>.
- (26) van Santen, R. a; Markvoort, a J.; Filot, I. a W.; Ghouri, M. M.; Hensen, E. J. M. Mechanism and Microkinetics of the Fischer-Tropsch Reaction. *Phys. Chem. Chem. Phys.* **2013**, *15*, 17038–17063. <https://doi.org/10.1039/c3cp52506f>.
- (27) Pestman, R.; Chen, W.; Hensen, E. Insight into the Rate-Determining Step and Active Sites in the Fischer-Tropsch Reaction over Cobalt Catalysts. *ACS Catal.* **2019**, *9* (5), 4189–4195. <https://doi.org/10.1021/acscatal.9b00185>.
- (28) Weststrate, C. J.; Loosdrecht, J. Van De; Niemantsverdriet, J. W. Spectroscopic Insights into Cobalt-Catalyzed Fischer-Tropsch Synthesis : A Review of the Carbon Monoxide Interaction with Single Crystalline Surfaces of Cobalt. *J. Catal.* **2016**, *342*, 1–16. <https://doi.org/10.1016/j.jcat.2016.07.010>.
- (29) Ge, Q.; Neurock, M. Adsorption and Activation of CO over Flat and Stepped Co Surfaces: A First Principles Analysis. *J. Phys. Chem. B* **2006**, *110* (31), 15368–15380. <https://doi.org/10.1021/jp060477i>.

- (30) Qin, C.; Hou, B.; Wang, J.; Wang, Q.; Wang, G.; Yu, M.; Chen, C.; Jia, L.; Li, D. Crystal-Plane-Dependent Fischer-Tropsch Performance of Cobalt Catalysts. *ACS Catal.* **2018**, *8* (10), 9447–9455. <https://doi.org/10.1021/acscatal.8b01333>.
- (31) Liu, J. X.; Su, H. Y.; Sun, D. P.; Zhang, B. Y.; Li, W. X. Crystallographic Dependence of CO Activation on Cobalt Catalysts: HCP versus FCC. *J. Am. Chem. Soc.* **2013**, *135* (44), 16284–16287. <https://doi.org/10.1021/ja408521w>.
- (32) Khodakov, A. Y.; Chu, W.; Fongarland, P. Advances in the Development of Novel Cobalt Fischer – Tropsch Catalysts for Synthesis of Long-Chain Hydrocarbons and Clean Fuels Advances in the Development of Novel Cobalt Fischer – Tropsch Catalysts for Synthesis of Long-Chain Hydrocarbons and Clean Fue. *Am. Chem. Soc.* **2007**, *107* (5), 1692–1744. <https://doi.org/10.1021/cr050972v>.
- (33) Morales, F.; Weckhuysen, B. M. *Promotion Effects in Co-Based Fischer – Tropsch Catalysis*; Royal Society of Chemistry, 2006; Vol. 19.
- (34) Morales, F.; De Groot, F. M. F.; Gijzeman, O. L. J.; Mens, A.; Stephan, O.; Weckhuysen, B. M. Mn Promotion Effects in Co/TiO₂ Fischer-Tropsch Catalysts as Investigated by XPS and STEM-EELS. *J. Catal.* **2005**, *230*, 301–308. <https://doi.org/10.1016/j.jcat.2004.11.047>.
- (35) Johnson, G. R.; Werner, S.; Bell, A. T. An Investigation into the Effects of Mn Promotion on the Activity and Selectivity of Co/SiO₂ for Fischer–Tropsch Synthesis: Evidence for Enhanced CO Adsorption and Dissociation. *ACS Catal.* **2015**, *5* (10), 5888–5903. <https://doi.org/10.1021/acscatal.5b01578>.
- (36) De La Peña O’Shea, V. A.; Consuelo Álvarez Galván, M.; Platero Prats, A. E.; Campos-Martin, J. M.; Fierro, J. L. G. Direct Evidence of the SMSI Decoration Effect: The Case of Co/TiO₂ Catalyst. *Chem. Commun.* **2011**, *47* (25), 7131–7133. <https://doi.org/10.1039/c1cc10318k>.
- (37) Beck, A.; Huang, X.; Artiglia, L.; Zabilskiy, M.; Wang, X.; Rzepka, P.; Palagin, D.; Willinger, M. G.; van Bokhoven, J. A. The Dynamics of Overlayer Formation on Catalyst Nanoparticles and Strong Metal-Support Interaction. *Nat. Commun.* **2020**, *11* (1), 1–8. <https://doi.org/10.1038/s41467-020-17070-2>.
- (38) Parastaev, A.; Muravev, V.; Huertas Osta, E.; van Hoof, A. J. F.; Kimpel, T. F.; Kosinov, N.; Hensen, E. J. M. Boosting CO₂ Hydrogenation via Size-Dependent Metal–Support Interactions in Cobalt/Ceria-Based Catalysts. *Nat. Catal.* **2020**, *3* (6), 526–533. <https://doi.org/10.1038/s41929-020-0459-4>.
- (39) Melaet, G.; Ralston, W. T.; Li, C.-S.; Alayoglu, S.; An, K.; Musselwhite, N.; Kalkan, B.; Somorjai, G. A. Evidence of Highly Active Cobalt Oxide Catalyst for the Fischer–Tropsch Synthesis and CO₂ Hydrogenation. *J. Am. Chem. Soc.* **2014**, *136* (6), 2260–2263. <https://doi.org/10.1021/ja412447q>.
- (40) Hernández Mejía, C.; van Deelen, T. W.; de Jong, K. P. Activity Enhancement of Cobalt Catalysts by Tuning Metal-Support Interactions. *Nat. Commun.* **2018**, *9* (1), 1–8. <https://doi.org/10.1038/s41467-018-06903-w>.
- (41) Lv, L. B.; Yang, S. Z.; Ke, W. Y.; Wang, H. H.; Zhang, B.; Zhang, P.; Li, X. H.; Chisholm, M. F.; Chen, J. S. Mono-Atomic Fe Centers in Nitrogen/Carbon Monolayers for Liquid-Phase Selective Oxidation Reaction. *ChemCatChem* **2018**, *10* (16), 3539–3545. <https://doi.org/10.1002/cctc.201800707>.

- (42) Kitakami, O.; Sato, H.; Shimada, Y.; Sato, F.; Tanaka, M. Size Effect on the Crystal Phase of Cobalt Fine Particles. *Phys. Rev. B - Condens. Matter Mater. Phys.* **1997**, *56* (21), 13849–13854. <https://doi.org/10.1103/PhysRevB.56.13849>.
- (43) Santen, R. a V. a N. Complementary Structure Sensitive and Insensitive Catalytic Relationships. *Acc. Chem. Res.* **2009**, *42* (1).
- (44) Flores, A. F.; Jr, L. B.; Butt, J. Structure Sensitivity of Benzene Hydrogenation on Supported Pt Catalysts. *J. CHEM. SOC. FARADAY TRANS* **1992**, *88* (8), 1191–1196.
- (45) Joo, S. H.; Park, J. Y.; Renzas, J. R.; Butcher, D. R.; Huang, W.; Somorjai, G. A. Size Effect of Ruthenium Nanoparticles in Catalytic Carbon Monoxide Oxidation. *Nano Lett.* **2010**, *10* (7), 2709–2713. <https://doi.org/10.1021/nl101700j>.
- (46) Bezemer, G. L.; Bitter, J. H.; Kuipers, H. P. C. E.; Oosterbeek, H.; Holeyijn, J. E.; Xu, X.; Kapteijn, F.; Dillen, a J. Van; Jong, K. P. De. Cobalt Particle Size Effects in the Fischer – Tropsch Reaction Studied with Carbon Nanofiber Supported Catalysts Cobalt Particle Size Effects in the Fischer-Tropsch Reaction Studied with Carbon Nanofiber Supported Catalysts. *J. Am. Chem. Soc.* **2006**, No. 6, 11568–11569. <https://doi.org/10.1021/ja058282w>.
- (47) Vogt, C.; Groeneveld, E.; Kamsma, G.; Nachtegaal, M.; Lu, L.; Kiely, C. J.; Berben, P. H.; Meirer, F.; Weckhuysen, B. M. Unravelling Structure Sensitivity in CO₂ Hydrogenation over Nickel. *Nat. Catal.* **2018**, *1* (2), 127–134. <https://doi.org/10.1038/s41929-017-0016-y>.
- (48) Van Den Berg, R.; Prieto, G.; Korpershoek, G.; Van Der Wal, L. I.; Van Bunningen, A. J.; Lægsgaard-Jørgensen, S.; De Jongh, P. E.; De Jong, K. P. Structure Sensitivity of Cu and CuZn Catalysts Relevant to Industrial Methanol Synthesis. *Nat. Commun.* **2016**, *7*. <https://doi.org/10.1038/ncomms13057>.
- (49) den Breejen, J. P.; Radstake, P. B.; Bezemer, G. L.; Bitter, J. H.; Froseth, V.; Holmen, a.; P., D. J. K. On the Origin of the Cobalt Particle Size Effects In. *J. Am. Chem. Soc.* **2009**, *131* (22), 7197–7203. <https://doi.org/10.1016/j.cattod.2008.10.036>.
- (50) Castillo, J.; Arteaga-Pérez, L. E.; Karelovic, A.; Jiménez, R. The Consequences of Surface Heterogeneity of Cobalt Nanoparticles on the Kinetics of CO Methanation. *Catal. Sci. Technol.* **2019**, *9* (22), 6415–6427. <https://doi.org/10.1039/c9cy01753d>.
- (51) Van Helden, P.; Ciobica, I. M.; Coetzer, R. L. J. The Size-Dependent Site Composition of FCC Cobalt Nanocrystals. *Catal. Today* **2016**, *261*, 48–59. <https://doi.org/10.1016/j.cattod.2015.07.052>.

Chapter 2 - Fundamentals of Mn promotion of Co-based Fischer-Tropsch catalysts

Abstract

Although Mn is a common promoter for Co-based Fischer-Tropsch catalysts, literature reports contradicting results on the impact of this promoter on activity and selectivity. This work focuses on the influence of reaction pressure on Mn promotion of Co/SiO₂ in a pressure range of 2-20 bar. Characterization emphasizes the strong interaction between Co and Mn, initially in a spinel oxide and upon reduction in the form of MnO covering part of the metallic Co surface. While increasing the reaction pressure for Co/SiO₂ leads to the expected result of higher rates, higher C₅₊ selectivity and less CH₄, the presence of Mn leads to a different trend. At pressures above 4 bar Mn addition leads to an increase of the C₂-C₄ olefins selectivity at the expense of C₅₊ selectivity. Low-pressure SSITKA shows the promotion of CO dissociation and a higher CH_x coverage by MnO, which can be interpreted as MnO providing additional CO dissociation sites at the Co/MnO interface. Temperature-programmed IR spectroscopy supports easier CO dissociation and formation of longer hydrocarbons in the presence of Mn. The peculiar dependence of the higher hydrocarbon selectivity on reaction pressure for CoMn/SiO₂ is explained by decoupling of CO dissociation and chain-growth sites. At increasing pressure, migration of CH_x species formed on the formed to the latter is hindered due to the high surface coverage.

Published as Tobias F. Kimpel, Jin-Xun Liu, Wei Chen, Robert Pestman, Emiel J.M. Hensen, *Journal of Catalysis* 425 (2023) 181–195

2.1 Introduction

The Fischer-Tropsch reaction is a catalyzed reaction in which hydrocarbons and water are formed from synthesis gas. Several large-scale industrial plants have been constructed based on either synthesis gas derived from coal or natural gas. The interest in future energy scenarios derives from the possibility to obtain synthesis gas from feedstock such as biomass and CO₂ with renewable energy. While most group VIII transition metals exhibit activity in Fischer-Tropsch synthesis (FTS), only Fe and Co have been used in practical FTS catalysts. For FTS with coal-derived synthesis gas with a low H₂/CO ratio, Fe-based catalysts are preferred due to their high water-gas shift activity. When synthesis gas is derived from natural gas, supported Co catalysts are typically used because of their higher activity and higher chain-growth probability in combination with a low water-gas shift activity.^{1,2,3}

A drawback of Co- and Fe-catalyzed FTS is the high methane yield, which often even exceeds the yield predicted by the Anderson-Schulz-Flory (ASF) distribution for polymeric chain growth⁴. Therefore, a lot of research has concentrated on increasing the selectivity to desired longer-chain hydrocarbons. For this purpose, addition of promoters has been studied extensively. Noble metal promoters (e.g., Cu, Pt, Re) are known to increase the reducibility or dispersion of the active phase, but hardly affect the selectivity.⁵ On the other hand, oxides of metals such as Mn, V, Th, Ce, and Cr can improve the selectivity, besides modifying activity and stability. Their promotional effect is however less well understood^{5, 6}.

Since 2000, a large number of works have been devoted to Mn-promoted Co catalysts^{7,8,9,10,11,12,13}. It was found that the use of Mn can enhance the activity and suppresses hydrogenation, leading to a higher chain-growth probability (α) and lower methane selectivity. However, many of the catalytic performance tests in these studies were performed at ambient pressure, which is quite different from the typical industrial conditions (medium total pressures in the range of 10-30 bar). Moreover, studies employing elevated pressure report contradicting results regarding the olefins-to-paraffins (O/P) ratio and the product distribution (C₅₊ and methane selectivity). Thus, the nature of Mn promotion has not been resolved yet. In the past, improved CO dissociation has been ascribed to the binding of the oxygen atom of dissociating adsorbed CO to a redox center^{14,15,16}. More recently, Morales et al.¹⁰ suggested that Mn²⁺ is able to withdraw electron density from Co⁰, leading to more linearly bound CO, thereby suppressing hydrogenation activity¹². The group of Bell^{17,18,6} developed a mechanistic model for Mn promotion where Mn²⁺ acts as a Lewis acid, which facilitates the dissociation of CO. This hypothesis was supported by studying a wide range of metal oxides that showed a similar enhancement of the catalytic performance⁶. Mn has also been said to enhance Co₂C formation.^{19,20} Theoretical studies have shown that Co catalysts operate in the monomer formation limit in which the dissociation of the CO bond is the rate-limiting step²¹. As a result, it seems reasonable to assume that Mn helps to dissociate CO. However, a direct proof is still missing. The aim of this paper is to shed light on the mechanism of Mn promotion and on the abovementioned contradictions about the influence of Mn on Co-catalyzed FTS at practical reaction pressures. We have carried out catalytic tests at low and medium pressure to scrutinize the role of the composition of the surface adsorbed layer on the activity and the

product distribution. To minimize the interference of the support when studying the interaction between Mn and CoSiO₂ was chosen as a support for the research presented in this chapter. Based on the activity data in combination with steady-state isotopic kinetic analysis (SSITKA) and density functional theory (DFT) data, we discuss the role of Mn promotion on Co.

2.2 Methods

2.2.1 Preparation

The silica-supported Co catalysts were prepared by incipient wetness impregnation of SiO₂ (Shell, sieve fraction 120–250 μm , 136 m²/g) with an aqueous solution of Co(NO₃)₂·6H₂O (Merck, 99.99%) and Pt(NH₃)₄·(NO₃)₂ (Alfa Aesar, 99.995 %). Pt (0.04 wt%) was added as a reduction promoter. To study the effect of Mn promotion, Mn(NO₃)₂·xH₂O was added to the solution at atomic Mn/Co ratios of 0.05, 0.1 and 0.25. The impregnated catalysts were dried at 80°C in a flow of 80 vol% He and 20 vol% O₂ for 2h, followed by calcination at 350°C for 2 h (rate 2°C/min). The Co and Mn loadings were determined by ICP-OES elemental analysis (Spectroblue, AMETEK Inc.). The metals were extracted from the catalyst samples by heating in a solution of concentrated HCl. The Co-only catalyst is denoted by Co/Si, while the Mn-promoted Co catalysts are referred to as CoMn(x)/Si with x being the atomic Mn/Co ratio.

2.2.2 X-ray diffraction (XRD)

In situ X-ray diffraction (XRD) patterns were obtained on a Rigaku D/max-2600 X-ray diffractometer. The size of the Co-oxide particles in the calcined catalysts was determined by applying the Scherrer equation to the (311) reflection of the Co₃O₄ phase. Based on the particle size of the cobalt oxide, an estimation can be made of the metal particle size obtained after reduction by multiplication with a factor of 0.75²². The samples were reduced in a flow composed of 10 vol% H₂ in He at a rate of 5°C/min. XRD patterns were recorded every 25°C.

2.2.3 Hydrogen-Temperature Programmed Reduction (H₂-TPR)

H₂-TPR measurements were conducted in a Micromeritics AutoChem II 2920 apparatus, consisting of a U-shaped quartz reactor, a computer-controlled oven and a thermal conductivity detector (TCD) for determining H₂ consumption. In a typical experiment, 50 mg of sample was dried in a flow of He for 1 h at 100°C before ramping to 1000°C at a rate of 10°C/min in a flow of 4 vol% H₂ in He.

2.2.4 XPS

The oxidation state of Co and Mn was characterized using *quasi in situ* XPS in a Kratos AXIS Ultra 600 spectrometer equipped with a monochromatic Al K α X-ray source (Al K α 1486.6 eV). Survey scans were recorded at a pass energy of 160 eV, detailed region scans at 40 eV. The step size was 0.1 eV in both cases. The background pressure during the experiment was kept below 5×10⁻⁹ mbar. A high-temperature reaction cell (Kratos, WX-530) was used to pretreat the sample. The sample was supported on an alumina stub, allowing in vacuo sample transfer into the measurement chamber. Initial reduction was performed in an equimolar mixture of H₂ and Ar flow at atmospheric pressure and 450°C for 8 h. After reduction, the sample was allowed to cool to 150°C and subsequently transferred to the measurement chamber. The XPS data were analyzed with CasaXPS (version 2.3.16 PR 1.6) software.

2.2.5 TEM

TEM measurements were performed on a FEI Tecnai 20 electron microscope at an electron acceleration voltage of 200 kV with a LaB₆ filament. A few milligrams of sample were ultrasonicated in ethanol and dispersed over a carbon-coated Cu grid. The average particle size and particle size distribution was determined by measuring at least 100 particles.

2.2.6 H₂ chemisorption

The metal surface area of the reduced Co catalysts was determined by H₂ chemisorption in a Micromeritics ASAP 2010 apparatus. After reduction of typically 200 mg of catalyst in a flow of 2 vol% H₂ in He at 450°C, the sample was evacuated for 30 min at 470°C to desorb chemisorbed hydrogen. H₂ uptake was determined at 110°C as a function of the H₂ pressure and extrapolated to zero H₂ pressure. The amount of adsorbed H₂ at the ordinate was used to determine the available metal surface area assuming that one H atom adsorbs per surface Co atom.

2.2.7 Infrared spectroscopy

Infrared (IR) spectra were recorded with a Bruker Vertex V70v instrument by averaging 32 scans at a 2 cm⁻¹ resolution. Typically, an amount 15 mg sample was pressed into a self-supporting wafer with a diameter of 13 mm and placed in a homemade controlled-environment transmission IR cell. Prior to IR measurements, the sample was reduced in a flow of H₂ at 450°C for 4 h using a heating rate of 5°C/min. After evacuating for 30 min at 450°C, the sample was cooled *in vacuo*. Prior to CO dosing, a background spectrum was recorded. CO was dosed using a sample loop of 10 µl connected to a 6-way valve. Temperature-programmed IR (TP-IR) spectra were recorded in the presence of synthesis gas (60 mbar H₂, 30 mbar CO) in the temperature range of 50 - 300°C. For these TP-IR measurements, the number of scans was reduced to 16.

2.2.8 Catalytic activity measurements

The catalytic performance of the Co samples was determined in a Microactivity Reference unit (PID Eng&Tech) at a temperature of 220°C and a pressure of 20 bar. In a typical experiment, 150 mg catalyst was homogeneously mixed with SiC particles of the same sieve fraction and placed in a tubular reactor with an internal diameter of 9 mm. The reactor temperature was controlled using a thermocouple located in the center of the catalytic bed. Reduction was carried by heating to 450°C at a rate of 3°C/min in an equimolar flow of H₂ and He, followed by a dwell of 8 h. Then, the reactor was cooled to 220°C and the gas feed was replaced by the reaction mixture, which was synthesis gas with a H₂/CO ratio of 2 diluted with He (volumetric He/H₂/CO = 40/40/20) and containing 4 vol% Ar as an internal standard. The gas-hourly space velocity (GHSV) of the total gas flow was 1000 h⁻¹, which resulted in typical conversion levels in the range of 5 to 15%. A TRACE 1300 gas chromatograph of Thermo Scientific Instruments equipped with a TCD and FID was used to analyze the effluent reaction mixture. Hydrocarbons (C₁-C₁₂) were separated using a Rt-Silica BOND column and subsequently analyzed using an FID. The analysis of light gases H₂, CO₂, CH₄, C₂H₄, C₂H₆, Ar, and CO was performed with a TCD in combination with Molsieve 5A (mesh 60/80, 2 m) and two Rt-XL Sulfur columns (0.25 m and 1 m). Under the applied reaction conditions, CO₂ was not detected as a reaction product and

the carbon-based selectivity of oxygenates was lower than 1 %. Liquid products and waxes were collected in a rearward cold trap. The CO conversion (X_{CO}) was determined based on equation (2.1), the selectivity to product i (S_i) by equation (2.2), the reaction rate (r_{CO}) by equation (2.3) and the turnover frequencies TOF_{CO} and TOF_{CH_4} by equations 2.4 and 2.5, respectively.

$$X_{CO} = \left(1 - \frac{\frac{CO_{out}}{Ar_{out}}}{\frac{CO_{in}}{Ar_{in}}}\right) \quad (2.1)$$

$$S_i = \frac{Ar_{in} \cdot \nu_i \cdot C_i}{Ar_{out} CO_{in} X_{CO}} * 100 \% \quad (2.2)$$

$$r_{CO} = \frac{F_{CO}^0 X_{CO}}{m_{Co}} \quad (2.3)$$

$$TOF_{CO} = \frac{X_{CO} \cdot F_{CO}^0}{mol\ Co \cdot D_{H_2}} \quad (2.4)$$

$$TOF_{CH_4} = \frac{X_{CO} \cdot F_{CO}^0 \cdot S_{CH_4}}{mol\ Co \cdot D_{H_2}} \quad (2.5)$$

where CO_{in} / CO_{out} and Ar_{in} / Ar_{out} represent the CO/Ar concentration in the inlet/outlet flow, respectively. ν_i stands for the number of carbon atoms in species i , F_{CO}^0 represents the inlet flow of CO (mol/s), m_{Co} the mass of cobalt (g), $mol\ Co$ the number Co atoms (mol) and D_{H_2} the dispersion (-) determined by H_2 chemisorption.

2.2.9 Steady-state isotopic transient kinetic analysis (SSITKA)

Steady-state isotopic transient kinetic analysis (SSITKA) was used to determine coverages and residence times of reaction intermediates under steady-state conditions. The details of the SSITKA setup have been described elsewhere²³. Typically, an amount of 200 mg catalyst diluted with SiC of the same sieve fraction was loaded in a low dead-volume stainless-steel tubular reactor with an inner diameter of 5 mm and a bed length of 80 mm. The sample was reduced at 450°C using a rate of 3°C/min at ambient pressure for 8 h in a flow of 50 mL/min consisting of 10 vol% H_2 in Ar. Subsequently, the reactor was cooled to 220°C in an Ar flow and the pressure was increased to 1.85 bar. Then, the reactor feed was switched to a mixture of ^{12}CO , H_2 , and Ar for 16 h. The H_2 flow was varied to change the H_2/CO ratio, while the Ar flow was adjusted such that a total flow rate of 50 mL/min was maintained. A SSITKA switch was made from $^{12}CO/H_2/Ar$ to $^{13}CO/H_2/Ne$. The transients of ^{12}CO ($m/z = 28$) and ^{13}CO ($m/z = 29$), the main hydrocarbon product $^{12}CH_4$ ($m/z = 15$) and $^{13}CH_4$ ($m/z = 17$), and the inert tracers (Ne, $m/z = 22$) were recorded by online mass spectroscopy (quadrupole mass spectrometer, ESS, GeneSys Evolution). Surface residence times were calculated via the area under the normalized transient curves N_i , while a correction was applied for the gas-phase hold-up with the use of the inert Ne tracer:

$$\tau_i = \int_0^\infty (N_i - N_{Ne}) dt \quad (2.6)$$

The CH_x intermediate (precursor to CH_4) residence time was corrected for the chromatographic effect of CO by subtracting half of the CO residence time by [9, 20, 21]:

$$\tau_{CH_4}(corrected) = \tau_{CH_4} - \frac{1}{2}\tau_{CO} \quad (2.7)$$

The amount of CH_x and reversibly adsorbed CO species can be estimated from the residence time and effluent flow of these species. The coverage of the two species (θ_i) was calculated by dividing the number of relevant adsorbed species by the number of Co surface atoms determined by H₂ chemisorption.

$$\theta_{CO} = \frac{\tau_{CO}F_{CO}(1-X_{CO})}{A_{Co}} \quad (2.8)$$

$$\theta_{CH_4} = \frac{\tau_{CH_4}F_{CO}X_{CO}S_{CH_4}}{A_{Co}} \quad (2.9)$$

where F_{CO} refers to the CO feeding, X_{CO} and S_{CH_4} refer to the CO conversion and CH₄ selectivity, respectively, determined by online GC analysis.

2.2.10 Density functional theory (DFT) calculations

All spin-polarized DFT calculations were performed using projector augmented wave (PAW)²⁴ potentials and the Perdew–Burke–Ernzerhof (PBE) functional²⁵ as implemented in the Vienna ab initio simulation package (VASP).^{26,27} The surface model consisted of a Mn₄O₄ cluster placed on the dense (0001) surface of hcp Co. The Co(0001) surface unit cell is a p(3×3) slab model with three atomic layers of Co. Details about the genetic algorithm (GA) to identify the global minimum structure of the Mn₄O₄ cluster on the Co(0001) surface have been given elsewhere.²⁸ To accelerate the GA calculations, the cutoff energy was limited to 300 eV, the convergence threshold for geometry optimization was set to 10⁻³ eV and Brillouin zone sampling was restricted to the Γ point. The GA optimization procedure yielded 600 structures in 80 cycles. Using the most stable Mn₄O₄/Co(0001) structure, we determined reaction energy diagrams for the dissociation of CO at the interface of Co and MnO, inspired by similar pathways explored for a Mn₄O₄/Ni(111) model.²⁹ The cutoff energy for the plane waves was 400 eV. The geometry optimization was converged until the maximal residual force was smaller than 0.02 eV/Å and the electronic self-consistent field was converged to 1 × 10⁻⁴ eV. Neighboring slabs were separated by a vacuum of 15 Å to avoid self-interactions. A Monkhorst-Pack k-points sampling of 2×2×1 was employed.³⁰ Transition states were located by the force reversed³¹ and climbing-image nudged elastic band (CI-NEB)^{32,33} methods with a force tolerance of 0.02 eV/Å.

2.3 Results

2.3.1 Characterization

The metal content of the silica-supported Co catalysts was determined by ICP elemental analysis (Table 2.1). The Co loading was slightly lower than the intended 20 wt%, which is likely due to the presence of crystal water in the metal salt precursors. The actual atomic Mn/Co ratios were as targeted. The XRD patterns in Fig. 2.1 show Co₃O₄ as the only crystalline phase in the calcined precursors. The broad scattering feature around 23° is typical for amorphous silica. The XRD patterns do not contain indications of separate Mn-oxide phases. Nevertheless, a shift was observed in the diffraction angle of the Co₃O₄ reflections to lower angles with increasing Mn content together with a broadening of these reflections (Fig. 2.1b). These changes can be explained by the incorporation of Mn in the spinel structure of Co₃O₄. Substitution of Co by Mn leads to an expansion of the unit cell, explaining the decrease in the Bragg angles of the Co₃O₄ reflections. The observed isotropic peak broadening is likely the consequence of an increasing non-uniform strain caused by Mn substitution. The peak broadening could also be caused by a decrease in Co₃O₄ particle size. This explanation can nevertheless be discarded as TEM analysis (Appendix Fig. A3) displays a nearly constant size of the Co₃O₄ particles (12.6 ± 4.1 nm for Co/Si vs. 11.9 ± 2.7 nm for CoMn(0.1)/Si). Therefore, the peak broadening can be ascribed to non-uniform deformation of the unit cells. The decrease in the intensity of the main diffraction lines is most likely due to a change in the structure factor, which depends on the crystal system and the atomic scattering factor of the species occupying the unit cell (Fig. A1). Mn exhibits a lower atomic scattering factor than Co, contributing to the decreasing intensity. The XRD analysis emphasizes the strong interaction of Co and Mn in the oxidic precursor.

Table 2.1. Characterization of CoMn/Si catalysts.

Sample	Co (wt%)	Mn (wt%)	Mn/Co ratio	d _{XRD} Co ₃ O ₄ (nm) ¹	d _{XRD} Co metal (nm) ²	TEM Co ₃ O ₄ (nm)	H ₂ chem. (mmol H ₂ /g)
Co/Si	19.2	0	0	14.6	11.0	12.6 ± 4.1	0.097
CoMn(0.05)/Si	18.8	0.95	0.05	10.1	7.6		0.086
CoMn(0.1)/Si	17.4	1.68	0.1	10.8	8.1	11.9 ± 2.7	0.055
CoMn(0.25)/Si	16.3	3.85	0.25	9.9	7.4		0.042

¹ Particle size determined via the Scherrer equation of the (311) reflection; ² Estimated metal particle size derived from the size of Co₃O₄ particle by multiplication with 0.75.

We also used H₂ chemisorption to compare the available surface area of metallic Co in the reduced catalysts. The data in Table 2.1 show that the amount of chemisorbed H₂ strongly decreases with Mn content. As the particle sizes do not differ much, this decrease can be assigned to partial coverage of metallic Co surface by Mn-oxide species.^{12,34,18} These earlier studies also concluded that the presence of Mn did not significantly change the particle size of the Co upon reduction.

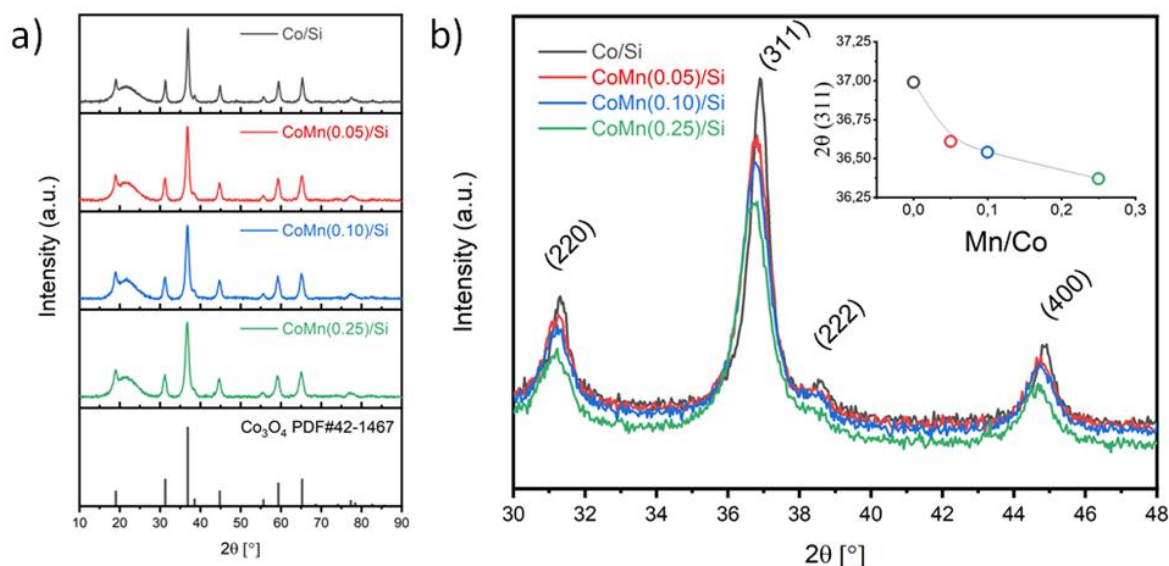


Figure 2.1. XRD analysis of calcined Co/Si and CoMn/Si catalysts: (a) XRD patterns, (b) zoom to emphasize the shift in the XRD reflections of Co_3O_4 (the inset shows the peak position of the (311) reflection of Co_3O_4 as a function of the Mn/Co ratio).

The reduction behavior of the catalysts was studied with H_2 -TPR (Fig. 2.2). Two distinct peaks observed at 303°C and 371°C can be explained by the sequential reduction steps $\text{Co}_3\text{O}_4 \rightarrow \text{CoO} \rightarrow \text{Co}^0$.³⁵ The initial reduction $\text{Co}_3\text{O}_4 \rightarrow \text{CoO}$ is only slightly affected by Mn addition, while subsequent reduction from $\text{CoO} \rightarrow \text{Co}^0$ is delayed from 371°C to 465°C. This implies that the initial reduction of the spinel Co_3O_4 structure is hardly influenced by the incorporation of Mn, but that the last reduction step of CoO to metallic cobalt is strongly hindered by the presence of Mn, indicating a strong interaction between manganese oxide and cobalt remains after the spinel structure has ceased to exist.

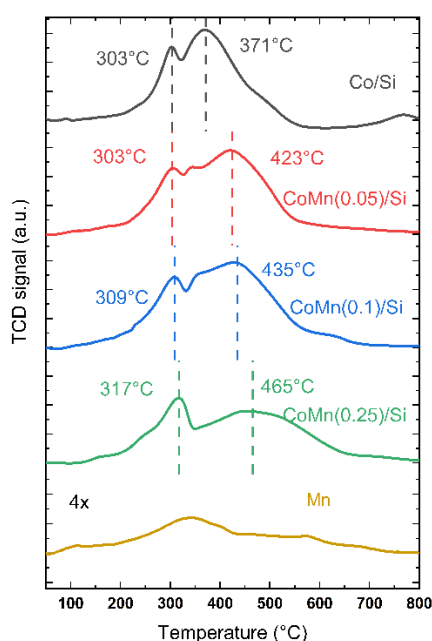


Figure 2.2. TPR of Co/Si and CoMn/Si catalysts including a Mn/Si reference (1.5 wt% Mn on SiO_2).

The structural evolution of the Co/Si and CoMn(0.1)/Si samples (CoMn(0.1)/Si was used as a reference for Mn-promoted samples as it showed the best performance during SSITKA experiments) during reduction was also monitored by *in situ* XRD (Fig. 2.3). Consistent with the TPR results, the reduction of Co_3O_4 proceeds in two steps via an intermediate CoO phase. The onset of Co_3O_4 reduction is just above 200°C. The resulting CoO phase is reduced at lower temperature for Co/Si than for the Mn-containing sample, which is in agreement with the TPR results. XRD shows that metallic Co is already formed at 275°C with a slight delay for the CoMn(0.1)/Si sample.

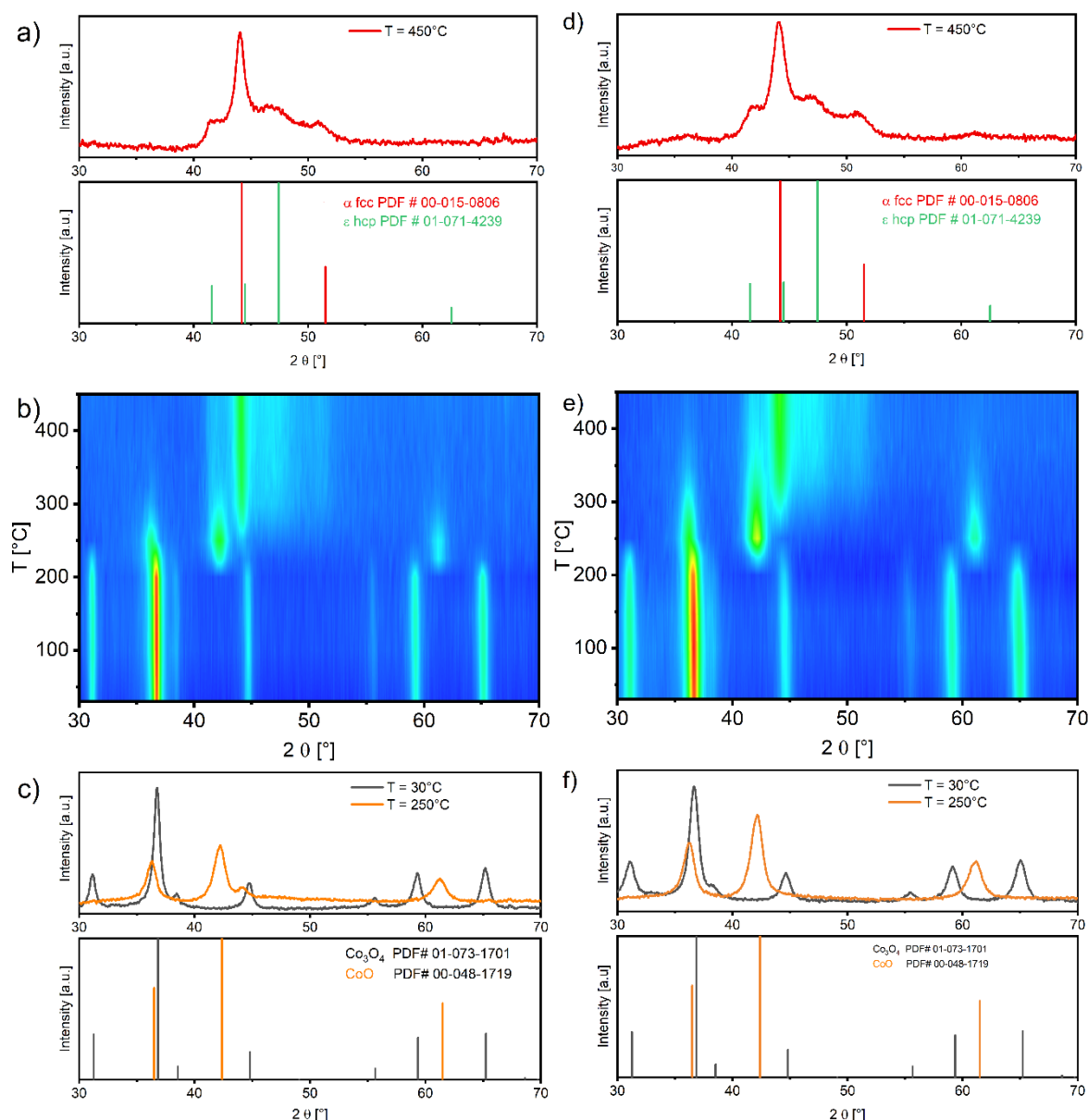


Figure 2.3. *In situ* XRD of reduction of (left panels) Co/Si and (right panels) CoMn(0.1)/Si: (a) and (d) after reduction at 450°C, (b) and (e) heat plot of XRD patterns as a function of temperature, and (c) and (f) after reduction at 30°C and 250°C. Reference spectra of hcp and fcc Co, CoO and Co_3O_4 are included.

Analysis of the patterns obtained after reduction at 450°C indicates that the metallic Co nanoparticles consist of fcc and hcp crystal structures with the former dominating. The hcp/fcc

ratio can have a substantial impact on the catalytic performance of Co nanoparticles with hcp Co being suggested to be more active than fcc Co²⁸. Although it has been observed that unusual bcc phases induced by the presence of Mn can influence the fcc/hcp ratio of supported CoMn catalysts,³⁶ the XRD patterns of the reduced catalysts (Fig. 2.3) do not evidence a substantial difference in the hcp/fcc ratio with changing Mn content. Structural characterization by EXAFS suggested that the reduced Co nanoparticles are not a simple mixture of fcc and hcp nanoparticles, but instead can be represented by intergrown structures of fcc and hcp Co, exhibiting stacking faults that cannot be detected by XRD.³⁷ The main influence of Mn appears to be a slower reduction of CoO to metallic Co, likely by forming double Mn-Co-oxides. It has been reported that such double oxides reduce at a higher temperature than Co oxide or a physical mixture of Mn- and Co-oxide.³⁵

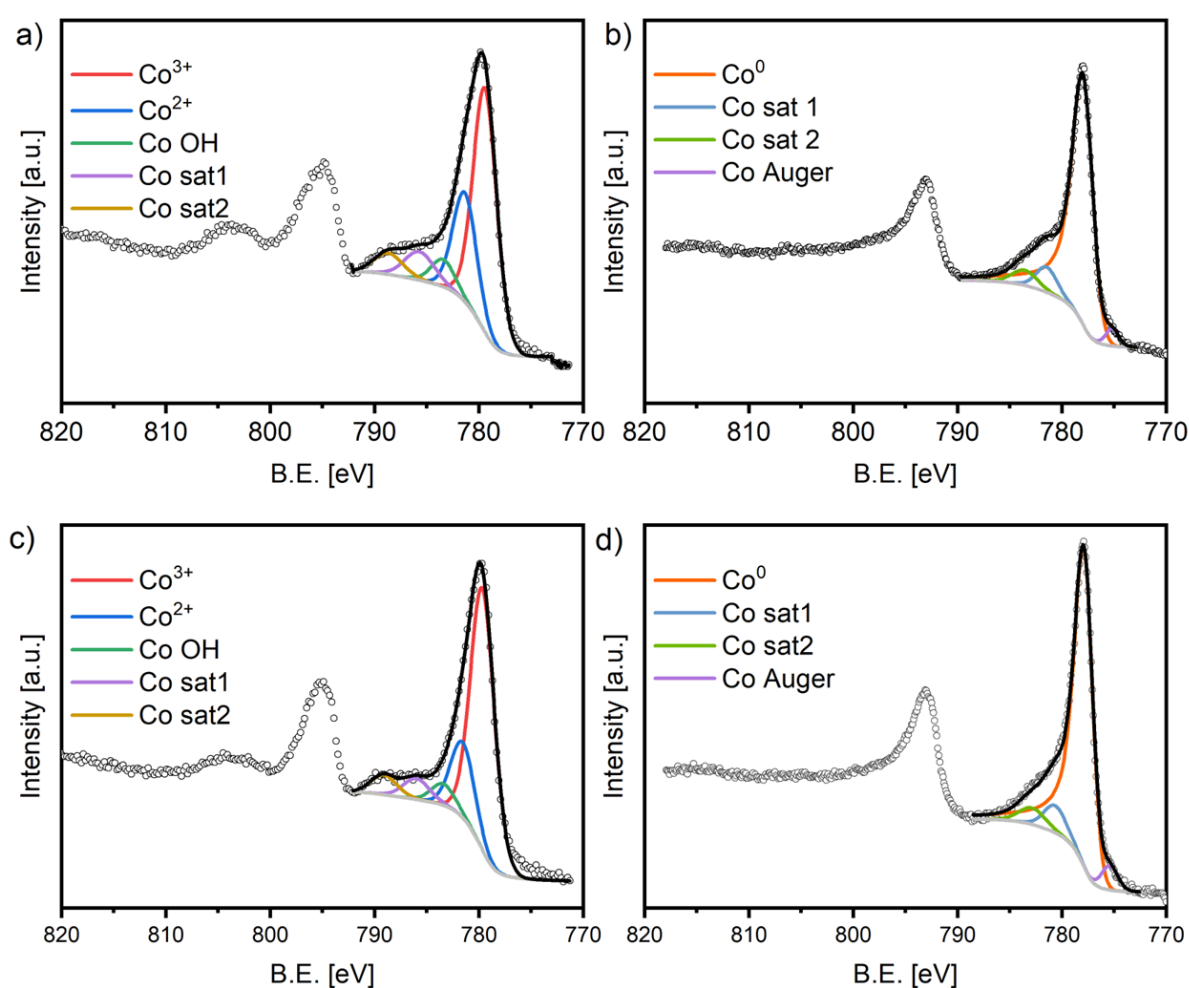


Figure 2.4. Quasi in situ XPS spectra of the Co 2p region of calcined and reduced (450°C) catalysts: (a) calcined Co/Si, (b) reduced Co/Si, (c) calcined CoMn(0.1)/Si, and (d) reduced CoMn(0.1)/Si.

Fig. 2.4 shows the Co 2p XPS spectra for Co/Si and CoMn(0.1)/Si before and after reduction at 450°C. Reduction was done in the pretreatment chamber directly connected to the XPS analysis chamber, permitting *quasi in situ* XPS characterization. The spectra of the calcined precursors contain contributions of Co²⁺ and Co³⁺ at 781.4 and 779.6 eV, respectively. This assignment is supported by the presence of satellite features characteristic for Co₃O₄³⁸. The

presence of Mn decreases the Co^{2+} peak intensity of $\text{CoMn}(0.1)/\text{Si}$ compared to the Mn-free sample. The $\text{Co}^{3+}/\text{Co}^{2+}$ ratio increases from 2.2 for the Co/Si to 3.5 for the $\text{CoMn}(0.1)/\text{Si}$ sample, which indicates a preferential substitution of Co^{2+} by Mn^{2+} ions in the mixed oxide spinel structure. After reduction at 450°C for 8 h, the XPS spectra are dominated by a feature at 778.1 eV assigned to Co^0 , suggesting a nearly complete reduction of Co in both samples.

The oxidation state of Mn was also investigated by XPS. The Mn 2p XPS spectra of the calcined and reduced $\text{CoMn}(0.1)/\text{Si}$ catalyst are given in the appendix (Fig. A4). Both spectra are dominated by satellite features characteristic for MnO, which are typically not observed for Mn_2O_3 and MnO_2 ³⁸. Resolving the Mn oxidation state from the 2p core line is challenging due to overlapping features at similar binding energies³⁸. Instead, analysis of the Mn 3s XPS spectra can provide insight into the Mn oxidation state. The splitting of the Mn 3s core line in these spectra originates from the exchange coupling of 3s holes and 3d electrons of Mn.³⁹ Typical reported splitting values are 4.5-4.8 eV for MnO_2 , 5.3-5.4 eV for Mn_2O_3 , 5.5-5.6 eV for Mn_3O_4 , and 5.6-5.8 eV for MnO.^{40,41,42} Comparison of the Mn 3s peak splitting values of $\text{CoMn}(0.1)/\text{Si}$ before and after calcination shows that Mn is reduced from Mn^{3+} (3s splitting of 5.0 eV) to Mn^{2+} (spin-orbital splitting for the Mn 3s 5.8 eV). Finally, it is worthwhile to note that the Mn/Co ratio after reduction (0.98) is higher than before reduction (0.57). It can thus be inferred that Mn migrates from the oxide precursor as Mn^{3+} to the surface of the metallic Co particles as MnO. The presence of MnO at the surface of reduced Co nanoparticles has been reported before⁸. Based on the XPS analysis, it cannot be determined on which kind of surface structure the MnO is located. However, as chain growth still occurs after Mn addition (see below), it is unlikely that MnO is located on stepped sites, which catalyze chain growth.

2.3.2 Catalytic activity measurements

The influence of Mn on Co was evaluated using typical industrial conditions, *i.e.*, at a pressure of 20 bar, a temperature of 220°C , and a H_2/CO ratio of 2. The reaction rate, product distribution, ASF plots, and olefins-to-paraffins (O/P) ratios as a function of increasing Mn content are shown in Fig. 2.5. Notably, the Co-weight-based activity decreases with increasing Mn content, while the TOF based on H_2 chemisorption remains relatively constant after $\text{Mn}/\text{Co} = 0.05$. Seemingly, the site-normalized activity is constant and the decrease in the weight-based activity can be ascribed to a decrease of the active surface area caused by Mn surface decoration. However, the selectivity of the remaining active surface sites is influenced significantly by Mn addition. The product distribution data show that Mn addition under these conditions results in an increase in the $\text{C}_2\text{-C}_4$ hydrocarbons selectivity from 7.7 % for $\text{Mn}/\text{Co} = 0$ to a maximum of 29 % for $\text{Co}/\text{Mn} = 0.1$. At higher Mn/Co values, a small decrease in the light hydrocarbon selectivity is observed. The CH_4 selectivity decreases slightly and monotonously from 8.8 % at $\text{Mn}/\text{Co} = 0$ to 7.3 % at $\text{Mn}/\text{Co} = 0.25$. The increased selectivity to $\text{C}_2\text{-C}_4$ hydrocarbons goes at the expense of C_{5+} formation, which decreases from 84 % to 60 %). These differences are also reflected in the ASF plots. Whereas the unpromoted sample follows the typical ASF distribution with a CH_4 selectivity higher than predicted by the ASF plot, Mn addition leads to a lower than predicted CH_4 selectivity. This is clearly due to a significant drop

in the chain-growth probability, while at the same time the CH₄ selectivity is hardly changed. It is also interesting to mention that the addition of Mn increases the O/P ratio (Fig. 2.5d).

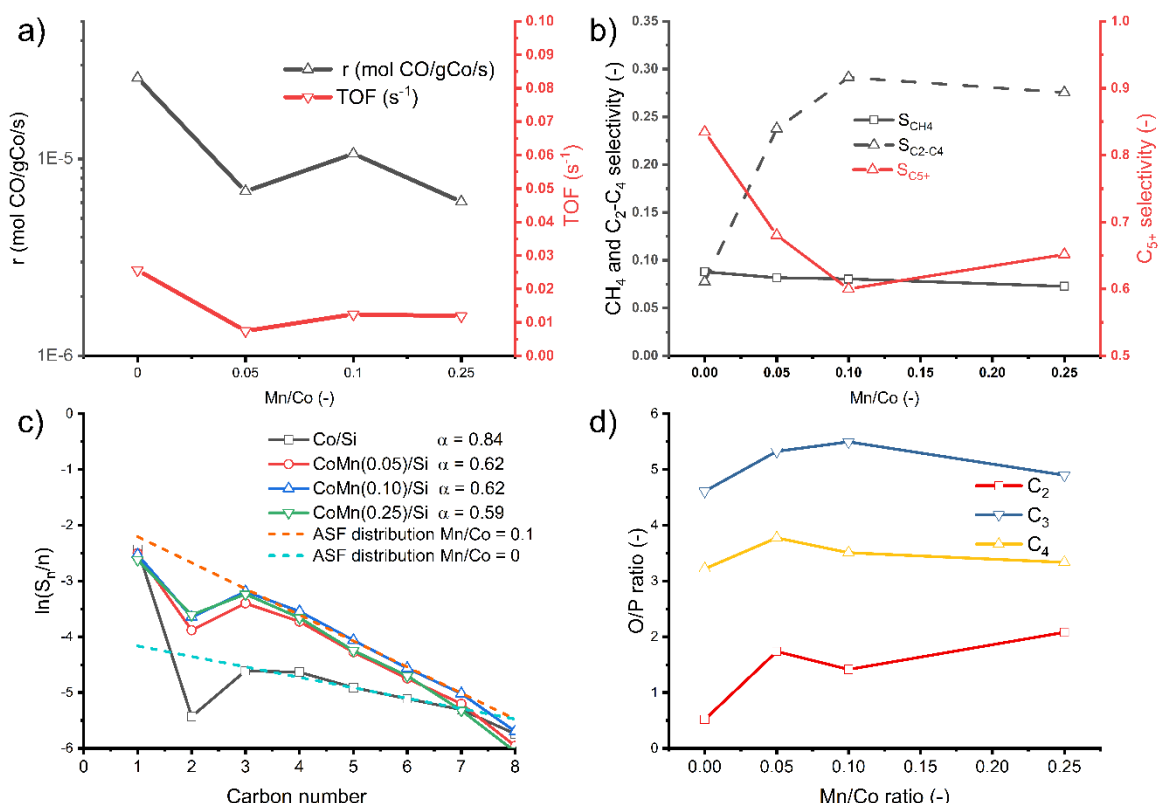


Figure 2.5. Catalytic performance of reduced Co/Si and CoMn/Si catalysts ($p = 20$ bar, $T = 220$ °C, $H_2/CO = 2$): (a) Reaction rate (mol CO/gCo) and TOF (s^{-1}) as a function of Mn/Co ratio, (b) CH₄, C₂-C₄ and C₅+ selectivity as a function of Mn/Co ratio, (c) Anderson-Schulz-Flory (ASF) plot, (d) O/P ratios for C₂, C₃ and C₄ hydrocarbons as a function of Mn/Co ratio.

It is worthwhile to compare these data with performance data published earlier for Mn-promoted catalysts. Especially early studies from Hutchings et al. emphasized exceptionally high alkene, in particular propylene, yields^{43,44,45} of up to 20 wt%, in conjunction with an improved activity and stability upon addition of Mn in relatively large amounts (Mn/Co > 1). Also patent literature from ExxonMobil reported about CoMn catalysts exhibiting a high C₂-C₄ selectivity of 26 % with a total C₂-C₄ olefins content of 83%⁴⁶. Zong et al.¹⁹ linked the increased light olefins selectivity to the formation of Co₂C. Yet, the CO₂ selectivity was close to 50 % in their study. The CO₂ selectivity in the present study and other earlier studies is less than 1 %, which is typical for metallic Co catalysts. Furthermore, *in situ* XRD (Fig. A8) data shows very limited signs of Co₂C formation, ruling out any dominant role of carburized Co. The data obtained at 20 bar and presented in Fig. 2.5 clearly show that Mn promotion suppresses the coupling of the chain-growth monomers (CH_x) as well as olefin hydrogenation. Decreased chain growth and suppressed hydrogenation of olefins might be a result of an increased surface coverage due to the presence of Mn, hindering olefin re-adsorption and possibly monomer coupling. To verify this hypothesis, the role of surface coverages was investigated further by studying the pressure dependence of the catalytic performance of both the promoted and unpromoted catalysts. Since pressure is also expected to influence the surface

coverages. The catalyst with an Mn/Co ratio of 0.1 was chosen as representative for the Mn-promoted catalysts, as it exhibits the largest influence of Mn promotion on the Co catalyst performance, not only at high pressure (see Fig. 2.5 above) but also at low pressure (see Fig. 2.7 below). The influence of the studied pressure dependence is shown in Fig. 2.6. It appears that the presence of Mn strongly influences the pressure dependence of the catalytic performance. As mentioned in the introduction, earlier catalytic tests at elevated pressure contradict each other regarding the influence on the O/P ratio and the selectivities to either C₅₊ or CH₄^{7,8,9,10,11,12,13,12,13,14}. As a consequence, the product distribution data reported here for high pressure cannot be in agreement with all literature. However, the unpromoted catalyst behaves in good keeping with most reports, since the rate and TOF increase with increasing pressure (see Fig. 2.6a)^{47,18,48}. Typically, reaction orders with respect to CO and H₂ for Co catalysts are slightly negative and close to unity, respectively^{49,18}. This results in an overall increase in reaction rate with increasing total pressure at constant H₂/CO. The selectivities of the unpromoted catalyst also behave as anticipated: at increasing pressure an increasing monomer coverage is expected, which results in a higher C₅₊ selectivity (Fig. 2.6c) and lower selectivity to CH₄ and C₂-C₄ products (Fig. 2.6b). However, in contrast to the unpromoted Co, the Mn-promoted catalyst has surprisingly a maximum in both the rate and the TOF at around 4 bar. Above this pressure, there is no clear increase (Fig. 2.6a). The Mn-promoted catalyst follows at increasing pressure the same trends in product distribution as the unpromoted one, but reaches a maximum C₅₊ selectivity at about 4 bar and a minimum for the C₂-C₄ selectivity at the same pressure (Fig. 2.6c). Only the CH₄ selectivity decreases with increasing pressure for both catalysts (Fig. 2.6b), although the influence of Mn promotion on the CH₄ selectivity diminishes with increasing pressure. Understandably, the C₅₊ selectivity mirrors the selectivity to the other hydrocarbons CH₄ and C₂-C₄ for both catalysts. Notably, at low pressure, the Mn-promoted catalyst has a higher C₅₊ selectivity and a lower C₂-C₄ selectivity than the unpromoted catalyst. However, an almost opposite selectivity distribution is observed at 20 bar, when the Mn-promoted catalyst has a lower C₅₊ selectivity and a higher C₂-C₄ selectivity. The turning point from one selectivity being higher than the other occurs around 4 bar. Fig. 6c also shows that over the whole pressure range Mn promotion increases the olefin to paraffin ratio of the C₃ hydrocarbons. It can thus be concluded that an increase in total pressure for the unpromoted catalyst leads to a similar effect as an increase in Mn content at low pressure, i.e., an increased activity, C₅₊ selectivity, and O/P ratio. These two similar effects can tentatively be explained in the same way: Mn promotion as well as an increased pressure enhance the coverage of surface species, hindering hydrogenation of olefins by re-adsorption and increasing the coupling probability of growth monomers. In order to determine the role of the surface adsorbed layer on the selectivity trends, the surface coverages were measured by steady-state isotopic transient kinetic analysis (SSITKA) experiments.

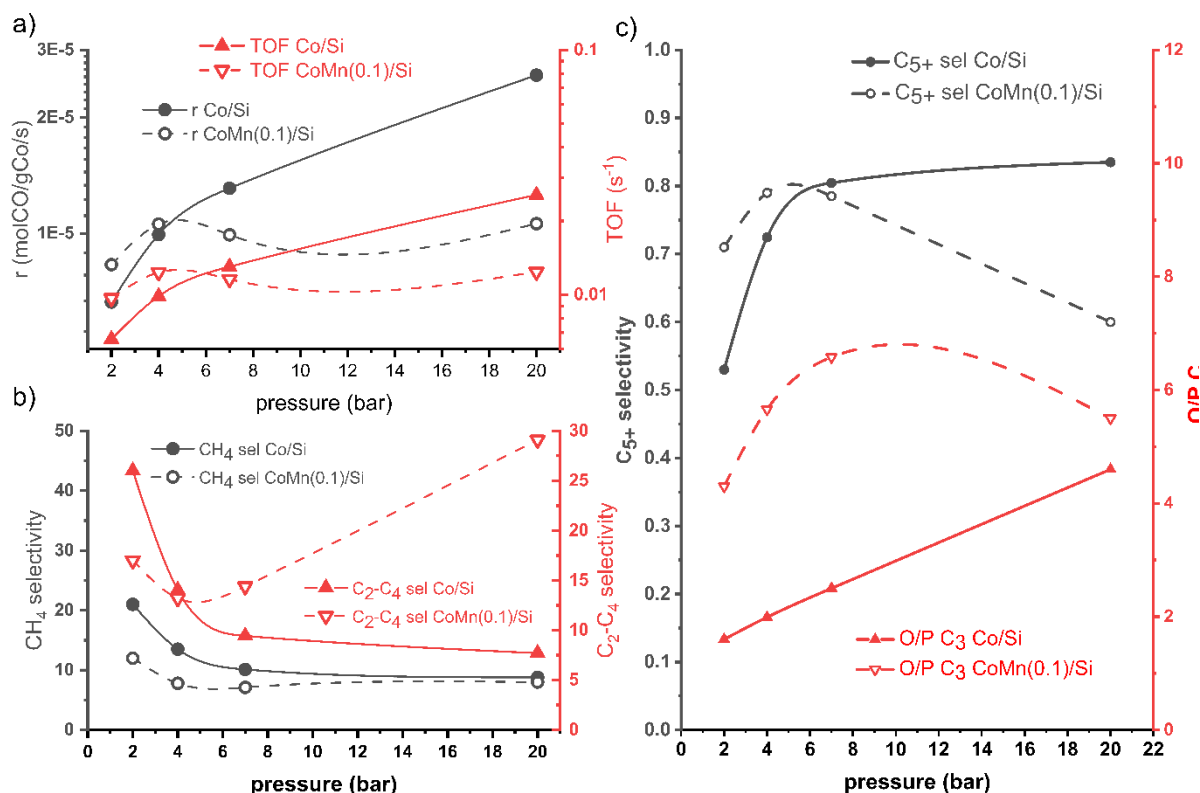


Figure 2.6. a) Reaction rate (mol CO/g_{Co}/s) and TOF (s^{-1}), b) CH_4 and C_2-C_4 selectivity, c) C_{5+} selectivity and CO conversion for Mn/Co = 0 (triangle) and Mn/Co = 0.1 (circle) as a function of total pressure and Mn/Co ratio. Conditions: $T = 220^\circ C$, $H_2/CO = 2$, $p_{total} = 2, 4, 7$ and 20 bar.

The TOF of the catalysts depends in different ways on the total pressure. The TOF of the Co/Si catalyst increases continuously from $6.5 \cdot 10^{-3} s^{-1}$ at 2 bar to $2.6 \cdot 10^{-2} s^{-1}$ at 20 bar. The CoMn(0.1)/Si catalyst displays a completely different pressure dependence. The TOF reaches a maximum value at 4 bar, after which no further increase is observed. The C_{5+} selectivity of the two catalysts also shows a different pressure dependence. Co/Si shows a significantly enhanced C_{5+} selectivity (and decreasing CH_4 and C_2-C_4 selectivity) at increasing pressure, while the Mn-promoted sample, displays a moderate increase in C_{5+} selectivity up to a maximum at 4 bar after which the selectivity drops substantially. As a result, the C_{5+} selectivity of the Mn-promoted catalyst at 20 bar is lower than that of the unpromoted one, even though it is higher at lower pressures. The opposite holds for the C_2-C_4 selectivity, which is lower for the Mn-promoted catalyst at low pressure but higher at increased pressure due to the significant increase after a minimum at 4 bar. Hence, the monomer formation and coupling rates appear to be enhanced by the presence of Mn below ca. 4 bar, yet not at higher pressure. Fig. 2.6 also shows that the O/P ratio for C_3 products increased by Mn addition over the whole measured pressure range, which is typically explained by a higher total coverage of reaction intermediates on Co, inhibiting re-adsorption and hydrogenation of primary olefinic products. The O/P ratio for the CoMn(0.1)/Si shows a maximum at 4 bar, mirroring the pressure dependence of the C_2-C_4 selectivity. Clearly, the addition of Mn to Co leads to a very different pressure dependence of the FT reaction, which implies that Mn affects the pressure-dependent composition of the surface-adsorbed layer.

SSITKA was carried out at model FT conditions, viz. at 220 °C and a total pressure of 1.85 bar with a H_2/CO ratio of 3. The steady-state catalytic performance of the catalysts under these conditions is displayed in Fig. 2.7, showing an overall beneficial influence of Mn on the CO conversion. TOF, C_{5+} selectivity, and chain-growth probability. Simultaneously, the CH_4 and C_2 - C_4 selectivity decrease with increasing Mn content. The changes in selectivities and activity upon Mn addition to Co is almost reversed to those observed at 20 bar (Fig. 2.5), as expected from the pressure dependency of the promotional effect of Mn (Fig. 2.6). Notably, in both cases the largest effect of Mn addition occurs at an Mn/Co ratio of 0.1. This has also been described before in literature,^{34,18,50} where it was ascribed to two counterbalancing effects. On the one hand, Mn promotes the FT reaction on the active Co sites. On the other hand, Mn is by itself catalytically inactive and henceforth blocks active cobalt sites. At too high Mn/Co ratios, the latter effect appears to be dominant. The residence times τ and surface coverages θ of CO and CH_x determined under the same conditions as the experiments presented in Fig. 2.7 are depicted in Fig. 2.8a as a function of the Mn/Co ratio.

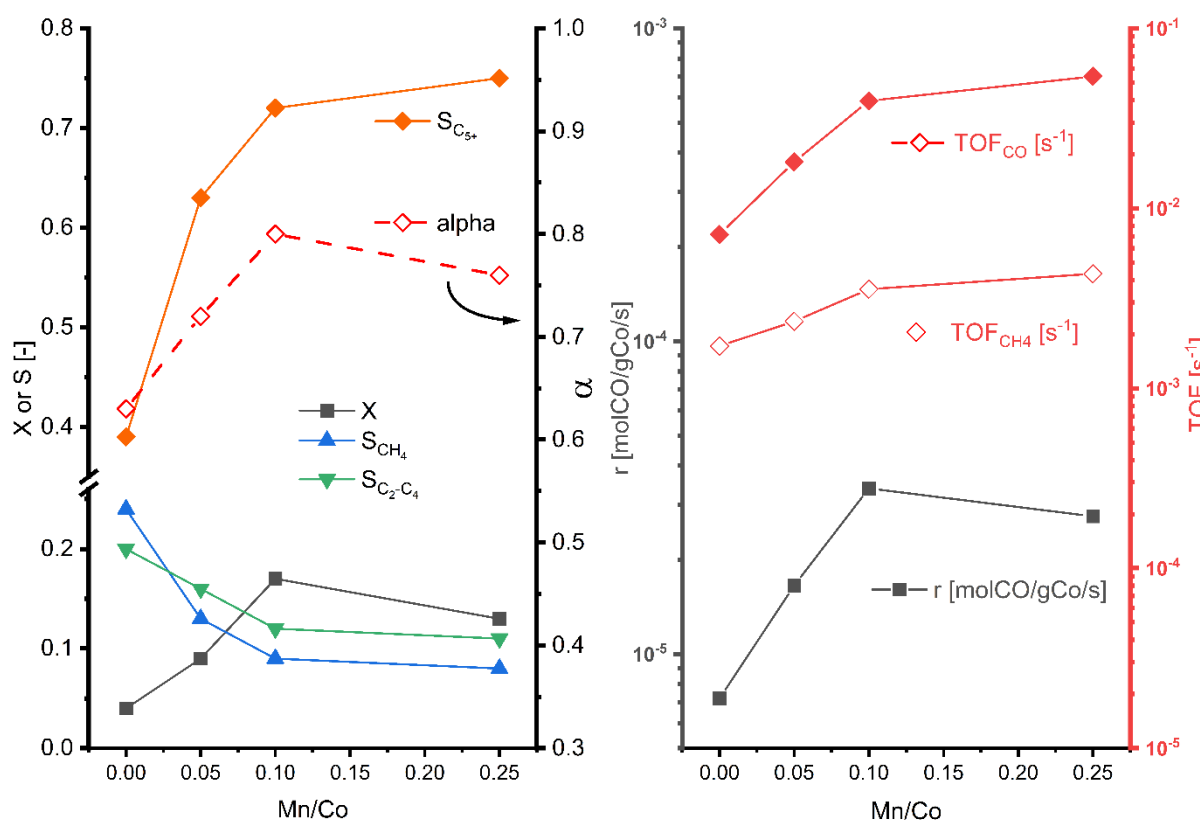


Figure 2.7. (left) CH_4 selectivity (triangle up), C_2 - C_4 selectivity (triangle down), C_{5+} selectivity (diamond), CO_2 selectivity (circle), and conversion (X) as a function of the Mn/Co ratio and (right) TOF_{CO} and TOF_{CH_4} and the Co-based reaction rate as a function of Mn/Co ratio. Conditions: $T = 220^\circ C$, $H_2/CO = 3$, $p_{total} = 1.85$ bar.

τ_{CO} is practically independent of the Mn content, while τ_{CH_x} increases with increasing Mn/Co ratio. The coverages of CO and CH_x species increase with increasing Mn content. A higher coverage of CH_x is expected to lead to a higher chain-growth probability. This is in line with the increasing C_{5+} selectivity (Fig. 2.7a) and with the increasing difference between TOF_{CO} and

TOF_{CH₄} at higher Mn/Co ratio (Fig. 2.7b), as this difference represents the rate of carbon conversion to C₂₊ hydrocarbons. Notably, though the kink at Mn/Co = 0.1 is also visible at high pressure (see Fig. 2.5), the selectivity and activity trends presented for this ratio differ substantially from those presented in Fig. 2.7, because the promoting effect depends strongly on the used pressure as shown in Fig. 2.6.

The residence times τ and surface coverages θ of CO and CH_x determined under the same conditions as the experiments presented in Fig. 2.7 are depicted in Fig. 2.8a as a function of the Mn/Co ratio. τ_{CO} is practically independent of the Mn content, while τ_{CH_x} increases with increasing Mn/Co ratio. The coverages of CO and CH_x species increase with increasing Mn content. A higher coverage of CH_x is expected to lead to a higher chain-growth probability. This is in line with the increasing C₅₊ selectivity (Fig. 2.7a) and with the increasing difference between TOF_{CO} and TOF_{CH₄} at higher Mn/Co ratio (Fig. 2.7b), as this difference represents the rate of carbon conversion to C₂₊ hydrocarbons. Notably, although Fig. 2.7a shows that above the Mn/Co ratio of 0.1, the C₅₊ selectivity increases, the calculated chain-growth probability α does not increase. The extreme increase in CH_x coverage leads thus to the formation of heavy hydrocarbons that are not included in the calculation of the chain-growth probability (C₃ to C₇).

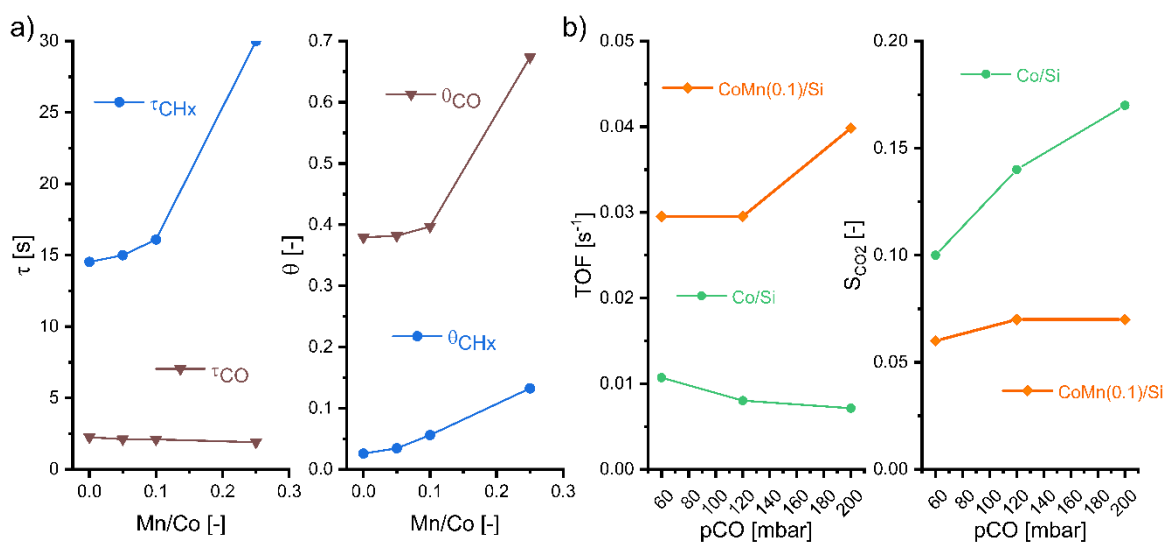


Figure 2.8. a) Residence time τ of CO (triangle down) and CH_x (circle) and surface coverage θ of CH_x (circle) CO (triangle down) as a function of the Mn/Co ratio. b) TOF as a function of CO partial pressure for unpromoted (circle) and Mn/Co = 0.1 (circle) catalysts. CO₂ selectivity as a function of CO partial pressure for unpromoted (circle) and Mn/Co = 0.1 (circle) catalysts. Conditions: $T = 220^\circ\text{C}$, $p_{\text{total}} = 1.85$ bar, $p_{\text{H}_2} = 600$ mbar, $p_{\text{CO}} = 200$ mbar. The reaction orders with respect to CO were obtained by keeping the H₂ partial pressure constant (600 mbar) and varying the CO partial pressure between 60 to 200 mbar.

Noteworthy is the increasing CO surface coverage with increasing Mn/Co ratio. Chen et al. determined by SSITKA that the CO coverage on (unpromoted) Co/SiO₂ can be as high as 0.4²³, just as we observe here for the samples up to an Mn/Co ratio of 0.1. From a theoretical perspective, the maximum attainable CO coverage on Co(0001) is 7/12 (0.58)⁵¹. Up to a Mn/Co ratio of 0.1, the measured coverages are below these two values. However, for a Mn/Co ratio

of 0.25, the CO coverage is as high as 0.67, indicating that an exceptionally high coverage can be obtained in the presence of Mn. Apparently, Mn enhances CO adsorption. In contrast to unpromoted cobalt catalysts, this adsorbed CO does not hinder CO dissociation. Hindrance of CO dissociation by co-adsorbed CO is often used to explain the negative order in CO for Co catalysts. As can be seen in Fig. 2.8b, the reaction order with respect to CO is indeed negative for unpromoted but positive for Mn-promoted Co. The change in CO reaction order from negative to positive through Mn promotion suggests that, in the presence of Mn, CO dissociation does not need vacancies on the metallic cobalt surface. It can thus be speculated that CO adsorption and dissociation take place on Mn-promoted cobalt sites. This aspect is investigated further with IR spectroscopy and density functional theory calculations. Most importantly, it is evident from Fig. 2.8a that the presence of Mn leads to a higher coverage of CH_x , despite the increasing CO coverage. A higher CH_x coverage explains the above described effects of Mn promotion at low pressure. Since a higher monomer coverage not only leads to a higher coupling rate at the expense of CH_4 formation, but also, in combination with the high CO coverage to less readsorption of olefins. Hence, these SSITKA results explain the appearance of longer chain products and a higher O/P ratio for Mn-promoted catalysts.

2.3.3 IR spectroscopy

IR spectroscopy was carried out to understand better the impact of Mn on the adsorption and reactivity of CO. In one set of measurements, IR spectra were recorded with increasing CO coverage (0 – 10 mbar CO) at room temperature, followed by ramping the temperature to 300°C. A second set of IR measurements was carried out *in situ* under a synthesis gas atmosphere ($\text{H}_2/\text{CO} = 2$), whilst ramping the temperature from 30°C to 300°C.

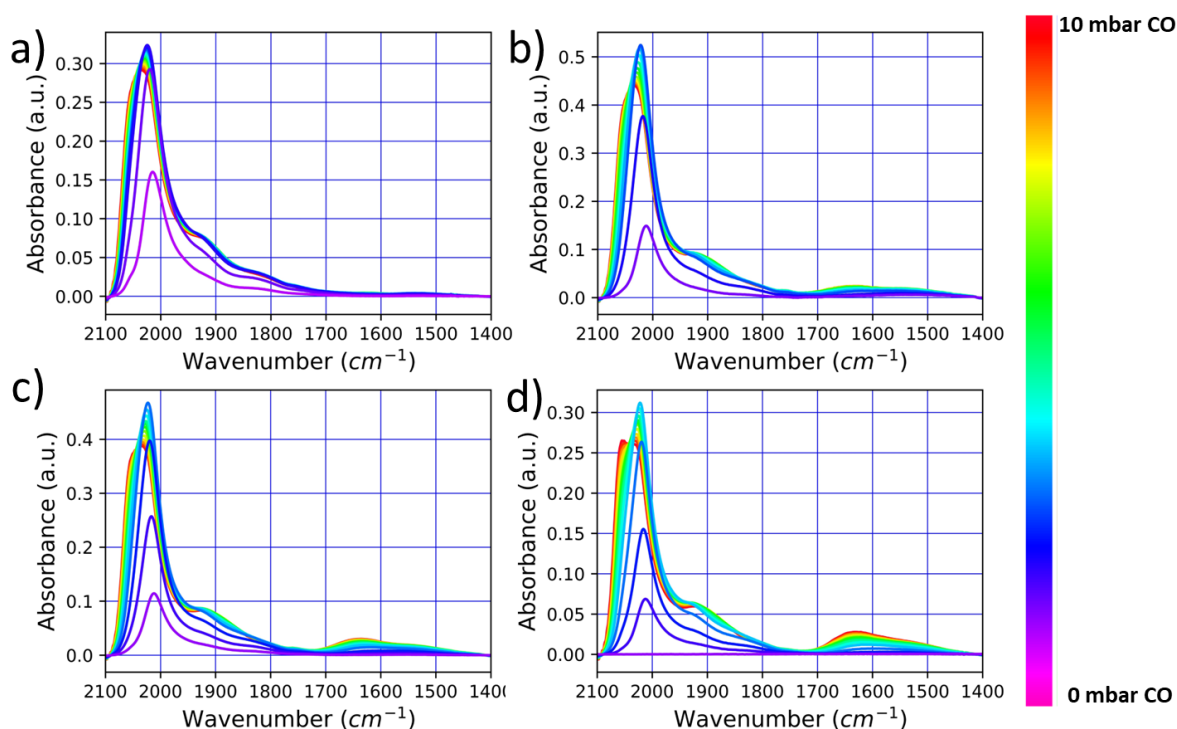


Figure 2.9. FTIR spectra of CO adsorption, p_{CO} 0–10 mbar, (a) Co/Si; (b) CoMn(0.05)/Si; (c) CoMn(0.1)/Si; (d) CoMn(0.25)/Si. Colors in indicate the increasing CO pressure from 0 – 10 mbar.

The CO IR spectra recorded at room temperature with increasing CO partial pressure (Fig. 2.9) are typical for CO adsorption on Co nanoparticles⁵². The bands at 2020 cm^{-1} , 1935 cm^{-1} and 1835 cm^{-1} can be respectively ascribed to linear (top), two-fold (bridged) and threefold (hollow) adsorbed CO on extended Co surfaces. Such assignment is amongst others supported by surface science studies on Co(0001).^{53 54} The blueshift of the IR band of top-adsorbed CO with increasing coverage can be attributed to lateral interactions. For instance, Weststrate et al.⁵⁴ showed that, up to a CO coverage of around 0.15 ML, the top-CO stretching frequency and the IR intensity increased linearly, leveling off when approaching a coverage of 0.33 ML.⁵⁵ DFT calculations support this interpretation⁵². The corresponding spectra for the Mn-promoted catalysts are qualitatively similar. The most obvious changes are a lower intensity of the CO adsorption bands at low CO pressure, which is in line with the decreasing metal surface upon Mn promotion as observed by H_2 chemisorption. The presence of Mn also leads to a loss of three-fold CO sites, which was also observed by Den Breejen et al.³⁴ Moreover, a shoulder at the high-frequency side of the top-CO band (2058 cm^{-1}) is observed, which becomes clearer with increasing Mn/Co ratio. Although it is not straightforward to assign this band, it is most likely due to lateral interactions between CO and other surface species. Chen et al. showed that this band can be due to CO adsorbed close to adsorbed C and O species originating from CO dissociation.⁵² Their presence might therefore point to CO dissociation at relatively low temperature for the CoMn/Si catalysts. The CO IR spectra of the Mn-promoted catalysts also contain a feature at 1650 cm^{-1} , which becomes more intense with increasing CO coverage. This band, which is also stronger for higher Mn/Co ratios, is a CO_3^{2-} stretching vibration. Such carbonates can originate from the reaction of CO and CO_2 with metal oxides such as MnO ⁵⁶. Although we cannot exclude that the carbonates are formed by CO interacting with MnO , it is likely that they are formed by interaction with CO_2 , which would imply that the CoMn/Si catalysts contain sites that can dissociate CO leading to surface C species and CO_2 .

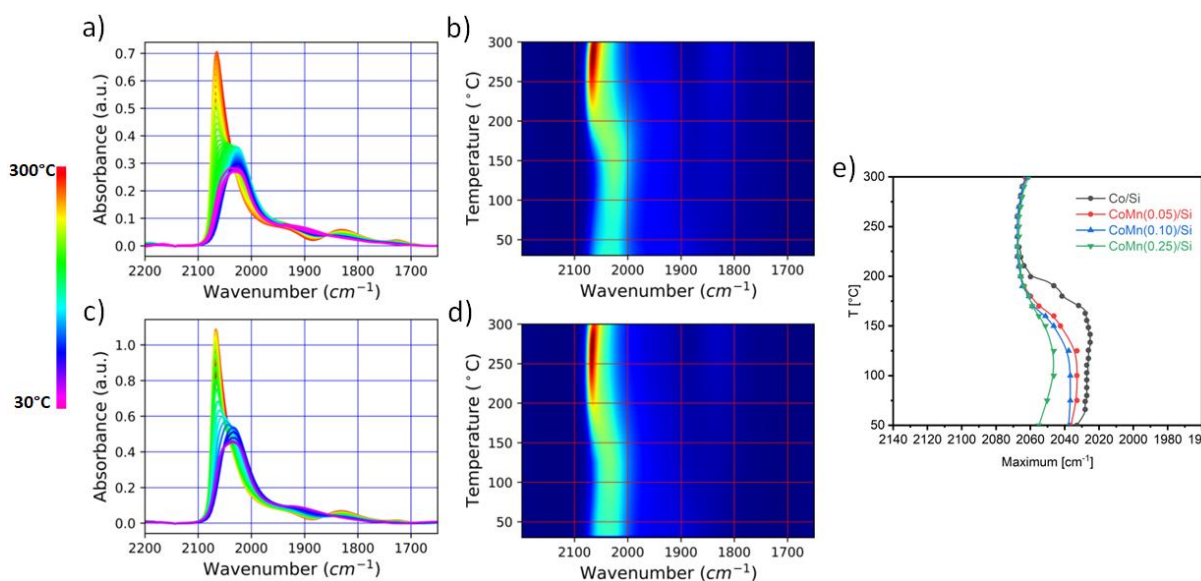


Figure 2.10. Temperature-programmed in situ IR spectroscopy ($p_{\text{CO}} = 10 \text{ mbar}$) (a), (b) CO stretch region as a function of temperature for Co/Si. (c), (d) CO stretch region as a function of temperature for CoMn(0.1)/Si. Colors in heat map (b) and (d) indicate the increasing IR intensity from violet to red. (e) plot of the position of the peak maximum of linear CO as a function of temperature and Mn content.

A temperature-programmed IR experiment at a CO partial pressure of 10 mbar leads to pronounced changes of the IR spectra (Fig. 2.10). The CO IR spectra for the Co/Si catalyst are very similar to those reported for a similar Co/SiO₂ catalyst by Chen et al.⁵² The small red shift of top-adsorbed CO towards slightly lower wavenumbers during heating to 150 °C can be explained by desorption of CO, resulting in a decrease of lateral interactions. A clear blueshift of top-adsorbed CO from 2022 cm⁻¹ to 2068 cm⁻¹ is observed in the 150 – 175 °C range. This shift goes together with a strong increase of the IR intensity. Model experiments by Chen et al.⁵² indicated that these changes can be attributed to co-adsorbed C and O. DFT calculations predict such frequency shift and increase in the extinction coefficient due to co-adsorbed C and O species. Others also reported a similar shift and mentioned the role of co-adsorbed O or C.^{53 52 54 57} The blueshift occurring during the temperature programmed IR spectroscopy can thus be linked with CO dissociation. Comparing the shift on Co/Si (Fig. 2.10b) with the shift on CoMn(0.1)/Si (Fig. 2.10d) shows that Mn addition lowers the onset temperature of the blueshift by nearly 50 °C (from 175 °C to 125 °C) indicating that CO dissociation is facilitated by the presence of Mn. The blue shift occurs for all CoMn/Si samples (Fig. 2.10e).

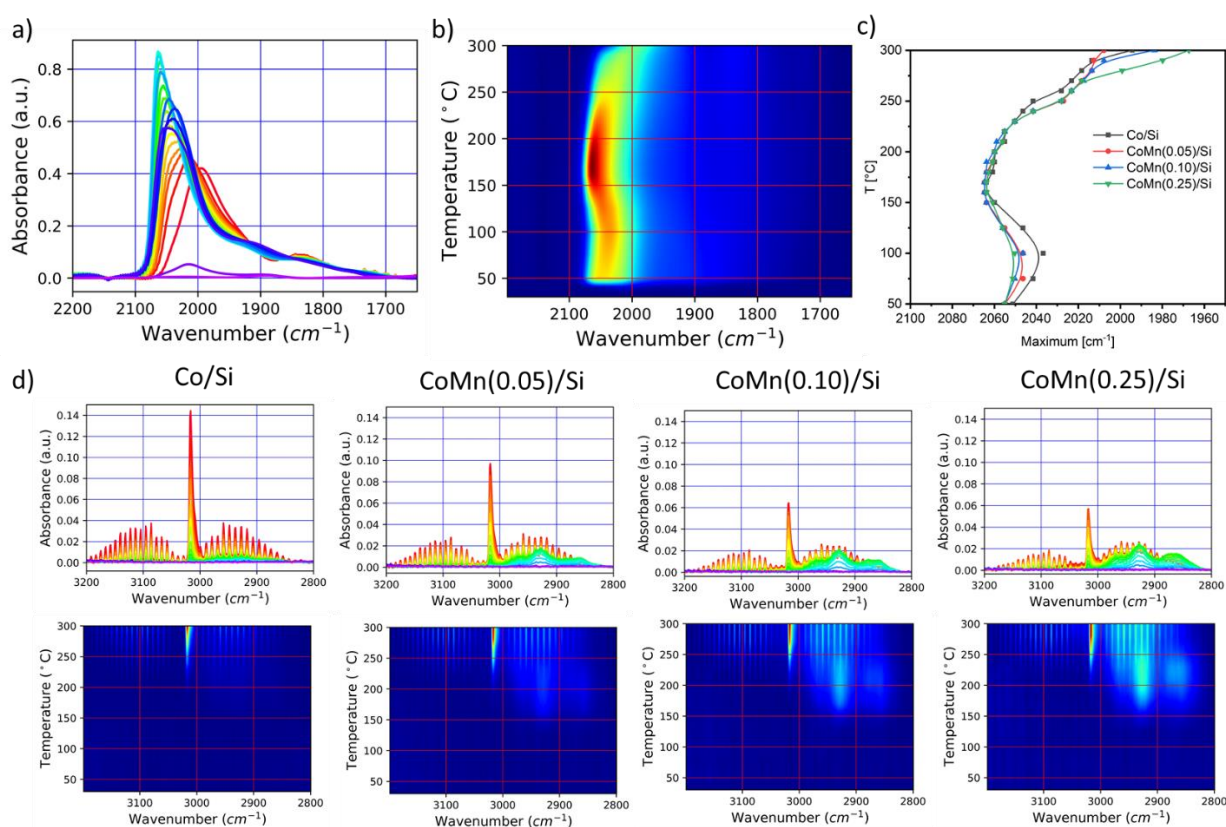


Figure 2.11. Temperature-programmed in situ IR spectroscopy in synthesis gas ($H_2/CO = 2$, $p_{total} = 100$ mbar) (a), (b) CO stretch region as a function of temperature for CoMn(0.1)/Si. Colors in heat map (b) indicate IR intensity (a.u.) which increases from violet to red. (c) plot of the position of the peak maximum of linear CO as a function of temperature and Mn content. (d) 3200-2800 cm⁻¹ region representing hydrocarbon C-H stretch vibrations during temperature-programmed reaction in synthesis gas for Co/Si and CoMn/Si catalysts and the corresponding heat maps in which the colors indicate IR intensity (a.u.) which increases from violet to red.

Temperature-programmed IR spectra were recorded in a synthesis gas atmosphere ($\text{H}_2/\text{CO} = 2$, $p_{\text{total}} = 100$ mbar). Fig. 2.11a and 2.11b show the IR spectra for CoMn(0.1)/Si as a function of the temperature and a heat map emphasizing the band of linearly adsorbed CO. In comparison to the IR spectra in Fig. 2.10, the surface also contains hydrogen. In the presence of hydrogen, the position of linearly adsorbed CO at room temperature is shifted from 2020 cm^{-1} to 2050 cm^{-1} , which is most likely due to lateral interactions. The trends upon heating are qualitatively the same as seen during heating in a CO atmosphere. For instance, the initial red-shift from 2050 cm^{-1} to 2035 cm^{-1} due to desorption of CO is followed by a blue-shift to 2068 cm^{-1} , which can be attributed to CO dissociation. The temperature at which the blue-shift occurs is lower in synthesis gas than in a CO atmosphere. The influence of Mn on the onset of the blue-shift is much less pronounced in this case. A significant difference between the two sets of experiments in Figs. 2.10 and 2.11 is that the presence of H_2 leads to a much stronger red-shift above $200\text{ }^\circ\text{C}$. We explain this by the hydrogenation of C-containing species, which decreases the lateral interactions with CO.

Fig. 2.11d depicts the C-H stretch region of hydrocarbons for the Co/Si and CoMn/Si catalysts. The spectra are dominated by bands due to gas-phase CH_4 . Above $150\text{ }^\circ\text{C}$, all catalysts show distinct vibrations in the range of 2900 to 3200 cm^{-1} typical of gaseous CH_4 and located on the low- and high-frequency side of the ν_3 C-H stretch vibration at 3020 cm^{-1} . The weaker and broader features in the $2800 - 3000\text{ cm}^{-1}$ regime are typical for hydrocarbons with C-C bonds. The main vibrations of gas-phase CH_4 (2800 - 3200 cm^{-1}) appear at $\sim 190\text{ }^\circ\text{C}$ independent of the Mn/Co ratio. Notably, the spectra for Co/Si only contain bands due to CH_4 , while the Mn-containing catalysts also form higher hydrocarbons as evidenced by the sp^3 C-H vibrations of CH_2 and CH_3 observed in the 3000 - 2800 cm^{-1} range (CH_2 at 2927 cm^{-1} and 2864 cm^{-1} and CH_3 at 2968 cm^{-1}), indicating that Mn promotes the formation of higher hydrocarbons as compared to Co/Si. These bands appear already at a relatively low temperature, *i.e.*, just below $150\text{ }^\circ\text{C}$. The absence of similar features in the 3100 - 3000 cm^{-1} region shows that no sp^2 C=C-H is present. We speculate that the observed hydrocarbon bands stem from adsorbed hydrocarbon fragments. The CH_2 and CH_3 bands are most intense in the 200 - $220\text{ }^\circ\text{C}$ range. Most likely, the surface coverage with such fragments is low at higher temperatures, which is in keeping with the red-shift of the linear CO band. Thus, the IR spectroscopy results show that Mn can promote the dissociation of CO, which goes in parallel with C-C coupling leading to higher hydrocarbons. Moreover, there is clear evidence for the presence of surface intermediates with C-C bonds on the CoMn/Si catalysts in the temperature range of the FT reaction (200 - $220\text{ }^\circ\text{C}$), whereas only CH_4 is observed for Co/Si. The high CH_4 selectivity for Co/Si is as expected under the low total pressure (100 mbar) conditions with a high H_2/CO ratio of 3.

2.4 Computational modeling

DFT calculations were employed to investigate how the presence of MnO on the metallic Co surface can affect CO dissociation. A relatively simple $\text{Mn}_4\text{O}_4/\text{Co}(0001)$ model was chosen to represent MnO on metallic Co. Various structures of $\text{Mn}_4\text{O}_4/\text{Co}(0001)$ as determined by the DFT-based GA method are given in Fig. A7. In the most stable structure, each Mn atom binds

to two surface Co atoms and two O atoms (Fig. 2.12a). This structure is very similar to the one determined for Mn_4O_4 on the Ni(111) surface by Vrijburg et al.²⁹ For such models, it was shown that CO and CO_2 dissociation barriers can be lowered by involving an O vacancy in the Mn_4O_4 cluster compared to Ni(111) and Ni(311) surfaces. Here, we explored similar pathways for CO dissociation, starting from a Mn_4O_4 cluster with a vacancy (Mn_4O_3). Specifically the elementary CO dissociation step is examined, as this supposedly is the rate limiting step in the whole Fischer-Tropsch reaction sequence. The reaction energy needed for the creation of such a vacancy was also calculated.

Fig. 2.13 shows the reaction energy diagram for CO dissociation on the $\text{Mn}_4\text{O}_3/\text{Co}(0001)$ model. Additional data including geometries and reference data for Co(0001) and Co(11 $\bar{2}$ 1) surfaces from literature are collected in Tables A2 and A3 in the Appendix. DFT calculations show that direct CO dissociation can occur on the step-edge sites of Co, i.e., the Co(11 $\bar{2}$ 1) model. A typical value for the stepped Co(11 $\bar{2}$ 1) surface is 1.06 eV²⁸. CO dissociation on the close-packed Co(0001) surface is very difficult with activation barriers of 2.46 eV for direct and 1.83 eV for H-assisted CO dissociation.²⁸ [ENREF 1](#) Three pathways were explored for the $\text{Mn}_4\text{O}_3/\text{Co}(0001)$ model (Fig. A10). The corresponding reaction energy paths are depicted in Fig. 2.13.

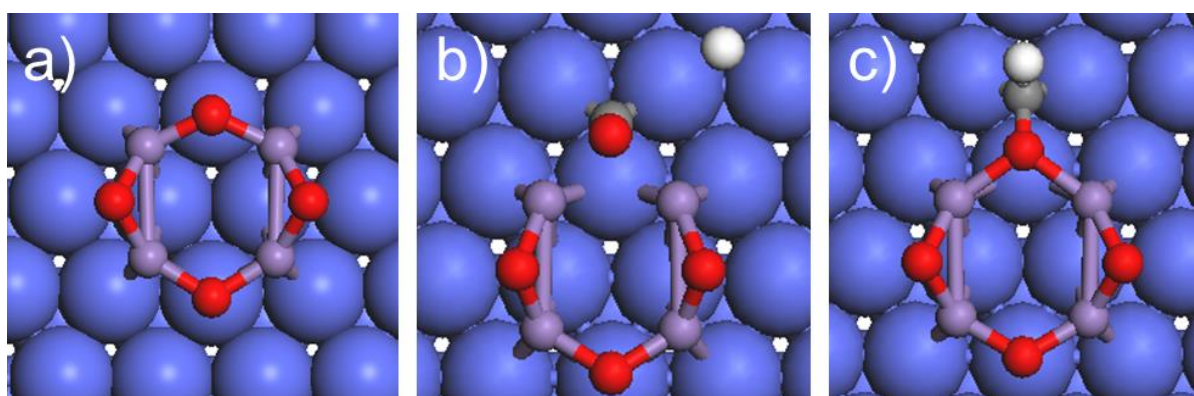


Figure 2.12. (a) DFT structure of a $\text{Mn}_4\text{O}_4/\text{Co}(0001)$ cluster, (b) CO adsorption configuration on $\text{Mn}_4\text{O}_3/\text{Co}$ catalyst, and (c) HCO transition state for CO dissociation.

The most favorable CO dissociation mechanism involves HCO as a surface intermediate with an overall barrier of 0.98 eV. The direct and COH pathways are much less favorable with overall barriers of 1.71 eV and 1.23 eV, respectively. Thus, these calculations show that H-assisted CO dissociation on the Co- Mn_4O_3 interface is much easier than on the planar surfaces of Co and slightly easier than on a step-edge site of Co.

Subsequently, the removal of O from the Mn_4O_4 cluster on the Co(0001) surface needed to regenerate the above-used Mn_4O_3 cluster was investigated. The relevant reaction energy diagrams are shown in Fig. 2.13c, the corresponding geometries and other data are given in the Appendix. The barrier for OH formation on the Mn_4O_4 cluster is 0.79 eV. Direct formation of adsorbed H_2O requires overcoming a barrier of 1.18 eV, while the overall barrier for H_2O formation is 1.49 eV. This is higher than the overall barrier of CO dissociation.

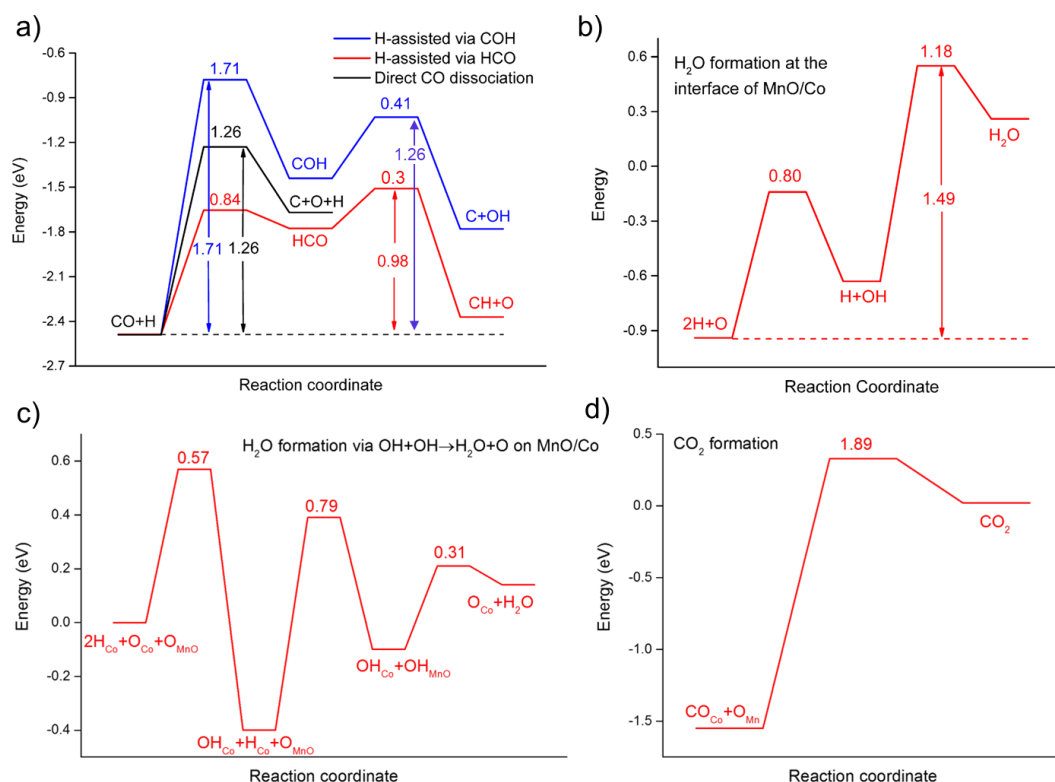


Figure 2.13. DFT calculations of (a) CO dissociation on the Mn₄O₃/Co(0001) surface model and (b-d) O vacancy formation on the Mn₄O₄/Co(0001) surface model via (b and c) H₂O formation and (d) CO₂ formation.

Another potential pathway is the reaction of OH on Mn₄O₄ with an OH intermediate adsorbed on the Co surface (Fig. A8). The barrier associated with this reaction step is only 0.30 eV. The occurrence of OH intermediates adsorbed on Co during reaction can be expected as water is a primary product of the FT reaction. Overall, the barrier for O removal in this manner is 0.97 eV, which is similar to the barrier of CO dissociation. We also computed the barrier for CO₂ formation involving CO adsorbed on Co(0001) with an O atom of the Mn₄O₄ cluster (Fig. A11). The barrier for this reaction is 1.89 eV, much higher than the computed barriers for CO dissociation and H₂O formation. This barrier is also higher than CO₂ formation barriers computed for Co(0001) and Co(11 $\bar{2}$ 1)⁵⁸.

In summary, these calculations on a simple surface model show a facile pathway for the dissociation of CO at the Co-MnO interface in CoMn/Si. CO dissociation involves an O vacancy in the MnO, which is the result of removal of O by formation of H₂O. The overall barrier for CO dissociation via this alternative pathway is slightly lower than the overall CO dissociation barrier on step-edge sites of Co. This can contribute to the higher CO conversion for the Mn-promoted Co catalysts. Another explanation can be that the presence of MnO on Co leads to an increase of the number of active sites for CO dissociation. In relation to the CO reaction orders discussed above, it can be mentioned that CO dissociation at the Co-MnO interface is not limited by intermediate CO coverage on the metal as CO dissociation is on unpromoted Co metal.

2.5 General discussion

Physicochemical characterization of the catalyst precursor shows that Mn is completely integrated in the mixed oxide spinel catalyst precursor. The presence of the mixed oxide spinel of Co and Mn retards the reduction of Co, especially the last reduction step of CoO to metallic Co. Nonetheless, according to XPS analysis after reduction at 450 °C, Co is completely reduced to metallic Co for all Mn-promoted catalysts, while Mn is converted to MnO with Mn in the 2+ oxidation state. H₂ chemisorption and the relative Co and Mn signals in XPS indicate that the metallic surface of Co nanoparticles is decorated with MnO. The presence of MnO in close interaction with the Co surface is in agreement with previous observations¹⁸. Mn does not significantly affect the Co particle size. All catalysts contain Co particles of about 12 nm. The FT performance of these catalysts is thus not affected by structure sensitivity that limits the activity of Co particles smaller than 6 nm^{13,59}. In the last two decades, a substantial amount of research has been devoted to study the impact of Mn promotion on the Co catalyzed FT reaction, often with contradicting outcomes. In this study, the influence of Mn promotion on silica supported Co was studied for the FT reaction at 220 °C and in the pressure range of 2 to 20 bar. The results indicate that the conflicting views in literature can mostly be attributed to different reaction conditions. Specifically, the total reaction pressure can significantly influence the effect of Mn promotion. At pressures below 4 bar, Mn acts as a promoter for Co in the FT reaction resulting in higher rates, turn over frequencies and C₅₊ selectivity. However, the opposite holds at higher pressure. This stems from substantially different pressure dependence of the unpromoted and Mn-promoted Co catalysts. For the unpromoted catalyst an increase in pressure leads to a higher reaction rate and higher C₅₊ selectivity with the most pronounced increase in the 2 to 6 bar pressure range. On the other hand, for the Mn-promoted catalyst, this trend is remarkably different. Though the activity and C₅₊ selectivity also initially increase with increasing pressure, the activity stabilizes and the C₅₊ selectivity starts to decrease steeply above 4 bar. As a result of these opposite trends Mn enhances C₅₊ selectivity at low pressure, but suppresses it at high pressure. Nonetheless, Mn promotion decreases the CH₄ selectivity over the whole studied pressure range. To explain the pressure dependence of the promotional effect of Mn, the role of pressure in the FT reaction and the mechanism of Mn promotion is discussed here. Mechanistic work of Chen et al.²³ has demonstrated that the increasing activity and C₅₊ selectivity when the reaction pressure is increased can be well explained by a higher CO coverage, which leads to a higher CH_x monomer coverage and, thus, higher activity and chain-growth probability. This clearly also holds for the unpromoted Co catalyst in this study, and for the Mn-promoted catalysts up to 4 bar. Temperature-programmed IR spectroscopy in the presence of CO shows a lower onset temperature for CO dissociation in the presence of Mn, indicating a positive role of MnO in the CO dissociation. Similar IR measurements in synthesis gas show that unpromoted Co produces under the conditions used only CH₄, but that Mn-promoted Co also forms larger hydrocarbons at a significantly lower temperature than the formation of CH₄. SSITKA carried out at a relatively low pressure confirms the positive impact of Mn on the activity and CH_x coverage. This can explain well the higher chain growth probability in the presence of Mn, yielding more longer

hydrocarbons and thus less CH₄ at low pressure. DFT calculations using a Mn₄O₄/Co(0001) model show that CO can dissociate at the Co-MnO interface with a lower overall activation barrier than on the most active metallic Co step-edge sites. The modelled catalytic cycle involves the generation of an oxygen vacancy by removal of O from MnO as H₂O, followed by H-assisted C-O dissociation. The oxygen atom of CO replenishes the oxygen vacancy, leaving behind a CH fragment on the metallic Co. Thus, according to DFT, the decoration of Co with MnO results in the formation of additional CO dissociation sites on Co nanoparticles with a lower activation energy. The enhanced CO dissociation observed by IR and SSITKA experiments is thus in agreement with the outcome of the DFT calculations. Since Co typically operates in the monomer formation limit regime with CO dissociation being the rate-limiting step^{21,60} enhanced CO dissociation by Mn promotion can explain the higher reaction rate. A CO activation mechanism via an O vacancy in Mn oxide as modelled by DFT is in line with the concept launched by Barrault et al. that redox centers are active sites for CO dissociation¹⁴, but seems in contradiction with the results of the group of Bell, who sees, when comparing different promoters, a direct correlation between the activity and the relative Lewis acidity of the promoter⁶. On the other hand, the Lewis acidity of a cation depends on the number of coordinating oxygen atoms⁶¹. It could thus be speculated that the same phenomenon of CO activation is just described by another parameter, i.e., Lewis acidity versus vacancy formation. Nonetheless, in contrast to previous literature, which only correlates activity with a specific parameter, a complete mechanistic understanding of the catalytic cycle is presented here. Notably, the reaction order with respect to CO is negative for unpromoted cobalt as widely reported for Co-based FT catalysts^{50,18} but positive for Mn-promoted Co. The negative order reflects the need of surface vacancies on the metallic Co surface for CO dissociation. The positive reaction order in CO for the Mn-promoted Co catalyst can be explained by the dissociation of CO at the Co-MnO interface. Since this mechanism does not require two neighboring vacant Co surface sites, self-poisoning by CO does not occur. This implies that at high CO coverage the reaction will mainly proceed at Co-MnO interfaces. Increasing the Mn content in promoted Co catalysts from Mn/Co = 0 to Mn/Co = 0.25 at a reaction pressure of 20 bar results in a decreased C₅₊ selectivity and chain-growth probability, whereas the CH₄ selectivity is hardly affected. As a result, the CH₄ yield is not higher than expected from the ASF distribution as is usually the case for Co but gets in line with the prediction of the AFS plot. The promotional effect of Mn reaches a maximum at an Mn/Co ratio of 0.1, at both low and high reaction pressures. This is in accordance with previous literature for Co on various supports^{6,48,50,18,34} and has tentatively been ascribed to the formation of an optimum mixed Mn-Co-oxide crystal structure of the calcined catalyst precursor, which would just yield the desired MnO covered metallic cobalt after reduction^{50,20}. As stated above, for the Mn-promoted catalysts, the positive effect of pressure on activity and selectivity only holds up to a pressure of 4 bar after which a maximum is reached and a negative effect of increasing pressure on the product distribution is seen. It is uncertain why a similar pressure dependence has not been reported before in literature. The group of Bell reports a continuous increase in reaction rate with total pressure, but observed a peculiar maximum in rate at about 1 bar CO partial pressure¹⁸, which would be roughly in line with 4 bar total pressure at a H₂/CO ratio of

2. The occurrence of a maximum can be explained by taking into account that MnO catalyzes the CO dissociation and CH_x formation, but not C–C coupling. On the unpromoted Co catalyst, the CO dissociation sites are the same as the chain-growth sites, viz. step-edge sites^{62,63,64,65,66,67} and enhanced CH_x formation at increasing pressure will immediately lead to an increased chain growth rate. However, on Mn-promoted catalysts, the CH_x monomers are formed at the interface of MnO and Co and have to migrate to chain-growth sites on the metallic cobalt. In general, migration of surface adsorbates is easy on empty Co surfaces^{68,69}. Increasing the pressure, however, increases the coverage of adsorbed species other than CH_x and most prominently CO, which might hinder the migration of CH_x monomers. Apparently, this hindrance starts to dominate over the positive effect of Mn on the CO dissociation rate at pressures above 4 bar. Methane formation does not require stepped sites but occurs on sites that cover the majority of the surface⁵⁹ and does thus not rely on migration. As a consequence, the methane selectivity is rather independent of the pressure. This results in a maximum C₅₊ selectivity and thus also to a minimum in the selectivity to other products like of CH₄ and C₂-C₄ hydrocarbons at 4 bar. The hypothesis that the MnO-Co interface site does not catalyze chain growth also explains the observation that at high pressures, at which the metal sites but not the Mn-promoted sites are poisoned by adsorbed CO, the C₅₊ selectivity is not enhanced by Mn addition.

2.6 Conclusion

In this study Mn-promoted Co catalysts on silica were studied in the FT reaction in a pressure range from 2 to 20 bar. After reduction of the oxidic catalyst precursor at 450 °C, metallic cobalt particles are formed, which are decorated with MnO. In situ IR spectroscopy and SSITKA measurements indicate that the presence of Mn enhances the CO dissociation and hydrocarbon formation. DFT calculations on an MnO/Co(0001) model cluster shows that CO can be activated by vacancies in the Mn oxide with a lower activation energy than on regular step-edge sites. At low pressure, Mn promotion results in a higher activity and C₅₊ selectivity, which both can be explained by the increased CO activation rate and resulting higher monomer coverage. At high pressure, however, Mn promotion results in a lower C₅₊ selectivity. This is a result of peculiar differences in pressure dependence between the unpromoted and Mn-promoted catalysts. Increasing pressure leads to an increased activity and C₅₊ selectivity for the unpromoted Co catalyst. The Mn-promoted catalyst shows the same trend but only up to 4 bar. Above this pressure, the activity stabilizes and the C₅₊ selectivity drops dramatically at increasing pressure. This behavior is tentatively ascribed to hindered migration of CH_x growth monomers at increasing pressure. On unpromoted Co catalysts, the catalytic site for CO dissociation and chain growth is the same, viz. a stepped site. Mn promotion enhances CO dissociation but likely not C–C coupling. Hence, CH_x fragments formed at the Co-MnO interface have to migrate to stepped sites for chain growth. This migration can be hindered by surface adsorbates. Since the coverage of adsorbed reactants and intermediates increases with pressure, an higher reaction pressure can suppress migration and chain growth. Apparently, the hindrance of migration by adsorbed species dominates at pressures above 4 bar, leading to a decreasing C₅₊ selectivity. As a consequence, Mn promotion on silica supported Co at low

pressure leads to an increase in chain-growth probability, while it decreases the C₅₊ selectivity at high pressure.

References

- (1) Dry, M. E.; Hoogendoorn, J. C. Technology of the Fischer-Tropsch Process. *Catal. Rev.* **1981**, *23* (1–2), 265–278. <https://doi.org/10.1080/03602458108068078>.
- (2) Dry, M. E. The Fischer-Tropsch Process: 1950–2000. *Catal. Today* **2002**, *71* (3–4), 227–241. [https://doi.org/10.1016/S0920-5861\(01\)00453-9](https://doi.org/10.1016/S0920-5861(01)00453-9).
- (3) Schulz, H. Short History and Present Trends of Fischer–Tropsch Synthesis. *Appl. Catal. A Gen.* **1999**, *186* (1–2), 3–12. [https://doi.org/10.1016/S0926-860X\(99\)00160-X](https://doi.org/10.1016/S0926-860X(99)00160-X).
- (4) Weststrate, C. J.; van Helden, P.; Niemantsverdriet, J. W. Reflections on the Fischer-Tropsch Synthesis: Mechanistic Issues from a Surface Science Perspective. *Catal. Today* **2016**, *275*, 100–110. <https://doi.org/10.1016/j.cattod.2016.04.004>.
- (5) Khodakov, A. Y.; Chu, W.; Fongarland, P. Advances in the Development of Novel Cobalt Fischer – Tropsch Catalysts for Synthesis of Long-Chain Hydrocarbons and Clean Fuels Advances in the Development of Novel Cobalt Fischer – Tropsch Catalysts for Synthesis of Long-Chain Hydrocarbons and Clean Fue. *Am. Chem. Soc.* **2007**, *107* (5), 1692–1744. <https://doi.org/10.1021/cr050972v>.
- (6) Johnson, G. R.; Bell, A. T. Effects of Lewis Acidity of Metal Oxide Promoters on the Activity and Selectivity of Co-Based Fischer – Tropsch Synthesis Catalysts. *J. Catal.* **2016**, *338*, 250–264. <https://doi.org/10.1016/j.jcat.2016.03.022>.
- (7) Morales, F.; de Groot, F. M. F.; Glatzel, P.; Kleimenov, E.; Bluhm, H.; Hävecker, M.; Knop-Gericke, A.; Weckhuysen, B. M. In Situ X-Ray Absorption of Co/Mn/TiO₂ Catalysts for Fischer–Tropsch Synthesis. *J. Phys. Chem. B* **2004**, *108* (41), 16201–16207. <https://doi.org/10.1021/jp0403846>.
- (8) Morales, F.; De Groot, F. M. F.; Gijzeman, O. L. J.; Mens, A.; Stephan, O.; Weckhuysen, B. M. Mn Promotion Effects in Co/TiO₂ Fischer-Tropsch Catalysts as Investigated by XPS and STEM-EELS. *J. Catal.* **2005**, *230* (2), 301–308. <https://doi.org/10.1016/j.jcat.2004.11.047>.
- (9) Morales, F.; Grandjean, D.; de Groot, F. M. F.; Stephan, O.; Weckhuysen, B. M. Combined EXAFS and STEM-EELS Study of the Electronic State and Location of Mn as Promoter in Co-Based Fischer-Tropsch Catalysts. *Phys. Chem. Chem. Phys.* **2005**, *7*, 568–572. <https://doi.org/10.1039/b418286c>.
- (10) Morales, F.; Grandjean, D.; Mens, A.; de Groot, F. M. F.; Weckhuysen, B. M. X-Ray Absorption Spectroscopy of Mn/Co/TiO₂ Fischer-Tropsch Catalysts: Relationships between Preparation Method, Molecular Structure, and Catalyst Performance. *J. Phys. Chem. B* **2006**, *110*, 8626–8639. <https://doi.org/10.1021/jp0565958>.
- (11) Bezemer, G. L.; Radstake, P. B.; Falke, U.; Oosterbeek, H.; Kuipers, H. P. C. E.; Van Dillen, A. J.; De Jong, K. P. Investigation of Promoter Effects of Manganese Oxide on Carbon Nanofiber-Supported Cobalt Catalysts for Fischer-Tropsch Synthesis. *J. Catal.* **2006**, *237* (1), 152–161. <https://doi.org/10.1016/j.jcat.2005.10.031>.
- (12) Morales, F.; de Smit, E.; de Groot, F. M. F.; Visser, T.; Weckhuysen, B. M. Effects of Manganese Oxide Promoter on the CO and H₂ Adsorption Properties of Titania-Supported Cobalt Fischer-Tropsch Catalysts. *J. Catal.* **2007**, *246*, 91–99. <https://doi.org/10.1016/j.jcat.2006.11.014>.
- (13) Bezemer, G. L.; Bitter, J. H.; Kuipers, H. P. C. E.; Oosterbeek, H.; Holeywijn, J. E.; Xu, X.; Kapteijn, F.; Van Dillen, A. J.; De Jong, K. P. Cobalt Particle Size Effects in the Fischer-Tropsch Reaction Studied with Carbon Nanofiber Supported Catalysts. *J. Am. Chem. Soc.* **2006**, *128* (12), 3956–3964. <https://doi.org/10.1021/ja058282w>.

- (14) Barrault, J.; Guilleminot, A.; Achard, J. C.; Paul-Boncour, V.; Percheron-Guegan, A. Hydrogenation of Carbon Monoxide on Carbon-Supported Cobalt Rare Earth Catalysts. *Appl. Catal.* **1986**, 21 (2), 307–312. [https://doi.org/10.1016/S0166-9834\(00\)81363-9](https://doi.org/10.1016/S0166-9834(00)81363-9).
- (15) Barrault, J.; Guilleminot, A.; Achard, J. C.; Paul-Boncour, V.; Percheron-Guegan, A.; Hilaire, L.; Coulon, M. Syngas Reaction over Lanthanum-Cobalt Intermetallic Catalysts. *Appl. Catal.* **1986**, 22 (2), 273–287. [https://doi.org/10.1016/S0166-9834\(00\)82636-6](https://doi.org/10.1016/S0166-9834(00)82636-6).
- (16) Boffa A., Lin C., Bell A.T., S. G. A. Promotion of CO and CO₂ Hydrogenation over Rh by Metal Oxides: The Influence of Oxide Lewis Acidity and Reducibility. *J. Catal.* **1994**, 149 (1), 149–158.
- (17) Dinse, A.; Aigner, M.; Ulbrich, M.; Johnson, G. R.; Bell, A. T. Effects of Mn Promotion on the Activity and Selectivity of Co/SiO₂ for Fischer–Tropsch Synthesis. *J. Catal.* **2012**, 288, 104–114. <https://doi.org/10.1016/j.jcat.2012.01.008>.
- (18) Johnson, G. R.; Werner, S.; Bell, A. T. An Investigation into the Effects of Mn Promotion on the Activity and Selectivity of Co/SiO₂ for Fischer–Tropsch Synthesis: Evidence for Enhanced CO Adsorption and Dissociation. *ACS Catal.* **2015**, 5 (10), 5888–5903. <https://doi.org/10.1021/acscatal.5b01578>.
- (19) Zhong, L.; Yu, F.; An, Y.; Zhao, Y.; Sun, Y.; Li, Z.; Lin, T.; Lin, Y.; Qi, X.; Dai, Y.; Gu, L.; Hu, J.; Jin, S.; Shen, Q.; Wang, H. Cobalt Carbide Nanoprisms for Direct Production of Lower Olefins from Syngas. *Nature* **2016**, 538 (7623), 84–87. <https://doi.org/10.1038/nature19786>.
- (20) Athariboroujeny, M.; Raub, A.; Iablokov, V.; Chenakin, S.; Kovarik, L.; Kruse, N. Competing Mechanisms in CO Hydrogenation over Co-MnO_x Catalysts. *ACS Catal.* **2019**, 9 (6), 5603–5612. <https://doi.org/10.1021/acscatal.9b00967>.
- (21) Pilot, I. a. W.; van Santen, R. a.; Hensen, E. J. M. The Optimally Performing Fischer-Tropsch Catalyst. *Angew. Chemie Int. Ed.* **2014**, 53, 12746–12750. <https://doi.org/10.1002/anie.201406521>.
- (22) Schanke, D.; Vada, S.; Blekkan, E. A.; Hilmen, A. M.; Hoff, A.; Holmen, A. Study of Pt-Promoted Cobalt CO Hydrogenation Catalysts. *Journal of Catalysis*. 1995, pp 85–95. <https://doi.org/10.1006/jcat.1995.1234>.
- (23) Chen, W.; Pilot, I. A. W.; Pestman, R.; Hensen, E. J. M. Mechanism of Cobalt-Catalyzed CO Hydrogenation: 2. Fischer-Tropsch Synthesis. *ACS Catal.* **2017**, 7 (12), 8061–8071. <https://doi.org/10.1021/acscatal.7b02758>.
- (24) Blöchl, P. E.; Jepsen, O.; Andersen, O. K. Improved Tetrahedron. *Phys. Rev. B* **1994**, 49 (23), 16223–16233.
- (25) Perdew, J. P.; Burke, K.; Ernzerhof, M. Generalized Gradient Approximation Made Simple. *Phys. Rev. Lett.* **1996**, 77 (18), 3865–3868. <https://doi.org/10.1103/PhysRevLett.77.3865>.
- (26) Kresse, G.; Hafner, J. Ab Initio Molecular Dynamics for Liquid Metals. *Phys. Rev. B* **1993**, 47 (1), 558–561. <https://doi.org/10.1103/PhysRevB.47.558>.
- (27) Kresse, G.; Furthmüller, J. Efficient Iterative Schemes for Ab Initio Total-Energy Calculations Using a Plane-Wave Basis Set. *Phys. Rev. B - Condens. Matter Mater. Phys.* **1996**, 54 (16), 11169–11186. <https://doi.org/10.1103/PhysRevB.54.11169>.
- (28) Liu, J. X.; Su, H. Y.; Sun, D. P.; Zhang, B. Y.; Li, W. X. Crystallographic Dependence of CO Activation on Cobalt Catalysts: HCP versus FCC. *J. Am. Chem. Soc.* **2013**, 135 (44), 16284–16287. <https://doi.org/10.1021/ja408521w>.
- (29) Vrijburg, W. L.; Moiola, E.; Chen, W.; Zhang, M.; Terlingen, B. J. P.; Zijlstra, B.; Pilot, I. A. W.; Züttel, A.; Pidko, E. A.; Hensen, E. J. M. Efficient Base-Metal NiMn/TiO₂ Catalyst for CO₂

- Methanation. *ACS Catal.* **2019**, 9 (9), 7823–7839. <https://doi.org/10.1021/acscatal.9b01968>.
- (30) Pack, J. D.; Monkhorst, H. J. “special Points for Brillouin-Zone Integrations”-a Reply. *Phys. Rev. B* **1977**, 16 (4), 1748–1749. <https://doi.org/10.1103/PhysRevB.16.1748>.
 - (31) Sun, K.; Zhao, Y.; Su, H. Y.; Li, W. X. Force Reversed Method for Locating Transition States. *Theor. Chem. Acc.* **2012**, 131 (2), 1–10. <https://doi.org/10.1007/s00214-012-1118-x>.
 - (32) Henkelman, G.; Uberuaga, B. P.; Jónsson, H. Climbing Image Nudged Elastic Band Method for Finding Saddle Points and Minimum Energy Paths. *J. Chem. Phys.* **2000**, 113 (22), 9901–9904. <https://doi.org/10.1063/1.1329672>.
 - (33) Henkelman, G.; Jónsson, H. Improved Tangent Estimate in the Nudged Elastic Band Method for Finding Minimum Energy Paths and Saddle Points. *J. Chem. Phys.* **2000**, 113 (22), 9978–9985. <https://doi.org/10.1063/1.1323224>.
 - (34) Den Breejen, J. P.; Frey, A. M.; Yang, J.; Holmen, A.; Van Schooneveld, M. M.; De Groot, F. M. F.; Stephan, O.; Bitter, J. H.; De Jong, K. P. A Highly Active and Selective Manganese Oxide Promoted Cobalt-on-Silica Fischer-Tropsch Catalyst. *Top. Catal.* **2011**, 54, 768–777. <https://doi.org/10.1007/s11244-011-9703-0>.
 - (35) Bulavchenko, O. A.; Gerasimov, E. Y.; Afonasenkov, T. N. Reduction of Double Manganese-Cobalt Oxides:: In Situ XRD and TPR Study. *Dalt. Trans.* **2018**, 47 (47), 17153–17159. <https://doi.org/10.1039/c8dt04137g>.
 - (36) Colley, S. E.; Copperthwaite, R. G.; Hutchings, G. J. Unusual Cobalt Phases in CO-Hydrogenation Catalysts, Studies by in-Situ x-Ray Diffraction. *Catal. Today* **1991**, 9 (1–2), 203–209. [https://doi.org/10.1016/0920-5861\(91\)85025-4](https://doi.org/10.1016/0920-5861(91)85025-4).
 - (37) Scalbert, J.; Cléménçon, I.; Legens, C.; Diehl, F.; Decottignies, D.; Maury, S. Développement d’un Prototype DRX-DRIFTS Innovant Permettant Des Caractérisations Operando de Catalyseurs à Base de Cobalt Pendant La Synthèse de Fischer-Tropsch En Conditions Représentatives. *Oil Gas Sci. Technol.* **2015**, 70 (3), 419–428. <https://doi.org/10.2516/ogst/2014031>.
 - (38) Biesinger, M. C.; Payne, B. P.; Grosvenor, A. P.; Lau, L. W. M.; Gerson, A. R.; Smart, R. S. C. Resolving Surface Chemical States in XPS Analysis of First Row Transition Metals, Oxides and Hydroxides: Cr, Mn, Fe, Co and Ni. *Appl. Surf. Sci.* **2011**, 257 (7), 2717–2730. <https://doi.org/10.1016/j.apsusc.2010.10.051>.
 - (39) Galakhov, V. R.; Demeter, M.; Bartkowski, S.; Neumann, M.; Ovechkina, N. A.; Kurmaev, E. Z.; Lobachevskaya, N. I.; Mukovskii, Y. M.; Mitchell, J.; Ederer, D. L. Mn (Formula Presented) Exchange Splitting in Mixed-Valence Manganites. *Phys. Rev. B - Condens. Matter Mater. Phys.* **2002**, 65 (11), 1–4. <https://doi.org/10.1103/PhysRevB.65.113102>.
 - (40) Chigane, M.; Ishikawa, M. Manganese Oxide Thin Film Preparation by Potentiostatic Electrolyses and Electrochromism. *J. Electrochem. Soc.* **2000**, 147 (6), 2246. <https://doi.org/10.1149/1.1393515>.
 - (41) Nelson, A. J.; Reynolds, J. G.; Roos, J. W. Core-Level Satellites and Outer Core-Level Multiplet Splitting in Mn Model Compounds. *J. Vac. Sci. Technol. A Vacuum, Surfaces, Film.* **2000**, 18 (4), 1072–1076. <https://doi.org/10.1116/1.582302>.
 - (42) Huynh, M.; Shi, C.; Billinge, S. J. L.; Nocera, D. G. Nature of Activated Manganese Oxide for Oxygen Evolution. *J. Am. Chem. Soc.* **2015**, 137 (47), 14887–14904. <https://doi.org/10.1021/jacs.5b06382>.
 - (43) Copperthwaite, R. G.; Hutchings, G. J.; Der Riet, M. Van; Woodhouse, J. Carbon Monoxide Hydrogenation Using Manganese Oxide Based Catalysts: Effect of Operating Conditions on

- Alkene Selectivity. *Ind. Eng. Chem. Res.* **1987**, 26 (5), 869–874.
<https://doi.org/10.1021/ie00065a002>.
- (44) Colley, S.; Copperthwaite, R. G.; Hutchings, G. J.; Van der Riet, M. Carbon Monoxide Hydrogenation Using Cobalt Manganese Oxide Catalysts: Initial Catalyst Optimization Studies. *Ind. Eng. Chem. Res.* **1988**, 27 (8), 1339–1344. <https://doi.org/10.1021/ie00080a001>.
- (45) Riet, M. Van Der; Hutchings, G. J.; Copperthwaite, R. G. Selective Formation of C3 Hydrocarbons from CO +H2 Using Cobalt-Manganese Oxide Catalysts. **2001**, 1 (798), 798–799.
- (46) Iglesia, E.; Soled, S. L.; Fiato, R. A. Fischer-Tropsch Synthesis on Cobalt and Ruthenium. Metal Dispersion and Support Effects on Reaction Rate and Selectivity. *J. Catal.* **1992**, 137 (1), 212–224. [https://doi.org/10.1016/0021-9517\(92\)90150-G](https://doi.org/10.1016/0021-9517(92)90150-G).
- (47) Johnson, G. R.; Werner, S.; Bustillo, K. C.; Ercius, P.; Kisielowski, C.; Bell, A. T. Investigations of Element Spatial Correlation in Mn-Promoted Co-Based Fischer–Tropsch Synthesis Catalysts. *J. Catal.* **2015**, 328, 111–122. <https://doi.org/10.1016/j.jcat.2014.12.011>.
- (48) Bezemer, G. L.; Radstake, P. B.; Falke, U.; Oosterbeek, H.; Kuipers, H. P. C. E.; Van Dillen, a. J.; De Jong, K. P. Investigation of Promoter Effects of Manganese Oxide on Carbon Nanofiber-Supported Cobalt Catalysts for Fischer-Tropsch Synthesis. *J. Catal.* **2006**, 237, 152–161. <https://doi.org/10.1016/j.jcat.2005.10.031>.
- (49) Chen, W.; Pestman, R.; Zijlstra, B.; Pilot, I. A. W.; Hensen, E. J. M. Mechanism of Cobalt-Catalyzed CO Hydrogenation: 1. Methanation. *ACS Catal.* **2017**, 7 (12), 8050–8060. <https://doi.org/10.1021/acscatal.7b02757>.
- (50) Dinse, A.; Aigner, M.; Ulbrich, M.; Johnson, G. R.; Bell, A. T. Effects of Mn Promotion on the Activity and Selectivity of Co/SiO2 for Fischer–Tropsch Synthesis. *J. Catal.* **2012**, 288, 104–114. <https://doi.org/10.1016/j.jcat.2012.01.008>.
- (51) Zhuo, M.; Borgna, A.; Saeys, M. Effect of the CO Coverage on the Fischer – Tropsch Synthesis Mechanism on Cobalt Catalysts. *J. Catal.* **2013**, 297, 217–226. <https://doi.org/10.1016/j.jcat.2012.10.008>.
- (52) Chen, W.; Zijlstra, B.; Pilot, I. A. W.; Pestman, R.; Hensen, E. J. M. Mechanism of Carbon Monoxide Dissociation on a Cobalt Fischer–Tropsch Catalyst. *ChemCatChem* **2018**, 10 (1), 136–140. <https://doi.org/10.1002/cctc.201701203>.
- (53) Beitel, G. A.; Laskov, A.; Oosterbeek, H.; Kuipers, E. W. Polarization Modulation Infrared Reflection Absorption Spectroscopy of CO Adsorption on Co(0001) under a High-Pressure Regime. *J. Phys. Chem.* **1996**, 100 (30), 12494–12502. <https://doi.org/10.1021/jp960045f>.
- (54) Weststrate, C. J.; Loosdrecht, J. Van De; Niemantsverdriet, J. W. Spectroscopic Insights into Cobalt-Catalyzed Fischer-Tropsch Synthesis : A Review of the Carbon Monoxide Interaction with Single Crystalline Surfaces of Cobalt. *J. Catal.* **2016**, 342, 1–16. <https://doi.org/10.1016/j.jcat.2016.07.010>.
- (55) Toomes, R. L.; King, D. A. The Adsorption of CO on Co{1010}. *Surf. Sci.* **1996**, 349 (1), 1–18. [https://doi.org/10.1016/0039-6028\(95\)01049-1](https://doi.org/10.1016/0039-6028(95)01049-1).
- (56) Zhu, Y.; Pan, X.; Jiao, F.; Li, J.; Yang, J.; Ding, M.; Han, Y.; Liu, Z.; Bao, X. Role of Manganese Oxide in Syngas Conversion to Light Olefins. *ACS Catal.* **2017**, 7 (4), 2800–2804. <https://doi.org/10.1021/acscatal.7b00221>.
- (57) Couble, J.; Bianchi, D. Heats of Adsorption of Linearly Adsorbed CO Species on Co2+ and Co° Sites of Reduced Co/Al2O3 Catalysts in Relationship with the CO/H2 Reaction. *Appl. Catal. A Gen.* **2012**, 445–446, 1–13. <https://doi.org/10.1016/j.apcata.2012.07.017>.

- (58) Zijlstra, B.; Broos, R. J. P.; Chen, W.; Filot, I. A. W.; Hensen, E. J. M. First-Principles Based Microkinetic Modeling of Transient Kinetics of CO Hydrogenation on Cobalt Catalysts. *Catal. Today* **2020**, *342* (March 2019), 131–141. <https://doi.org/10.1016/j.cattod.2019.03.002>.
- (59) Pestman, R.; Chen, W.; Hensen, E. Insight into the Rate-Determining Step and Active Sites in the Fischer-Tropsch Reaction over Cobalt Catalysts. *ACS Catal.* **2019**, *9* (5), 4189–4195. <https://doi.org/10.1021/acscatal.9b00185>.
- (60) Markvoort, A. J.; Van Santen, R. a.; Hilbers, P. a J.; Hensen, E. J. M. Kinetics of the Fischer-Tropsch Reaction. *Angew. Chemie - Int. Ed.* **2012**, *51*, 9015–9019. <https://doi.org/10.1002/anie.201203282>.
- (61) Brown, I. D.; Skowron, A. Electronegativity and Lewis Acid Strength. *J. Am. Chem. Soc.* **1990**, *112* (9), 3401–3403. <https://doi.org/10.1021/ja00165a023>.
- (62) Geerlings, J. J. C.; Zonneville, M. C.; de Groot, C. P. M. Structure Sensitivity of the Fischer-Tropsch Reaction on Cobalt Single Crystals. *Surf. Sci.* **1991**, *241* (3), 315–324. [https://doi.org/10.1016/0039-6028\(91\)90091-6](https://doi.org/10.1016/0039-6028(91)90091-6).
- (63) Qin, C.; Hou, B.; Wang, J.; Wang, Q.; Wang, G.; Yu, M.; Chen, C.; Jia, L.; Li, D. Crystal-Plane-Dependent Fischer-Tropsch Performance of Cobalt Catalysts. *ACS Catal.* **2018**, *8* (10), 9447–9455. <https://doi.org/10.1021/acscatal.8b01333>.
- (64) Liu, Z. P.; Hu, P. A New Insight into Fischer-Tropsch Synthesis. *J. Am. Chem. Soc.* **2002**, *124* (39), 11568–11569. <https://doi.org/10.1021/ja012759w>.
- (65) Shetty, S. G.; Ciobîcă, I. M.; Hensen, E. J. M.; van Santen, R. a. Site Regeneration in the Fischer-Tropsch Synthesis Reaction: A Synchronized CO Dissociation and C-C Coupling Pathway. *Chem. Commun. (Camb)*. **2011**, *47* (35), 9822–9824. <https://doi.org/10.1039/c1cc11499a>.
- (66) Zijlstra, B.; Broos, R. J. P.; Chen, W.; Oosterbeek, H.; Filot, I. A. W.; Hensen, E. J. M. Coverage Effects in CO Dissociation on Metallic Cobalt Nanoparticles. *ACS Catal.* **2019**, *9* (8), 7365–7372. <https://doi.org/10.1021/acscatal.9b01967>.
- (67) Zijlstra, B.; Broos, R. J. P.; Chen, W.; Bezemer, G. L.; Filot, I. A. W.; Hensen, E. J. M. The Vital Role of Step-Edge Sites for Both CO Activation and Chain Growth on Cobalt Fischer-Tropsch Catalysts Revealed through First-Principles-Based Microkinetic Modeling Including Lateral Interactions. *ACS Catal.* **2020**, *10* (16), 9376–9400. <https://doi.org/10.1021/acscatal.0c02420>.
- (68) Swart, J. C. W.; Ciobîcă, I. M.; Van Santen, R. A.; Van Steen, E. Intermediates in the Formation of Graphitic Carbon on a Flat FCC-Co(111) Surface. *J. Phys. Chem. C* **2008**, *112* (33), 12899–12904. <https://doi.org/10.1021/jp803305s>.
- (69) Joos, L.; Filot, I. A. W.; Cottenier, S.; Hensen, E. J. M.; Waroquier, M.; Van Speybroeck, V.; Van Santen, R. A. Reactivity of CO on Carbon-Covered Cobalt Surfaces in Fischer-Tropsch Synthesis. *J. Phys. Chem. C* **2014**, *118* (10), 5317–5321. <https://doi.org/10.1021/jp4109706>.
- (70) Li, Z.; Lin, T.; Yu, F.; An, Y.; Dai, Y.; Li, S.; Zhong, L.; Wang, H.; Gao, P.; Sun, Y.; He, M. Mechanism of the Mn Promoter via CoMn Spinel for Morphology Control : Formation of Co₂C Nanoprisms for Fischer – Tropsch to Olefins Reaction. **2017**, 8023–8032. <https://doi.org/10.1021/acscatal.7b02144>.
- (71) Liu, J. X.; Su, H. Y.; Li, W. X. Structure Sensitivity of CO Methanation on Co (0 0 0 1), (1 0 1 - 2) and (1 1 2 - 0) Surfaces: Density Functional Theory Calculations. *Catal. Today* **2013**, *215*, 36–42. <https://doi.org/10.1016/j.cattod.2013.04.024>.

Appendix A: Chapter 2

A1. Atomic radii

Table A1. Atomic radii of Co and Mn in different oxidation states.

Metal	Oxidation state 0	Oxidation state ⁺²	Oxidation state ⁺³
Co	0.1252 nm	0.089 nm hs	0.075 nm hs
Mn	0.1264 nm	0.097 nm hs	0.079 nm hs

hs = high spin complex

A2. Structure factor

Intensity $I \propto |F_{hkl}|^2$

Structure factor $F_{hkl} = \sum_j^n f^j(q) \exp [2\pi i(hx^j + ky^j + lz^j)]$

A3. Atomic scattering factor $f^j(q)$ $q = 4\pi \sin \frac{\theta}{\lambda}$

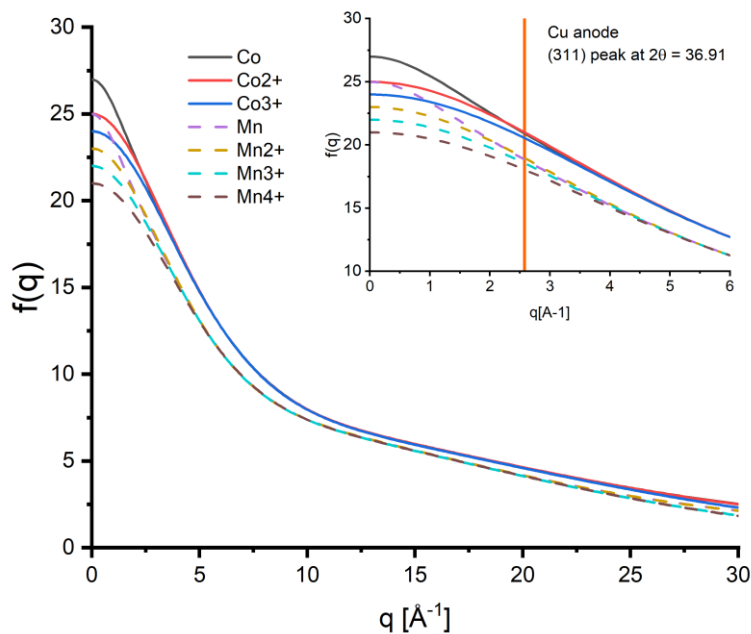


Figure A1. Atomic scattering factor as a function of q .

A4. TEM Particle size

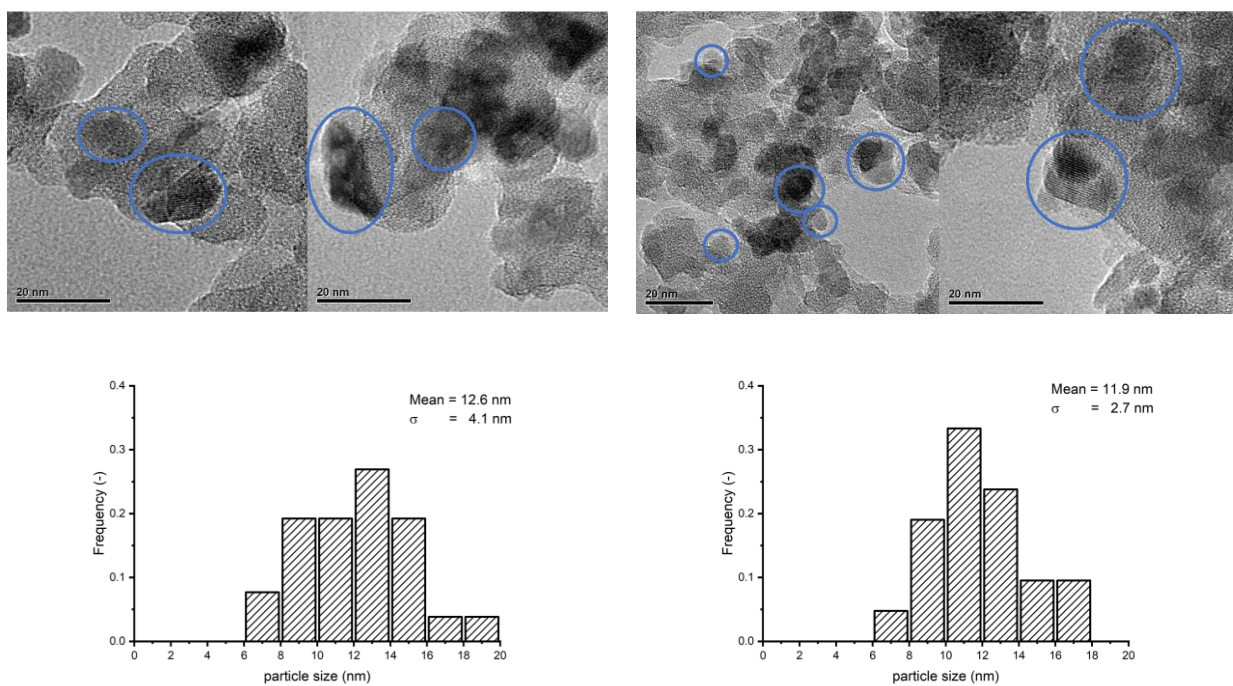


Figure A2. (a) TEM images of Co/Si (left) and CoMn(0.1)/Si (right).

A5. Quasi in situ XPS CO exposure

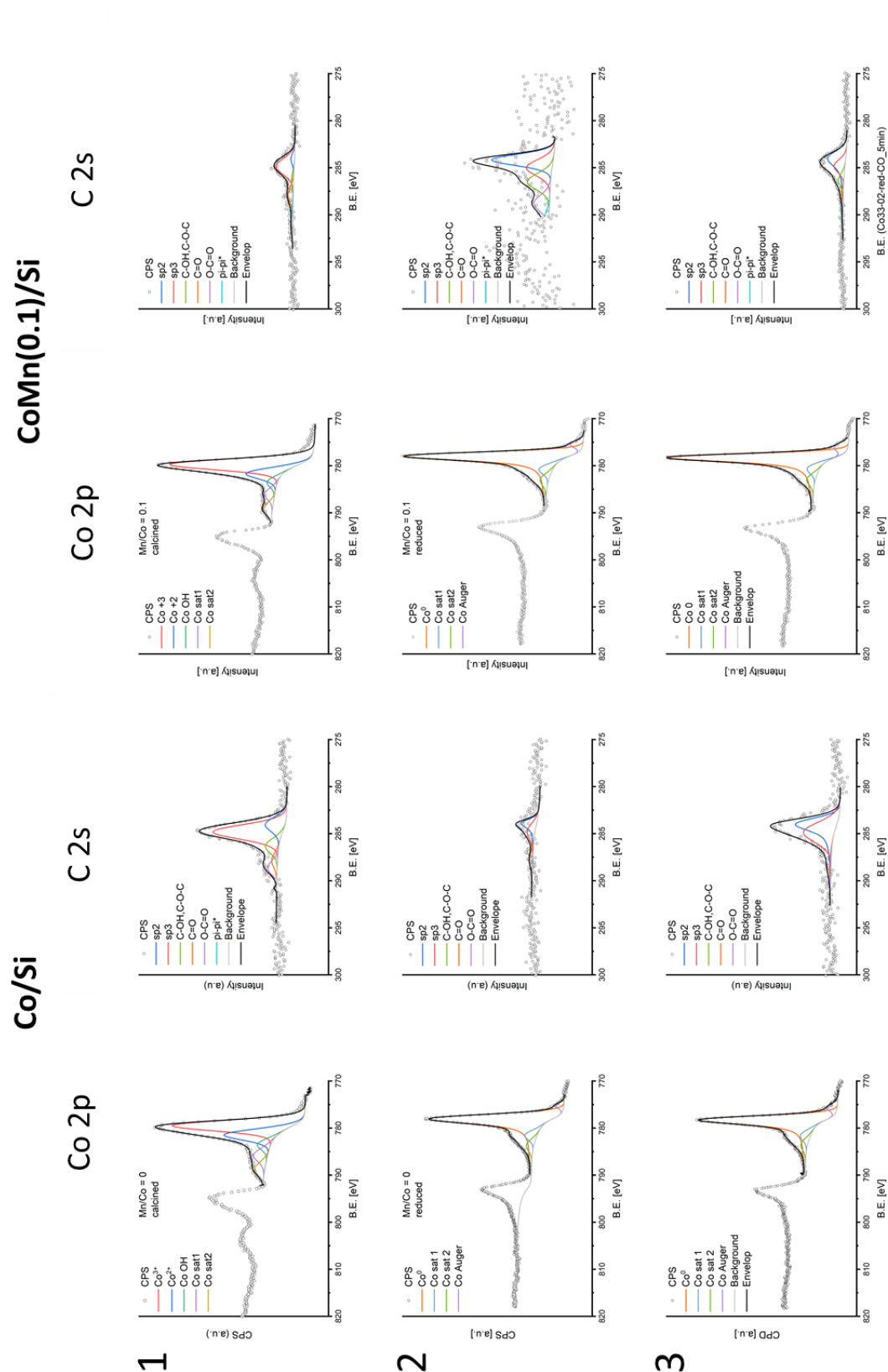


Figure A3-1. XPS spectra of Co 2p and C 2s region for Co/Si and CoMn(0.1)/Si catalysts as a function of treatment. 1) calcined, 2) reduction at 450°C, 3) 5 min CO exposure at 260°C.

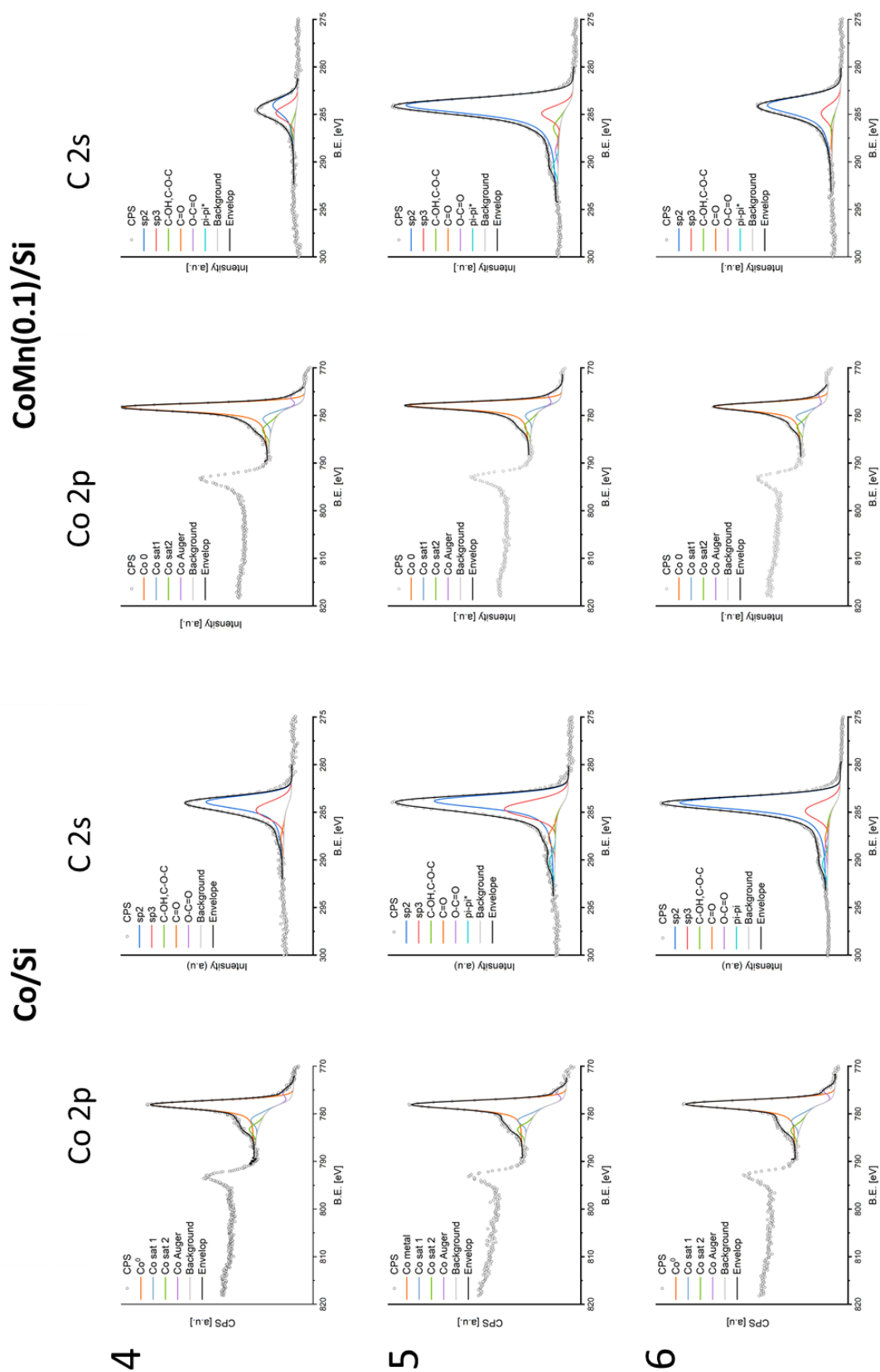


Figure A3-2. XPS spectra of Co 2p and C 2s region for Co/Si and CoMn(0.1)/Si catalysts as a function of treatment. 4) 30 min, 5) 60 min, 6) 120 min CO exposure at 260°C.

A6. Quasi in situ XPS of Mn 2p region

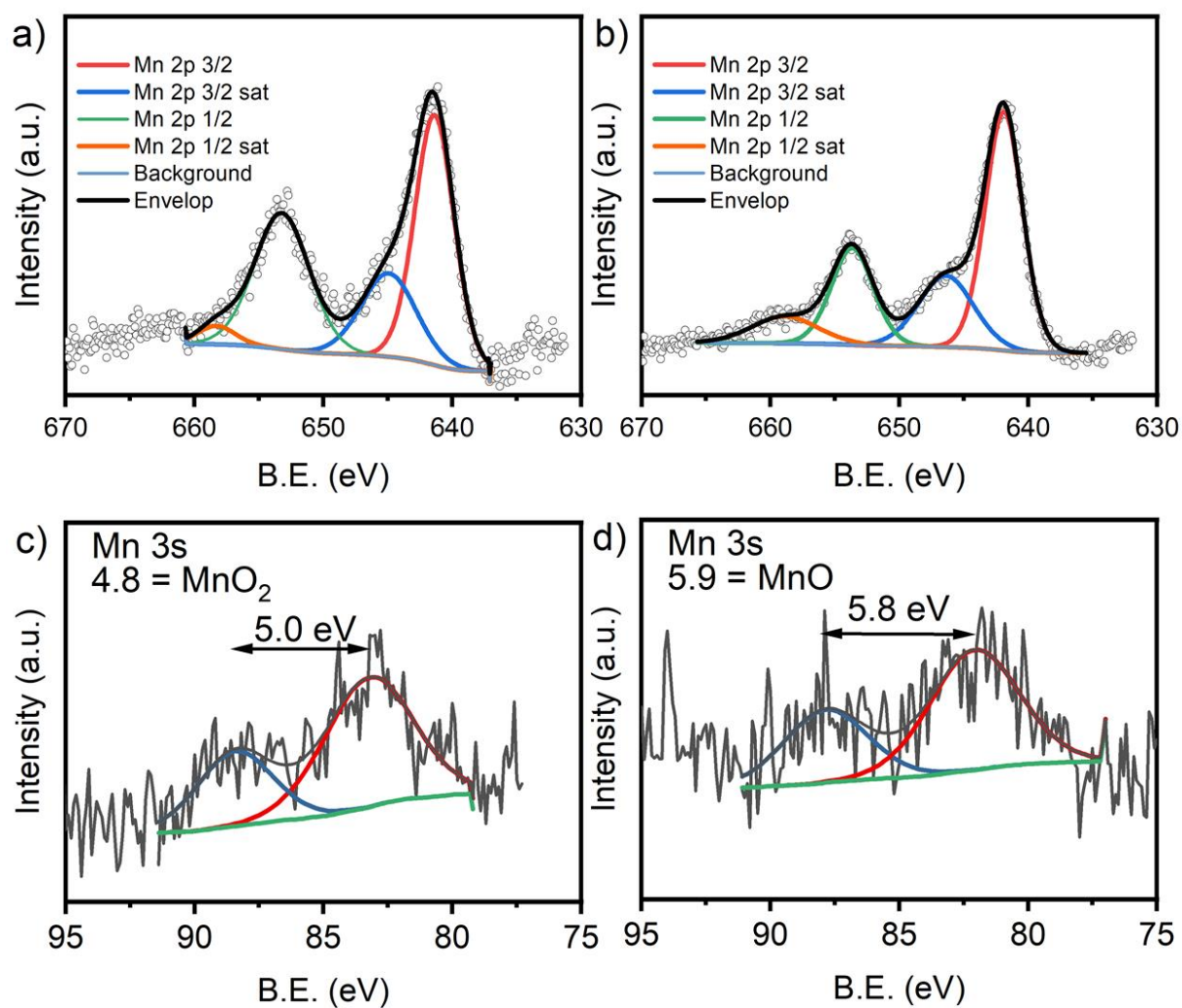


Figure A4. Quasi in situ XPS of CoMn(0.1)/Si of (a,b) the Mn 2p region and (c,d) the Mn 3s region: (a,c) before and (b,d) after reduction at 450°C.

A7. IR spectroscopy after CO exposure

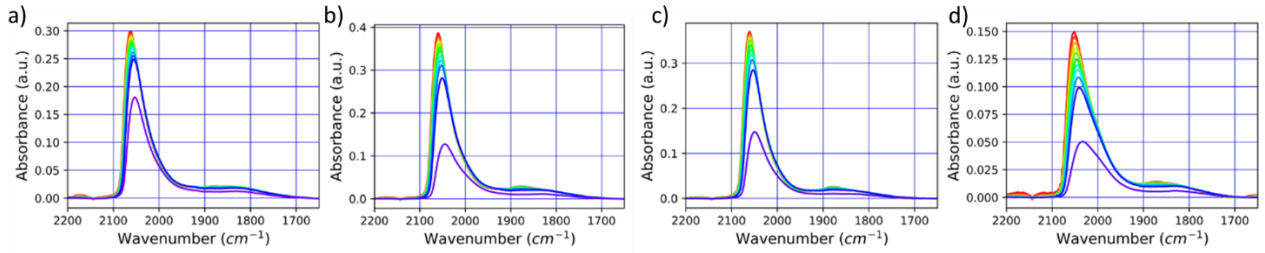


Figure A5. CO IR spectra after reduction at 450°C and CO TPR, $p_{CO} = 0 - 10$ mbar. a) Co/Si, b) CoMn(0.05)/Si, c) CoMn(0.1)/Si, d) CoMn(0.25)/Si.

A8. Internal mass transfer limitations

Internal mass transfer Weisz-Prater criterion

$$C_{WP} = \frac{r^{eff} \rho_{cat} d_{cat}^2}{4D_{eff} C_{CO}} < 1$$

$$C_{WP} = 3.7 * 10^{-4}$$

r^{eff} = observed reaction rate

ρ_{cat} = solid catalyst density

d_{cat} = catalyst particle diameter

D_{eff} = effective diffusion coefficient for CO

C_{CO} = concentration of CO

External mass transfer Carberry number

$$Ca = \frac{r^{eff}}{k_f a_s C_{CO}} < 0.05$$

$$Ca = 4.0 * 10^{-4}$$

r^{eff} = observed reaction rate

k_f = mass transfer coefficient

a_s = the specific external surface area of the pellet

C_{CO} = concentration of CO

Thus, we can exclude mass transfer limitations for the catalytic activity measurements. Both criteria were calculated for CO as it has a lower diffusion coefficient than H₂.

A9. *In situ* XRD during CO exposure

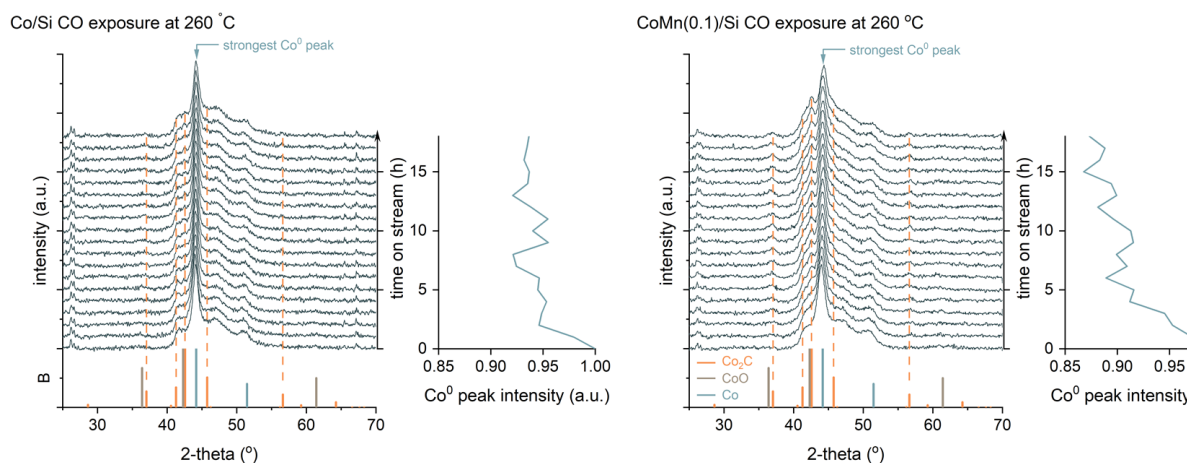


Figure A6. *In situ* XRD carburation during reaction at 260°C and ambient pressure followed in time. The decrease in peak intensity of the metallic cobalt peak is singled out in the line graphs next to the XRD patterns.

Several works report the formation of Co₂C in relation to a high selectivity to light olefins for Co-based catalysts.^{19,70} *In situ* XRD was used to investigate the formation of Co-carbide upon exposure of the reduced catalysts to a CO atmosphere at 260°C for 17 h (Fig. A6). A very small amount of cobalt carbide (Co₂C) was observed for both catalysts. For Co/Si, the amount of Co₂C under such harsh conditions was about 5%, while it was around 10 % for the CoMn(0.1)/Si catalyst. It is also seen that about 5% of metallic Co is converted to Co₂C already after 3 h in both catalysts. We also studied carburation with *quasi in situ* XPS (Appendix Fig. A3-3). After exposure to CO at 260 °C for up to 2 h and TPH analysis at 180°C, 220°C, 260°C and 450°C we were not able to detect any carbide formation. Together these results show that there is a very small amount of Co-carbide formed under harsh carburizing conditions. It is therefore not likely that formation of Co-carbide is responsible for deviating performance observed by Mn-promoted samples.

A10. Model for DFT calculations

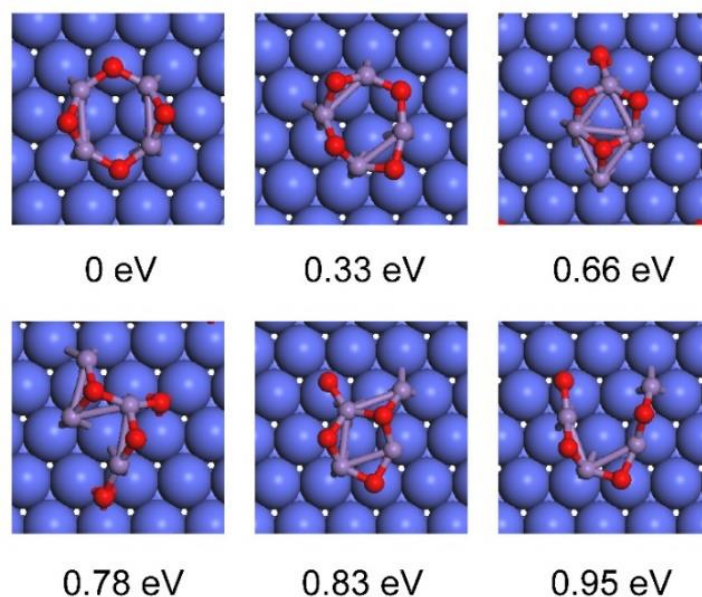


Figure A7. Structures of the six candidate models for the lowest-energy isomers of $\text{Mn}_4\text{O}_4/\text{Co}(0001)$ structure identified by the genetic algorithm in combination with DFT. The energies are relative to the energy of the most stable structure.

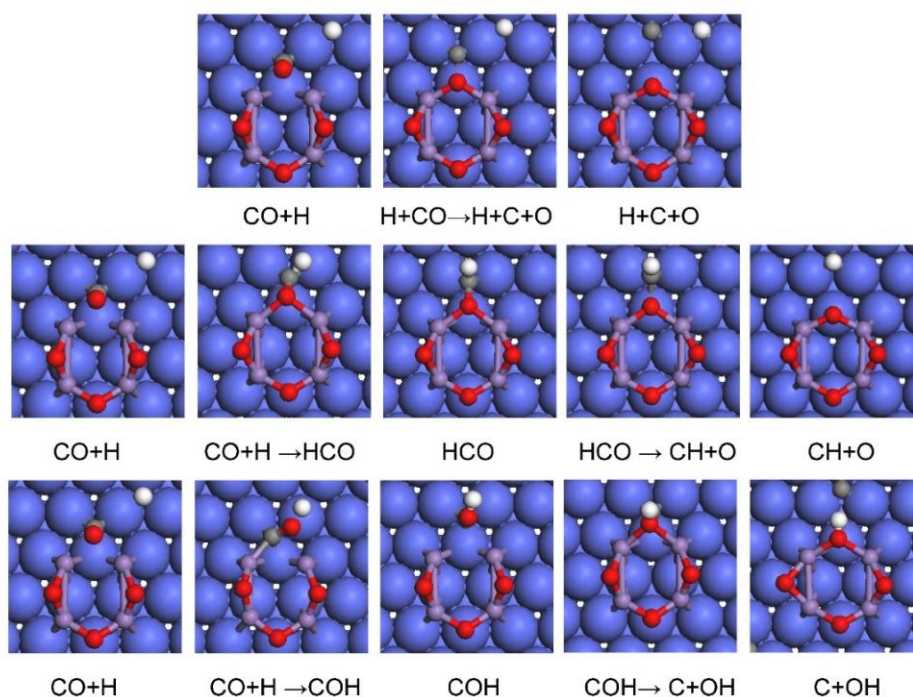


Figure A8. The calculated adsorption and transition states involved in direct and hydrogen-assisted CO activation on $\text{Mn}_4\text{O}_3/\text{Co}(0001)$ structure.

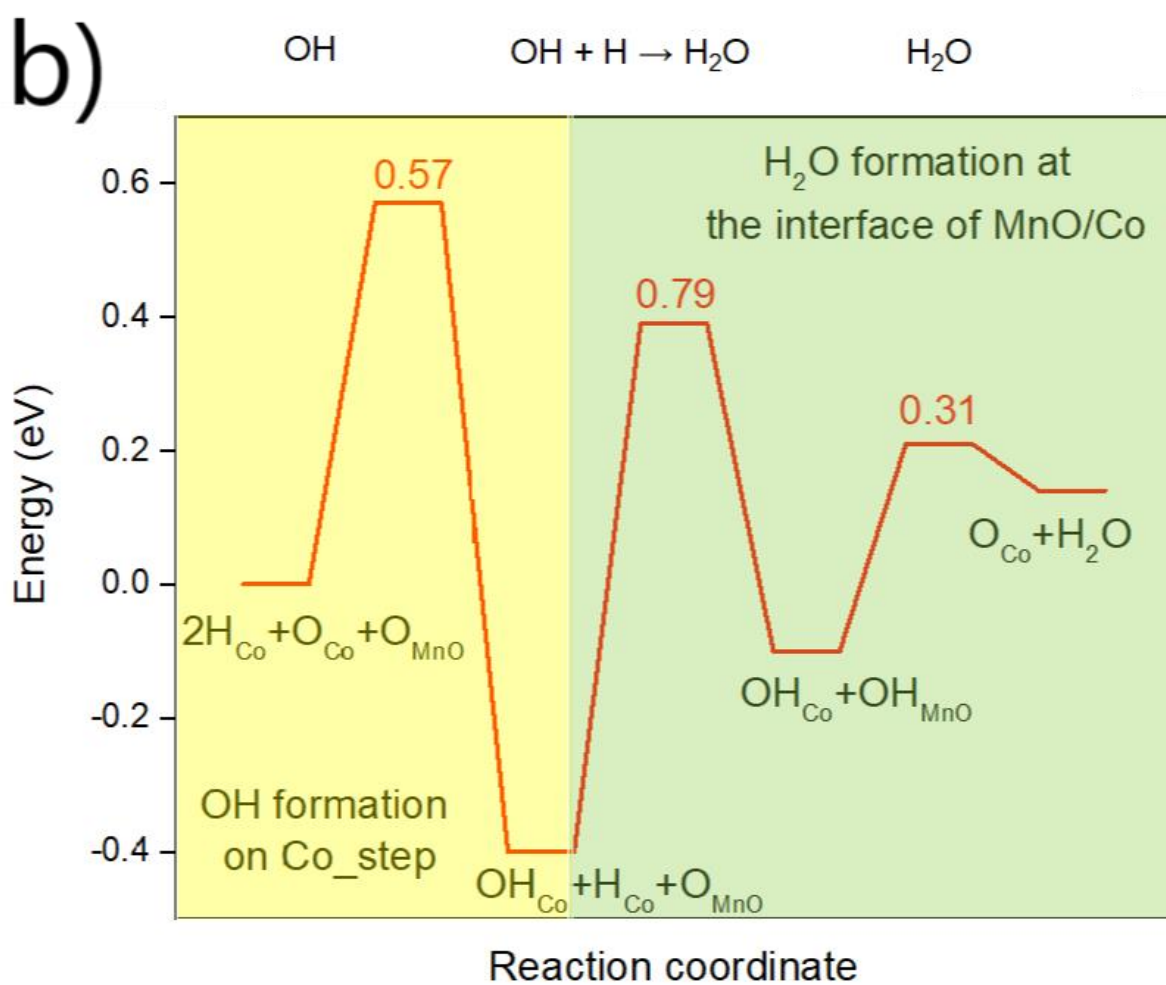
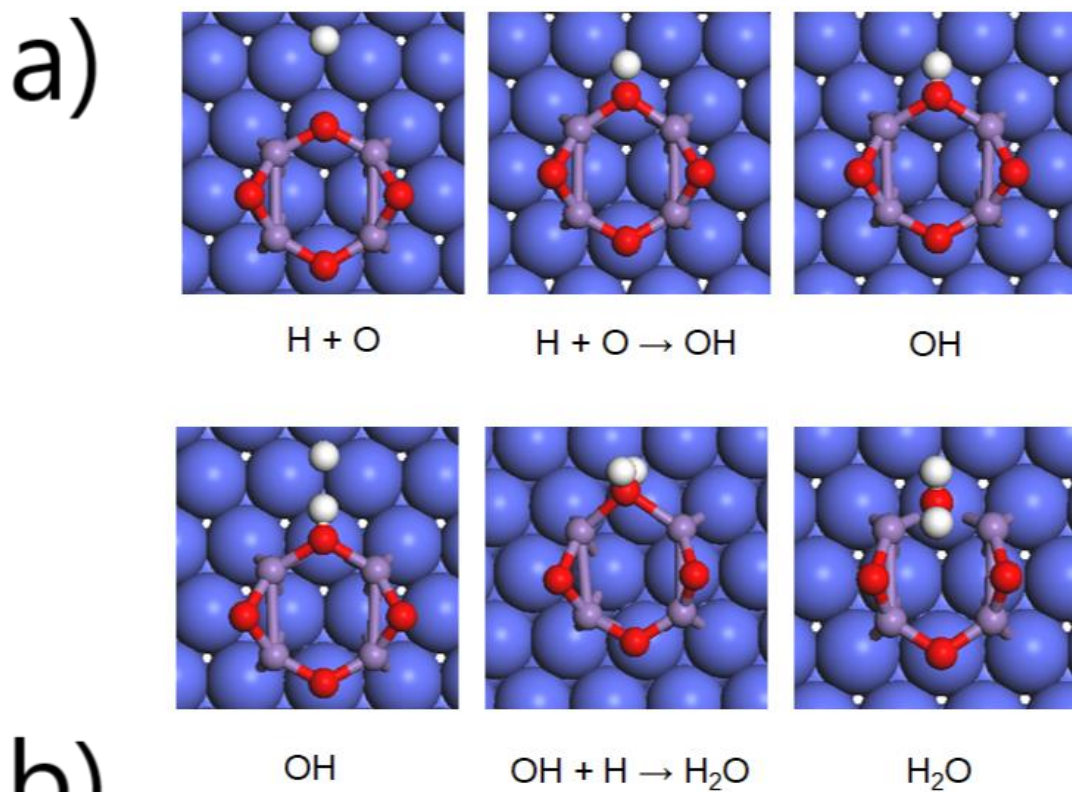


Figure A9. a) The calculated adsorption and transition states involved in H_2O formation at the interface of $Mn_4O_3/Co(0001)$ structure. b) Energy diagram of H_2O formation.

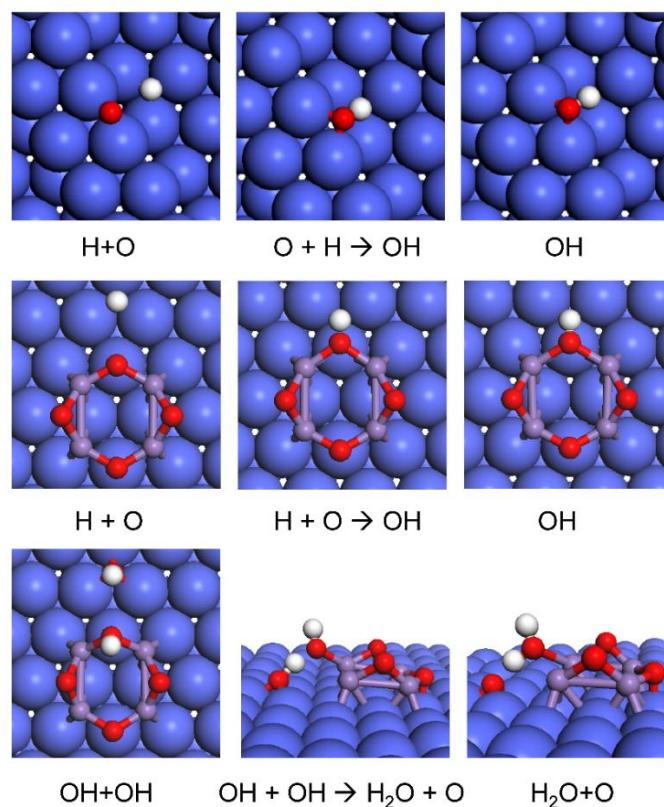


Figure A10. Adsorption and transition states involved in H_2O formation via $\text{OH} + \text{OH} \rightarrow \text{H}_2\text{O} + \text{O}$ at the interface of $\text{Mn}_4\text{O}_3/\text{Co}(0001)$.

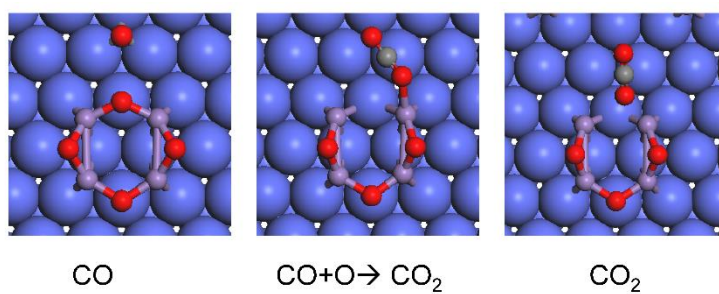


Figure A11. Adsorption and transition states involved in CO_2 formation at the interface of $\text{Mn}_4\text{O}_3/\text{Co}(0001)$.

Table A2. Computed direct CO dissociation barriers on $\text{Co}(0001)$, $\text{Co}(11\bar{2}1)$ and $\text{Mn}_4\text{O}_3/\text{Co}(0001)$.

Surfaces	E_{co} (eV)	E_{a} (eV)	ΔH (eV)
$\text{Co}(0001)^{28}$	-1.64	2.46	0.69
$\text{Co}(11\bar{2}1)^{28}$	-1.82	1.07	-0.05
$\text{Mn}_4\text{O}_3/\text{Co}(0001)$	-1.99	1.29	0.69

Table A3. Computed H-assisted CO dissociation barriers on Co(0001), Co(11 $\bar{2}$ 1) and Mn₄O₃/Co(0001).

Surfaces	CO*+H*→HCO*		HCO*→CH*+O*		CO*+H*→CH*+O*
	E_1 (eV)	ΔH_1 (eV)	E_1 (eV)	ΔH_1 (eV)	E_{total} (eV)
Co(0001) ⁷¹	1.18	1.10	0.73	-0.80	1.83
Co(11 $\bar{2}$ 1) ²⁸	1.03	1.03	0.63	-0.12	1.66
Mn ₄ O ₃ /Co(0001)	0.83	0.71	0.27	-0.59	0.98

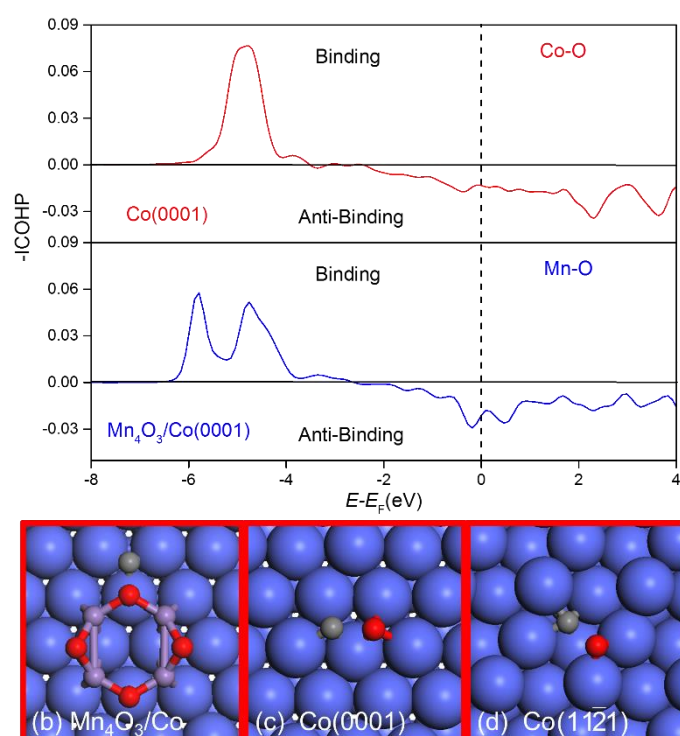


Figure A12. (top) Crystal orbital Hamilton population (COHP) analysis for O adsorption on Co(0001) and Mn₄O₃/Co(0001); (bottom) (a) transition state geometries for direct CO activation on (b) Mn₄O₃/Co(0001), (c) Co(0001) and (d) Co(11 $\bar{2}$ 1).

Chapter 3 - The influence of Co reduction degree on the particle size dependence of CoMn/TiO₂ Fischer-Tropsch catalysts

Abstract

The impact of Mn promotion on small and large Co particles on a TiO₂ support for the Fischer-Tropsch reaction was investigated. A precursor decomposition impregnation method was used to prepare ~4 nm Co particles on TiO₂, while larger ~10 nm Co particles were obtained by incipient wetness impregnation. Mn-promoted samples were obtained by co-impregnation. The method uses a CoCO₃ precursor and citric acid as complexing agent to decrease the particle size. As expected, these small nanoparticles show little activity in the Fischer-Tropsch reaction and a high methane selectivity. A Mn promotor in combination with partially oxidized Co enhances the activity and selectivity of the small particles to a level comparable with large Co particles at ambient pressure and to a lesser extent also at 20 bar reaction pressure. Steady-state isotopic transient kinetic analysis measurements in combination with XPS, Mössbauer and IR characterization revealed that the best Mn-promoted catalysts were obtained after reduction at moderate temperature, resulting in incomplete Co reduction. It is speculated that reaction sites comprising interfaces between metallic Co and Mn- and Co-oxides constitute additional sites for facile CO dissociation in addition to step-edge sites. A new and efficient Co catalyst was thus successfully developed, although further optimization will still be needed for industrial applications.

3.1 Introduction

The Fischer-Tropsch (FT) reaction is a heterogeneously catalyzed reaction for the formation of hydrocarbons from synthesis gas, a mixture of hydrogen and carbon monoxide. Despite investigations for more than hundred years, only recently it has been turned into a commercial technology for the conversion of coal and natural gas to transportation fuels and high-value chemicals^{1,2}. While most group VIII transition metals exhibit activity in Fischer-Tropsch synthesis, only Fe and Co are commercially feasible. For FT synthesis with coal-derived synthesis gas with a low H₂/CO ratio, Fe-based catalysts are preferred due to their high water-gas shift activity. When synthesis gas is derived from natural gas, supported Co catalysts are typically used because of their higher activity and higher chain-growth probability in combination with a low water-gas shift activity^{2,3}.

Several approaches have been developed to optimize the catalytic performance of Co-based catalysts. As the FT product distribution follows the Anderson-Schulz-Flory (ASF) distribution for polymeric chain growth, methane is the most likely product. Therefore, a lot of research has concentrated on increasing the selectivity to more valuable higher hydrocarbons. For this purpose, the addition of promoters has been studied extensively⁴. Among the tested elements, Mn exhibits outstanding performance in terms of reaction rate and selectivity to longer hydrocarbon chains at low pressure⁵. However, its promotional effect is highly pressure dependent and, specifically at elevated pressure relevant to commercial operation, the effect of Mn can also lower the overall activity (Chapter 2). Additionally, noble metal promoters (e.g., Cu, Pt, Re) were shown to increase the reducibility or dispersion of the active phase leading to an improved utilization of cobalt and better performance. However, in recent years there are also several reports indicating that incomplete reduction of cobalt on reducible oxide supports such as TiO₂⁶ and Nb₂O₅⁷, benefiting also from the absence of a reduction promoter, can lead to improved catalytic performance in terms of activity and yield towards higher hydrocarbons.

Given the relatively high price of cobalt metal, reducing the cobalt particle size has been targeted to reduce the metal use. However, it has been firmly established that Co particles smaller than about 6 nm in diameter lose their FT activity due to a lack of active sites for CO dissociation, resulting moreover in an increased CH₄ selectivity.^{8,9} On the other hand, there is also some evidence that small cobalt particles might still be active FT catalysts.¹⁰

Here, we considered the possibility to use Mn promoter to compensate for the loss in CO dissociation sites on small Co nanoparticle catalysts in TiO₂-supported catalysts. As shown in chapter 2, Mn-oxide can provide additional active sites for the dissociation of CO¹¹. Moreover, as there are also indications that the presence of Co-oxide on TiO₂ is beneficial for CO hydrogenation compared to fully reduced Co⁶ we also explored the influence of incomplete Co reduction by lowering the reduction temperature. We prepared small and large titania-supported Co particles with and without Mn promoter. A precursor decomposition method involving CoCO₃ in combination with the chelating agent citric acid was used to obtain small Co-oxide precursor particles of ca. 4 nm, while conventional incipient wetness was employed for obtaining ~10 nm particles. The reduction of the samples at low (280 °C) and high (450 °C)

temperature was investigated by TPR, XPS, X-ray absorption spectroscopy and Mössbauer spectroscopy, while H₂ chemisorption was used to determine the available metallic surface area.

3.2 Method section

3.2.1 Preparation

Titania-supported Co catalysts were prepared by conventional incipient wetness impregnation of TiO₂ (AEROXIDE® TiO₂ P25, Evonik, sieve fraction 120–250 µm, BET surface area of 54 m²/g) with an aqueous solution of Co(NO₃)₂·6H₂O (Merck, 99.99 %) and Pt(NH₃)₄·(NO₃)₂ (Alfa Aesar, 99.995%). Pt was added as a reduction promoter. An Mn-promoted catalyst was prepared by adding Mn(NO₃)₂·xH₂O to the impregnation solution using a Mn/Co ratio of 0.1. This ratio was chosen because it corresponds to optimal promotion in terms of activity¹² (Chapter 2). The impregnated catalysts were dried at 80 °C in a flow of 80 % He and 20 % O₂ for 2 h followed by calcination by heating to 350 °C at a rate of 2 °C/min and an isothermal dwell of 2 h.

A catalyst with small Co particles was prepared by employing a precursor decomposition impregnation method (PDI). Instead of Co(NO₃)₂·6H₂O, CoCO₃ (Merck, 99.99 %) was used together with an aqueous solution of citric acid (Merck, 99.99 %), which acted as a complexing agent for Co²⁺ (molar citric acid/cobalt ratio of 1.5). Under the acidic conditions, insoluble CoCO₃ was slowly decomposed. Gentle heating was used to facilitate slow conversion of Co(CO₃) giving rise to a Co(citrate) complex, which is known to lead to an increased Co dispersion upon deposition¹³. As the solution is slightly acidic, the TiO₂ support will be positively charged, resulting in the interaction with the negatively charged Co-citrate complexes in the solution. As a result of the gradual formation of the citrate complex in the presence of the TiO₂ support, a controlled deposition and thus high dispersion is expected. The subsequent drying and calcination steps were same as for the conventional Co(NO₃)₂·6H₂O incipient wetness impregnation procedure. Pt (0.04 wt%) was added as a reduction promoter.

The Co and Mn contents were determined by ICP-OES (Spectroblue, AMETEK Inc.) analysis after metal extraction in a mixture of H₂SO₄ and HCl at elevated temperature.

3.2.2 X-ray absorption spectroscopy (XAS)

Catalyst reducibility and structural properties were studied using operando XAS performed at the DUBBLE beamline (BM26A) of the European Synchrotron Radiation Facility (ESRF). The samples were measured in transmission mode at the Co K-edge (7.7 keV) selected with a Si(111) monochromator. XANES spectra were normalized and fitted using linear combination fitting (LCF) in the Athena software package. The calcined sample, a CoO sample and a Co metal foil served as references for the respective oxidation states. Extended X-ray absorption fine structure (EXAFS) measurements were analyzed using Artemis on the k³ weighted data. Plotted spectra have a k-weight of 3 and are not phase-corrected. In a typical experiment 30 mg catalyst sample was placed in a stainless steel XAS reactor equipped with two fire rods and diamond glassy carbon windows. Catalysts were reduced in this cell by heating with 5 °C/min to either 280 °C or 450 °C followed by an isothermal dwell of 1 h in a flow of 10 % H₂ in He.

The reduction procedure was followed by XANES. EXAFS spectra were collected at room temperature before and after the reduction.

3.2.3 Temperature-programmed reduction

Temperature-programmed reduction (TPR) was conducted in a Micromeritics AutoChem II 2920 setup equipped with a U-shaped quartz reactor, a computer-controlled oven and a thermal conductivity detector (TCD). In a typical experiment, 50 mg of sample was dried in a flow of He at 100 °C for 1 h following by ramping to 1000 °C at a rate of 10 °C/min in a flow of 4 vol% H₂/He.

3.2.4 X-ray photoelectron spectroscopy (XPS)

Quasi in situ XPS using was performed using a Kratos AXIS Ultra 600 spectrometer, equipped with a monochromatic Al K α X-ray source (Al K α 1486.6 eV). Survey scans were recorded at a pass energy of 160 eV, while a pass energy of 40 eV was used for region scans. The step size was 0.1 eV and the background pressure during the experiment was below 5.10⁻⁹ bar. Samples were pretreated in a high-temperature reaction cell (Kratos, WX-530). For this purpose, the sample was supported on an aluminum stub, allowing *in vacuo* sample transfer into the analysis chamber. Reduction was performed in an equimolar flow of H₂ and Ar at atmospheric pressure at a temperature of 280 °C or 450 °C for 8 h. After reduction, the sample was allowed to cool to 150 °C before transfer to the analysis chamber. The XPS spectra were analyzed using the CasaXPS software (Version 2.3.16 PR 1.6).

3.2.5 Transmission electron microscopy (TEM)

TEM measurements were performed on a FEI Tecnai 20 electron microscope at an electron acceleration voltage of 200 kV with a LaB6 filament. A few milligrams of sample were ultrasonicated and dispersed over a carbon-coated Cu grid. The average particle size and particle size distribution was determined by measuring at least 100 particles.

3.2.6 Chemisorption

The metal surface area was determined by H₂ and CO chemisorption on a Micromeritics ASAP 2010 apparatus. After the reduction of typically 200 mg of catalyst in a flow of 4 vol% H₂ in He at either 280 °C or 450 °C, the sample was evacuated for 30 min at respectively 300 °C or 470 °C to remove remaining hydrogen from the surface. The hydrogen and CO uptake was measured at 110 °C and 30 °C, respectively as a function of pressure and extrapolated with a straight line to 0 mbar. The amount of adsorbed H₂ molecules obtained from the ordinate was used to calculate the available surface area based on the assumption that one H atom or one CO molecule adsorbs per surface Co atom.

3.2.7 Mössbauer emission spectroscopy

For Mössbauer spectroscopy, similar Co catalysts supported on TiO₂ were prepared from solutions to which an appropriate amount of ⁵⁷Co was added to introduce the necessary radioactivity. The details of the Mössbauer spectroscopy setup and the *in situ/operando* cell used for these measurements has been described elsewhere¹⁴. Typically, 20 mg of catalyst was

pretreated at 450 °C in a flow of 25 ml/min He and 25 ml/min H₂ for 4 h. Subsequently, the temperature was lowered to 220 °C and the gas flow was switched to reaction conditions (20/10/20 ml/min H₂/CO/He, 20 bar). The reaction process was monitored using mass spectrometry. Mössbauer spectra were recorded before and after reduction as well as after 20 h of FT operation.

3.2.8 IR spectroscopy

IR spectra were recorded in transmission mode with a Bruker Vertex V70v instrument averaging 32 scans recorded at a 2 cm⁻¹ resolution for CO adsorption experiments. Typically, 15 mg of sample was pressed into a self-supporting wafer and positioned in a homemade controlled-environment infrared transmission cell. CO was admitted to the sample as pulses using a sample loop (10 µl) connected to a six-port sampling valve. CO pulsing was continued until saturation of the CO IR region was observed. This typically led to a final CO pressure of 10 mbar. Prior to IR experiments, the samples were reduced in a flow of H₂ at 450°C for 4 h preceded by heating at 5 °C/min. After evacuating for 30 min at 450°C, the sample was cooled in dynamic vacuum. Prior to the CO dosing, a background spectrum was recorded. During temperature-programmed IR (TPIR), the number of scans for averaging was reduced to 16. Temperature-programmed IR (TPIR) spectra were recorded in the presence of CO (100 mbar) or synthesis gas (60 mbar H₂, 30 mbar CO). For TPIR, spectra were recorded in the 50 – 300 °C range in steps of 25°C.

3.2.9 Catalytic activity measurements at ambient pressure

CO hydrogenation at atmospheric pressure was carried out in a 10-flow parallel plug-flow reactor setup. The catalyst samples (50 mg, 75-125 µm sieved fraction) were diluted with 150 mg SiC of about the same sieve fraction and loaded in quartz tube reactors. The catalysts were reduced *in situ* at either 280 °C or 450 °C for 8 h after heating to this temperature at a rate of 5 °C/min in a 50 ml/min flow of 10 % H₂ in He. After reduction, the temperature was decreased to 200 °C and the feed was switched to a synthesis gas mixture composed of 7% CO and 35% H₂ balanced with He (total flow 50 ml/min). In a typical experiment, the conversion and selectivity were determined at a fixed temperature starting at 200 °C followed by ramping to 300°C in steps of 25 °C. Effluent products were analyzed by online gas chromatography (Interscience CompactGC) accommodated with Restek Rt-Q-bond (equipped with a TCD) and Restek Rtx-1 (equipped with FID) columns. Under these conditions, the formation of higher hydrocarbons could be neglected (selectivity below 1 %). The CO conversion and methane selectivity can thus be calculated as follows

$$X_{CO} = \frac{[CH_4] + [CO_2]}{[CH_4] + [CO] + [CO_2]} \quad (3.1)$$

$$S_{CH_4} = \frac{[CH_4]}{[CH_4] + [CO_2]} \quad (3.2)$$

CO₂ hydrogenation was also investigated in the same reactor setup. The experimental details were the same as for CO hydrogenation, except for the feed mixture that was composed of 20 % H₂ and 5 % CO₂ in He. The CO₂ conversion and product distribution were calculated as follows

$$X_{CO_2} = \frac{[CH_4] + [CO]}{[CO_2] + [CH_4] + [CO]} \quad (3.3)$$

$$S_{CH_4} = \frac{[CH_4]}{[CH_4] + [CO]} \quad (3.4)$$

$$S_{CO} = \frac{[CO]}{[CH_4] + [CO]} \quad (3.5)$$

The catalytic performance at elevated pressure was determined in a Microactivity Reference unit (PID Eng&Tech) at a temperature of 220 °C and a pressure of 20 bar. In a typical experiment, 150 mg catalyst was mixed with SiC particles of the same sieve fraction and placed in a tubular reactor with an internal diameter of 9 mm. The reactor temperature was controlled using a thermocouple located in the center of the catalyst bed. The catalyst was reduced in an equimolar flow of H₂ and He using at 450 °C for 8 h after heating to this temperature at a rate of 3 °C/min. After cooling to 220 °C, the gas feed was replaced by the reaction mixture containing synthesis gas with a H₂/CO ratio of 2 and He with 4 vol% Ar as an internal standard. The gas-hourly space velocity (GHSV) was 2000 h⁻¹, which resulted in CO conversion levels in the range of 5-15 %. A Thermo Scientific TRACE 1300 gas chromatograph equipped with a TCD and FID was used to analyze the effluent reaction mixture. Hydrocarbons (C1-C12) were separated using a Rt-Silica BOND column and subsequently analyzed by FID. The analysis of light gases H₂, CO₂, CH₄, C₂H₄, C₂H₆, Ar, and CO was done with a TCD in combination with Molsieve 5A (mesh 60/80, 2 m) and two Rt-XL Sulfur columns (0.25 m and 1 m). Liquid products and waxes were collected in a rearward cold trap. Under the applied reaction conditions, CO₂ formation was below the detection limit and the carbon-based selectivity of oxygenates was lower than 1 %. The CO conversion (X_{CO}) was determined based on equation (3.6), the carbon-based selectivity of product i (S_i) by equation (3.7), the reaction rate (r_{CO}) by equation (3.8) and the turnover frequencies TOF_{CO} and TOF_{CH_4} by equation (3.9) and (3.10) respectively.

$$X_{CO} = \left(1 - \frac{\frac{CO_{out}}{Ar_{out}}}{\frac{CO_{in}}{Ar_{in}}}\right) \quad (3.6)$$

$$S_i = \frac{Ar_{in} * \nu_i * C_i}{Ar_{out} CO_{in} X_{CO}} * 100 \% \quad (3.7)$$

$$r_{CO} = \frac{F_{CO}^0 X_{CO}}{m_{CO}} \quad (3.8)$$

$$TOF_{CO} = \frac{X_{CO} * F_{CO}^0}{mol\ CO * D_{H_2}} \quad (3.9)$$

$$TOF_{CH_4} = \frac{X_{CO} * F_{CO}^0 * S_{CH_4}}{mol\ CO * D_{H_2}} \quad (3.10)$$

where CO_{in} , Ar_{in} and Ar_{out} represent the CO and Ar concentrations in the inlet and outlet flows, respectively. ν_i stands for the number of carbon atoms in species i , F_{CO}^0 represents the

inlet flow of CO (mol/s), m_{Co} the mass of Co (g), $mol\ Co$ the number Co atoms (mol) and D_{H_2} the dispersion (-) determined via H₂ chemisorption.

3.2.10 Steady-state isotopic transient kinetic analysis (SSITKA)

Steady-state isotopic transient kinetic analysis (SSITKA) was used to determine coverages and residence times of reaction intermediates under steady-state conditions. The details of the SSITKA setup have been described elsewhere¹⁵. Typically, an amount of 200 mg catalyst diluted with SiC of the same sieve fraction was loaded in a low dead-volume stainless-steel tubular reactor with an inner diameter of 5 mm and a bed length and 80 mm. The sample was reduced at 450°C for 8 h using a rate of 3 °C/min and ambient pressure in a flow of 50 ml/min consisting of 10 vol% H₂ in Ar. Subsequently, the reactor was cooled to 220 °C in an Ar flow and the pressure was increased to 1.85 bar. Then, the reactor feed was switched to a mixture of ¹²CO, H₂, and Ar for 16 h. The H₂ flow of the reactants was varied to change the H₂/CO ratio, while the Ar flow was adjusted in order to maintain a total flow rate of 50 ml/min. A SSITKA switch was made from ¹²CO/H₂/Ar to ¹³CO/H₂/Ne. The transients of ¹²CO ($m/z = 28$) and ¹³CO ($m/z = 29$), the main hydrocarbon product ¹²CH₄ ($m/z = 15$) and ¹³CH₄ ($m/z = 17$), and the inert tracers (Ne, $m/z = 22$) were recorded by online mass spectroscopy (quadrupole mass spectrometer, ESS, GeneSys Evolution). Surface residence times were calculated via the area under the normalized transient curves N_i , while a correction was applied for the gas-phase hold-up with the use of the inert Ne tracer:

$$\tau_i = \int_0^\infty (N_i - N_{Ne}) dt \quad (3.11)$$

The CH_x intermediate (precursor to CH₄) residence time was corrected for the chromatographic effect of CO by subtracting half of the CO residence time by [9, 20, 21]:

$$\tau_{CH_4}(\text{corrected}) = \tau_{CH_4} - \frac{1}{2} \tau_{CO} \quad (3.12)$$

The amount of CH_x and reversibly adsorbed CO species can be estimated from the residence time and effluent flow of these species. The coverage of the two species (θ_i) was calculated by dividing the number of adsorbed species by the number of Co surface atoms determined by H₂-chemisorption, A_{Co} .

$$\theta_{CO} = \frac{\tau_{CO} F_{CO} (1 - X_{CO})}{A_{Co}} \quad (3.13)$$

$$\theta_{CH_4} = \frac{\tau_{CH_4} F_{CO} X_{CO} S_{CH_4}}{A_{Co}} \quad (3.14)$$

where F_{CO} refers to the CO feeding, X_{CO} and S_{CH_4} refer to the CO conversion and CH₄ selectivity, respectively, determined by inline GC analysis.

3.3 Results and discussion

3.3.1 Characterization

The influence of Mn on TiO₂-supported large and small Co particles on the FT reaction was investigated. Large Co-oxide particles (~10 nm) were obtained by conventional incipient wetness impregnation (IWI) on the support, while small Co-oxide particles (~4 nm) were obtained using a precursor decomposition impregnation method (PDI). This method is based on the use of citric acid as a chelating agent to increase the dispersion of Co¹³, which was by using insoluble CoCO₃ instead of Co(NO₃)₂. After impregnation and drying, the catalyst precursors were calcined at 350°C. Table 3.1 shows the metal content of the prepared catalysts as determined by ICP analysis. The metal loadings and Mn/Co ratios deviate only slightly from the targeted values for all catalysts. TEM analysis of the calcined precursors (Table 3.1 and Fig. B1 in the Appendix) shows that IWI and PDI loading methods lead to catalysts containing large and small Co-oxide particles with average particle sizes of 10.3 nm and 4.1 nm, respectively. These catalysts are labeled Co(L) and Co(S), respectively. The Mn-promoted catalysts prepared in the same way with Mn present in the impregnation solutions led to respective particles sizes of 11.2 nm and 3.3 nm (catalysts labeled as CoMn(L) and CoMn(S), respectively). The Co(L) and CoMn(L) catalysts yielded relatively large precursor particles. As a result, they are assumed to be located in the plateau region of the structure-sensitivity trend for which a particle size independent TOF is expected for the FT reaction. In contrast, the PDI method yields Co-oxide nanoparticles smaller than 6 nm, which likely yield metallic cobalt particles with a size smaller than 6 nm such that a suppressed activity due to the particle size effect can reasonably be expected. Thus, controlled decomposition of CoCO₃ in the presence of citrate can lead to small Co-oxide particles on titania. The observed release of CO₂ during the preparation indicates CoCO₃ decomposition. Moreover, the PDI method leads to a relatively narrow particle size distribution (Appendix Fig. B1). Compared to colloidal methods^{16,17}, the absence of surfactants that stabilize colloidal particles is an advantage as these organic modifiers or their residuals usually have a detrimental effect on the catalytic properties.¹⁸ We next studied the reduction of these calcined precursors at two different reduction temperatures and its effect on the particle size and available metal surface area.

Table 3.1. Metal content and average particle size as determined by respectively ICP analysis and TEM.

Sample	Co (wt% ^a)	Mn (wt%)	Mn/Co (at/at)	Co ₃ O ₄ particle size (nm)
Co(L)	7.7	n.d.	0	10.3 ± 2.8
CoMn(L)	8.2	0.78	0.11	11.2 ± 3.4
Co(S)	7.4	n.d.	0	4.1 ± 1.1
CoMn(S)	7.2	0.70	0.10	3.3 ± 1.1

The reduction behavior of the catalysts was studied by TPR (Fig. 3.1). As known from literature, Co₃O₄ is reduced in two steps¹⁹. The first step forms CoO and is followed by a second one that reduces CoO to metallic cobalt. Co(S) and CoMn(S) were more difficult to reduce than Co(L)

and CoMn(L). Fig. 3.1 shows that the second reduction step of CoO to metallic Co is shifted to higher temperatures by around 75 °C for the small particles. This can point to stronger Co-support interactions, in line with the delayed reduction of highly dispersed Co as described in literature for Co for on Al₂O₃²⁰, SiO₂²¹, and TiO₂^{22,23} supports. The addition of Mn does not have a significant effect on the final reduction step. Based on these data, we selected reduction temperatures of 280 °C and 450 °C for further investigations on the effect of partial or complete reduction.

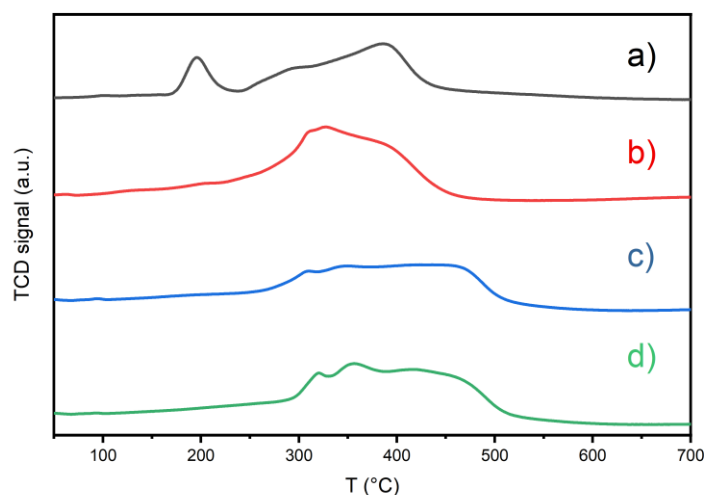


Figure 3.1. TPR profiles of the calcined (a) Co(L), (b) CoMn(L), (c) Co(S) and (d) CoMn(S) catalysts.

Fig. 3.2 shows *quasi in situ* XPS spectra of the calcined catalysts and the catalysts reduced at 280 °C and 450 °C. The calcined catalysts only contain oxidic Co species. Analysis of the XPS intensities of Co and Ti in the calcined catalysts revealed an increasing $\frac{I_{Co}}{I_{Ti}}$ ratio from 0.25 for Co(L) to 0.65 for Co(S), indicating a higher Co dispersion. Using the method of Houalla and Delmon²⁴, the particle size of calcined Co(S) was estimated to be 3.9 nm, which is close to the value obtained from TEM. The XPS fitting results are given in Table 3.2. The Co 2p XPS spectra of the calcined large-particle catalysts, Co(L) and CoMn(L), show distinctive Co₃O₄ features, i.e., contributions of Co³⁺ (779.7 eV), Co²⁺ (781.4 eV), and three accompanying satellite peaks (783.4 eV, 786.1 eV, 789.3 eV).²⁵ The observed Co²⁺/Co³⁺ ratios are close to the theoretical value of 0.5 for pure Co₃O₄ spinel with calcined Co(S) as the exception with a slightly lower ratio of 0.43. The Co 2p XPS spectra for Co(L) and CoMn(L) are very similar. The spectra for the calcined small-particle catalysts Co(S) and CoMn(S) are qualitatively similar to each other, however with a larger contribution of the satellite peak at 786.1 eV as compared to the large particles. Earlier, significant changes in the Co²⁺/Co³⁺ ratios were observed when Co/SiO₂ was doped with Mn. The relatively inert silica leads to complete incorporation of Mn in the Co-oxide as indicated by the shift of the diffraction patterns for Co₃O₄. For CoMn/TiO₂, it seems that most of the Mn is located at the surface of the support, as the Co²⁺/Co³⁺ is hardly affected by Mn addition, reflecting the stronger metal-support interactions for titania.

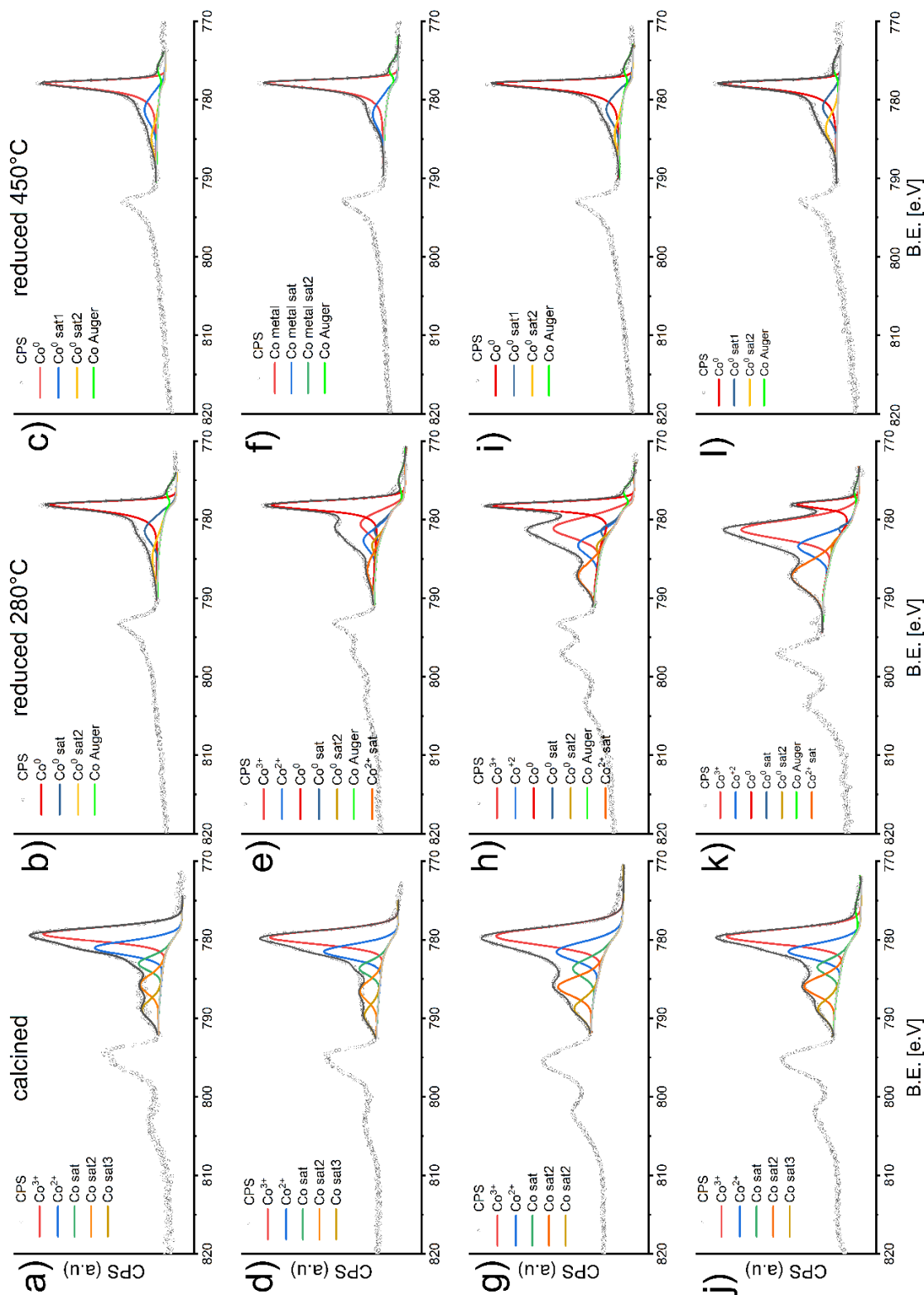


Figure 3.2. Quasi in situ XPS spectra of the Co 2p region of calcined and reduced (280 °C and 450 °C) catalysts: (a) calcined Co(L), (b) Co(L) reduced at 280 °C, (c) Co(L) reduced at 450 °C, (d) calcined CoMn(L), (e) CoMn(L) reduced at 280 °C, (f) CoMn(L) reduced at 450 °C, (g) calcined Co(S), (h) Co(S) reduced at 280 °C, (i) Co(S) reduced at 450 °C, (j) calcined CoMn(S), (k) CoMn(S) reduced at 280 °C, (l) CoMn(S) at reduced 450 °C.

After reduction at 280 °C, the Co phase in Co(L) is fully reduced as evidenced by the main asymmetric feature at 778.1 eV. The degree of reduction (DOR) as determined by the contribution of Co⁰ to the total line intensity of Co decreased significantly when Mn was present, i.e., from 100 % for Co(L) to 58 % for CoMn(L). This lower reduction degree is in keeping with our earlier findings (Chapter 2) and is likely due to a strong interaction between Mn and Co in the oxide precursor. The DOR after reduction at 280 °C of Co(S) and CoMn(S) were even lower at 39 % and 13 %, respectively. This is in qualitative agreement with the TPR results and further confirms the role of a stronger interaction between Co and the support in the small-particle catalysts. Reduction at 450 °C leads to complete reduction of Co in all samples.

Table 3.2. Co 2p_{3/2} XPS fit results and degree of reduction (DOR) upon reduction at 280 °C or 450 °C for 4 h.

Catalyst	Co ²⁺ /Co ³⁺ ratio	Co ⁰	Co ³⁺	Co ²⁺	DOR
Co(L) calcined	0.56	-	64	36	0
Co(L) red 280 °C	-	100	-	-	100
Co(L) red 450 °C	-	100	-	-	100
CoMn(L) calcined	0.49	-	67	33	0
CoMn(L) red 280 °C	-	55	-	45	55
CoMn(L) red 450 °C	-	100	-	-	100
Co(S) calcined	0.43	-	70	30	0
Co(S) red 280 °C	-	39	-	61	39
Co(S) red 450 °C	-	100	-	-	100
CoMn(S) calcined	0.52	-	66	34	0
CoMn(S) red 280 °C	-	13	-	87	13
CoMn(S) red 450 °C	-	100	-	-	100

Mössbauer emission spectra of as-prepared Co(L) and Co(S) doped with ⁵⁷Co are shown in Fig. 3.3. The calcined precursors contain two doublets, which belong to Co³⁺ and Co²⁺. Table B1 in the appendix presents the corresponding fit parameters. Next to the presence of Co³⁺ in the spinel Co₃O₄ compound, Co³⁺ can also stem from the Auger cascade upon decay of the ⁵⁷Co probe²⁶. Specifically, Co³⁺ has also been observed in pure CoO, because neighboring Co²⁺ atom can stabilize Co³⁺ formed during the Auger cascade of ⁵⁷Co long enough to be measured. As such, the observation of Co³⁺ can be an indication for a low dispersion of Co-oxide²⁷. The larger contribution of Co³⁺ in Co(L) in comparison to Co(S) is thus pointing to a lower dispersion, which is in line with the difference in particle size determined by TEM. This explanation in terms of after-effects can also explain the discrepancy with the similar Co²⁺/Co³⁺ ratios for

calcined Co(S) and Co(L) as determined by XPS. After reduction at 450 °C, only a sextuplet of metallic cobalt is observed for both Co catalysts. Exposure to FT reaction conditions does not change the spectra significantly. The occurrence of magnetically split spectra for these reduced catalysts indicates the presence of Co particles with a size larger than 6 nm. Based on the values for the magnetic hyperfine splitting, it can be estimated that the Co particle size is between 15 and 20 nm for both reduced Co(L) and Co(S). Notably, the product distribution of the FT reaction recorded during the Mössbauer measurements under *in situ* conditions (after 20 hours on stream, see Fig. B2 in the appendix) show significant differences, suggesting an effect of the precursor state on the final performance despite the complete reduction of Co and the seemingly similar particle size after reduction.

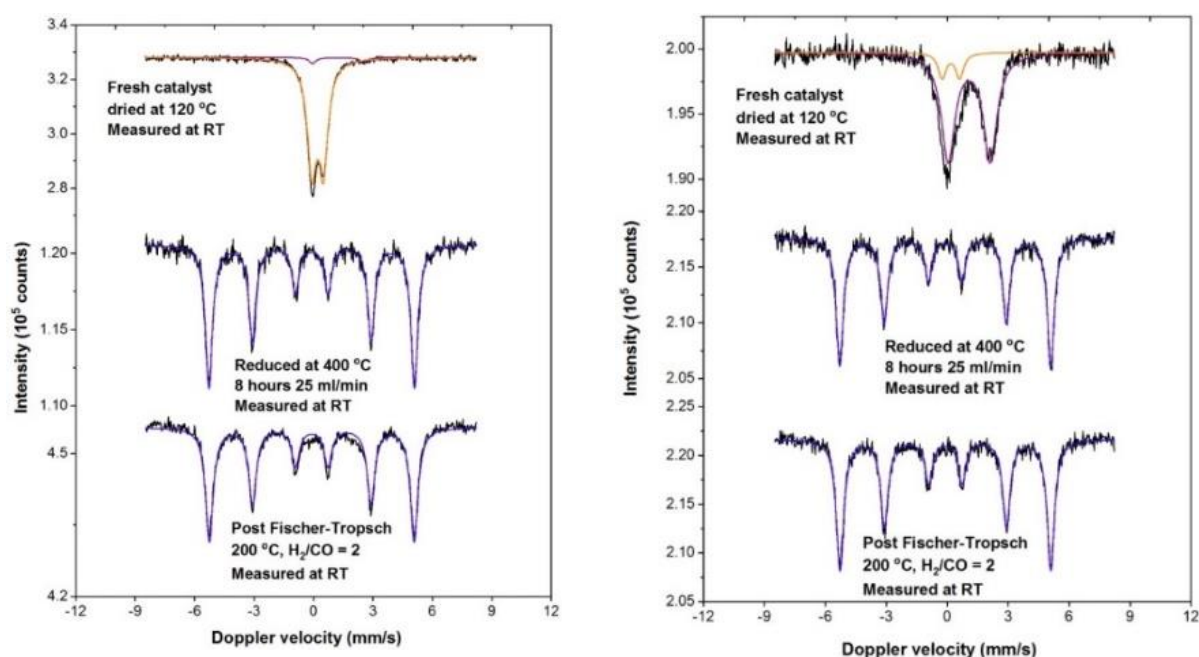


Figure 3.3. Mössbauer spectra of Co/TiO₂ catalysts after calcination, reduction at 450 °C, and after FT synthesis: (left) Co(L) prepared by IWI and (right) Co(S) prepared by PDI.

In situ XANES spectra recorded during the reduction of the samples are depicted in Fig. 3.4. The difference spectra highlight variations in reduction behavior. The reduction of Co(L) proceeds in two steps. The first reduction step, which starts at 200 °C, relates to the reduction of Co₃O₄ to CoO. The second reduction step to metallic Co starts at 400 °C. The corresponding spectra for CoMn(L) show that the first reduction step starts at a slightly higher temperature of 231 °C, when Mn is present in the large-particle catalyst. The final reduction step occurs at 391 °C which is slightly lower compared to the Co(L) sample. While Co₃O₄ reduction for Co(S) starts at nearly the same temperature (195 °C) as for Co(L), the reduction to metallic Co occurs at a substantially lower temperature for the small-particle catalyst (327 °C). Already at intermediate temperatures, some reduced Co seems to be present. However, the complete reduction to Co⁰ proceeds over a large temperature range with CoO_x and Co⁰ coexisting. Addition of Mn to Co(S) results in a delay in both reduction features.

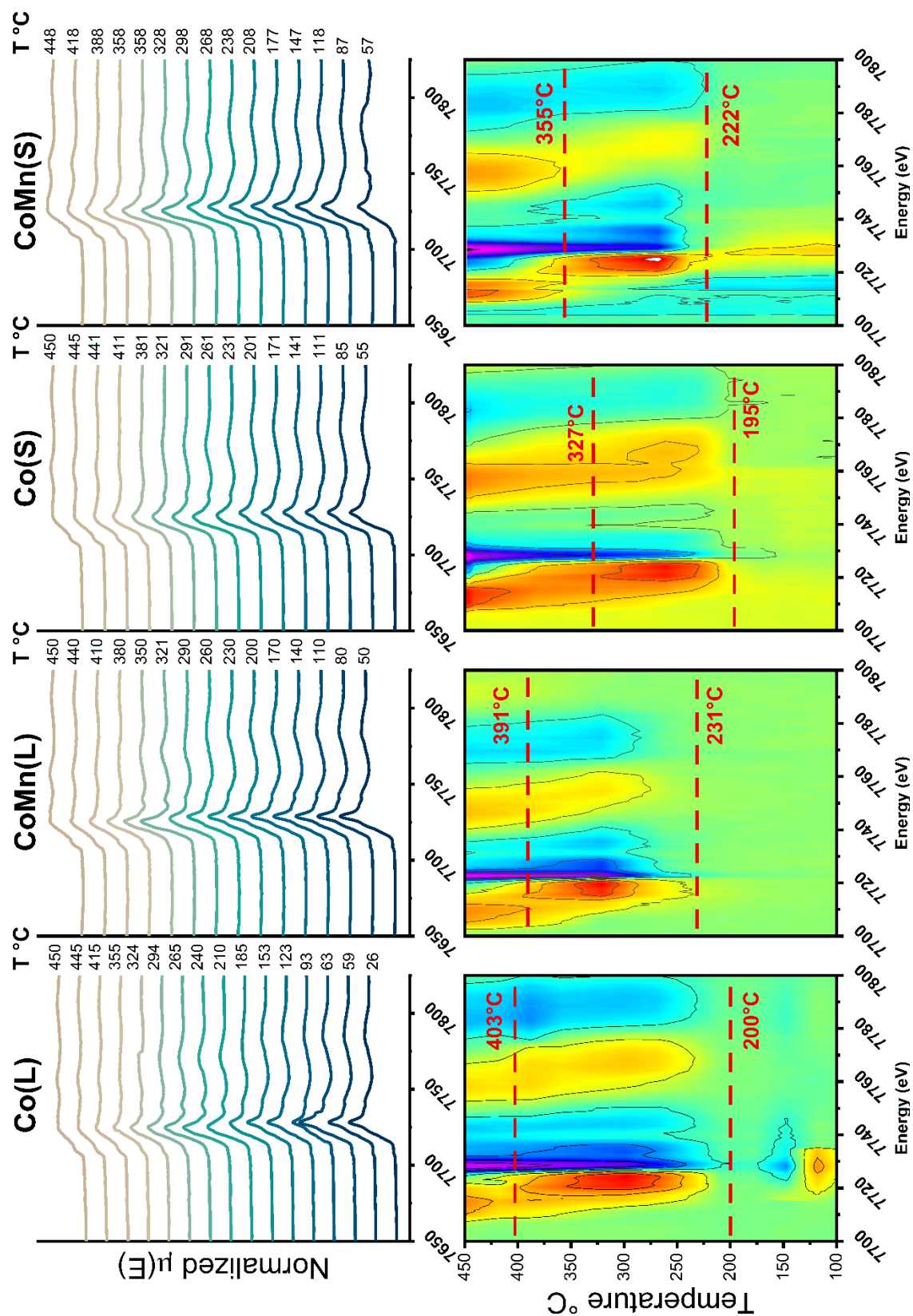


Figure 3.4. In situ XANES spectra at the Co K-edge during reduction of Co(L), CoMn(L), Co(S) and CoMn(S): (top) normalized XANES spectra, (bottom) contour maps of difference XANES spectra with respect to the XANES spectrum of the calcined sample. The red color represents an intensity increase of the signal and the blue color an intensity decrease, in comparison to the calcined sample.

To obtain a quantitative picture of the reduction process, these XANES spectra were deconvoluted by linear combination fitting (LCF), making use of Co_3O_4 , CoO , and Co^0 foil reference spectra (Fig 3.5b). Fig. 3.5a shows that the two-step reduction for Co(L) starts at 250°C with the conversion of Co_3O_4 to CoO , while the final reduction step to metallic Co starts at 300°C . CoMn(L) , which contains Mn , shows a delayed reduction of Co_3O_4 at 325°C (Fig. 3.5), whereas the reduction to metallic Co seems to start at practically the same temperature. As a result, CoO is only observed in a narrow temperature window (i.e., around 325°C). Small Co -oxide particles both with and without Mn contain a higher fraction of CoO than their large counterparts, already from the start of the reduction, in agreement with the high Co^{2+} signal in the Mössbauer and XPS analyses. This is likely related to stronger Co -support interactions. The onset of reduction of Co_3O_4 to CoO occurs at a lower temperature for Co(S) than for the other catalysts. This also holds for the reduction of CoO to metallic Co . CoO and metallic Co co-exist in a wider temperature range than for Co(L) . In the presence of Mn , the large and small particles samples contain less CoO in the precursor, which might be due to competition of Co and Mn for positions that stabilize divalent cations at the surface. Overall, Mn delays the initial reduction step and small-particle oxide precursors contain more CoO and are reduced over a broader temperature range than the large-particle catalysts, which agrees with the TPR results. The degree of reduction at 280°C is, according to the LCF results presented here, negligible. This finding disagrees with the DOR derived from XPS measurements (Table 3.2). This difference is likely caused by the low H_2 partial pressure and short reduction time used in these experiments as compared to the XPS experiment. Nevertheless, both analysis methods lead to the same conclusion that lower reduction temperatures of the non-promoted catalysts leads to the presence of oxidic cobalt in the catalysts. Furthermore, upon Mn addition, the DOR is lower for all catalysts, except at 450°C , at which temperature the Co in all catalysts is completely reduced.

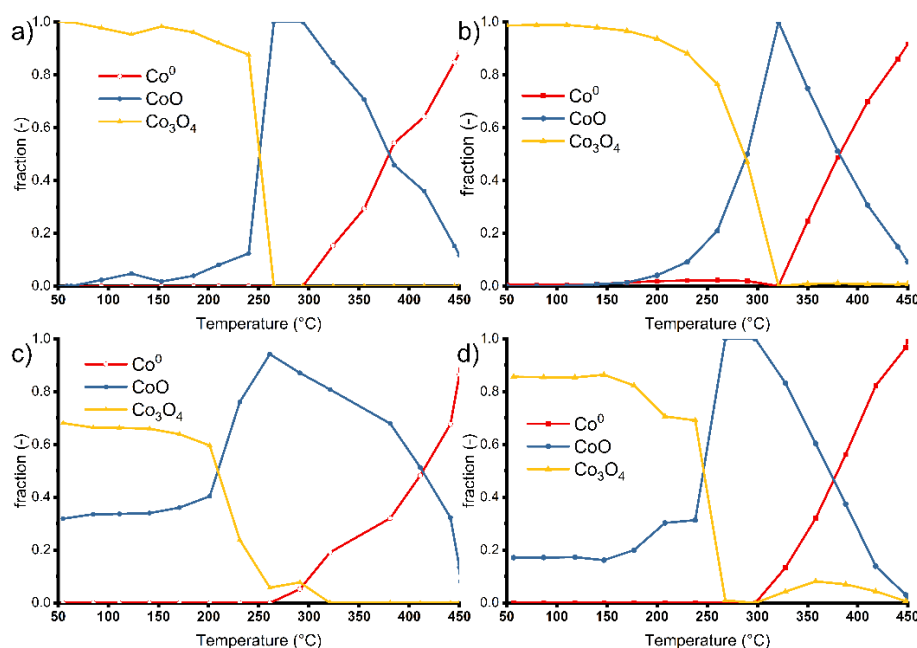


Figure 3.5. Linear combination fitting of the in situ XANES spectra at the Co K-edge during reduction of (a) Co(L) , (b) CoMn(L) , (c) Co(S) and (d) CoMn(S) .

Fig. 3.6 displays the Co K-edge Fourier-transformed (FT) k^3 -weighted EXAFS spectra of Co(L), CoMn(L), Co(S) and CoMn(S) after calcination and reduction at 280 °C and 450 °C²⁸. The Fourier transforms (FT) of the Co K-edge EXAFS spectra of the calcined samples (a, d, g, j) in Fig. 3.6 exhibit a Co-O shell at 1.90 Å and two Co-Co shells at 2.85 Å and 3.36 Å (all distances uncorrected), which are typical for Co₃O₄. The coordination numbers can be correlated to the Co oxide particle sizes. Table 3.3 shows a lower Co-O coordination number in Co(S) of (4.5) than in Co(L), (6.5) consistent with the presence of smaller Co-oxide particles in the former sample. Comparison of the 2 Co-Co shells of the oxide confirms this difference in coordination number. The same trends are observed for the samples containing Mn, although the error margins are larger which may have to do with the distortion of the Co₃O₄ lattice due to substitution of Mn for Co.

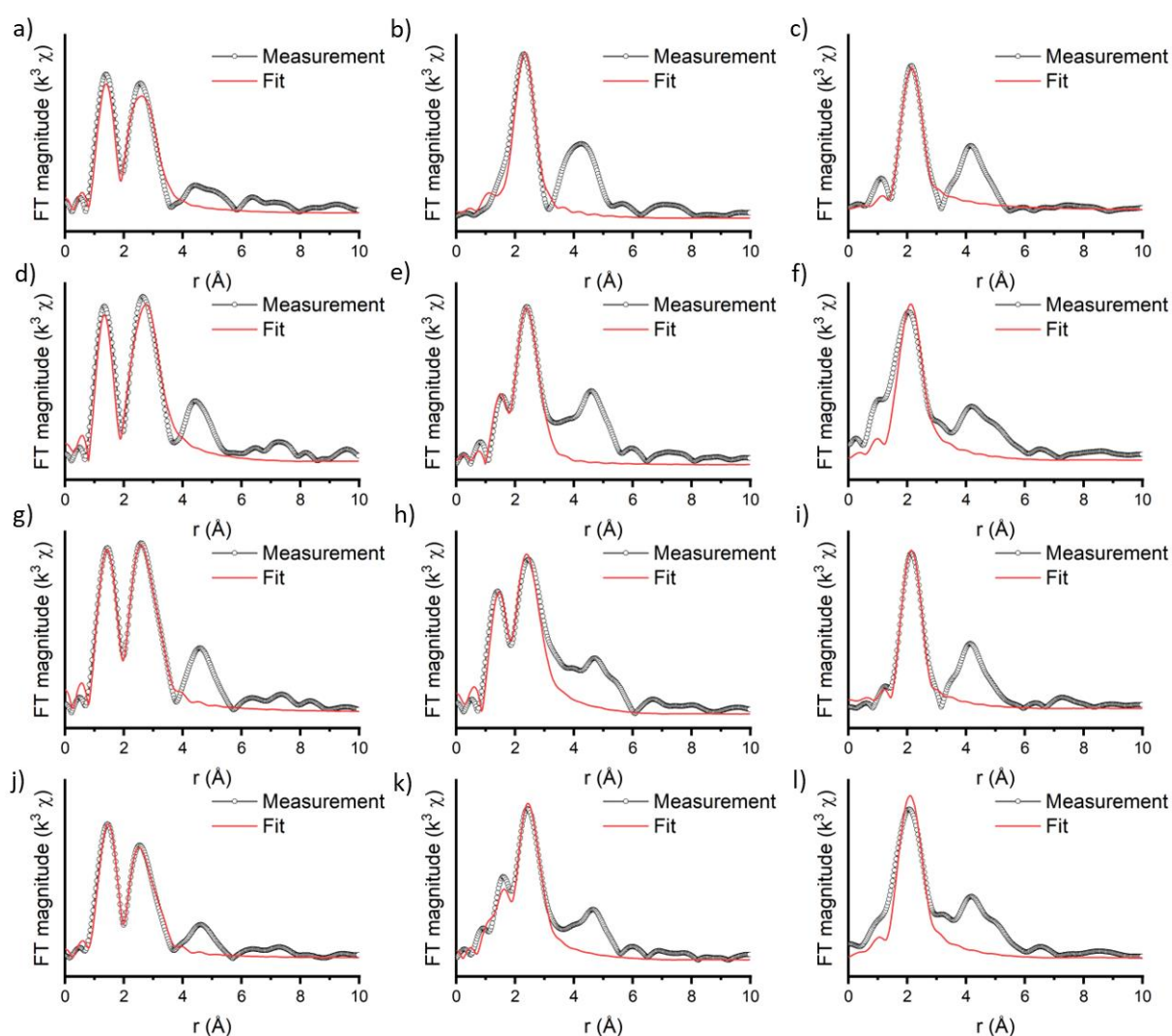


Figure 3.6. Co K-edge Fourier transformed k^3 weighted EXAFS spectra of Co(L), CoMn(L), Co(S) and CoMn(S). (a) Co(L) calcined, (b) Co(L) reduced at 280°C, (c) Co(L) reduced at 450°C, (d) CoMn(L) calcined, (e) CoMn(L) reduced at 280 °C, (f) CoMn(L) reduced at 450°C, (g) Co(S) calcined, (h) Co(S) reduced at 280 °C, (i) Co(S) reduced at 450°C, (j) CoMn(S) calcined, (k) CoMn(S) reduced at 280 °C, (l) CoMn(S) reduced at 450°C.

The FT EXAFS of Co(L) in Fig. 3.6b is dominated by the first Co-Co shell in metallic Co, suggesting complete reduction at 280 °C. This result is in line with the XPS results. CoMn(L) contains an additional Co-O1 coordination shell at 2.1 Å, indicative of the incomplete reduction in the presence of Mn. This is qualitatively in agreement with the DOR of 58 % determined by XPS. The catalysts containing smaller particles exhibit a larger remaining Co-O shell. As the particle size shrinks a larger contribution from the oxidic Co-O shell can be observed. For small particles, however, it seems that Mn addition reduces the Co-O contributions as can be seen in Fig. 3.6k. After reduction at 280 °C the coordination number remains smaller for Co(S) compared to Co(L), which confirms a smaller particle size of Co(S) compared to Co(L) even after reduction. After reduction at 450°C this does not seem to be the case as all catalysts are in the state of complete reduction and have similar the coordination numbers.

Table 3.3. Co K-edge EXAFS fit results of Co catalysts as a function of particle size and Mn content. Error margins are reported in brackets.

Catalyst	Path	CN (error)	R [Å] (error)	E ₀ /eV	σ ² /Å ²	R-factor
Co(L) calcined	Co-O	6.6 (0.35)	1.90 (0.005)	0.88	0.00189	0.0063
	Co-Co1	5.8 (0.68)	2.85 (0.008)		0.00403	
	Co-Co2	6.3 (0.77)	3.36 (0.008)		0.00061	
Co(S) calcined	Co-O	4.9 (0.24)	1.93 (0.005)	0.14	0.00252	0.0046
	Co-Co1	4.8 (0.66)	2.86 (0.010)		0.00885	
	Co-Co2	5.4 (0.77)	3.38 (0.010)		0.00538	
CoMn(L) calcined	Co-O	4.6 (0.76)	1.87 (0.017)	-1.93	0.0019	0.04
	Co-Co1	5.6 (2.99)	2.82 (0.042)		0.01044	
	Co-Co2	6.3 (2.00)	3.33 (0.022)		0.00016	
CoMn(S) calcined	Co-O	4.4 (0.56)	1.91 (0.012)	-2.89	0.00208	0.035
	Co-Co1	4.6 (1.69)	2.84 (0.028)		0.00845	
	Co-Co2	5.3 (1.66)	3.34 (0.022)		0.00302	
Co(L) reduced 280 °C	Co-O1	4.6 (1.41)	1.958 (0.027)	-14.79	0.01245	0.024
	Co-Co	0.97	2.491	-9.31	0.00175	
	Co-O2	12.43 (1.27)	3.033 (0.008)	-14.79	0.00804	
Co(S) reduced 280 °C	Co-O1	2.87 (0.36)	1.997 (0.013)	-5.95	0.00427	0.017
	Co-Co	1.84	2.456	-17.79	0.01331	
	Co-O2	10.08 (1.09)	2.935 (0.009)	-5.95	0.01128	
CoMn(L) reduced 280 °C	Co-O1	3.24 (0.32)	2.144 (0.010)	-7.94	0.00321	0.010
	Co-Co	1.98	2.577	9.97	0.01157	
	Co-O2	12.44 (0.74)	2.981 (0.005)	-7.94	0.00826	
	Co-O1	5.47 (0.55)	2.002 (0.011)	-5.40	0.0127	0.012

CoMn(S)	Co-Co	2.04	2.513	-14.28	0.01661	
reduced						
280 °C	Co-O2	11.62 (0.81)	2.962 (0.005)	-5.40	0.00825	
Co(L)						
reduced	Co-Co	10.94 (2.15)	2.49 (0.014)	6.07	0.00677	0.013
450 °C						
Co(S)						
reduced	Co-Co	12.19 (2.32)	2.49 (0.014)	5.99	0.00771	0.015
450 °C						
CoMn(L)						
reduced	Co-Co	10.54 (3.75)	2.47 (0.021)	4.91	0.00624	0.019
450 °C						
CoMn(S)						
reduced	Co-Co	11.68 (1.53)	2.47 (0.030)	4.81	0.00672	0.045
450 °C						

The metallic surface area per gram of Co as measured by H₂ chemisorption depends on several factors such as the DOR, the particle size and the coverage by MnO. All catalysts reduced at 450 °C as well as Co(L) reduced at 280 °C are completely reduced. The lower measured metal surface area of CoMn(L) as compared to Co(L) after reduction at 450°C is thus likely caused by coverage of the catalyst surface by MnO. On the other hand, the lower surface area of Co(L) reduction at 450 °C is likely caused by sintering at high temperatures. The same counts in extension for Co(S) which, even though it starts from smaller particles, yields the same particle size after reduction at 450°C in agreement with Mössbauer observations. After reduction at 280 °C, the particle size of Co(L) derived from the measured surface area is only 9.7 nm, which implies that at this temperature no sintering occurred.

Table 3.4. H₂ chemisorption data after reduction at 280 °C and 450 °C, particle sizes derived from the H₂ chemisorption assuming spherical particles, and sizes corrected for the DOR obtained from XPS analysis (Table 3.2).

		Reduced at 280 °C			Reduced at 450 °C	
Sample	Mn/Co	mmol H ₂ /gCo	Size	corrected for DOR	mmol H ₂ /gCo	Size
			nm	nm		nm
Co(L)	0	0.88	9.7	9.7	0.35	24
CoMn(L)	0.1	0.80	11	n.a.	0.17	n.a.
Co(S)	0	0.67	13	5.0	0.38	22
CoMn(S)	0.1	0.54	16	n.a.	0.16	n.a.

After reduction at 280 °C, Mn-promoted CoMn(L) has a slightly lower measured metallic surface per gram Co than Co(L). When taking into account that the DOR of CoMn(L) is much lower (55 %) and a part of the catalyst could be covered by MnO, it has to be concluded that the Mn-promoted particles are much smaller than the non-promoted Co(L) particles, indicating that Mn stabilizes the Co particles on the TiO₂ support during low-temperature reduction.

3.3.2 Catalytic performance

Fig. 3.7 gives an overview of the catalytic performance of all catalysts. As can be seen, catalysts that are partially reduced at 280 °C display a similar or higher weight-based activity than when reduced at 450 °C.

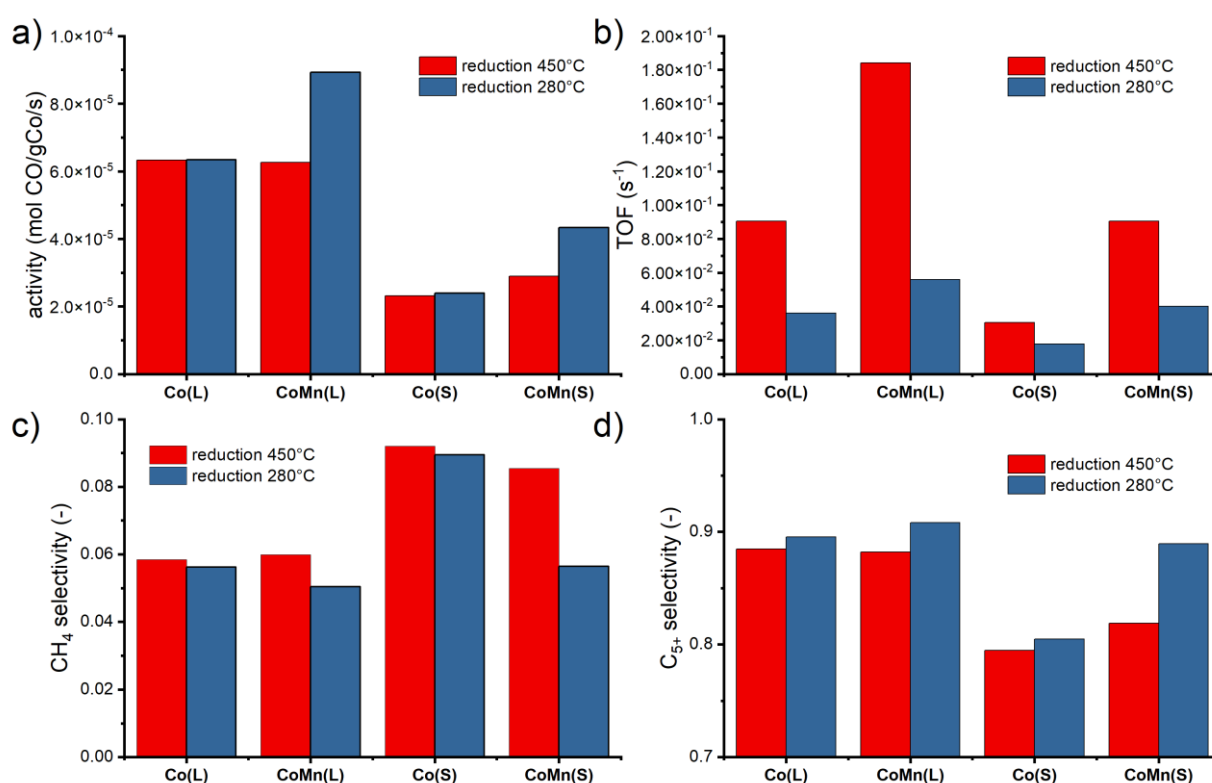


Figure 3.7. Catalytic performance during FT synthesis at 220 °C, 20 bar, H₂/CO = 2, as a function of reduction temperature (450°C, 280 °C), particle size and Mn content. Catalytic data obtained after 24h of operation: (a) activity (mol CO/gCo/s), b) TOF (s⁻¹), c) CH₄ selectivity, d) C₅₊ selectivity.

The beneficial effect of low-temperature reduction on the activity is most prominent for the Mn-promoted samples. For example, on Co(L) reduced at 450°C, Mn addition has hardly an effect on the activity in line with our previous activity data obtained at similar elevated pressure (Chapter 2), but a promotional effect of Mn on the activity is clear upon reduction at 280 °C. Low-temperature reduction also has a beneficial effect on the product distribution for all catalysts. Yet, the beneficial effect on the selectivity is most pronounced in the presence of

Mn. Partial reduction of Co and the presence of Mn seem to strengthen each other's promotional effect.

As there are differences in available Co metal surface area due to changes in particle size and the presence of oxide species on Co, it is useful to compare the performance on the basis of the available metal surface area (turnover frequency, TOF). The TOFs were calculated using the metal surface area measured by H₂ chemisorption. Thus, although the catalysts reduced at 450 °C exhibit a lower weight-based activity than those reduced at 280 °C, they exhibit higher TOFs. Notably, the TOF of Co(S) is lower than the TOF of Co(L) as can be expected based on the particle size effect. However, after Mn addition to Co(S), the TOFs increase substantially and reaches values comparable to Co(L) catalysts treated at the same reduction temperature. These results clearly show that Mn can act as a promoter for small Co particles, which have intrinsically a lower activity in CO dissociation. We mention here that care has to be taken with the interpretation of the H₂ chemisorption data, which may be influenced by spillover effects. Nevertheless, the present data show that small Co particles can be suitable FT catalysts when promoted by Mn. Fig. 3.7 also emphasizes that the product distribution of CoMn(S) reduced at 280 °C is comparable to the Co(L) particles during the FT reaction at 20 bar. From the above, it is clear that the addition of Mn and reduction at low temperature can have synergistic beneficial effects on the TOF and the product distribution in the FT reaction. Data from Melaet et al.⁶ and Hernández Mejía et al.⁷ suggest that the successive reduction-oxidation treatments lead to the formation of CoO_x-Ti³⁺ compounds acting as Lewis acids, facilitating CO dissociation²⁹. In our case, XPS spectroscopy show that a significant amount of oxide species is maintained at low reduction temperature (Fig. 3.2), especially in the presence of Mn. Although we did not perform successive reduction-oxidation cycles, a promotional effect of Co-oxide is also observed, and it is stronger when Mn-oxide is also present.

To develop further understanding of the mechanism underlying the promotional effect of Mn, we studied the olefin to paraffin ratio (O/P) for C₂-C₅ hydrocarbons, because this parameter is a good indicator for the hydrogenation ability of the catalyst. The results presented in Fig. 3.8 follow the generally accepted order with the O/P of the different hydrocarbons C₃ > C₄ > C₅ > C₂. The O/P ratio decreases with increasing chain length due to longer residence time on the surface as well as increased re-adsorption with C₂ being a common exception³⁰. Fig. 3.8 shows that a lower reduction temperature and Mn addition both increase the O/P ratio. A lower hydrogenation ability suppresses termination by hydrogenation and thus enhances chain growth and increases simultaneously the O/P ratio. This results in the linear correlation between chain growth and the O/P ratio as shown in Fig. 3.8b. Co(L)280 and Co(Mn(L)450 display a clearly higher O/P ratio than expected in this correlation. Both these catalysts have a high oxide content, either due to the presence of Mn or due to the lower reduction temperature. Apparently, the hydrogenation ability is suppressed by the presence of oxide. In previous literature^{31,32} hydrogenation is said to run over planar sites. This would imply that MnO is mainly located at the planar sites of the Co particles.

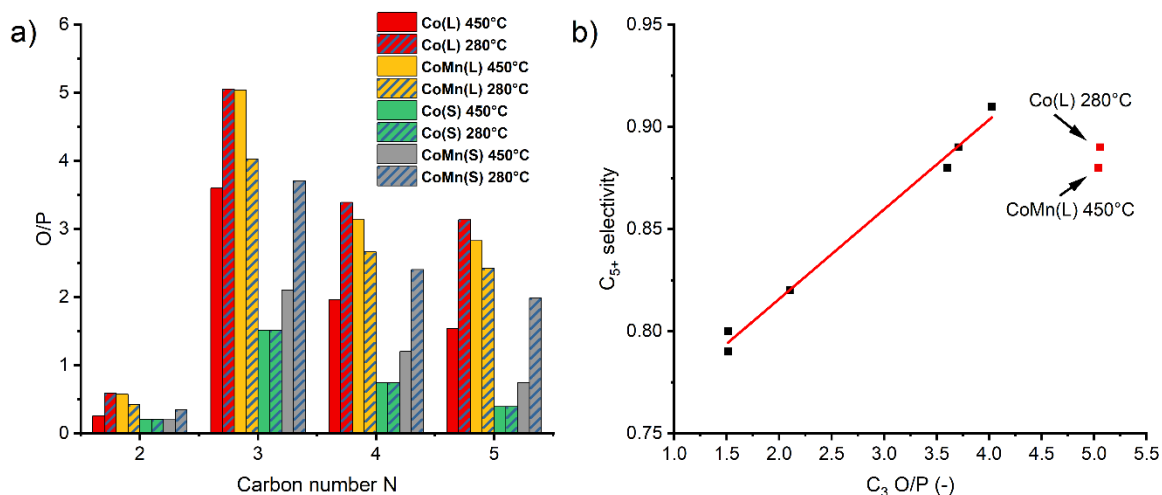


Figure 3.8. (a) O/P ratio for C₂-C₅ for the Co(L), CoMn(L), Co(S), CoMn(S) after reduction at 280 °C and 450 °C and (b) Correlation of C₅⁺ selectivity and the propene to propane ratio (C₃ O/P).

As mentioned above, the presence of Mn in combination with partly oxidized Co is ideal for obtaining a high TOF, likely due to an improved CO activation mechanism. In order to study the mechanistic changes in more detail, the activation energies of the catalysts were determined in a for FT relevant temperature range of 220 to 240°C (at 20 bar H₂/CO = 2) (Fig. 3.9). The apparent activation energy (E_a^{app}) for Co(L) and CoMn(S) reduced at 450 °C are very close to each other with 105 kJ/mol and 103 kJ/mol. The values increase further for CoMn(L) 110 kJ/mol reaching a maximum for Co(S) with 119 kJ/mol. The Arrhenius plot (Fig. 3.9b) shows a linear dependency from temperature excluding further reduction of the catalysts. If mass transfer limitations were relevant, the value of E_a^{app} would be equal to half of the activation energy without mass transfer limitations.

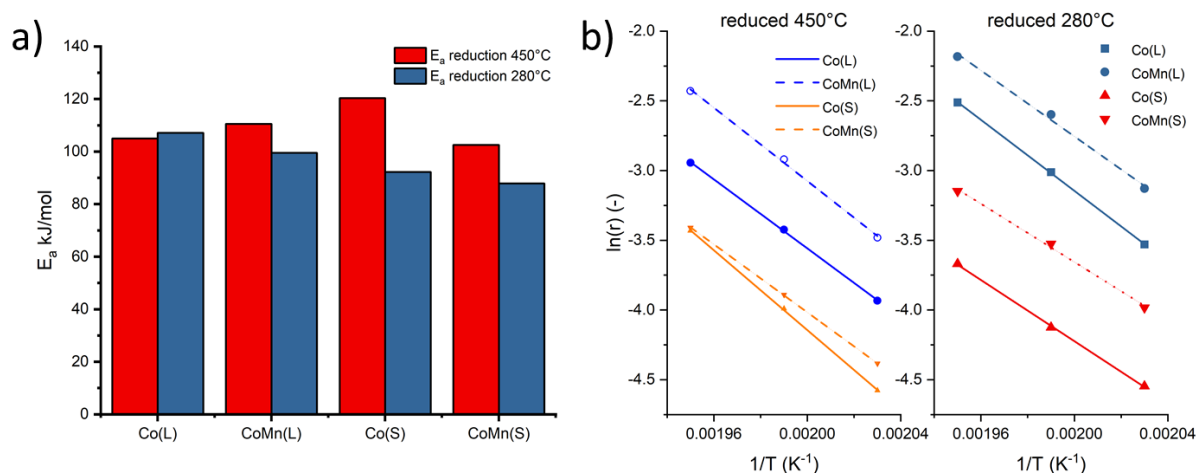


Figure 3.9. (a) Apparent activation energy E_a^{app} as a function of particle size, Mn content and reduction at 20 bar, and (b) Arrhenius plot based on the CO conversion rate, the blue lines refer to the catalysts reduced at 280 °C, the red lines to reduction at 450 °C (20 bar, H₂/CO = 2).

However, the apparent activation energies for FTS displayed in Figure 3.9 are typically in the range of the activation energies reported in literature (80-120 kJ/mol), the observed activation energies thus indicate the absence of mass transfer limitations. While lowering the reduction temperature from 450 °C to 280 °C does not affect E_a^{app} for Co(L), which is already completely reduced at low temperatures as confirmed by *quasi in situ* XPS (Fig. 3.2). In all other cases, catalysts reduced at a lower temperature display a lower E_a^{app} than their completely reduced counterparts. This suggests a contribution of an alternative reaction pathway with a lower activation energy. A role of Co-oxide species as promoter for the rate-controlling CO dissociation step can explain this. Addition of Mn lowers the activation energy for all catalysts except Co(L) reduced at 450 °C. The largest differences in activation energy are observed between non-promoted catalysts reduced at 450 °C and Mn-promoted catalysts reduced at 280 °C. A lower activation energy is directly correlated with a higher rate of the rate-controlling CO dissociation and will thus result in a higher monomer coverage. Indeed Fig. 3.7 shows that only the catalysts that are both reduced at low temperature and are promoted with Mn show a higher activity and C₅₊ selectivity than catalysts that have only one of the two promoting effects, i.e., no partial reduction nor Mn promotion.

In addition, regarding the catalysts reduced at 280 °C, the smaller particles exhibit a lower activation energy than their larger counterparts, while their activity is not always higher. The reason is that activation energy is not the only factor determining the reaction rate, the pre-exponential factor, which also scales with the number of sites. Small particles are known to have less sites that are active in CO dissociation. Furthermore, partial oxidation leads to less available active metal sites. A particle-size-dependent E_a^{app} as shown in Fig. 3.9a was also observed by Pour et al.^{33,34} who found that at 20 bar the heat of adsorption of CO increased with decreasing particle size ($-E_{CO}^{ads}$ from 63 kJ/mol to 74 kJ/mol) leading to an E_a^{app} of 98 kJ/mol for particles of 12.4 nm and E_a^{app} 89 kJ/mol for particles of 4.8 nm. This is in line with the observation of Den Breejen et al.⁹ who reported an increasing amount of irreversibly adsorbed CO for smaller particles. CO chemisorption data on our catalysts showed that the contribution of irreversibly adsorbed CO increases from 80 % of the total amount of CO for Co(L) to 90 % for Co(S), confirming a stronger adsorption of CO on small particles (Table Appendix B3). Based on a Langmuir-Hinshelwood mechanism with CO dissociation as the rate-determining step, the following equation for the apparent activation energy can be derived:

$$E_{app\ CO\ diss}^{act} = E_{CO\ diss}^{act} - (1 - 2\theta_{CO}) \cdot E_{CO}^{ads} \quad (3.11)$$

Thus, at higher CO coverage ($\theta_{CO} > \frac{1}{2}$), which are likely at the high pressure of 20 bar used here, a stronger CO adsorption can lead to a higher E_a^{app} resulting in a stronger impact of the CO adsorption energy. This holds for small particles evaluated. Although the apparent activation energy is lower for the smaller particles, their activity is significantly smaller. This should thus be due to a lower concentration of active sites. The data show that Mn decreases the E_a^{app} for both large and small particles with the effect being more pronounced after reduction at low temperature (Fig. 3.9a). The promotional effect of Mn is likely caused by an easier rate-determining C-O bond dissociation step. This would agree with the hypothesis presented in

our previous work for Mn promotion of Co/SiO₂ (Chapter 2). Fig. 3.7 shows that Mn promotion is absent for catalysts reduced at 450 °C. Clearly, the promotional effect observed for catalysts reduced at 280 °C is due to the lower reduction degree of Co. From the present data, we cannot distinguish between the likely role of manganese as a promoter for CO dissociation and the increase in the amount of oxidized Co.

3.3.3 Temperature-programmed IR spectroscopy

Temperature-programmed IR spectroscopy was used to study the evolution of CO adsorbed on the catalysts as a function of temperature. The initial CO pressure in the cell was 10 mbar and the temperature was increased from 50 °C to 300 °C at a rate of 5 °C/min. For comparison, CO spectra recorded at 30 °C as a function of CO pressure are available in Appendix Fig. A5. These spectra show a typical absorption band at 2020 cm⁻¹ typical for linearly adsorbed CO on metallic Co particles with relatively small contributions of CO adsorbed in two- and three-fold sites³⁵. As observed before for metallic Co,^{36,37} heating of samples in the presence of CO leads to a blueshift of the main linear CO adsorption band, which has been explained by lateral interactions of adsorbed CO with C and O atoms obtained by dissociation of CO. Part of the O atoms are removed as CO₂. The temperature at which this blueshift occurs can be taken as an indication for the CO dissociation activity of the surface.

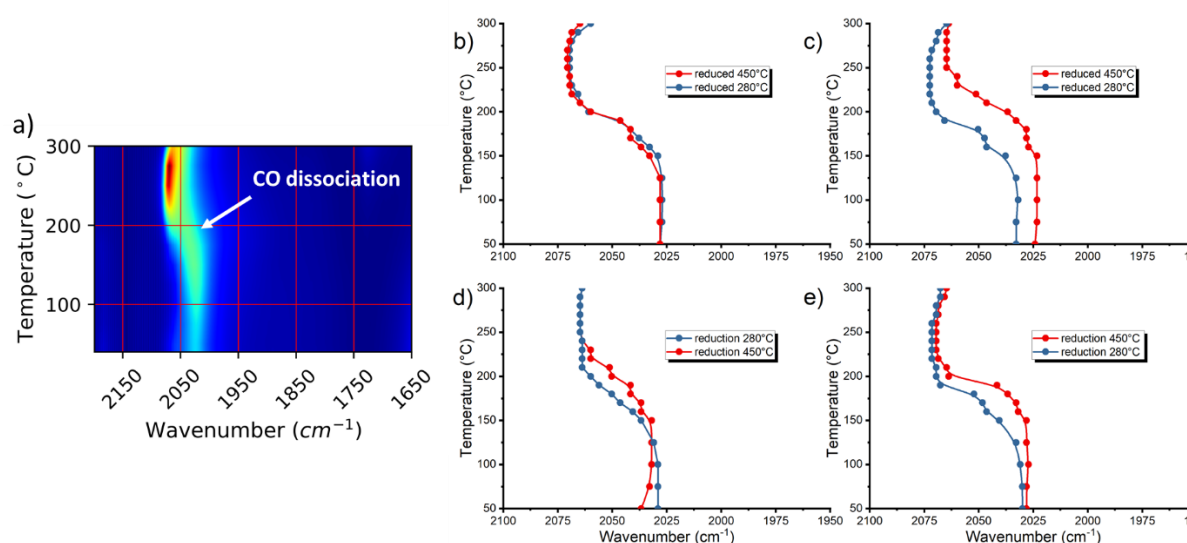


Figure 3.10. (a) Representative heatmap of IR region of adsorbed CO during temperature-programmed IR measurements and (b)-(e) the position of the peak maximum of the linear CO absorption band as a function of temperature for (b) Co(L), (c) CoMn(L), (d) Co(S), and (e) CoMn(S). Catalysts reduced at 280 °C or 450 °C. CO pressure 10 mbar, heating rate 5 °C/min.

The evolution of the linearly adsorbed CO absorption band is plotted as a function of temperature in Fig. 3.10. The corresponding IR spectra are provided in Appendix Fig. A7. Except for Co(L), reduction at 280 °C results in a lower onset temperature for CO dissociation than reduction at 450 °C. As Co(L) is the only catalyst for which the Co phase is completely reduced already at 280 °C, the data for Co(S) suggest that the presence of Co-oxide has a positive effect on the CO dissociation. These results are qualitatively in agreement with the activity differences reported in Fig. 3.7. The onset temperature of CO dissociation for the catalysts

reduced at 450 °C is independent of the presence of Mn, whereas the presence of Mn results in a substantially lower onset temperature for the catalysts reduced at 280 °C. The most significant shift of CO dissociation to lower temperatures is for the Mn-promoted catalysts reduced at 280 °C. These data indicate that the presence of both Co- and Mn-oxide can promote CO dissociation.

We also carried out temperature-programmed measurements in a synthesis gas mixture ($H_2/CO = 2$, $p_{\text{total}} = 100$ mbar). Fig. 3.11 shows the corresponding IR spectra in the C-H stretch region.

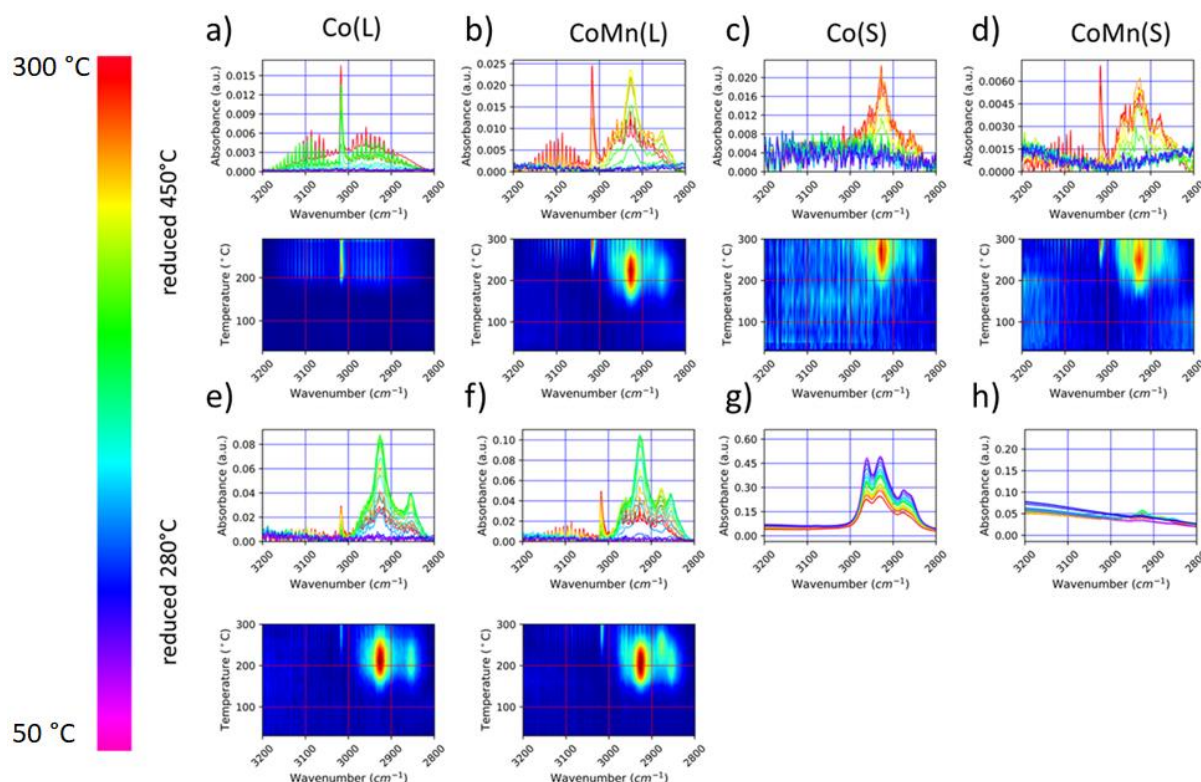


Figure 3.11. Temperature-programmed IR experiments in synthesis gas ($H_2/CO = 2$, $p_{\text{tot}} = 100$ mbar) (a)-(d) catalysts reduced at 450 °C: (a) Co(L), (b) CoMn(L), (c) Co(S), (d) CoMn(S) and (e)-(h) catalysts reduced at 280 °C: (e) Co(L), (f) CoMn(L), (g) Co(S), and (h) CoMn(S). Colors indicate increasing temperature from 50 – 300 °C. In the heat maps colors indicate the increasing IR intensity from violet to red.

During heating, vibrational bands due to adsorbed CH_x species ($\nu_{\text{as}}(CH_2) = 2927 \text{ cm}^{-1}$, $\nu_s(CH_3) = 2876 \text{ cm}^{-1}$, and $\nu_s(CH_2) = 2855 \text{ cm}^{-1}$) precede the evolution of the absorption bands of gas-phase methane consisting of a clear central band at 3015 cm^{-1} (q band of CH_4) accompanied by the rotational-vibrational fine spectrum of methane. The contribution of CH_x species is very small for Co(L) in comparison to the relatively strong signals for CoMn(L). Moreover, the methane signal for CoMn(L) is lower at intermediate temperatures. The higher contribution of CH_x species for the Mn-promoted catalyst is in line with the enhanced CO dissociation suggested by temperature-programmed IR measurements in a CO atmosphere. In the synthesis gas TPIR measurements, the C atoms will be hydrogenated to surface CH_x species. The spectra for Co(L) and CoMn(L) reduced at 280 °C point to suppressed methane formation

and a larger contribution of CH_x species compared to the fully reduced samples. These differences can most likely be attributed to a promoting effect of Co- and Mn-oxide on CO dissociation. Although this result is not expected for Co(L) reduced at 280 °C as it is fully reduced, we speculate that *in-situ* reduction of Co in the TPIR set up at low partial pressures might not be complete. It is likely that the suppressed methane formation is caused by a higher contribution of C₂₊-hydrocarbon products formed due to the higher CH_x coverage. The spectra for Co(S) and CoMn(S) reduced at 450 °C show a lower intensity of methane. The intensity of the CH_x species for Co(S) is comparable to the intensity for CoMn(L), while the CoMn(S) shows a much lower intensity in the regime of CH_x species. As the observed CH_x vibrations relate to species adsorbed on Co metal, these differences can be explained by the lower metal surface area available for these samples with a lower reduction degree. The spectra of Co(S) and CoMn(S) reduced at 280 °C are not shown because of the very low signal due to CH_x species, which we tentatively attribute to the low reduction degree of these samples.

3.3.4 SSITKA

Steady-state isotopic transient kinetic analysis (SSITKA) has been frequently used for mechanistic investigations of CO hydrogenation on Co catalysts including the study of the particle size dependent activity during FT synthesis^{9,38,39}. The typical decrease in catalytic activity for Co particles smaller than 6 nm is reflected by the higher residence time of CH_x (τ_{CH_x}), which is inversely correlated with the methane formation rate during SSITKA measurements.⁸ Usually, pseudo-first-order behavior is assumed for methane formation, meaning that the rate constant for CH_x hydrogenation to methane can be expressed as $k_{CH_x} = \frac{1}{\tau_{CH_x}}$.

The τ_{CH_x} for the Co(S) and CoMn(S) samples are larger than for the Co(L) and CoMn(L) (Fig. 3.12), which implies a lower intrinsic reaction rate for the former samples. This is also reflected in the lower TOF and activity per gram CO for Co(S) and especially CoMn(S) (Fig. 3.13). The lower reaction rate is expected to be a consequence of a lower CO dissociation rate. A lower dissociation rate does not only lead to a lower surface averaged activity (conversion) but also to a drop in the CH_x coverage, abating C-C coupling probability and thus resulting in an increased methane selectivity at the expense of the formation of higher hydrocarbons. Fig. 3.12a shows that when the particle size decreases from 10.3 (Co(L)) to 4.1 (Co(S)) nm, the methane selectivity increases from 31 % to 39 % and the C₅₊ selectivity decreases from 31 % to 23 %. Furthermore, Fig. 3.7 shows that also under high pressure FT conditions, the reaction rate per gram Co and the TOF decrease with the particle size (by about 50 %), in accordance with previous literature^{40,39,9}.

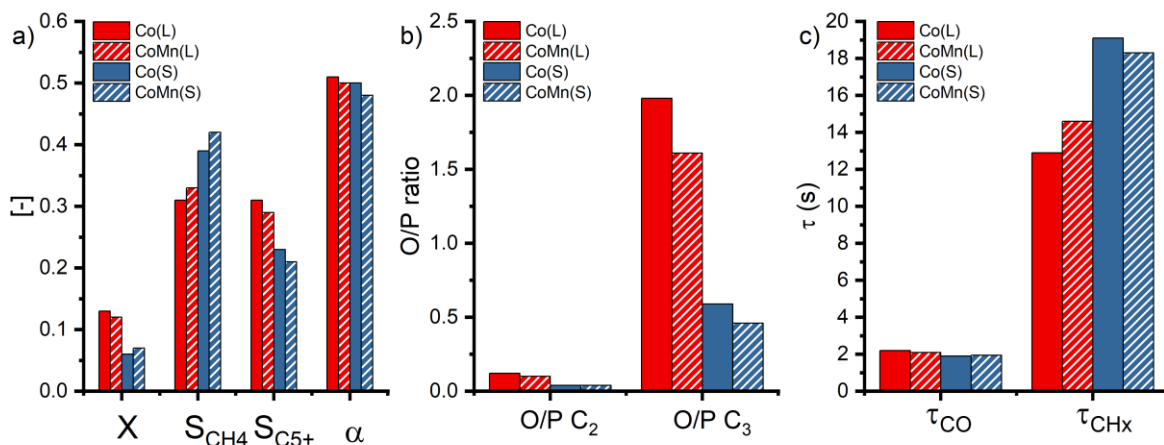


Figure 3.12. Results of SSITKA measurements: (a) CO conversion (X), selectivity to methane (S_{CH_4}), C_{5+} hydrocarbons ($S_{C_{5+}}$) and the chain-growth probability α , (b) the O/P ratio for C_2 and C_3 products, (c) τ_{CO} and τ_{CH_4} . Conditions: 220°C, 2 bar, $H_2/CO = 5$, reduction at 450 °C for 8 h. SSITKA data obtained after 16 h reaction.

Since the dispersion increases with decreasing particle size more metallic Co surface is available in the catalyst bed in case of small particles. Re-adsorption and subsequent hydrogenation of olefins becomes thus more probable at decreasing particle size. The outcome can be seen in Fig. 3.12b, which clearly shows a drop in O/P ratio for C_2 and C_3 by about 70 % when the particle size decreases. These results are similar to those shown in Fig. 3.8. In the preceding chapter it is demonstrated that Mn facilitates CO dissociation. Since the particle size effect is mainly rationalized by a loss in CO dissociation ability, it was expected that the lower CO dissociation activity of small particles, would be compensated by adding Mn. However, Mn addition has limited effect on the parameters shown in Fig. 3.12. This could be caused by the fact that the Mn-promoted small catalyst particles are smaller than the unpromoted particles (3.3 nm vs. 4.1 nm). It was therefore decided to measure the FT reaction rates and turn over frequencies by SSITKA in order to monitor the effect of Mn addition on specifically the CO dissociation rate. The results are presented in Fig. 3.13. Indeed, the reaction rate for the smallest particles (3.3 nm) is increased by Mn addition, while hardly any effect is observed for the larger particles, which already exhibit a high activity. Nevertheless, the activity of the small Mn-promoted particle remains dramatically lower than for the large particles.

Numerous studies have shown that the promotional effect of Mn addition is highly dependent on operating conditions with high pressure and low temperature being unfavorable¹². Hence, to study the promotion effect of Mn better, the catalytic performance was studied as a function of temperature. The results of the CO hydrogenation experiments ($H_2/CO = 5$) in the range of 200-300 °C, at ambient pressure are depicted in Fig. 3.14. In general, the activities of all Mn containing catalysts are higher or equivalent to their unpromoted counterparts over the whole temperature range. This is unexpected as SSITKA experiments presented above showed only negligible effects of Mn addition (Figs. 3.12 and 3.13).

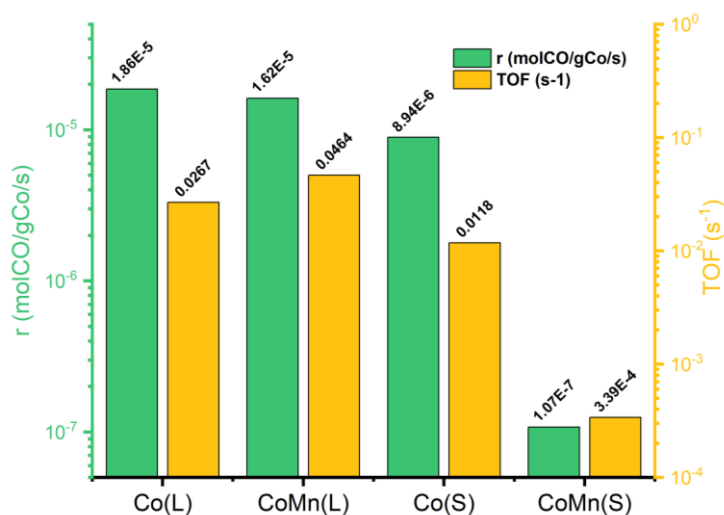


Figure 3.13. TOF(s^{-1}) and activity r (molCO/gCo/s) during SSITKA experiments. Conditions: 220 °C, $H_2/CO = 5$, 2 bar, reduction 8 h at 450°C. Catalytic data obtained after 16 h of operation.

As can be seen in Fig. 3.14, this seemingly contradictory result stems from the temperature used in the SSITKA experiments. Whereas the activity of the small Mn-promoted Co particles is the highest at elevated temperatures, this is less evident around 220 °C, which is exactly the temperature used for the SSITKA study. The hypothesis that Mn addition can compensate for the particle size effect is thus only justified for higher temperatures. Notably, high temperatures are undesirable for Co catalyzed FT, due to the increased methane selectivity, which could, by the way be, suppressed by Mn addition.

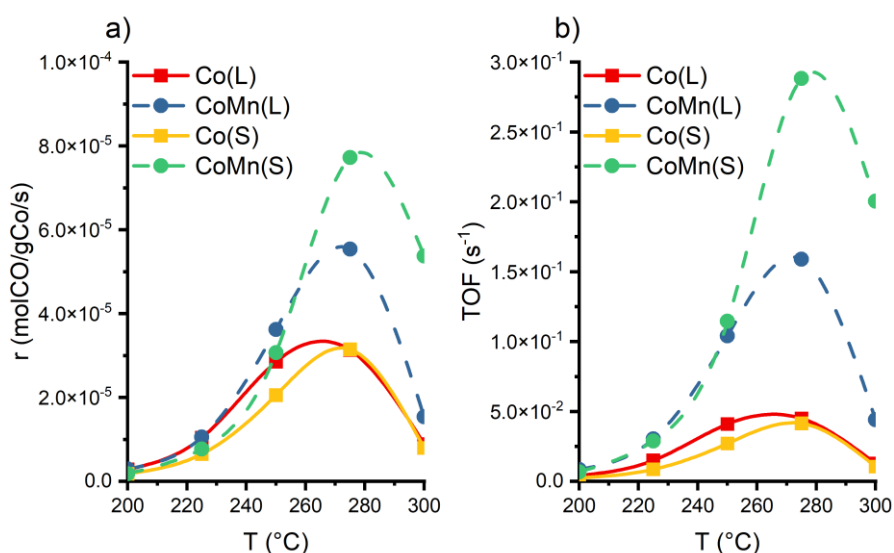


Figure 3.14. Temperature-programmed CO hydrogenation experiments (reduction at 450°C, $H_2/CO = 5$, 1 bar): (a) reaction rate r (molCO/gCo/s) and (b) TOF (s^{-1}).

A concomitant issue at elevated temperatures is the drop in activity above 275°C (see Fig. 3.14), which is most likely caused by carbon deposition. While Mn(S) has a lower activity than Co(L) at moderate temperatures, in agreement with the particle size effect, the activities of the large and small Co particles start to coincide beyond 275 °C, most likely due to the

abovementioned deactivation of the active sites, making the difference in number of active sites between small and large particles disappear.

Above this temperature, CoMn(S) is still superior to all other catalysts, but also suffers from deactivation. In order to circumvent coke formation and to confirm the deteriorating effect of carbon deposition, CO₂ was chosen as a probe molecule. Due to its higher oxygen content, CO₂ will not as easily form carbon deposits via the Boudouard reaction and suppress other routes forming carbonaceous deposits. Co is known to have a moderate activity in CO₂ hydrogenation⁴¹, while Mn-oxide was shown to be a promoter for CO₂ activation during Ni-catalyzed CO₂ hydrogenation⁴². The results shown in Fig. 3.15a show the absence of catalyst deactivation at elevated temperature with an exponential increase in the reaction rate up to 300°C. The catalytic performance at 300°C shown in Fig. 3.15b demonstrates the significantly higher activity of the Mn-promoted catalysts. For both large and small particles, the presence of Mn enhances the catalytic activity. Furthermore, our hypothesis that Mn can compensate for a loss of active sites when decreasing the particle size is reconfirmed as CoMn(S) has a higher activity than Co(L) in CO₂ hydrogenation.

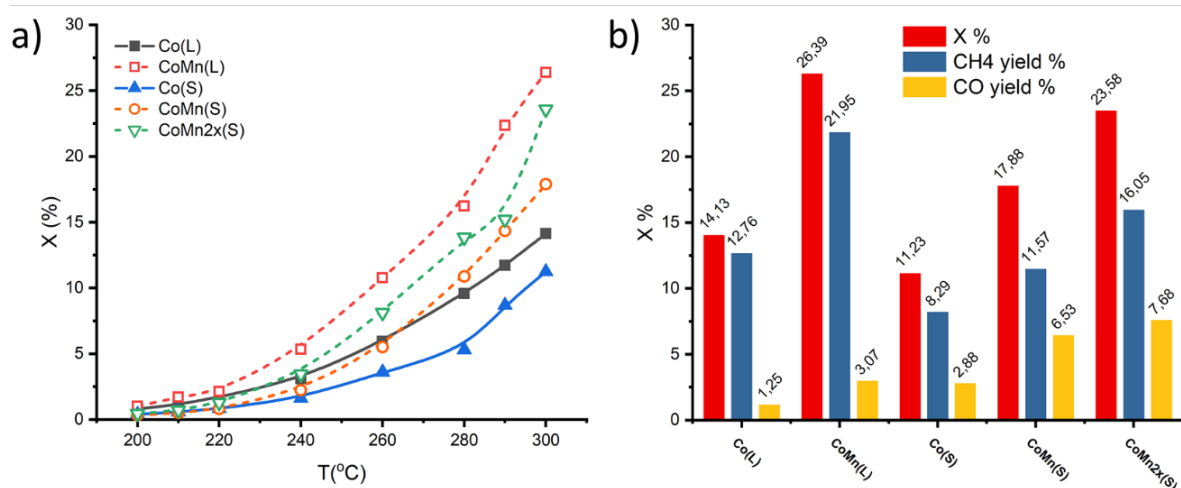


Figure 3.15. (a) CO₂ conversion during temperature-programmed CO₂ hydrogenation (reduction at 450°C, H₂/CO₂ = 5, 1 bar) and (b) catalytic performance at 300 °C as a function of particle size and Mn content (CoMn2x(S) refers to a catalyst with a two times higher Mn content).

It should be noted that when using CO₂ as a reactant, the classical particle size effect is still observed for unpromoted catalyst as the conversion of Co(S) particles is lower than for the Co(L) samples, despite the high temperature used here (300°C), which is expected to cause sintering.

3.4. Discussion

The study of the particle size dependent activity of Co catalyst for the FT synthesis reaction has come a long way from the initial experiments claiming structure insensitivity of CO hydrogenation by Iglesia and co-workers⁴³ to the reports of De Jong's group^{44,9} showing that small particles (<6 nm) lose their activity due to a loss of active sites for CO dissociation, presumably step-edge sites. Such particle size dependence for CO hydrogenation has been

identified also for other late transition metals⁴⁵. Another topic of intense investigation is the impact of Mn as a promoter for Co. Whereas Mn is an effective promotor for the catalytic performance at ambient pressure, its effect at practical pressures of the FT reaction (>10 bar) is very small⁴⁶. In Chapter 2, it was shown that Mn facilitates CO dissociation in fully reduced and relatively large Co particles in Co/SiO₂. As it would be beneficial to increase the activity of small Co particles for achieving a better Co utilization, it is interesting to explore the promoting effect of Mn on small and large Co particles. The hypothesis behind this approach was thus to explore whether the loss of active sites on Co nanoparticles smaller than 6 nm particles could be compensated by adding Mn, resulting in a higher activity. Obviously, such an effect might be pressure dependent. For this purpose, a preparation method was developed which involves the complexation of Co²⁺ with citric acid to yield smaller than 6 nm particles and the addition of Mn. A SSITKA investigation confirmed literature findings⁹ that small particles with a size below 6 nm exhibit a decreased activity and C₅₊ selectivity compared to particles larger than 6 nm. However, in contrast to SiO₂-supported Co catalysts¹¹, Mn addition had no significant effect on the performance at ambient pressure. On the other hand, performance studies at elevated pressure and TPIR measurements showed a promoting effect of Mn, especially in combination with a low temperature of reduction that led to the remaining presence of Co oxide. The highest catalytic performance in the FT reaction obtained for CoMn(S) was confirmed in a comparison of the activity of the catalysts in CO₂ methanation at higher temperature. Despite the feasibility of the concept of combining small Co particles with Mn promotion for FT synthesis at low pressure, further optimization is required before these catalysts can be used under realistic FT conditions. The Mn promotion effect was substantially enhanced at elevated total pressure (20 bar) by only partially reducing Co at 280 °C. The improved performance in this case is attributed to the combination of Mn-oxide and Co-oxide. Remarkably, the clear positive effect of Mn promotion for titania-supported Co catalysts at high pressure was not observed for silica supported catalysts. Possibly, strong metal-support interactions (SMSI) causing intimate contact of TiO_x with Co enhances the promotional effect of Mn. This would imply that optimal performance at high pressure is not just obtained by a synergy between Mn oxide and Co oxide, but by an Mn-Co-Ti-oxide combination. Apparently, the active sites formed by the combination of these oxides have a promotional effect without being poisoned by a high CO coverage at elevated pressure. The FT performance comparison shown in Fig. 3.7 clearly confirms the much better performance of catalysts reduced at 280 °C. For all catalysts the catalytic performance was enhanced by combining low-temperature reduction with the addition of Mn promoter. Even CoMn(S) showed a lower CH₄ and higher C₅₊ selectivity compared to Co(L) samples, which is different from earlier observations for small-particle Co catalysts. *Quasi in situ* XPS studies underlined the importance of Co-oxide remaining after reduction at 280 °C for the effective utilization of Mn. We further strengthened our hypothesis by performing temperature-programmed IR experiments that clearly demonstrated more facile C-O bond activation in adsorbed CO for catalysts containing Mn and being reduced at 280 °C. IR experiments in syngas confirmed these differences.

The group of Somorjai reported about the FT activity of Co-oxide in titania-supported Co catalysts⁶. Bell and co-workers emphasized the promoting role of metal oxide promoters for

Co by noting a linear correlation between the Lewis acidity of promoter oxides and the FT reaction rate.⁴⁷ As the Lewis acidity of MnO and CoO are comparable⁴⁸, the promotional effect of CoO can be expected to be of a similar magnitude as that of MnO. However, as we showed before for CoMn/SiO₂ that the formation of an oxygen vacancy is essential for enhanced CO dissociation on MnO-promoted Co, a comparison based on metal-oxygen bond strength is more relevant when discussing the promotional effects of Mn- and Co-oxides. Yet, as estimated from the formation enthalpy per metal-oxygen bond, the oxygen vacancy formation energies for MnO and CoO are not very different. Thus, based on the available data, we cannot discern between a promotional effect by Mn or Co. The results above, however, suggest that the simultaneous presence of the oxides of Co and Mn works best.

3.5. Conclusion

The influence of the particle size and reduction temperature was studied for Co/TiO₂ catalysts including its impact on Mn promotion at reaction temperatures of 220 - 300°C and reaction pressures in the range of 2-20 bar. A preparation method was developed that led to relatively large (> 6 nm) and small (< 6 nm) Co particles with and without Mn promoter. Characterization revealed a less pronounced interaction of Mn and Co₃O₄ on TiO₂ in comparison to SiO₂, highlighting a substantial difference in the Mn-Co interactions between these two supports. *Quasi in situ* XPS was used to determine the oxidation states of Co and Mn, showing that the DOR of Co is lower for small Co particles and with increasing Mn content after reduction at 280°C, while reduction at 450°C led to a complete reduction of Co in all catalysts. Despite their lower DOR, the partially reduced catalysts performed better under typical FT conditions at elevated pressure (20 bar) than their fully reduced counterparts. Not only did the optimal catalysts exhibit higher activity but also lower methane and higher C₅₊ selectivity. Especially, Mn-promoted catalysts benefitted from reduction at low temperature. The CoMn(S) sample reduced at 280°C exhibited similar methane and C₅₊ selectivity as the Co(L) sample. Moreover, reduction at low temperature led to a decrease of the activation energy E_a confirming the promoting influence of oxidic Mn-Co species as discussed in Chapter 2. The promotional effect of Mn was also observed during temperature-programmed IR measurements, showing enhanced CO dissociation for catalysts reduced at 280 °C. Temperature-programmed IR measurements in syngas demonstrated that fully reduced large Co particles (Co(L) reduced at 450°C) mainly led to the formation of methane, while Co(S) catalysts reduced at 280 °C exhibited suppressed methane formation and a higher amount of CH_x species which are thought to be precursors to chain growth. This effect was more pronounced for Mn-containing samples. The important corollary of this work is that the presence of Mn-oxide and Co-oxide on small Co particles with a size smaller than 6 nm can increase the catalytic performance in the FT reaction. Such an approach can be a starting point to further optimize small Co particles with a more efficient usage of the expensive Co metal for practical FT.

References

- (1) Dry, M. E. The Fischer-Tropsch Process: 1950-2000. *Catal. Today* **2002**, 71 (3–4), 227–241. [https://doi.org/10.1016/S0920-5861\(01\)00453-9](https://doi.org/10.1016/S0920-5861(01)00453-9).
- (2) Schulz, H. Short History and Present Trends of Fischer–Tropsch Synthesis. *Appl. Catal. A Gen.* **1999**, 186 (1–2), 3–12. [https://doi.org/10.1016/S0926-860X\(99\)00160-X](https://doi.org/10.1016/S0926-860X(99)00160-X).
- (3) Van der Laan, G. P.; Beenackers, A. A. C. M. Kinetics and Selectivity of the Fischer–Tropsch Synthesis: A Literature Review. *Catal. Rev.* **1999**, 41 (3–4), 255–318. <https://doi.org/10.1081/CR-100101170>.
- (4) Khodakov, A. Y.; Chu, W.; Fongarland, P. Advances in the Development of Novel Cobalt Fischer – Tropsch Catalysts for Synthesis of Long-Chain Hydrocarbons and Clean Fuels Advances in the Development of Novel Cobalt Fischer – Tropsch Catalysts for Synthesis of Long-Chain Hydrocarbons and Clean Fue. *Am. Chem. Soc.* **2007**, 107 (5), 1692–1744. <https://doi.org/10.1021/cr050972v>.
- (5) Dinse, A.; Aigner, M.; Ulbrich, M.; Johnson, G. R.; Bell, A. T. Effects of Mn Promotion on the Activity and Selectivity of Co/SiO₂ for Fischer–Tropsch Synthesis. *J. Catal.* **2012**, 288, 104–114. <https://doi.org/10.1016/j.jcat.2012.01.008>.
- (6) Melaet, G.; Ralston, W. T.; Li, C.-S.; Alayoglu, S.; An, K.; Musselwhite, N.; Kalkan, B.; Somorjai, G. A. Evidence of Highly Active Cobalt Oxide Catalyst for the Fischer–Tropsch Synthesis and CO₂ Hydrogenation. *J. Am. Chem. Soc.* **2014**, 136 (6), 2260–2263. <https://doi.org/10.1021/ja412447q>.
- (7) Hernández Mejía, C.; van Deelen, T. W.; de Jong, K. P. Activity Enhancement of Cobalt Catalysts by Tuning Metal-Support Interactions. *Nat. Commun.* **2018**, 9 (1), 1–8. <https://doi.org/10.1038/s41467-018-06903-w>.
- (8) Bezemer, G. L.; Bitter, J. H.; Kuipers, H. P. C. E.; Oosterbeek, H.; Holewijn, J. E.; Xu, X.; Kapteijn, F.; Van Diilen, A. J.; De Jong, K. P. Cobalt Particle Size Effects in the Fischer-Tropsch Reaction Studied with Carbon Nanofiber Supported Catalysts. *J. Am. Chem. Soc.* **2006**, 128 (12), 3956–3964. <https://doi.org/10.1021/ja058282w>.
- (9) den Breejen, J. P.; Radstake, P. B.; Bezemer, G. L.; Bitter, J. H.; Froseth, V.; Holmen, a.; P., D. J. K. On the Origin of the Cobalt Particle Size Effects In. *J. Am. Chem. Soc.* **2009**, 131 (22), 7197–7203. <https://doi.org/10.1016/j.cattod.2008.10.036>.
- (10) Mitchell, R. W.; Lloyd, D. C.; Van De Water, L. G. A.; Ellis, P. R.; Metcalfe, K. A.; Sibbald, C.; Davies, L. H.; Enache, D. I.; Kelly, G. J.; Boyes, E. D.; Gai, P. L. Effect of Pretreatment Method on the Nanostructure and Performance of Supported Co Catalysts in Fischer-Tropsch Synthesis. *ACS Catal.* **2018**, 8 (9), 8816–8829. <https://doi.org/10.1021/acscatal.8b02320>.
- (11) Kimpel, T. F.; Liu, J. X.; Chen, W.; Pestman, R.; Hensen, E. J. M. Pressure Dependence and Mechanism of Mn Promotion of Silica-Supported Co Catalyst in the Fischer-Tropsch Reaction. *J. Catal.* **2023**, 425, 181–195. <https://doi.org/10.1016/j.jcat.2023.06.010>.
- (12) Johnson, G. R.; Werner, S.; Bell, A. T. An Investigation into the Effects of Mn Promotion on the Activity and Selectivity of Co/SiO₂ for Fischer–Tropsch Synthesis: Evidence for Enhanced CO Adsorption and Dissociation. *ACS Catal.* **2015**, 5 (10), 5888–5903. <https://doi.org/10.1021/acscatal.5b01578>.
- (13) Soled, S. L.; Iglesia, E.; Fiato, R. a.; Baumgartner, J. E.; Vroman, H.; Miseo, S. Control of Metal Dispersion and Structure by Changes in the Solid-State Chemistry of Supported Cobalt Fischer-Tropsch Catalysts. *Top. Catal.* **2003**, 26 (1–4), 101–109. <https://doi.org/10.1023/B:TOCA.0000012990.83630.f9>.

- (14) Crajé, M. W. J.; Van der Kraan, A. M.; Van de Loosdrecht, J.; Van Berge, P. J. The Application of Mössbauer Emission Spectroscopy to Industrial Cobalt Based Fischer-Tropsch Catalysts. *Catal. Today* **2002**, *71* (3–4), 369–379. [https://doi.org/10.1016/S0920-5861\(01\)00464-3](https://doi.org/10.1016/S0920-5861(01)00464-3).
- (15) Chen, W.; Pilot, I. A. W.; Pestman, R.; Hensen, E. J. M. Mechanism of Cobalt-Catalyzed CO Hydrogenation: 2. Fischer-Tropsch Synthesis. *ACS Catal.* **2017**, *7* (12), 8061–8071. <https://doi.org/10.1021/acscatal.7b02758>.
- (16) Gual, A.; Godard, C.; Castellón, S.; Curulla-Ferré, D.; Claver, C. Colloidal Ru, Co and Fe-Nanoparticles. Synthesis and Application as Nanocatalysts in the Fischer-Tropsch Process. *Catal. Today* **2012**, *183* (1), 154–171. <https://doi.org/10.1016/j.cattod.2011.11.025>.
- (17) Iablokov, V.; Beaumont, S. K.; Alayoglu, S.; Pushkarev, V. V.; Specht, C.; Gao, J.; Alivisatos, P.; Kruse, N.; Somorjai, G. a. Size-Controlled Model Co Nanoparticle Catalysts for CO₂ Hydrogenation: Synthesis, Characterization, and Catalytic Reactions. *Nano Lett.* **2012**, *12*, 3091–3096. <https://doi.org/10.1021/nl300973b>.
- (18) Hoof, A. J. F. Van; Michel-ligthart, D. A. J.; Friedrich, H.; Hensen, E. J. M. The Influence and Removability of Colloidal Capping Agents on Carbon Monoxide Hydrogenation by Zirconia-Supported Rhodium Nanoparticles. **2017**, 1018–1024. <https://doi.org/10.1002/cctc.201601378>.
- (19) Bulavchenko, O. A.; Gerasimov, E. Y.; Afonasenkov, T. N. Reduction of Double Manganese-Cobalt Oxides: In Situ XRD and TPR Study. *Dalt. Trans.* **2018**, *47* (47), 17153–17159. <https://doi.org/10.1039/c8dt04137g>.
- (20) Jacobs, G.; Das, T. K.; Zhang, Y.; Li, J.; Racoillet, G.; Davis, B. H. Fischer-Tropsch Synthesis: Support, Loading, and Promoter Effects on the Reducibility of Cobalt Catalysts. *Appl. Catal. A Gen.* **2002**, *233*, 263–281. [https://doi.org/10.1016/S0926-860X\(02\)00195-3](https://doi.org/10.1016/S0926-860X(02)00195-3).
- (21) Wolf, M.; Gibson, E. K.; Olivier, E. J.; Neethling, J. H.; Catlow, C. R. A.; Fischer, N.; Claeys, M. In-Depth Characterisation of Metal-Support Compounds in Spent Co/SiO₂ Fischer-Tropsch Model Catalysts. *Catal. Today* **2020**, *342* (January 2019), 71–78. <https://doi.org/10.1016/j.cattod.2019.01.065>.
- (22) Lögdberg, S.; Yang, J.; Lualdi, M.; Walmsley, J. C.; Järås, S.; Boutonnet, M.; Blekkan, E. A.; Rytter, E.; Holmen, A. Further Insights into Methane and Higher Hydrocarbons Formation over Cobalt-Based Catalysts with γ -Al₂O₃, A-Al₂O₃ and TiO₂ as Support Materials. *J. Catal.* **2017**, *352*, 515–531. <https://doi.org/10.1016/j.jcat.2017.06.003>.
- (23) Voß, M.; Borgmann, D.; Wedler, G. Characterization of Alumina, Silica, and Titania Supported Cobalt Catalysts. *J. Catal.* **2002**, *212* (1), 10–21. <https://doi.org/10.1006/jcat.2002.3739>.
- (24) Houalla, M.; Delmon, B. Use of XPS to Detect Variations in Dispersion of Impregnated and Ion-exchanged NiO/SiO₂ Systems. *Surf. Interface Anal.* **1981**, *3* (3), 103–105. <https://doi.org/10.1002/sia.740030302>.
- (25) Biesinger, M. C.; Payne, B. P.; Grosvenor, A. P.; Lau, L. W. M.; Gerson, A. R.; Smart, R. S. C. Resolving Surface Chemical States in XPS Analysis of First Row Transition Metals, Oxides and Hydroxides: Cr, Mn, Fe, Co and Ni. *Appl. Surf. Sci.* **2011**, *257* (7), 2717–2730. <https://doi.org/10.1016/j.apsusc.2010.10.051>.
- (26) Pollak, H. Fe³⁺ Ion Lifetime in COO Deduced from the Auger and Mossbauer Effects. **1962**, *720*, 720–724.
- (27) Wivel, C.; Clausen, B. S.; Candia, R.; Mørup, S.; Topsøe, H. Mössbauer Emission Studies of Calcined CoMo Al₂O₃ Catalysts: Catalytic Significance of Co Precursors. *J. Catal.* **1984**, *87* (2), 497–513. [https://doi.org/10.1016/0021-9517\(84\)90210-0](https://doi.org/10.1016/0021-9517(84)90210-0).

- (28) Chu, W.; Chernavskii, P. a.; Gengembre, L.; Pankina, G. a.; Fongarland, P.; Khodakov, A. Y. Cobalt Species in Promoted Cobalt Alumina-Supported Fischer-Tropsch Catalysts. *J. Catal.* **2007**, *252*, 215–230. <https://doi.org/10.1016/j.jcat.2007.09.018>.
- (29) Hinchiranan, S.; Zhang, Y.; Nagamori, S.; Vitidsant, T.; Tsubaki, N. TiO₂ Promoted Co/SiO₂ Catalysts for Fischer-Tropsch Synthesis. *Fuel Process. Technol.* **2008**, *89* (4), 455–459. <https://doi.org/10.1016/j.fuproc.2007.11.007>.
- (30) Yang, J.; Shafer, W. D.; Pendyala, V. R. R.; Jacobs, G.; Chen, D.; Holmen, A.; Davis, B. H. Fischer–Tropsch Synthesis: Using Deuterium as a Tool to Investigate Primary Product Distribution. *Catal. Letters* **2013**, *144* (3), 524–530. <https://doi.org/10.1007/s10562-013-1164-6>.
- (31) Chen, W.; Kimpel, T. F.; Song, Y.; Chiang, F. K.; Zijlstra, B.; Pestman, R.; Wang, P.; Hensen, E. J. M. Influence of Carbon Deposits on the Cobalt-Catalyzed Fischer-Tropsch Reaction: Evidence of a Two-Site Reaction Model. *ACS Catal.* **2018**, *8* (2), 1580–1590. <https://doi.org/10.1021/acscatal.7b03639>.
- (32) Chen, W.; Pestman, R.; Chiang, F. K.; Hensen, E. J. M. Silver Addition to a Cobalt Fischer–Tropsch Catalyst. *J. Catal.* **2018**, *366* (2018), 107–114. <https://doi.org/10.1016/j.jcat.2018.07.028>.
- (33) Pour, A. N.; Hosaini, E.; Izadyar, M.; Housaindokht, M. R. Particle Size Effects in Fischer-Tropsch Synthesis by Co Catalyst Supported on Carbon Nanotubes. *Cuihua Xuebao/Chinese J. Catal.* **2015**, *36* (8), 1372–1378. [https://doi.org/10.1016/S1872-2067\(15\)60840-3](https://doi.org/10.1016/S1872-2067(15)60840-3).
- (34) Pour, A. N.; Hosaini, E.; Tavasoli, A.; Behroozsarand, A.; Dolati, F. Intrinsic Kinetics of Fischer-Tropsch Synthesis over Co/CNTs Catalyst: Effects of Metallic Cobalt Particle Size. *J. Nat. Gas Sci. Eng.* **2014**, *21*, 772–778. <https://doi.org/10.1016/j.jngse.2014.10.008>.
- (35) Weststrate, C. J.; Loosdrecht, J. Van De; Niemantsverdriet, J. W. Spectroscopic Insights into Cobalt-Catalyzed Fischer-Tropsch Synthesis : A Review of the Carbon Monoxide Interaction with Single Crystalline Surfaces of Cobalt. *J. Catal.* **2016**, *342*, 1–16. <https://doi.org/10.1016/j.jcat.2016.07.010>.
- (36) Beitel, G. A.; Laskov, A.; Oosterbeek, H.; Kuipers, E. W. Polarization Modulation Infrared Reflection Absorption Spectroscopy of CO Adsorption on Co(0001) under a High-Pressure Regime. *J. Phys. Chem.* **1996**, *100* (30), 12494–12502. <https://doi.org/10.1021/jp960045f>.
- (37) Chen, W.; Zijlstra, B.; Filot, I. A. W.; Pestman, R.; Hensen, E. J. M. Mechanism of Carbon Monoxide Dissociation on a Cobalt Fischer–Tropsch Catalyst. *ChemCatChem* **2018**, *10* (1), 136–140. <https://doi.org/10.1002/cctc.201701203>.
- (38) Yang, J.; Tveten, E. Z.; Chen, D.; Holmen, A. Understanding the Effect of Cobalt Particle Size on Fischer-Tropsch Synthesis: Surface Species and Mechanistic Studies by SSITKA and Kinetic Isotope Effect. *Langmuir* **2010**, *26* (21), 16558–16567. <https://doi.org/10.1021/la101555u>.
- (39) Yang, J.; Frøseth, V.; Chen, D.; Holmen, A. Particle Size Effect for Cobalt Fischer-Tropsch Catalysts Based on in Situ CO Chemisorption. *Surf. Sci.* **2016**, *648*, 67–73. <https://doi.org/10.1016/j.susc.2015.10.029>.
- (40) Park, J. Y.; Lee, Y. J.; Karandikar, P. R.; Jun, K. W.; Ha, K. S.; Park, H. G. Fischer-Tropsch Catalysts Deposited with Size-Controlled Co 304 Nanocrystals: Effect of Co Particle Size on Catalytic Activity and Stability. *Appl. Catal. A Gen.* **2012**, *411–412*, 15–23. <https://doi.org/10.1016/j.apcata.2011.10.010>.
- (41) Suppiah, D. D.; Daud, W. M. A. W.; Johan, M. R. Supported Metal Oxide Catalysts for CO₂ Fischer–Tropsch Conversion to Liquid Fuels - A Review. *Energy and Fuels* **2021**, *35* (21),

- 17261–17278. <https://doi.org/10.1021/acs.energyfuels.1c02406>.
- (42) Vrijburg, W. L.; Moiola, E.; Chen, W.; Zhang, M.; Terlingen, B. J. P.; Zijlstra, B.; Pilot, I. A. W.; Züttel, A.; Pidko, E. A.; Hensen, E. J. M. Efficient Base-Metal NiMn/TiO₂ Catalyst for CO₂ Methanation. *ACS Catal.* **2019**, *9* (9), 7823–7839. <https://doi.org/10.1021/acscatal.9b01968>.
 - (43) Iglesia, E.; Soled, S. L.; Fiato, R. A. Fischer-Tropsch Synthesis on Cobalt and Ruthenium. Metal Dispersion and Support Effects on Reaction Rate and Selectivity. *J. Catal.* **1992**, *137* (1), 212–224. [https://doi.org/10.1016/0021-9517\(92\)90150-G](https://doi.org/10.1016/0021-9517(92)90150-G).
 - (44) Bezemer, G. L.; Bitter, J. H.; Kuipers, H. P. C. E.; Oosterbeek, H.; Holewijn, J. E.; Xu, X.; Kapteijn, F.; Dillen, a J. Van; Jong, K. P. De. Cobalt Particle Size Effects in the Fischer – Tropsch Reaction Studied with Carbon Nanofiber Supported Catalysts Cobalt Particle Size Effects in the Fischer-Tropsch Reaction Studied with Carbon Nanofiber Supported Catalysts. *J. Am. Chem. Soc.* **2006**, No. 6, 11568–11569. <https://doi.org/10.1021/ja058282w>.
 - (45) Pestman, R.; Chen, W.; Hensen, E. Insight into the Rate-Determining Step and Active Sites in the Fischer-Tropsch Reaction over Cobalt Catalysts. *ACS Catal.* **2019**, *9* (5), 4189–4195. <https://doi.org/10.1021/acscatal.9b00185>.
 - (46) Bezemer, G. L.; Radstake, P. B.; Falke, U.; Oosterbeek, H.; Kuipers, H. P. C. E.; Van Dillen, A. J.; De Jong, K. P. Investigation of Promoter Effects of Manganese Oxide on Carbon Nanofiber-Supported Cobalt Catalysts for Fischer-Tropsch Synthesis. *J. Catal.* **2006**, *237* (1), 152–161. <https://doi.org/10.1016/j.jcat.2005.10.031>.
 - (47) Johnson, G. R.; Bell, A. T. Effects of Lewis Acidity of Metal Oxide Promoters on the Activity and Selectivity of Co-Based Fischer – Tropsch Synthesis Catalysts. *J. Catal.* **2016**, *338*, 250–264. <https://doi.org/10.1016/j.jcat.2016.03.022>.
 - (48) Jeong, N. C.; Lee, J. S.; Tae, E. L.; Lee, Y. J.; Yoon, K. B. Acidity Scale for Metal Oxides and Sanderson’s Electronegativities of Lanthanide Elements. *Angew. Chemie - Int. Ed.* **2008**, *47* (52), 10128–10132. <https://doi.org/10.1002/anie.200803837>.

Appendix B: Chapter 3

B1. TEM Particle size

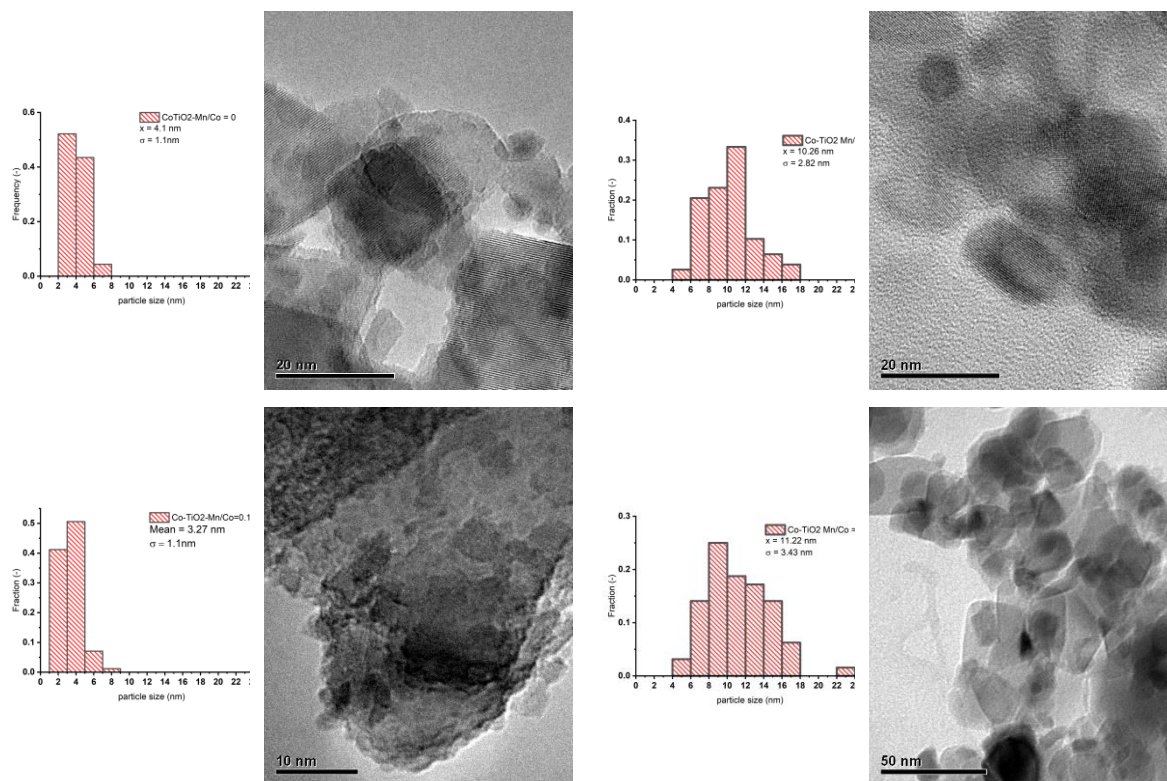


Figure B1. Particles size determination of calcined catalysts (Co_3O_4) via TEM. a) $\text{Co}(\text{NO}_3)_2 \cdot 6\text{H}_2\text{O}$ precursor (IWI), b) $\text{Co}(\text{NO}_3)_2 \cdot 6\text{H}_2\text{O}$ precursor (IWI) with Mn addition, c) CoCO_3 + citric acid (DPI), d) CoCO_3 + citric acid (DPI) with Mn addition

B2. Mössbauer spectroscopy

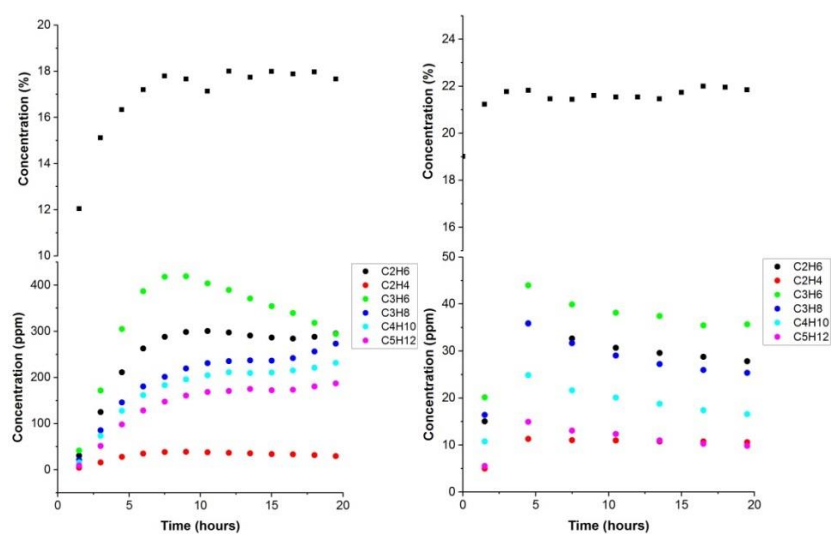


Figure B2. Product composition of in-situ Fischer-Tropsch during Mossbauer spectroscopy experiment. Colored circles: product selectivity; black squares: total conversion

Table B1. Fitting parameters for Mössbauer spectroscopy.

IWI		Fresh	Reduced	FTS	Post-FTS
		T = 20 °C	T = 20 °C	T = 200 °C	T = 20 °C
Co^{2+}	I.S. ($mm\ s^{-1}$)	1.25	-	-	-
	Q.S. ($mm\ s^{-1}$)	2.59	-	-	-
Co^{3+}	I.S. ($mm\ s^{-1}$)	0.20	-	-	-
	Q.S. ($mm\ s^{-1}$)	0.58	-	-	-
Co^0	I.S. ($mm\ s^{-1}$)	-	-0.09	-0.22	-0.09
	H.F. (T)	-	32.2	30.9	32.1
DPI		Fresh	Reduced	FTS	Post-FTS
		T = 20°C	T = 20 °C	T = 200 °C	T = 20 °C
Co^{2+}	I.S. ($mm\ s^{-1}$)	1.08	-	-	-
	Q.S. ($mm\ s^{-1}$)	2.07	-	-	-
Co^{3+}	I.S. ($mm\ s^{-1}$)	0.18	-	-	-
	Q.S. ($mm\ s^{-1}$)	0.86	-	-	-
Co^0	I.S. ($mm\ s^{-1}$)	-	-0.09	-0.21	-0.09
	H.F. (T)	-	32.3	31.2	32.2

B3. SSITKA results

Cat- alyst	Mn /Co	H ₂ / CO	X [-]	S_CO ₂ [-]	S_CH ₄ [-]	S_C ₂₊ [-]	S_C ₅₊ [-]	α	OP C ₂	OP C ₃	τ _{CO} [s]	τ _{CH_x} [s]
Co(L)	0	5	0.13	0	0.31	0.38	0.31	0.51	0.12	1.98	2.2	12.9
CoMn(L)	0.1	5	0.12	0	0.33	0.38	0.29	0.50	0.10	1.61	2.1	14.6
Co(S)	0	5	0.06	0	0.39	0.38	0.23	0.50	0.04	0.59	1.9	19.1
CoMn(S)	0.1	5	0.07	0	0.42	0.38	0.21	0.48	0.04	0.46	1.95	18.3

Table B2. SSITKA results for catalysts reduced at 450 °C.

B4. Chemisorption results

Table B3. CO chemisorption results.

Catalyst	mmol CO/gCo 280 °C	CO 280 °C [nm]	CO 280 °C corrected for DOR	mmol CO/gCo 450°C	CO 450 °C [nm]	CO irrev. [%] 450°C	CO irrev. [%] 280 °C
Co(L)	0.60	28.3	28.3	0.70	24.4	80.2	70.2
CoMn(L)	0.57	29.6		0.66	25.6	74.0	29.3
Co(S)	0.43	38.8	15.2	0.70	24.2	89.6	88.0
CoMn(S)	0.43	39.7		0.50	33.7	93.0	83.4

B5. ASF plots belonging to FT catalytic tests

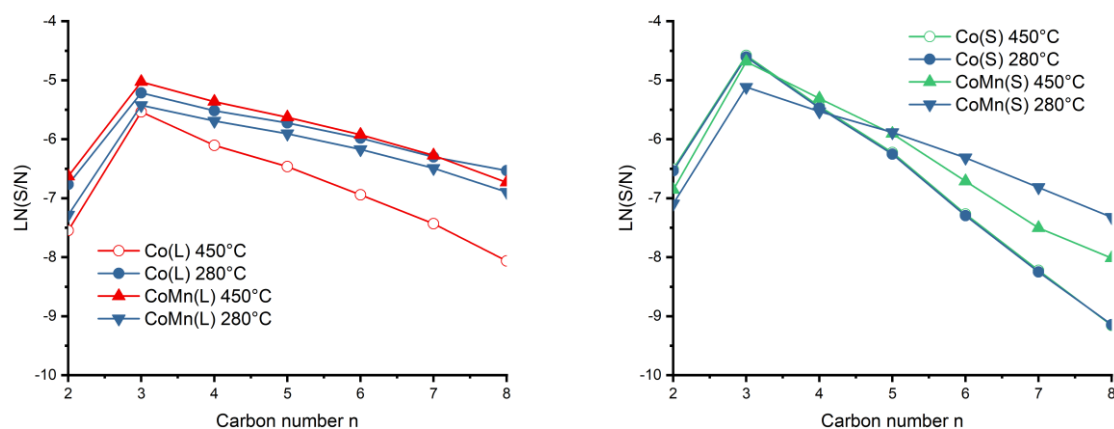


Figure B3. ASF plots for alpha olefins after reduction at 450 °C and 280 °C.

B6. FTIR Spectra of CO adsorption and TPIR

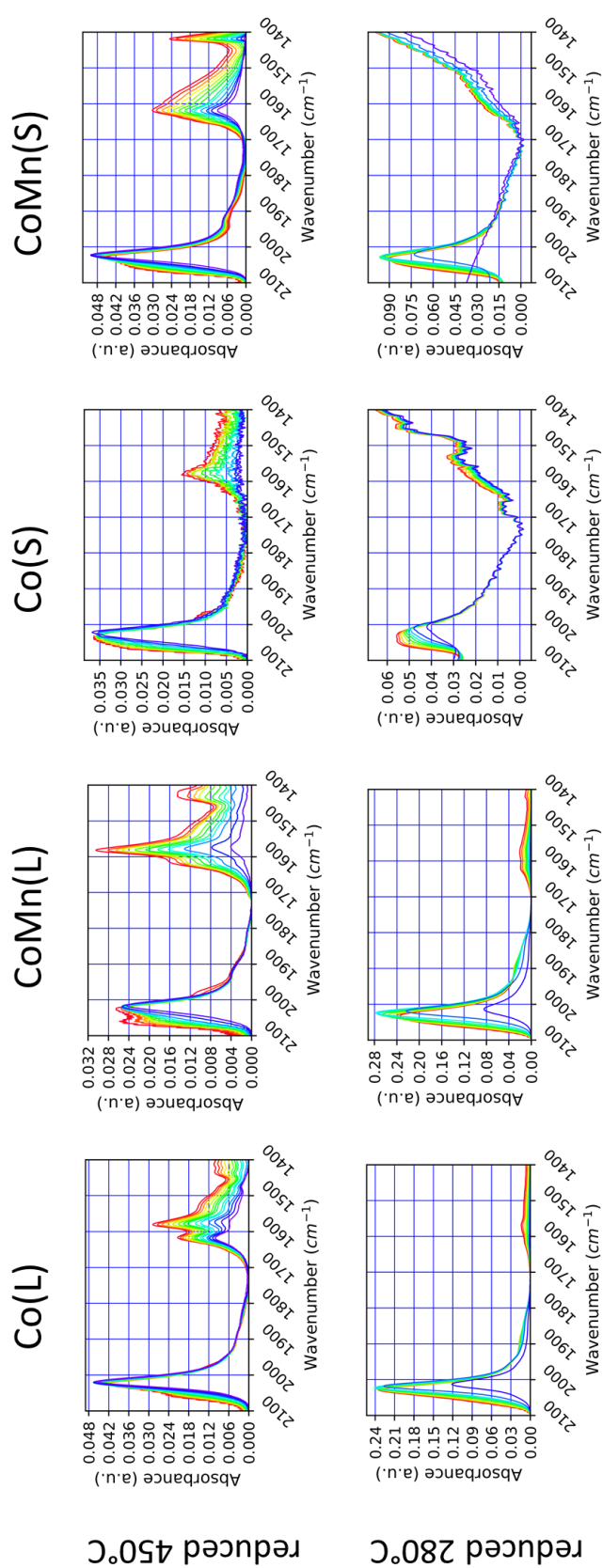


Figure B4. IR spectra of CO adsorption isotherms at room temperature.

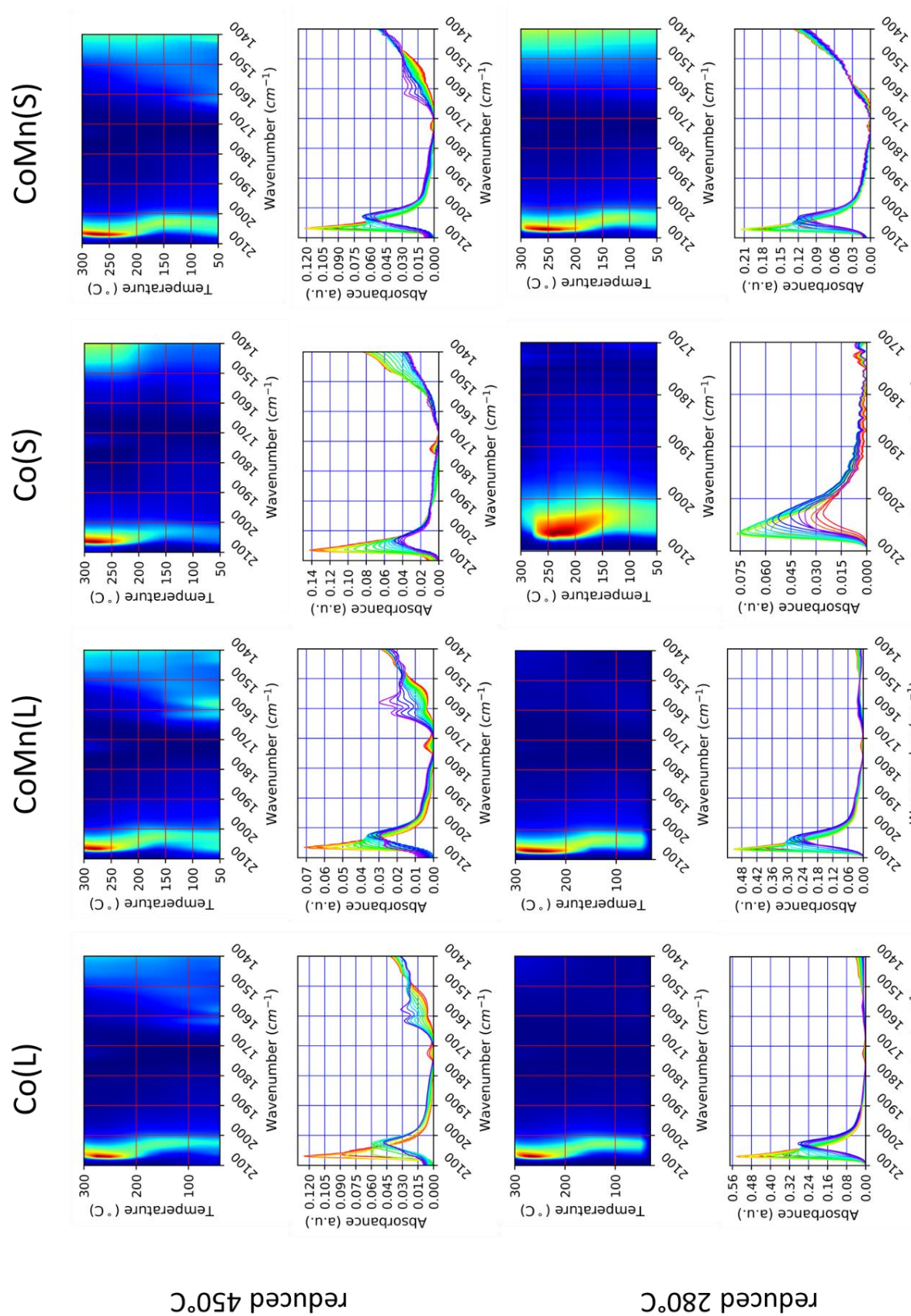


Figure B5. Temperature-programmed IR spectra in the presence of CO.

Chapter 4 - Highly active and selective CoMn/TiO₂ Fischer-Tropsch catalysts prepared by precipitation: on the impact of reduction temperature

Abstract

The Co particle size effect strongly limits the metal efficiency in the Fischer-Tropsch synthesis reaction, as the highest activity is obtained for particles with a size larger than 6 nm. A (co)precipitation method is presented to prepare small Co(Mn) particles on TiO₂ using citric acid as a chelating agent. Without citric acid, large particles are obtained. In stark contrast with the Co particle size effect, the highest Co-weight-based activity was observed for CoMn/TiO₂ containing small Co particles with a low Co reduction degree and promoted by Mn. Besides high activity, the small Co particles displayed decreased methane and increased C₅₊ selectivity compared to large particles. The low Co reduction degree is due to a low reduction temperature of 280 °C and the absence of Pt reduction promoter. Temperature-programmed IR measurements indicate that the presence of Co-oxide in combination with Co results in more CO dissociation sites, which suggest a similar promoting effect as known for MnO. An important corollary of these findings is that highly dispersed Co particles reduced at low temperature can display improved FT performance compared to large Co particles by lowering the Co reduction degree.

4.1 Introduction

The Fischer-Tropsch (FT) reaction is a surface polymerization reaction converting synthesis gas (a mixture of CO and H₂) from various carbon containing resources like natural gas, coal, biomass or CO₂ into hydrocarbons that can either function as liquid fuels or chemical building blocks. Due to price restrictions only Fe- and Co-based catalysts are commercially feasible¹.

Decreasing the particle size is an obvious way to increase metal usage efficiency in heterogeneous catalysts. However, in the FT reaction over Co, decreasing the particle size below 6 nm results in a loss of activity and an undesired increase in methane selectivity. This phenomenon is a consequence of “structure sensitivity” and has been studied extensively^{2,3,1}. It is argued that a loss of CO dissociation sites (B₅ sites) leads to a lower activity and lower surface coverage of carbon species decreasing the reaction rate and chain-growth probability and thus increasing the methane yield⁴.

Over time, many promoters have been studied to enhance the catalytic performance. Barrault et al.⁵ were the first to discover that Co catalysts can be promoted by adding redox centers that enhance the catalytic performance. In the last decades, Mn has been studied exhaustively, as it can enhance both the FT activity and selectivity to larger hydrocarbons and olefins⁶. The group of De Jong studied the effect of Mn on carbon-supported Co⁷, while the group of Bell did the same for SiO₂-supported Co^{8,9,10}. The Bell group linked the promotional effect of Mn to its Lewis acidity. Generally, Lewis acidity increases with the oxidation state of the metals. It remains unclear whether the promoting role is due to the intrinsic Lewis acidity of the metal cations or has to do with the reducible nature of the metal oxides.

Density functional theory (DFT) calculations have shown that CO dissociation can take place at the interface between Co metal and MnO, involving oxygen vacancies formed in MnO¹¹. Thus, Mn promotion could be useful to offset the activity loss associated with small particles, which is related to the structure sensitivity effect. The use of TiO₂ as a support has been reported to lead to superior performance compared to widely used catalyst supports¹², most likely due to a higher Co dispersion¹³ or by formation of oxidic Co-Ti compounds¹⁴.

In this chapter, the effect of Mn on both small and large Co particles dispersed on a TiO₂ support is investigated. We apply a precipitation approach that results in Co-oxide particles with a narrow size distribution and compare those to the particles of similar size obtained via impregnation. As the reduction temperature is known to have a strong impact on the catalytic performance, mainly through the degree of Co reduction¹⁵, we used two reduction temperatures, viz., a temperature of 280 °C leading to mixtures of Co metal and Co-oxide and a temperature of 450°C leading to fully reduced Co.

4.2 Experimental

4.2.1 Preparation

TiO₂ powder (AEROXIDE® TiO₂ P25, Evonik, sieve fraction 120–250 µm, 54 m²/g determined by BET) was used for all catalysts. A precipitation procedure was applied, involving two solutions. Solution A contained the metal salts Co(NO₃)₂ · 6 H₂O (Merck, 99.99 %) for an intended Co loading of 10 wt% and, for the Mn-promoted samples (Mn/Co = 0.1), Mn(NO₃)₂ · xH₂O. When small particle sizes (<6 nm) were desired, citric acid was added to this solution as well (Citric acid / Co(NO₃)₂ · 6 H₂O = 0.1). Solution B provided the basicity to precipitate the metals and consisted of a 1:1 mixture of NaOH and Na₂CO₃. The precipitation was performed by the simultaneous addition of solutions A and B within 30 min to a suspension of TiO₂ in water whose pH was adjusted to 7 by adding few drops of solution B prior to the precipitation. The precipitation was performed at 100°C under vigorous stirring within 30 min, keeping the pH constant at 7. The resulting mixture was aged for 1 h at 100°C and subsequently filtered and washed three times in order to remove all Na as confirmed by XPS (Appendix Fig. C2) and ICP-OES analysis, where the Na concentration was found to be below the detection limit. The samples were then dried in a flow of artificial air at 80°C for 2 h, followed by a calcination step at 350°C for 2 h using a rate of 2°C/min. Catalysts are denoted as follows: CoP(S) and CoMnP(S) were prepared by (co-)precipitation of Co (and Mn) in the presence of citric acid, while CoP(L) and CoMnP(L) were obtained without citric acid.

A TiO₂-supported Co catalyst, which acts as a reference for the precipitated large particle catalyst CoP(L) was prepared by conventional incipient wetness impregnation of TiO₂ (AEROXIDE® TiO₂ P25, Evonik, sieve fraction 120–250 µm, BET surface area of 54 m²/g) with an aqueous solution of Co(NO₃)₂ · 6H₂O (Merck, 99.99 %) and Pt(NH₃)₄ · (NO₃)₂ (Alfa Aesar, 99.995 %). Pt was added as a reduction promoter. The impregnated catalysts were dried at 80 °C in a flow of 80 % He and 20 % O₂ for 2 h followed by calcination by heating to 350 °C at a rate of 2 °C/min and an isothermal dwell of 2 h. This large particle reference catalyst is denoted as CoIWI(L). Another catalyst acting as a reference for small Co particles was prepared by employing a precursor decomposition impregnation method (PDI) as described in chapter 3. Instead of Co(NO₃)₂ · 6H₂O, CoCO₃ (Merck, 99.99 %) was used together with an aqueous solution of citric acid (Merck, 99.99 %), which acted as a complexing agent for Co²⁺ (molar citric acid/cobalt ratio of 1.5). Under the acidic conditions, insoluble CoCO₃ was slowly decomposed under gentle heating, resulting in Co-citrate complexes, which are known to lead to an increased Co dispersion upon deposition on oxide carrier materials¹⁶. As the solution is slightly acidic, the TiO₂ support will be positively charged, resulting in an interaction with the negatively charged Co-citrate complexes in the solution. As a result of the gradual formation of Co-citrate complexes the electrostatic interaction with the TiO₂ support, one can expect a high dispersion of the Co precursor. Subsequent drying and calcination steps were same as for the incipient wetness impregnation procedure described above. In this case also Pt was added as a reduction promoter in the amount of 0.04 wt%. This small particle reference sample is denoted as CoPDI(S).

4.2.2 Temperature-programmed reduction (TPR)

TPR experiments were conducted in a Micromeritics AutoChem II 2920 setup equipped with a U-shaped quartz reactor, a computer-controlled oven and a thermal conductivity detector (TCD). In a typical experiment 50 mg of sample was dried in a flow of He for 1h at 100 °C before heating to 1000 °C in a flow of 4 vol% H₂/He and at a rate of 10 °C/min.

4.2.3 X-ray photoelectron spectroscopy (XPS)

The oxidation state of Co and Mn was studied via *quasi in situ* XPS using a Kratos AXIS Ultra 600 spectrometer equipped with a monochromatic Al K α X-ray source (Al K α 1486.6 eV). Survey scans were recorded at a pass energy of 160 eV and at 40 eV for detailed region scans. The step size was 0.1 eV in both cases and the background pressure during the experiment was kept below 5.10⁻⁹ bar.

A high-temperature reaction cell (Kratos, WX-530) was used to pretreat the sample, which was supported on an alumina stub, allowing in vacuo sample transfer into the measurement chamber. Initial reduction was performed in a 50 vol% H₂ in Ar flow at atmospheric pressure at either 280 °C or 450 °C for 4 h. After reduction the sample was allowed to cool to 150 °C in the reduction gas mixture and, after evacuation, transferred to the measurement chamber.

Data treatment was conducted with the CasaXPS software. Energy calibration of the spectra was done on the basis of the cobalt 2p_{3/2} peak for metallic cobalt at 778.2 eV, while for the calcined samples the adventitious carbon 1s peak at 284.4 eV was used.

4.2.4 Transmission electron microscopy (TEM)

The volume-averaged particle size was determined by analysis of TEM images. TEM measurements were performed with a FEI Tecnai 20 electron microscope at an electron acceleration voltage of 200 kV with a LaB₆ filament. A few milligrams of ground sample were ultra-sonicated and dispersed over a carbon-coated Cu grid. The average particle size and particle size distribution were determined by measuring at least 100 particles¹⁷.

4.2.5 H₂ and CO chemisorption

In order to measure the available surface area, H₂ chemisorption was performed in a Micromeritics ASAP 2010 apparatus. After reduction of typically 200 mg of catalyst in a flow of 4 % H₂/He at 280 °C or 450 °C for 4 h, the sample was evacuated for 30 min at slightly higher temperatures of 300 °C or 470 °C, respectively, to remove all chemisorbed H₂. The H₂ uptake was measured at 110°C as a function of the H₂ pressure and extrapolated with a straight line to zero H₂ pressure. The amount of adsorbed H₂ molecules obtained from the ordinate was used to calculate the available surface area. The procedure for CO chemisorption was similar to H₂ chemisorption the only difference being that the chemisorption was carried out at 30°C¹⁸.

4.2.6 IR spectroscopy

IR spectra were recorded in transmission mode with a Bruker Vertex V70v instrument averaging 32 scans recorded at a 2 cm⁻¹ resolution for CO adsorption experiments. Typically,

15 mg of sample was pressed into a self-supporting wafer and positioned in a homemade controlled-environment infrared transmission cell. CO was admitted to the sample as pulses using a sample loop (10 μ l) connected to a six-port sampling valve. CO pulsing was continued until saturation of the CO IR region was observed. This typically led to a final CO pressure of 10 mbar. Prior to IR experiments, the samples were reduced in a H₂ flow at either 280 °C or 450 °C for 4 h preceded by heating at 5 °C/min. After evacuating for 30 min at the reduction temperature, the sample was cooled in dynamic vacuum. Prior to CO dosing, a background spectrum was recorded. Temperature-programmed IR spectra were recorded in the presence of CO (100 mbar) or synthesis gas (60 mbar H₂, 30 mbar CO). The spectra were recorded in the 50 – 300 °C range (5 °C/min) at steps of 25 °C. During temperature-programmed IR (TPIR), the number of scans for averaging was reduced to 16.

4.2.7 X-ray absorption spectroscopy (XAS)

Catalyst reducibility and structural properties were studied using operando XAS performed at the DUBBLE beamline (BM26A) of the European Synchrotron Radiation Facility (ESRF). The samples were measured in transmission mode at the Co K-edge (7.7 keV) selected with a Si(111) monochromator. XANES spectra were normalized and fitted using linear combination fitting (LCF) in the Athena software package. The calcined sample, a CoO sample and a Co metal foil served as references for the respective oxidation states. The extended X-ray absorption fine structure (EXAFS) part was fitted by the Artemis software using k^3 weighted data. In a typical experiment 30 mg catalyst sample was placed in a stainless-steel XAS reactor equipped with two fire rods and glassy carbon windows. Catalysts were reduced in this cell using a rate of 5 °C/min to reach either 280 °C or 450 °C followed by an isothermal dwell of 1 h in a flow of 10 vol% H₂ in He. The reduction procedure was followed by XANES. EXAFS spectra were collected at room temperature before and after the reduction.

4.2.8 Catalytic activity measurements

The catalytic performance of the Co samples was determined in a Microactivity Reference unit (PID Eng&Tech) at a temperature of 220 °C and a pressure of 20 bar. In a typical experiment, 150 mg (75-125 μ m sieved fraction) catalyst was homogeneously mixed with SiC particles of the same sieve fraction and placed in a tubular reactor with an internal diameter of 9 mm. The reactor temperature was controlled using a thermocouple located in the center of the catalyst bed. Reduction was carried out in the reactor by heating to 450 °C or 280 °C at a rate of 3 °C/min in an equimolar flow of H₂ and He at ambient pressure, followed by a dwell of 8 h. Afterwards, the reactor was cooled to 220 °C and the gas feed was replaced by the reaction mixture, which was synthesis gas with a H₂/CO ratio of 2 diluted with He (40 % of total flow) and contained 4 vol% Ar as an internal standard at 20 bar. The gas-hourly space velocity (GHSV) was 2000 h⁻¹, which resulted in typical conversion levels in the range of 5-15 %. Apparent activation energies were determined by measuring conversion as a function of temperature at 220, 230, and 240 °C. A TRACE 1300 gas chromatograph of Thermo Scientific Instruments equipped with a TCD and FID was used to analyze the effluent reaction mixture. Hydrocarbons (C1-C12) were separated by using an Rt-Silica BOND column and subsequently analyzed using

an FID. The analysis of light gases H₂, CO₂, CH₄, C₂H₄, C₂H₆, Ar, and CO was performed with a TCD in combination with Molsieve 5A (mesh 60/80, 2 m) and two Rt-XL Sulfur columns (0.25 m and 1 m). Under the applied reaction conditions, CO₂ was not detected as a reaction product and the carbon-based selectivity of oxygenates was lower than 1 %. Liquid products and waxes were collected in a rearward cold trap. The CO conversion (X_{CO}) was determined based on equation (4.1), the carbon-based selectivity of product i (S_i) by equation (4.2), the reaction rate (r_{CO}) by equation (4.3) and the turnover frequencies TOF_{CO} and TOF_{CH_4} by equation (4.4) and (4.5), respectively.

$$X_{CO} = \left(1 - \frac{\frac{CO_{out}}{Ar_{out}}}{\frac{CO_{in}}{Ar_{in}}}\right) \quad (4.1)$$

$$S_i = \frac{Ar_{in} \cdot \nu_i \cdot C_i}{Ar_{out} CO_{in} X_{CO}} * 100 \% \quad (4.2)$$

$$r_{CO} = \frac{F_{CO}^0 X_{CO}}{m_{Co}} \quad (4.3)$$

$$TOF_{CO} = \frac{X_{CO} * F_{CO}^0}{mol\ Co * D_{H_2}} \quad (4.4)$$

$$TOF_{CH_4} = \frac{X_{CO} * F_{CO}^0 * S_{CH_4}}{mol\ Co * D_{H_2}} \quad (4.5)$$

where CO_{in} / CO_{out} and Ar_{in} / Ar_{out} represent the CO/Ar concentration in the inlet/outlet flow, respectively. ν_i stands for the number of carbon atoms in species i , F_{CO}^0 represents the inlet flow of CO (mol/s), m_{Co} the amount of Co (g) and $mol\ Co$ the amount of Co atoms (mol) in the catalyst bed, and D_{H_2} the dispersion (-) determined by H₂ chemisorption.

4.3 Results

4.3.1 Basic characterization

Several preparation methods were employed to obtain Co particles with different sizes, Mn promotion and metal-support interactions. Catalysts containing small and large particles with or without Mn were prepared by a modified precipitation method. The use of citric acid led to small-particle catalysts denoted by CoP(S) and CoMnP(S), while large-particle catalysts CoP(L) and CoMnP(L) were obtained by leaving out citric acid during precipitation. These catalysts were compared with the catalysts CoPDI(S) and CoIWI(L) already described in Chapter 3.

Table 4.1 lists the metal loading and average particle size of the oxidic precursors. The precipitation method is effective in reaching a Co metal loading of ~10 wt% with Mn/Co ratios of 0.1 for the two Mn-promoted samples. The two reference samples have a slightly lower Co loading of ~7.5 wt%. CoIWI(L) serves as a reference catalyst with large relatively large Co-oxide particles (~10 nm), while CoPDI(S) contains ~4 nm Co-oxide particles. Besides the different preparation method, the reference samples differ from the new precipitated samples by the presence of Pt.

Table 4.1. Metal loadings and average particle size of the calcined catalysts.

Catalyst	Preparation method	Co loading wt% ^a	Mn loading wt% ^a	Mn/Co ratio	Particle size (nm) ^b
CoP(L)	Precipitation	10.5	-	0	9.1±2.7
CoMnP(L)	Precipitation	10.5	1.0	0.1	9.3±3.5
CoP(S)	Precipitation (with citrate)	10.0	-	0	4.0±0.9
CoMnP(S)	Precipitation (with citrate)	9.5	1.0	0.1	3.9±1.2
CoIWI(L) ^c	Incipient wetness impregnation	7.7	-	0	10.3±2.8
CoPDI(S) ^c	Precursor decomposition Impregnation (with citrate)	7.4	-	0	4.1±1.1

^a ICP-OES analysis; ^b TEM analysis; ^c contains Pt (~0.04 wt%).

Fig. 4.1 shows representative TEM images of the calcined precipitated catalysts and the corresponding particle size distributions. The average particle sizes are given in Table 4.1. The two catalysts prepared via precipitation using citric acid, CoP(S) and CoMnP(S), contain predominantly Co-oxide particles smaller than 6 nm. The average particle size of CoP(S) and CoMnP(S) were 4.0 nm and 3.9 nm, respectively. The particles in the two precipitated catalysts prepared without citric acid, CoP(L) and CoMnP(L), are significantly larger than 6 nm. The average particle size of the CoP(L) catalyst is 9.1 nm, while the CoMnP(L) catalyst contains particles with an average size of 9.3 nm. Thus, the impact of using citric acid on the particle

size after calcination is substantial, while the presence of Mn has only a minor influence. Without citric acid in the precipitation solution, the Co-oxide particles are not only larger but also exhibit a broader size distribution. The small-particle catalysts contain mainly Co-oxide particles in the range where after reduction, the metal particles would have a deteriorated catalyst performance as compared to the large-particle catalysts, due to structure sensitivity effect.

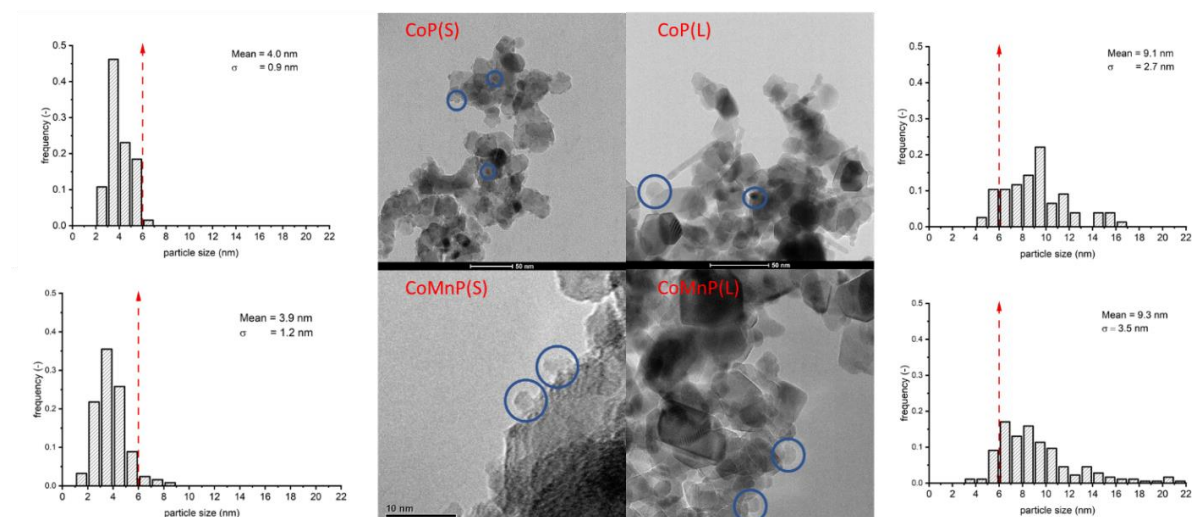


Figure 4.1. TEM analysis of calcined CoP(S), CoP(L), CoMnP(S), and CoMnP(L). The red dashed line in the histograms indicates the particle size below which a decrease in FT performance is expected.

The X-ray diffractograms of the catalysts obtained after calcination are presented in Fig. 4.2a and the Co_3O_4 reference pattern (PDF#42-1467) is displayed in Fig. 4.2b. Despite the relatively high Co loading (~ 10 wt%), the anatase and rutile reflections of TiO_2 dominate the XRD patterns and overlap with the most intense Co_3O_4 feature at $2\theta = 36.87^\circ$ (311). Therefore, we used the (220) reflection of Co_3O_4 to estimate the crystal size using the Scherrer equation. For CoP(L) and CoMnP(L), the resulting particle size of ~ 9.8 nm is in good agreement with the TEM analysis. The absence of the (220) feature in the XRD patterns of the catalysts with small particles (inset Fig. 4.2 a) is due to the much smaller size of the CoO particles. No reflections belonging to Mn-oxides are observed, indicative of the high Mn dispersion. In contrast to the SiO_2 -supported catalysts (Chapter 2), addition of Mn does not affect the Co-oxide diffraction peaks. This may indicate that, in comparison to the SiO_2 -supported catalysts, less Mn is incorporated in the Co spinel oxide precursor. A reasonable explanation is the much stronger interaction of Mn with TiO_2 than with SiO_2 , resulting in a preference for Mn to stay close to the TiO_2 support. It has also been suggested that Mn can form a mixed Ti/Mn spinel phase, i.e., Ti_2MnO_4 compounds¹⁹, however no evidence of the spinel formation was found by XRD.

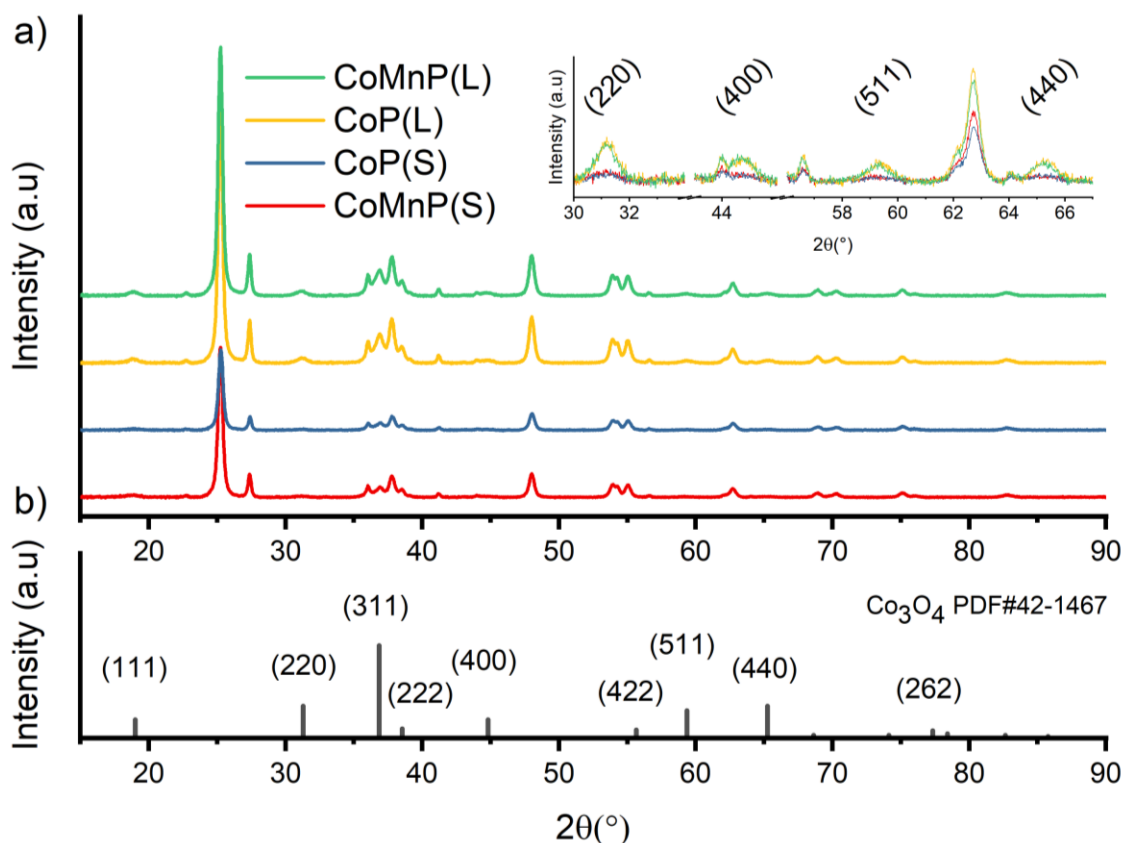


Figure 4.2. XRD patterns of (a) calcined samples and (b) reference diffraction pattern of Co_3O_4 PDF#42-1467. The inset shows the most prominent Co_3O_4 diffraction lines.

The reducibility of the catalysts was studied by H_2 -TPR. The corresponding profiles are displayed in Fig. 4.3. Two distinct peaks at 300°C and 500°C can be observed representing the two-step reduction process from Co_3O_4 to Co^0 via intermediate CoO .

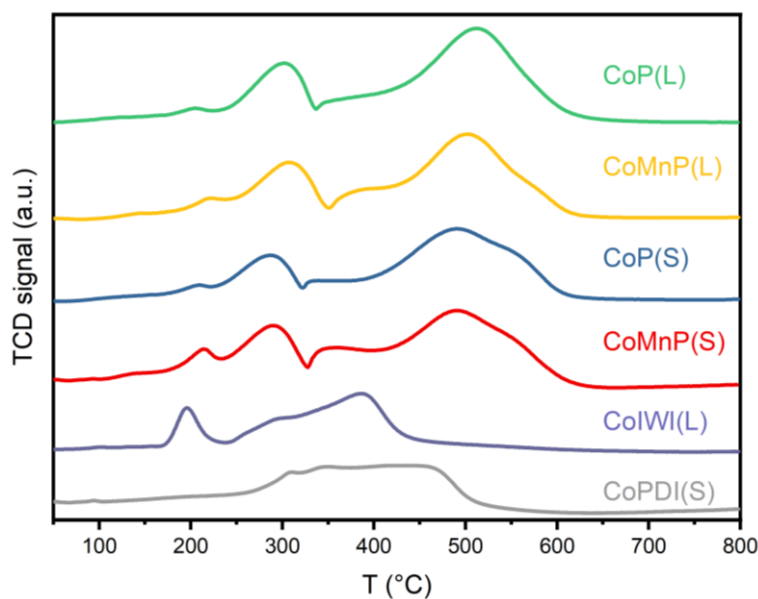


Figure 4.3. H_2 -TPR profiles of catalysts as a function of particle size and Mn content.

Despite the small differences between the precipitated catalysts, the CoMnP(L) , CoP(S) , and CoMnP(S) samples show a shoulder around 575 °C, implying that decreasing the particle size

for CoP(S) and CoMnP(S) as well as promotion by Mn in CoMnP(L) delays the complete reduction of Co. This suggests significant interactions between the support or the Mn promoter with the Co-oxide precursor²⁰. The precipitated samples reduce at higher temperatures than the reference catalysts (CoIWI(S) and CoPDI(S)), which is most likely due to the absence of Pt. While CoIWI(L) is completely reduced at 450 °C, decreasing the particle size via PDI preparation leads to a delay in the reduction by around 50 °C due to a stronger interaction of the small particles with the support.

4.3.3 Quasi in situ XPS

The Co oxidation states of the catalysts were determined by *quasi in situ* XPS of (i) in their calcined state, (ii) after reduction at 280 °C (equimolar mixture of H₂ and He, p = 1 bar, 4 h) and (iii) after subsequent exposure to model FT conditions (synthesis gas H₂/CO = 4, T = 260 °C, p = 1 bar, 4 h). The FT model conditions were selected to avoid the production of large amounts of wax products that can deposit on the catalyst. The FT reaction temperature was below the reduction temperature of 280 °C. The results are presented in Fig. 4.4. The XPS data show that all 4 precipitated catalysts contain mainly Co₃O₄ in the calcined state. The CoPDI(S) sample contains a larger contribution of Co²⁺ (Appendix Fig. A3) than expected for Co₃O₄. This is attributed to stronger Co²⁺-TiO₂ interactions obtained by this preparation method. From the lower value of the Co/Ti ratio of CoP(L) (0.84) in comparison to that for CoP(S) (1.5), it can be inferred that the Co dispersion is substantially higher in the small-particle catalyst CoP(S), which is in agreement with the TEM results.

After reduction at 280 °C, the catalysts typically contain a mixture of metallic and oxidic Co. The degree of reduction (DOR) based on the fraction of metallic Co as determined by XPS is presented in Table 4.2. The DOR is relatively low (<20 %) for all precipitated samples with a small influence of Mn. Notably, the DOR of the two reference catalysts is much higher, namely 100 % for CoIWI(L) and 46 % for CoPDI(S), which can be related to the presence of Pt. The CoPDI(S) is more difficult to reduce due to the stronger Co-TiO₂ interactions than CoIWI(L). Despite the higher Co²⁺ contribution in CoPDI(S) than in CoP(S), which points to stronger Co-TiO₂ interactions in the former, the Co oxide in CoPDI(S) is easier to reduce due to the presence of Pt.

Table 4.2. DOR as determined from fitting of the Co 2p_{3/2} XPS spectra after 4 h reduction at 280 °C and after subsequent 4 h FT reaction at 260 °C, a H₂/CO ratio of 4 and a pressure of 1 atm.

Catalyst	DOR (%) Reduction 280°C, 4 h	DOR (%) Reduction 280 °C, 4 h + CO hydrogenation, H ₂ /CO = 4, 260 °C, 4 h	$\frac{I_{Co}}{I_{Ti}}$ calcined	$\frac{I_{Co}}{I_{Ti}}$ after Reduction 280 °C	$\frac{I_{Co}}{I_{Ti}}$ CO hydrogenation, H ₂ /CO = 4, 260 °C, 4 h
CoP(L)	14	62	0.95	1.20	0.66
CoMnP(L)	9	29	1.18	1.35	0.73
CoP(S)	9	64	1.69	1.33	0.54
CoMnP(S)	11	52	1.47	1.31	0.48
CoIWI(L)	100	-	0.25	-	-
CoPDI(S)	46	-	0.65	-	-

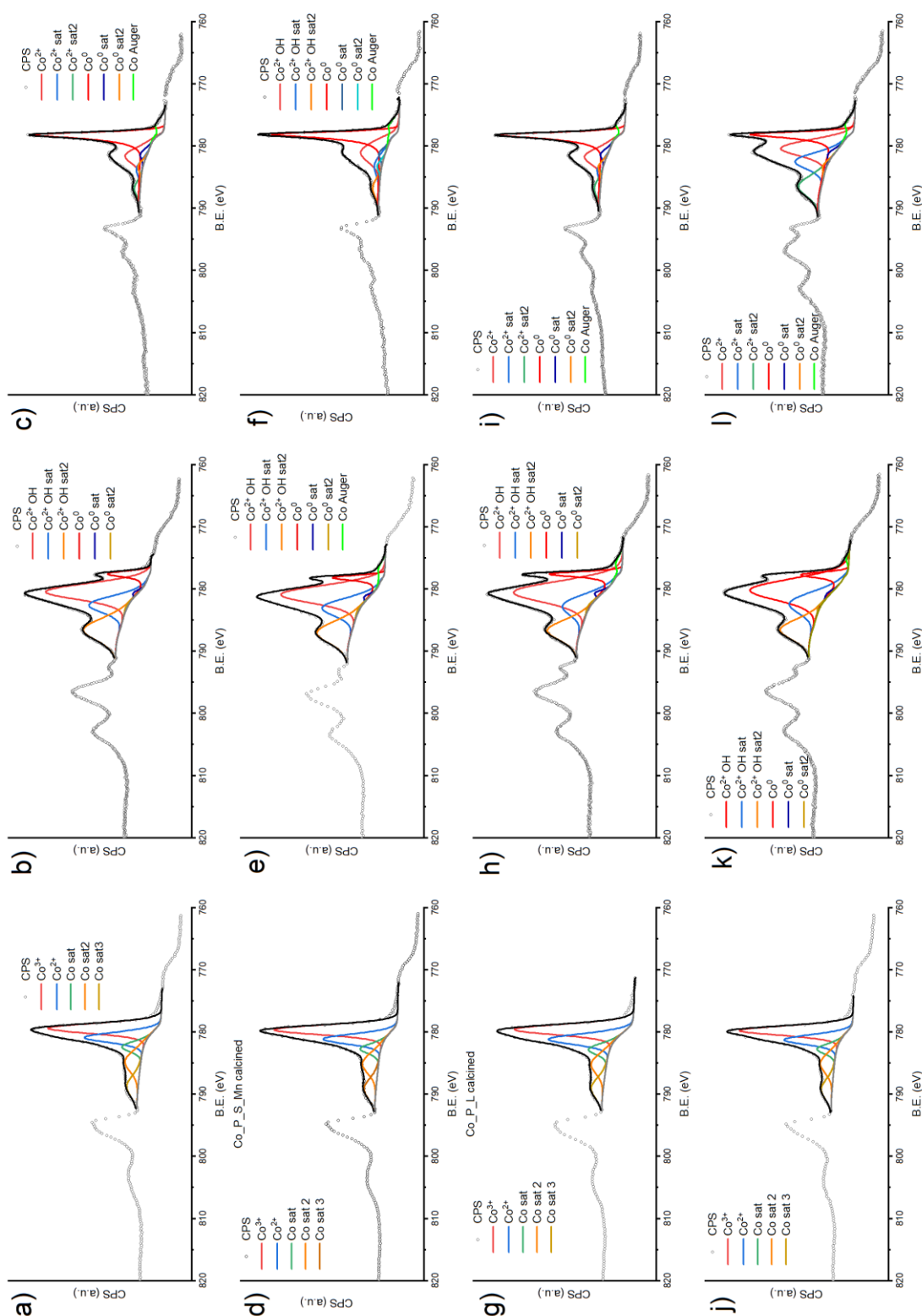


Figure 4.4. Co 2p XPS spectra after calcination, reduction at 280 °C for 4 h, and subsequent CO hydrogenation reaction at 260°C, 1 atm, a H₂/CO ratio of 4 for 4 h: (a) CoP(S) calcined, (b) CoP(S) reduced 280 °C, (c) CoP(S) subsequent CO hydrogenation, (d) CoMnP(S) calcined, (e) CoMnP(S) reduced 280°C, (f) CoMnP(S) subsequent CO hydrogenation, (g) CoP(L) calcined, (h) CoP(L) reduced 280 °C, (i) CoP(L) subsequent CO hydrogenation, (j) CoMnP(L) calcined, (k) CoMnP(L) reduced 280 °C, (l) subsequent CO hydrogenation.

Subsequent exposure to synthesis gas at 260 °C for 4 h results in a significantly higher DOR than after the initial reduction step at 280 °C. In this case, the Mn-promoted catalysts exhibit a lower DOR than the non-promoted samples. These findings show that reduction at 280 °C was slow and continued in the synthesis gas at 260°C. It was verified that these catalysts do not contain Co carbide as followed from the absence of its characteristic Co 2p_{3/2} feature at 283 eV. The formation of Co₂C has, for instance, been observed for Mn-promoted cobalt containing Na^{21,22}. Upon reduction at 450 °C, all catalysts were completely reduced (data not shown).

XPS was also used to investigate the oxidation state of Mn in the calcined and reduced precipitated catalysts. The Mn 2p spectra are presented in Fig. 4.5. In calcined samples, Mn exhibits an oxidation state of 3+ as in Mn₂O₃. The absence of the satellite feature at ~647 eV typical for Mn²⁺ shows that MnO is not present in the calcined precursor. However, after reduction at 280 °C, a clear MnO feature appears for CoMnP(S). MnO was not observed for CoMnP(L) upon reduction, which is in line with the lower reducibility of this sample during simulated FT conditions (Fig. 4.4, Table 4.2). Nevertheless, after further CO hydrogenation at 260 °C for 4 h, the satellite feature due to MnO is visible in both catalysts, showing that the reduction of Mn₂O₃ to MnO proceeds during CO hydrogenation.

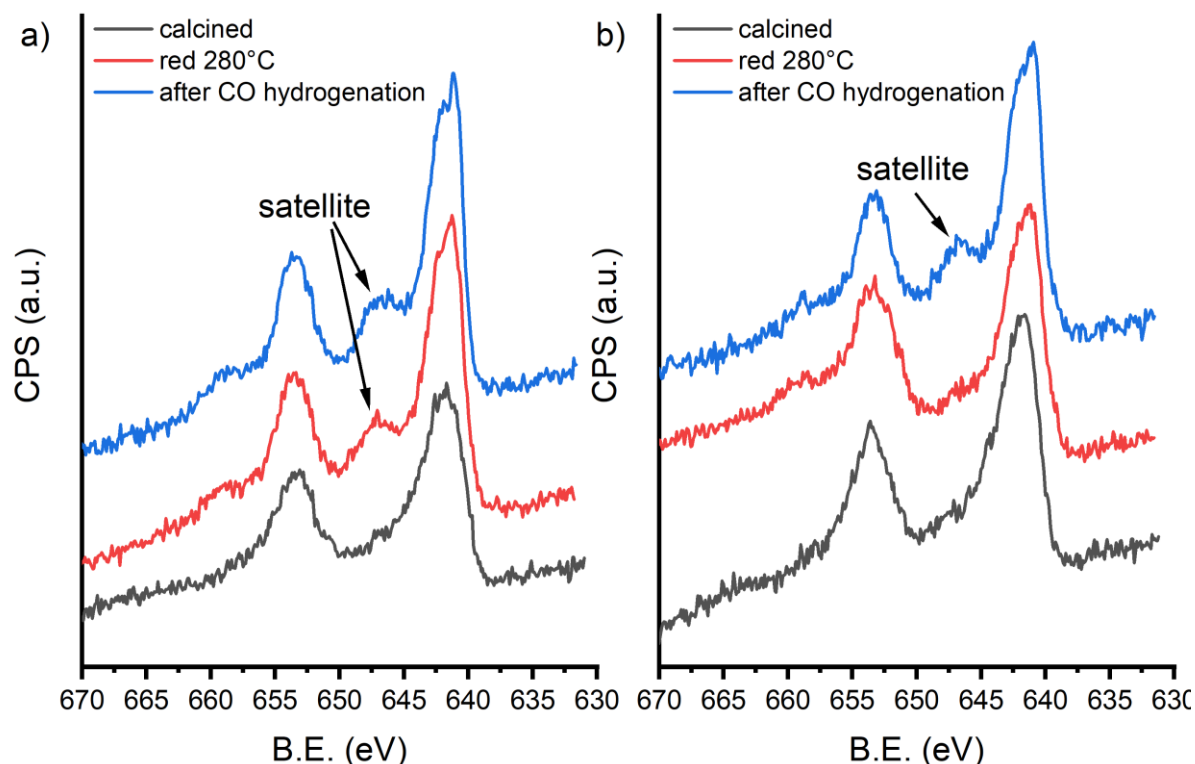


Figure 4.5. Mn 2p XPS spectra after calcination, reduction at 280 °C for 4 h, and CO hydrogenation reaction at 260 °C, 1 atm, a H₂/CO ratio for (a) CoMnP(S) and (b) CoMnP(L).

4.3.4 X-ray absorption spectroscopy (XAS)

In order to reveal structural differences between samples made by different approaches, we determined the structure of around the Co atoms using XAS. We first studied the reducibility of CoMnP(S) in comparison with the reference CoPDI(S) and CoIWI(L) samples by XANES under increasing temperature from 50 to 450 °C in an H₂ atmosphere. The resulting XANES spectra are displayed in Fig. 4.6.

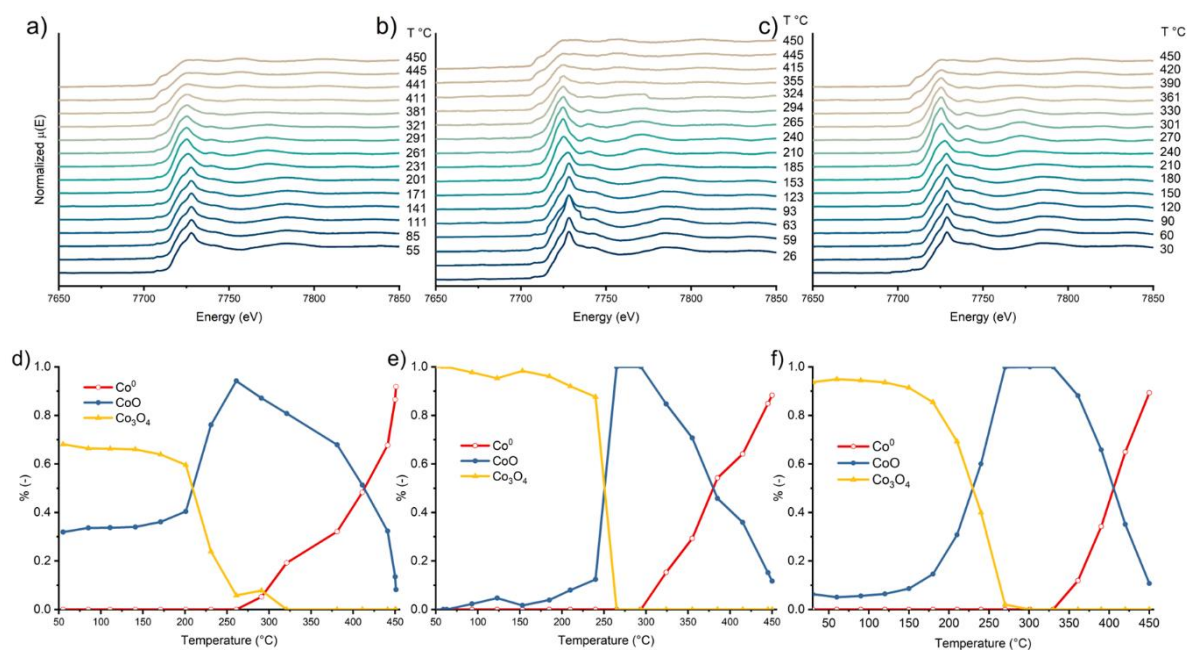


Figure 4.6. Co K-edge XANES spectra measured during catalyst reduction from 50 °C to 450 °C for (a) CoPDI(S), (b) CoIWI(L), and (c) CoMnP(S) and the contribution of different phases (Co⁰, CoO and Co₃O₄) determined by linear combination fitting as function of reduction temperature for (d) CoPDI(S), (e) CoIWI(L), and (f) CoMnP(S).

To better follow the differences as a function of the reduction temperature, the spectra were deconvoluted into contributions for Co⁰, CoO and Co₃O₄. The results of linear combination fitting are also shown in Fig. 4.6d-f and indicate that, among the calcined samples, the CoIWI(L) catalyst contains the largest amount of Co₃O₄, followed by CoMnP(S) and CoPDI(S) which contains only 70 % Co₃O₄ and consequently more CoO. Reduction of CoIWI(L) results in rapid reduction to CoO at 250 °C. The reduction of the other two small-particle catalysts starts at a lower temperature yet extends over wider temperature range. CoMnP(S) is completely converted to CoO at a slightly higher temperature than the small-particle reference catalyst CoPDI(S). CoMnP(S) also remains in the CoO state over a wider temperature range until ~300 °C as compared to CoPDI(S). This points already to a higher stability of CoO in the CoMnP(S) sample. Compared to the other two catalysts, reduction of CoO to Co metal is slowest for CoMnP(S), which is due to the absence of Pt. At the end of the XANES measurement, all three catalysts show a similar DOR of about 90 %.

Fig. 4.7 shows the Fourier transforms of the k³-weighted EXAFS. The corresponding fit results are given in Table 4.3. The calcined samples contain Co-O and Co-Co back scatterers, which can be related to Co oxide. There are only slight differences in the coordination numbers with the

stronger Co-Co backscattering for CoIWI(L) suggesting a lower dispersion. After reduction at 280 °C, all samples contain a weak Co-Co metal shell, reflecting the partial reduction of Co. As such, these samples contain a mixture of metallic Co and Co oxide. Upon reduction at 450 °C, all three catalysts are fully reduced and the high coordination numbers of the first Co-Co shell of metallic Co indicate that the particles should be relatively large. It is worthwhile to compare the higher coordination shells, which can provide indications for the presence of hcp and fcc phases according to Longo and co-workers²³. As such, it can be said that the fully reduced Co metal particles in CoPDI(S) and CoIWI(L) share common features in terms of a pronounced

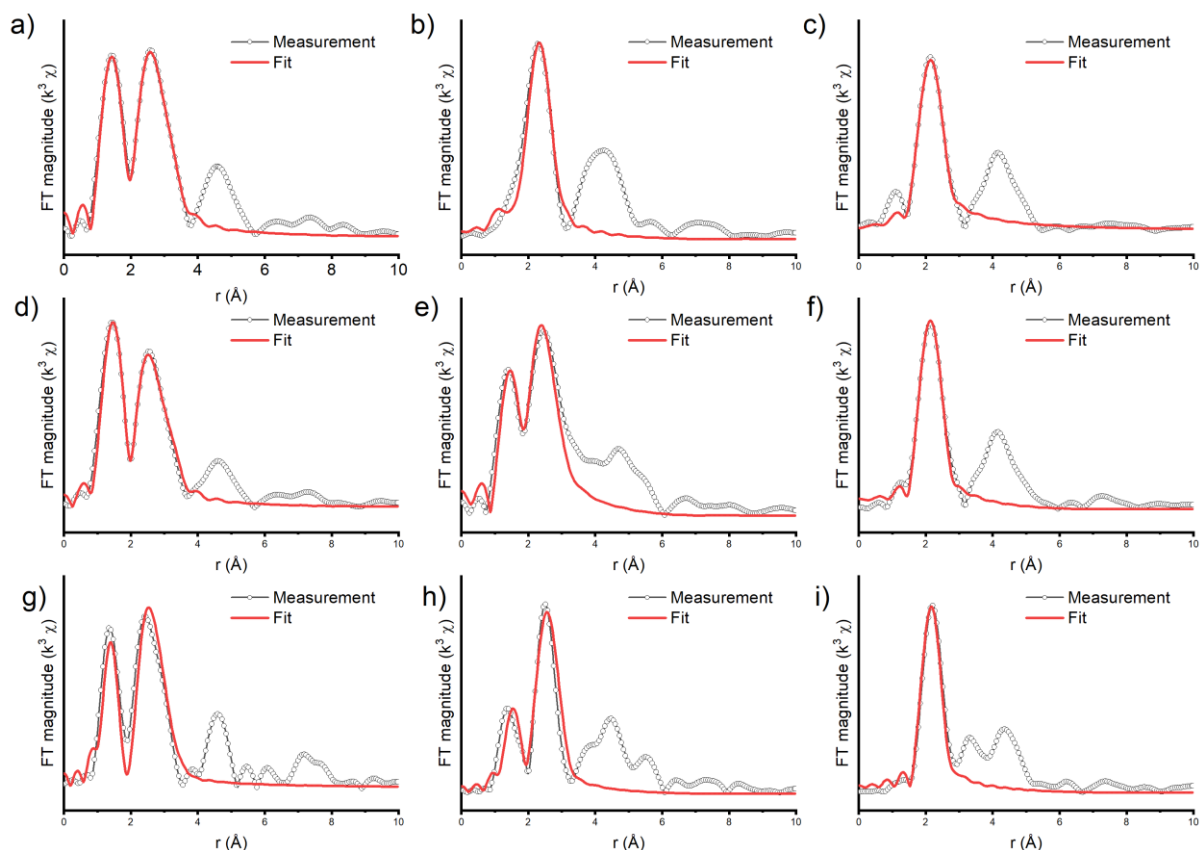


Figure 4.7. Co K-edge Fourier transformed k^3 weighted EXAFS spectra of CoMnP(S) and reference catalysts. CoIWI(L), calcined a), reduced 280 °C b) and reduced 450 °C c). CoPDI(S) calcined d), reduced 280 °C e) and reduced 450 °C f). CoMnP(S) calcined g), reduced 280 °C h) and reduced 450 °C i)

feature at around 4.2 Å and a much weaker one at 3.5 Å, which has been attributed to highly crystalline (i.e., non-distorted) metallic Co. For reduced CoMnP(S), on the other hand, two distinct peaks can be observed at different distances of 3.2 Å and 4.3 Å. Such differences have been associated with distorted structures²³. These differences can point towards varying contributions of hcp and fcc phases caused by different preparation methods.

Table 4.3. Co K-edge EXAFS fit results of Co catalysts as a function of particle size and Mn content. Error margins are reported in brackets.

Catalyst	Path	CN (error)	R [Å] (error)	E ₀ /eV	$\sigma^2/\text{\AA}^2$	R-factor
CoIWI(L) calcined	Co-O	6.6 (0.4)	1.90 (0.005)	0.9	0.002	0.0063
	Co-Co1	5.8 (0.7)	2.85 (0.008)		0.004	
	Co-Co2	6.3 (0.8)	3.36 (0.008)		0.001	
CoPDI(S) calcined	Co-O	4.9 (0.2)	1.93 (0.005)	0.1	0.003	0.0046
	Co-Co1	4.8 (0.7)	2.86 (0.010)		0.009	
	Co-Co2	5.4 (0.8)	3.38 (0.010)		0.005	
CoMnP(S) calcined	Co-O	5.8 (1.0)	1.928 (0.031)	-4.6	0.008	0.057
	Co-Co1	6.3 (1.3)	2.890 (0.026)		0.007	
	Co-Co2	4.1 (1.6)	3.390 (0.040)		0.003	
CoIWI(L) reduced 280 °C	Co-O1	4.6 (1.4)	1.958 (0.027)	-14.8	0.013	0.024
	Co-Co	0.97 (1.3)	2.491	-9.3	0.002	
	Co-O2	12.4 (1.3)	3.033 (0.008)	-14.8	0.008	
CoPDI(S) reduced 280 °C	Co-O1	2.9 (0.4)	1.997 (0.013)	-6.0	0.004	0.017
	Co-Co	1.8 (1.1)	2.456	-17.8	0.013	
	Co-O2	10.1 (1.1)	2.935 (0.009)	-6.0	0.011	
CoMnP(S) reduced 280 °C	Co-O1	5.3 (1.3)	2.094(0.026)	-2.1	0.008	0.046
	Co-Co	1.4 (1.3)	2.573(0.019)	10.4	0.008	
	Co-O2	11.4 (2.9)	3.037(0.062)	-2.1	0.005	
CoIWI(L) reduced 450 °C	Co-Co	10.9 (2.2)	2.49 (0.014)	6.1	0.007	0.013
CoPDI(S) reduced 450 °C	Co-Co	11.5 (2.0)	2.491(0.001)	6.5	0.006	0.013
CoMnP(S) reduced 450 °C	Co-Co	11.7 (1.5)	2.47 (0.030)	4.8	0.007	0.045

4.3.6 Chemisorption

The available metal surface of the catalysts was determined by H₂ chemisorption after reduction at 280 °C and 450 °C. It is difficult to calculate the Co particle size from these measurements, because only a small fraction of the Co-oxide precursor is reduced to the metallic form. Moreover, the amount of chemisorbed H₂ can be affected by spillover of hydrogen atoms to the TiO₂ support or unreduced Co oxide and Mn oxide. For the samples

reduced at 450°C, strong metal-support interactions (SMSI) can lead to coverage of metallic Co by Ti-containing species^{18,14}. The results in Table 4.4 show that the metallic Co surface is significantly larger after reduction 280 °C than after 450 °C, despite the lower DOR obtained at 280°C, suggesting that part of the metal surface is covered by Ti containing species due to the SMSI effect after reduction at 450 °C. Upon reduction at 280 °C, the metal surface areas of CoP(S) and CoMnP(S) are about two times higher than those of CoP(L) and CoMnP(L). These findings confirm the smaller size of the Co particles in the small-particle catalysts after reduction at 280°C. Moreover, the CoP(S) sample reduced at 280 °C has a much higher metal surface area than the CoPDI(S) reduced at the same temperature. The Co particle size of the CoPDI(S) catalyst was found to be 5 nm (Chapter 3), it is reasonable to conclude that the Co particles in the CoP(S) catalyst are even smaller. After correction for the DOR, the particle size would be less than 1 nm, which is unreasonable. We speculate that the initial size of ~4 nm particles of the oxide precursor is retained with part of the Co-oxide particles transforming into metallic Co. The significant difference in H₂ chemisorption between the precipitated samples and the reference ones underpins the strong impact of the preparation method. For the new samples, Mn promotion does not strongly impact the metal surface area with a slightly higher value for the CoMnP(S) catalyst as compared to CoP(S) while the reverse is observed for the large-particle catalysts. Upon reduction at 450 °C, the H₂ chemisorption values for the precipitated catalysts are slightly lower than for the reference catalysts. The much lower absolute values clearly point to significant Co sintering as can be expected. Notably, the values are lower for the Mn-promoted samples, which can be explained by the presence of Mn-oxide on the metallic Co surface.

Table 4.4. H₂ chemisorption data after reduction at 280 °C and 450 °C, particle sizes derived from the H₂ chemisorption assuming spherical particles, and sizes corrected for the DOR obtained from XPS analysis.

Sample	Mn/Co	Reduced at 280 °C	Reduced at 450 °C
		mmol H ₂ /g _{Co}	mmol H ₂ /g _{Co}
CoP(S)	0	1.19	0.20
CoMnP(S)	0.1	1.35	0.12
CoP(L)	0	0.70	0.26
CoMnP(L)	0.1	0.63	0.12
CoPDI(S)	0	0.67	0.38
CoIWI(L)	0	0.88	0.35

4.3.7 High-pressure catalytic activity measurements

The FT catalytic performance of the various samples was measured at a temperature of 220 °C, a H₂/CO ratio of 2 and a pressure of 20 bar (Fig. 4.8). The rates normalized to the Co catalyst weight (Fig. 4.8a) show a strong variation with particle size, promotor content and reduction temperature. We first note that the CoIWI(L) catalyst has a nearly two times higher activity

than the CoPDI(S) catalyst, which can be related to the particle size effect. The opposite counts for the Mn-promoted samples. The CoMnP(S) catalyst is more active than the CoMnP(L) catalyst independent of the reduction temperature. This is in line with the results in Chapter 3, which show that the presence of Mn can compensate for the suppressed activity of small particles due to the particle size effect, the reaction data for CoMnP(L) are probably an outlier (see below). For all samples, except CoMnP(L), it is observed that the reaction rate is higher for the samples reduced at 280 °C in comparison to their counterparts reduced at 450 °C. The higher weight-based activity after reduction at lower temperature has also been reported by Melaet et al.¹⁵ and Van Deelen et al.²⁴. As mentioned in Chapter 3, the strong influence of the Co particle size is also apparent when comparing CoP(S) with CoP(L), where the large particles are significantly more active than the smaller ones. Similar to the reference catalysts, the CoP(L) catalyst is twice as active as the CoP(S) catalyst after reduction at 450 °C. The difference is slightly less when these catalysts are reduced at a lower temperature of 280 °C. Most profoundly, it is observed that the CoMnP(S) catalyst reduced at 280 °C has the highest reaction rate, which is even significantly higher than the reaction rate of the CoIWI(L) reference. There is also a clear promoting effect of Mn-oxide as the CoMnP(S) catalyst is more active than the CoP(S) one. Thus, the structure sensitivity can be overcome. By partial reduction of Co with Mn can further promote the FT activity.

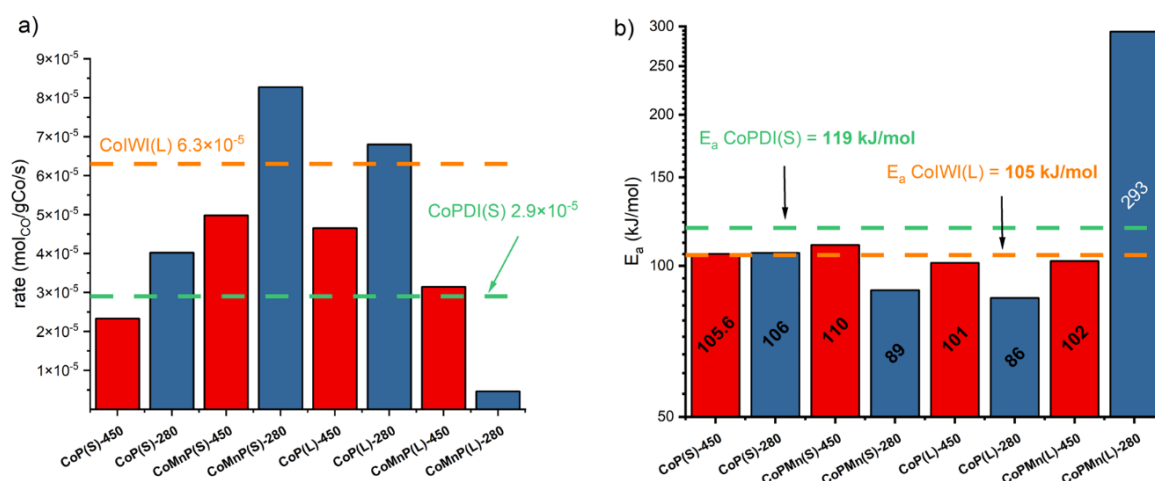


Figure 4.8. Catalytic performance of the various precipitated catalysts after reduction at 280 °C (blue bars) or 450 °C (red bars): (a) reaction rate normalized to the Co loading and (b) apparent activation energy (reaction conditions: $T = 220$ °C, $p = 20$ bar, $H_2/CO = 2$, values after 30 h of reaction, activation energies determined in the range 220-240 °C). The green and orange dotted lines indicate the reaction rates and apparent activation energies of CoPDI(S) and CoIWI(L) reduced at 450 °C.

The apparent activation energies determined for the precipitated catalysts show an influence of the presence of Mn oxide and Co oxide (Fig. 4.8b). The corresponding Arrhenius plots are shown in Appendix Fig. C3. The precipitated catalysts display apparent activation energies similar to or lower than the apparent activation energy of the CoIWI(L) sample (105 kJ/mol). The apparent activation energy of the CoPDI(S) sample is slightly higher (119 kJ/mol). The two most active samples, namely CoMnP(S) and CoP(L) reduced at 280 °C, exhibit substantially lower apparent activation energies. This suggests the presence of active sites with a higher reactivity, presumably due to the presence of Mn oxide and/or Co oxide species that can facilitate CO dissociation as discussed for Mn oxide promotion in Chapter 2. The very large

value of the apparent activation energy for CoMnP(L) is likely due to the ongoing reduction of this sample during reaction as suggested by the data obtained for the DOR after reduction at 280 °C and after reaction at 260 °C in Table 4.2. The increasing DOR during apparent activation energy measurements at increasing temperature will lead to a disproportionally strong increase in the catalytic performance.

Overall, these data show that the catalysts can be promoted by the presence of Mn-oxide and Co-oxide. In Chapter 2 it is shown that removal of O atoms from MnO leads to coordinatively unsaturated Co^{2+} sites that can facilitate dissociation of CO adsorbed on the adjacent metallic Co sites. The promotional effect of Co-oxide likely follows a similar mechanism as MnO^{11} . The apparent activation energies for CoMnP(S) and CoP(L) reduced at 280 °C are lower than the apparent activation energy of optimum CoMn/SiO₂. As in the latter catalyst all Co was reduced, this difference can point to a prominent role of Co-oxide. Overall, the data indicate that the presence of Co- and Mn-oxide in the precipitated catalysts yields the highest Co-weight-based reaction rate. In contrast to the catalyst prepared by other impregnation methods, where partial oxidation or Mn addition yielded better selectivities and higher TOFs, but not a higher weight-based reaction rate (see Chapter 3).

Turnover frequencies (TOFs) based on the metal surface area determined by H₂ chemisorption are presented in Fig. 4.9. The catalysts reduced at 450°C exhibit a higher TOF than their counterparts reduced at 280 °C. Thus, although the weight-based activity of the catalysts with presumably small (< 6 nm) particles are higher than the large-particle catalysts, their TOF is lower. This can either be the result of a much lower metal surface area of the particles reduced at 450°C due to SMSI. As such, we can infer that reducing a CoMn/TiO₂ catalyst prepared by precipitation in the presence of citric acid at 280 °C results in small (<6 nm) particles with a higher Co-weight-based activity than fully reduced TiO₂ supported Co catalysts. Next, we study the impact of promoter, particle size and reduction temperature on the product distribution.

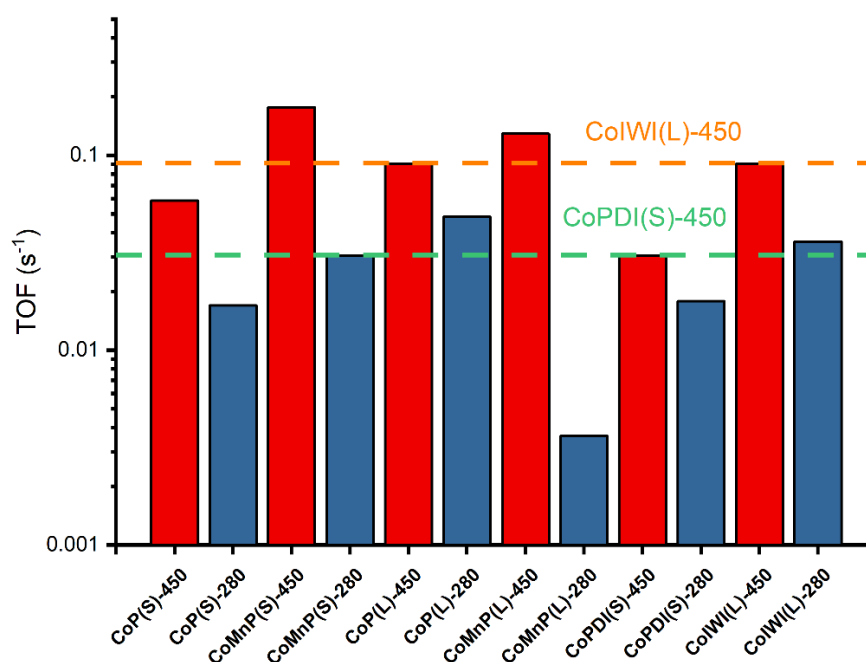


Figure 4.9. TOF for the catalysts reduced at 280 °C (blue) or 450 °C (red) after FT reaction at 220 °C, 20 bar, $H_2/CO = 2$ after 28 h time on stream. The green and blue dotted lines represent the TOF values of the reference catalysts CoPDI(S) and CoIWI(L) after reduction at 450 °C, respectively. The TOFs were determined using the H_2 chemisorption values reflecting the metallic Co surface area.

Fig. 4.10 reports the product distribution at the standard FT conditions. The less active CoPDI(S) catalyst shows a significantly higher methane selectivity than the CoIWI(L) reference, in line with the well-established finding that smaller particles yield more methane at the expense of C_{5+} products.²⁵ All the precipitated Co catalysts show a low methane selectivity. The highest methane selectivity is observed for CoP(L) reduced at 450°C, its value being close to the value for the CoIWI(L) reference. All the other samples except the outlier CoMnP(L) reduced at 280 °C, produce significantly less methane than the reference samples. The most outstanding difference is observed for the small-particle catalysts with values for the methane selectivity even lower than for the CoIWI(L) reference. It is also clear that Mn lowers the CH_4 selectivity in all relevant cases. The low CH_4 selectivity is mirrored by the increased C_{5+} selectivity for all catalysts except the outlier. The most favorable cases are for CoP(S) and CoMnP(S) reduced at 280 °C, presenting a C_{5+} selectivity close to 95 %.

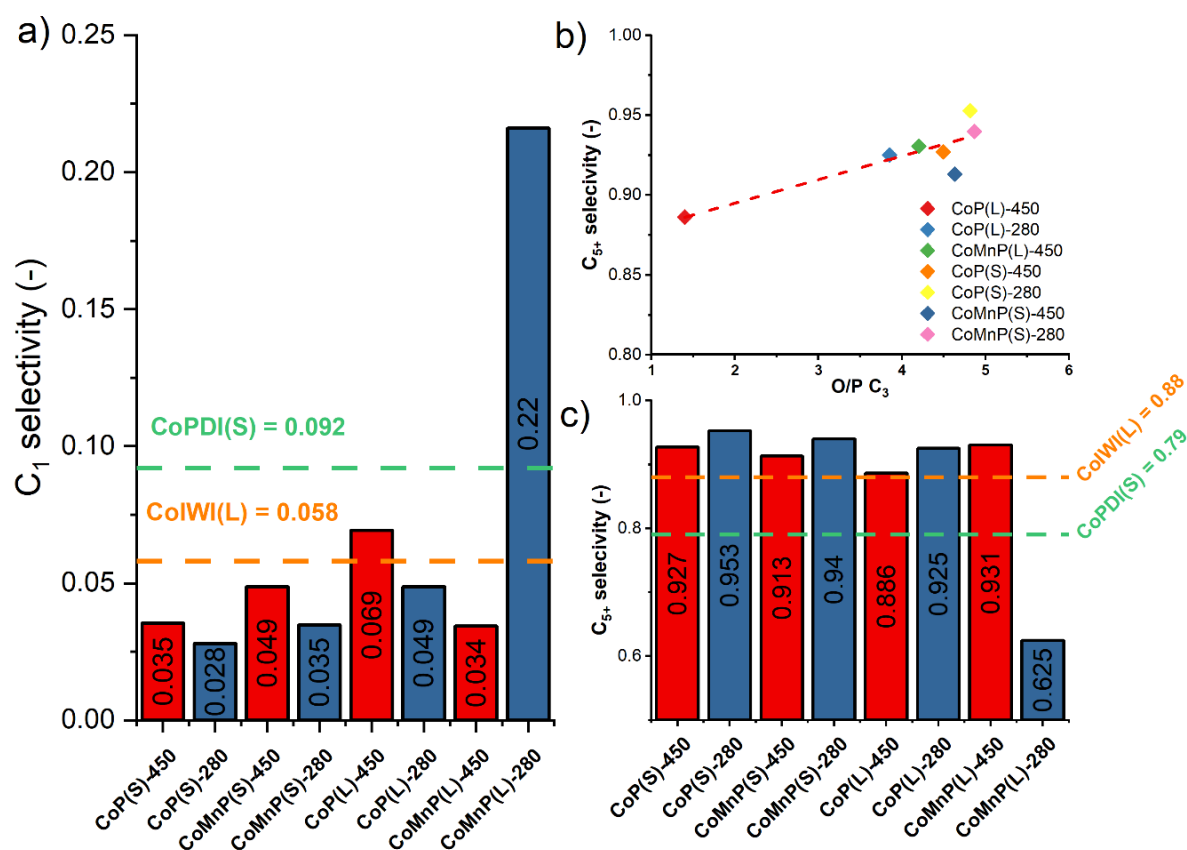


Figure 4.10. Product distribution data during the FT reaction at 220 °C, 20 bar, $H_2/CO = 2$ after 28h time on stream: (a) C_1 selectivity, (b) C_{5+} selectivity as a function of the O/P ratio of the C_3 products and (c) the C_{5+} selectivity. The corresponding values for the CoPDI(S) and CoIWI(L) reference catalysts are shown in green and blue dotted lines respectively in panels (a) and (c).

Fig. 4.10b shows a linear correlation between the C_{5+} selectivity and the olefins-to-paraffins (O/P) ratio for which the C_3 olefins and paraffins were used as a proxy. Such a correlation,

which has been reported before,²⁶ reflects the suppressed hydrogenation activity of the catalyst, which can explain the higher chain-growth probability. As such, the trends also correlate to the methane selectivity. It is also evident from these data that Mn promotes the O/P ratio and the C₅₊ selectivity at the expense of the C₁ selectivity. These trends are in line with the effect of MnO on Co as also found for CoMn/SiO₂.¹¹

4.3.8 IR spectroscopy

CO IR spectroscopy was used to characterize the catalytic surface after different pretreatment methods. IR spectra recorded at 30 °C are presented in Appendix Fig. C4 as a function of the CO partial pressure. Temperature-programmed IR measurements were used to study the evolution of adsorbed CO under increasing temperature. In these experiments, the CO pressure was 10 mbar and the temperature was ramped from 50°C to 300°C at a rate of 5°C/min. Fig. 4.11a shows a typical IR spectrum with the main CO absorption band being located in the range of 2028-2038 cm⁻¹. During heating to 125-150 °C, a blue-shift of this band by ~50 cm⁻¹ is observed, which can be linked to the appearance of mainly adsorbed C species that due to their lateral interactions shift the CO absorption band to the blue. The adsorbed C species originate from CO dissociation and the blue-shift can therefore be used as a proxy for CO dissociation.^{27,28,29}

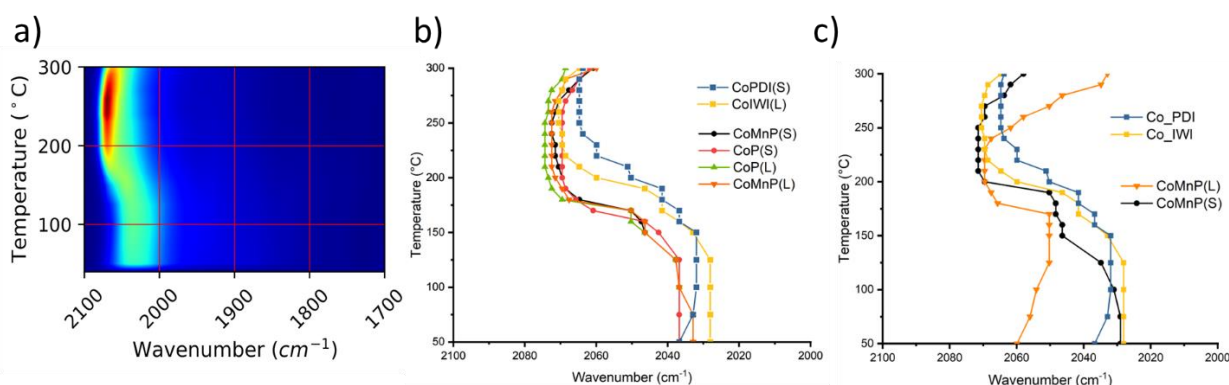


Figure 4.11. (a) Representative temperature-programmed IR experiment of the CO absorption range (1700 – 2100 cm⁻¹, (b) peak maxima for various catalysts reduced at 280 °C and (c) peak maxima for catalysts at 450°C. The CO pressure in the cell was 10 mbar CO and the heating rate 5 °C/min.

The shift of the linear CO absorption band for the catalysts reduced at 280 °C (Fig. 4.11b) and 450°C (Fig. 4.11c) all show a similar blue-shift. The corresponding IR spectra of these experiments are given in the Appendix C5. In agreement with the FT activity of the precipitated catalysts, the blue-shift occurs at a lower temperature than the reference samples. Despite this, the variations in the activity among the precipitated catalysts does not translate in significant differences in the temperature at which the blue-shift occurs. A tentative explanation is that the pressure in the IR experiments is much lower than in the FT tests. At high pressure, CO dissociation is more difficult due to the lack of surface vacancies on the metal surface³⁰. As such, the reaction will benefit more from additional sites for CO dissociation at high pressure. In the IR experiments, the CO pressure is low, implying that there are sufficient vacancies on the metal surface for CO dissociation. In contrast to the catalysts

reduced at 280 °C, those reduced at 450 °C show no consistent trend in the temperature of the blue-shift.

Additional temperature-programmed IR experiments were carried out in a synthesis gas mixture ($\text{H}_2/\text{CO} = 2$, 100 mbar). Fig. 4.12 shows the IR spectra for such measurements for the samples reduced at 450°C. The spectra contain a clear band due to gaseous CH_4 at 3015 cm^{-1} . Adsorbed CH_x species are also present as follows from the IR absorption bands at 2927 cm^{-1} due to $\nu_{\text{as}}(\text{CH}_2)$, 2876 cm^{-1} due to $\nu_{\text{s}}(\text{CH}_3)$, 2876 cm^{-1} due to $\nu_{\text{s}}(\text{CH}_3)$, and 2855 cm^{-1} due to $\nu_{\text{s}}(\text{CH}_2)$. The characteristic bands due to gaseous CH_4 are typically observed for all catalysts starting from a temperature of 200 °C. The intensity of these bands varies substantially among the samples. Moreover, it is clear that the bands due to adsorbed CH_2 species are much more intense for CoMnP(L) and CoMnP(S). Moreover, these bands appear before those of CH_4 in comparison to the reference catalysts, where the CH_2 bands were much weaker or even absent. These differences are comparable to the effect of Mn on CO dissociation probed by temperature-programmed IR measurements in Chapter 2. The higher rate of CO dissociation results in a higher coverage with CH_x species. Compared to the precipitated samples, CoPDI(S) reduced at 450 °C leads to less methane, reflecting the low activity as compared to the small-particle catalysts prepared by precipitation.

Fig. 4.13 depicts the corresponding IR spectra after reduction at 280 °C. In this case, the CH_x bands are much more intense, and the impact of particle size and the presence of Mn is only minor. The presence of Mn leads, however, to an additional CH_x band at 2876 cm^{-1} , which is absent in samples without Mn. This band can be attributed to $\nu_{\text{s}}(\text{CH}_3)$ ³¹. Besides the strongly shifting linear CO band present in all spectra, the spectra also contain other relatively sharp bands at 1842, 1892 and 1930 cm^{-1} . These bands shift less with temperature and are more intense for the small-particle catalysts. Recently, Parastaev et al. showed that low-temperature reduction of Co-oxide on a $\text{CeO}_2\text{-ZrO}_2$ support can lead to the formation of small Co clusters of a few atoms dispersion on Co-oxide³². The CO IR spectra of such catalysts recorded at ambient conditions exhibited similar sharp IR bands, which could be assigned on the basis of DFT calculations to top and bridged adsorption modes of CO on small Co clusters. These nanostructured catalysts were associated with high activity in the methanation of CO_2 . Given the similarity in the IR spectra, we speculate that the catalyst reduced at 280 °C contains some small Co clusters dispersed on Co-oxide next to the evidently present extended Co surfaces representative for Co particles. The high activity of the samples reduced at low temperature might at least in part be attributed by such small Co clusters in interaction with Co oxide.

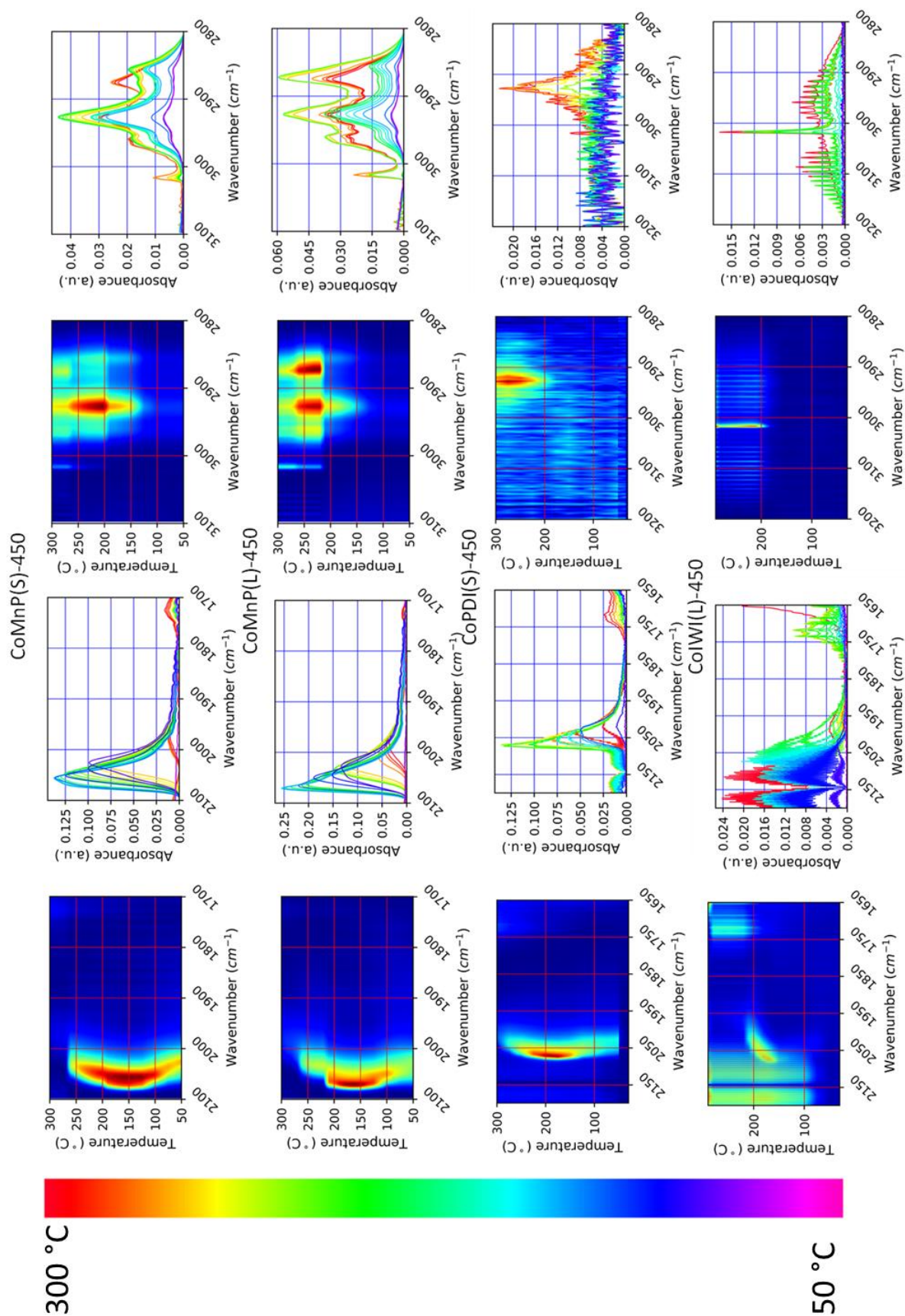


Figure 4.12. IR spectra in the range 2800-3200 cm⁻¹ of TPFTIR experiments after reduction at 450 °C in syngas ($H_2/CO = 2$, $p_{tot} = 100$ mbar). Colors indicate increasing temperature from 50 – 300 °C. In the heat maps colors indicate the increasing IR intensity from violet to red.

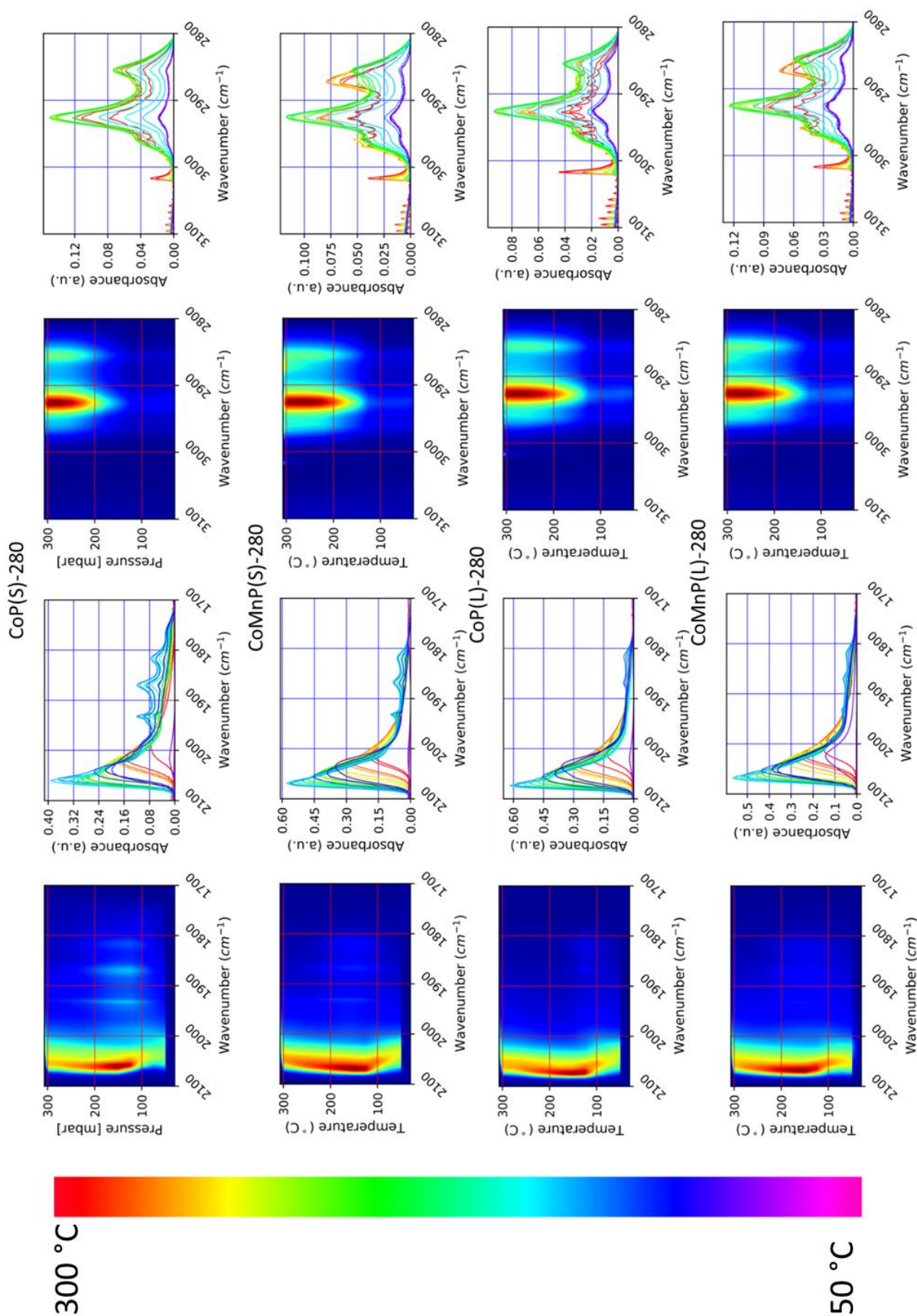


Figure 4.13. IR spectra in the range 2800-3200 cm^{-1} of TPFTIR experiments after reduction at 280 °C in syngas ($\text{H}_2/\text{CO} = 2$, $p_{\text{tot}} = 100$ mbar). Colors indicate increasing temperature from 50 – 300 °C. In the heat maps colors indicate the increasing IR intensity from violet to red.

4.4 General discussion

The way Co-based FT catalysts are prepared has a very strong impact on the catalytic performance. Many parameters such as the loading method, the drying conditions, the pretreatment procedure and the presence of promoters will strongly impact the active phase and catalytic performance, rendering it challenging to predict the optimal preparation method. However, a few design principles for optimal Co catalysts have been discussed³³. Another factor impacting FT performance is the Co particle size, as the FT reaction has been found to be strongly structure sensitive². By employing a novel precipitation method, Shimura et al. was able to achieve a remarkably low CH₄ selectivity³⁴. In combination with the complexing agent citric acid, which is known to increase Co dispersion¹⁶, we prepared homogeneously distributed <6 nm Co particles at a relatively high Co loading of 10 wt% supported on TiO₂. These catalysts showed extraordinary catalytic performance with the precipitated catalyst with small Co particles, CoP(S), exhibited a lower CH₄ and a higher C₅₊ selectivity than the precipitated catalyst with large particles, CoP(L). This difference is in contrast with the trends in literature with respect to particle size as confirmed by the difference between our reference small-particle and large-particle reference catalysts. As such, the present findings challenge the widely accepted assumption that <6 nm particles should be avoided for FT catalysts with high activity and high C₅₊ selectivity. Although it is commonly believed that completely reduced Co⁰ species are necessary for a high activity, this has already been questioned, especially for Co on reducible supports like TiO₂³⁵ or Nb₂O₅²⁴. A comparison of the DOR determined by XPS of the TiO₂ supported Co(Mn) catalysts after reduction at 280 °C and a FT model reaction at 260 °C shows the presence of large amounts of Co oxide (>85%). The Co atoms in the catalysts reduced at 450 °C were fully reduced. Despite the lower DOR, the catalytic performance of the low-temperature reduced catalysts was substantially higher. This difference is attributed to the presence of reducible CoO in close contact with Co metal, where similar chemistry can occur as at the Co-MnO interface as discussed in Chapter 2. It is also important to emphasize that the lower reduction temperature led to a higher metal surface area than reduction at 450 °C. The low surface area of the high-temperature reduced catalysts is most likely the result of SMSI overgrowth of Ti-containing species on metallic Co^{36,37,38}. Linear combination fitting of XANES spectra measured during reduction revealed a higher Co²⁺ content (which is associated with metal support species) for CoPDI(S) compared to the CoMnP(S) and Co(L) samples. In addition to that XANES revealed a higher stability over a large temperature range of the oxidic phase in the CoMnP(S) catalyst. A detailed comparison of the XANES spectra after reduction at 450 °C revealed minor differences between the Co edge of CoMnP(S) and the reference samples (Appendix Fig. C6), which could be associated to stacking faults as reported in literature¹⁴⁸. Temperature-programmed IR of adsorbed CO confirmed the higher activity towards CO dissociation of catalysts reduced at 280 °C compared to those reduced at 450 °C. Temperature-programmed IR in syngas after reduction at 280 °C revealed the presence of small Co metal clusters next to extended Co surface, indicating that the Co metal speciation is different from fully reduced catalysts. It is likely that the increased interface between reduced Co and Co-oxide can enhance CO dissociation in a similar manner as observed for MnO promotion.

4.5 Conclusion

In this work, we described a precipitation method for TiO₂-supported Co catalysts, allowing to obtain small Co particles using citric acid as a complexing agent and large Co particles without aid of a chelating agent. The promotion of these samples by Mn introduced by co-precipitation was studied as well. The influence of the reduction temperature (280 °C vs. 450 °C) was investigated for these samples in comparison to the samples in Chapter 3. Small Co particles obtained in this way were more active on a Co weight basis than the large particles at the low reduction temperature of 280 °C, showing that conventional structure sensitivity can be overcome. The reduction temperature has a substantial impact with the small particle catalysts being reduction at 280 °C exhibiting a twofold higher activity compared to reduction at 450°C. Mn-promoted samples are significantly more active on a Co weight basis. It is speculated that the increased activity for these small Co particles stems from the presence of Co-oxide, which may function in the same way as Mn-oxide, i.e., providing additional sites for CO dissociation. Notably, the most active catalysts have a low DOR, which can in part be explained by the absence of Pt reduction promoter as compared to the samples in Chapter 3. Besides the increased activity, the optimum samples exhibit low methane and increased C₅₊ selectivity as compared to conventional samples. Characterization of these samples indicates the presence of metallic Co clusters next to extended Co surfaces in nanoparticles, which are likely in contact with Co- and Mn-oxides stabilized by the TiO₂ support. XAS points to stacking faults in the metal Co particles, which may reflect their disorder as compared to larger metal particles reduced at conventional temperatures.

References

- (1) Van de Loosdrecht, J.; Botes, F. G.; Ciobica, I. M.; Ferreira, A.; Gibson, P.; Moodley, D. J.; Saib, A. M.; Visagie, J. L.; Weststrate, C. J.; Niemantsverdriet, J. W. *Fischer-Tropsch Synthesis: Catalysts and Chemistry*; 2013; Vol. 7. <https://doi.org/10.1016/B978-0-08-097774-4.00729-4>.
- (2) Bezemer, G. L.; Bitter, J. H.; Kuipers, H. P. C. E.; Oosterbeek, H.; Holeywijn, J. E.; Xu, X.; Kapteijn, F.; Van Dillen, A. J.; De Jong, K. P. Cobalt Particle Size Effects in the Fischer-Tropsch Reaction Studied with Carbon Nanofiber Supported Catalysts. *J. Am. Chem. Soc.* **2006**, *128* (12), 3956–3964. <https://doi.org/10.1021/ja058282w>.
- (3) Pestman, R.; Chen, W.; Hensen, E. Insight into the Rate-Determining Step and Active Sites in the Fischer-Tropsch Reaction over Cobalt Catalysts. *ACS Catal.* **2019**, *9* (5), 4189–4195. <https://doi.org/10.1021/acscatal.9b00185>.
- (4) den Breejen, J. P.; Radstake, P. B.; Bezemer, G. L.; Bitter, J. H.; Froseth, V.; Holmen, a.; P., D. J. K. On the Origin of the Cobalt Particle Size Effects In. *J. Am. Chem. Soc.* **2009**, *131* (22), 7197–7203. <https://doi.org/10.1016/j.cattod.2008.10.036>.
- (5) Barrault, J.; Guilleminot, A.; Achard, J. C.; Paul-Boncour, V.; Percheron-Guegan, A. Hydrogenation of Carbon Monoxide on Carbon-Supported Cobalt Rare Earth Catalysts. *Appl. Catal.* **1986**, *21* (2), 307–312. [https://doi.org/10.1016/S0166-9834\(00\)81363-9](https://doi.org/10.1016/S0166-9834(00)81363-9).
- (6) Copperthwaite, R. G.; Hutchings, G. J.; Der Riet, M. Van; Woodhouse, J. Carbon Monoxide Hydrogenation Using Manganese Oxide Based Catalysts: Effect of Operating Conditions on Alkene Selectivity. *Ind. Eng. Chem. Res.* **1987**, *26* (5), 869–874. <https://doi.org/10.1021/ie00065a002>.
- (7) Bezemer, G. L.; Radstake, P. B.; Falke, U.; Oosterbeek, H.; Kuipers, H. P. C. E.; Van Dillen, A. J.; De Jong, K. P. Investigation of Promoter Effects of Manganese Oxide on Carbon Nanofiber-Supported Cobalt Catalysts for Fischer-Tropsch Synthesis. *J. Catal.* **2006**, *237* (1), 152–161. <https://doi.org/10.1016/j.jcat.2005.10.031>.
- (8) Dinse, A.; Aigner, M.; Ulbrich, M.; Johnson, G. R.; Bell, A. T. Effects of Mn Promotion on the Activity and Selectivity of Co/SiO₂ for Fischer–Tropsch Synthesis. *J. Catal.* **2012**, *288*, 104–114. <https://doi.org/10.1016/j.jcat.2012.01.008>.
- (9) Johnson, G. R.; Werner, S.; Bell, A. T. An Investigation into the Effects of Mn Promotion on the Activity and Selectivity of Co/SiO₂ for Fischer–Tropsch Synthesis: Evidence for Enhanced CO Adsorption and Dissociation. *ACS Catal.* **2015**, *5* (10), 5888–5903. <https://doi.org/10.1021/acscatal.5b01578>.
- (10) Johnson, G. R.; Bell, A. T. Effects of Lewis Acidity of Metal Oxide Promoters on the Activity and Selectivity of Co-Based Fischer – Tropsch Synthesis Catalysts. *J. Catal.* **2016**, *338*, 250–264. <https://doi.org/10.1016/j.jcat.2016.03.022>.
- (11) Kimpel, T. F.; Liu, J. X.; Chen, W.; Pestman, R.; Hensen, E. J. M. Pressure Dependence and Mechanism of Mn Promotion of Silica-Supported Co Catalyst in the Fischer-Tropsch Reaction. *J. Catal.* **2023**, *425*, 181–195. <https://doi.org/10.1016/j.jcat.2023.06.010>.
- (12) Reuel, R. C.; Bartholomew, C. H. Effects of Support and Dispersion on the CO Hydrogenation Activity/Selectivity Properties of Cobalt. *J. Catal.* **1984**, *85* (1), 78–88. [https://doi.org/10.1016/0021-9517\(84\)90111-8](https://doi.org/10.1016/0021-9517(84)90111-8).
- (13) Hinchiranan, S.; Zhang, Y.; Nagamori, S.; Vitidsant, T.; Tsubaki, N. TiO₂ Promoted Co/SiO₂ Catalysts for Fischer-Tropsch Synthesis. *Fuel Process. Technol.* **2008**, *89* (4), 455–459. <https://doi.org/10.1016/j.fuproc.2007.11.007>.

- (14) Hernández Mejía, C.; van Deelen, T. W.; de Jong, K. P. Activity Enhancement of Cobalt Catalysts by Tuning Metal-Support Interactions. *Nat. Commun.* **2018**, *9* (1), 1–8. <https://doi.org/10.1038/s41467-018-06903-w>.
- (15) Melaet, G.; Ralston, W. T.; Li, C.-S.; Alayoglu, S.; An, K.; Musselwhite, N.; Kalkan, B.; Somorjai, G. A. Evidence of Highly Active Cobalt Oxide Catalyst for the Fischer–Tropsch Synthesis and CO₂ Hydrogenation. *J. Am. Chem. Soc.* **2014**, *136* (6), 2260–2263. <https://doi.org/10.1021/ja412447q>.
- (16) Soled, S. L.; Iglesia, E.; Fiato, R. a.; Baumgartner, J. E.; Vroman, H.; Miseo, S. Control of Metal Dispersion and Structure by Changes in the Solid-State Chemistry of Supported Cobalt Fischer–Tropsch Catalysts. *Top. Catal.* **2003**, *26* (1–4), 101–109. <https://doi.org/10.1023/B:TOCA.0000012990.83630.f9>.
- (17) Borodziński, A.; Bonarowska, M. Relation between Crystallite Size and Dispersion on Supported Metal Catalysts. *Langmuir* **1997**, *13* (21), 5613–5620. <https://doi.org/10.1021/la962103u>.
- (18) Reuel, R. C.; Bartholomew, C. H. The Stoichiometries of H₂ and CO Adsorptions on Cobalt: Effects of Support and Preparation. *J. Catal.* **1984**, *85* (1), 63–77. [https://doi.org/10.1016/0021-9517\(84\)90110-6](https://doi.org/10.1016/0021-9517(84)90110-6).
- (19) Morales, F.; Grandjean, D.; Mens, A.; de Groot, F. M. F.; Weckhuysen, B. M. X-Ray Absorption Spectroscopy of Mn/Co/TiO₂ Fischer–Tropsch Catalysts: Relationships between Preparation Method, Molecular Structure, and Catalyst Performance. *J. Phys. Chem. B* **2006**, *110* (17), 8626–8639. <https://doi.org/10.1021/jp0565958>.
- (20) Bulavchenko, O. A.; Gerasimov, E. Y.; Afonasenkov, T. N. Reduction of Double Manganese–Cobalt Oxides: In Situ XRD and TPR Study. *Dalt. Trans.* **2018**, *47* (47), 17153–17159. <https://doi.org/10.1039/c8dt04137g>.
- (21) Zhong, L.; Yu, F.; An, Y.; Zhao, Y.; Sun, Y.; Li, Z.; Lin, T.; Lin, Y.; Qi, X.; Dai, Y.; Gu, L.; Hu, J.; Jin, S.; Shen, Q.; Wang, H. Cobalt Carbide Nanoprisms for Direct Production of Lower Olefins from Syngas. *Nature* **2016**, *538* (7623), 84–87. <https://doi.org/10.1038/nature19786>.
- (22) Li, Z.; Lin, T.; Yu, F.; An, Y.; Dai, Y.; Li, S.; Zhong, L.; Wang, H.; Gao, P.; Sun, Y.; He, M. Mechanism of the Mn Promoter via CoMn Spinel for Morphology Control: Formation of Co₂C Nanoprisms for Fischer–Tropsch to Olefins Reaction. *ACS Catal.* **2017**, *7* (12), 8023–8032. <https://doi.org/10.1021/acscatal.7b02144>.
- (23) Longo, A.; Sciortino, L.; Giannici, F.; Martorana, A. Crossing the Boundary between Face-Centred Cubic and Hexagonal Close Packed: The Structure of Nanosized Cobalt Is Unraveled by a Model Accounting for Shape, Size Distribution and Stacking Faults, Allowing Simulation of XRD, XANES and EXAFS. *J. Appl. Crystallogr.* **2014**, *47* (5), 1562–1568. <https://doi.org/10.1107/S1600576714015970>.
- (24) van Deelen, T. W.; Hernández Mejía, C.; de Jong, K. P. Control of Metal-Support Interactions in Heterogeneous Catalysts to Enhance Activity and Selectivity. *Nat. Catal.* **2019**, *2* (11), 955–970. <https://doi.org/10.1038/s41929-019-0364-x>.
- (25) Bezemer, G. L.; Bitter, J. H.; Kuipers, H. P. C. E.; Oosterbeek, H.; Holewijn, J. E.; Xu, X.; Kapteijn, F.; Van Diilen, A. J.; De Jong, K. P. Cobalt Particle Size Effects in the Fischer–Tropsch Reaction Studied with Carbon Nanofiber Supported Catalysts. *J. Am. Chem. Soc.* **2006**, *128* (6), 3956–3964. <https://doi.org/10.1021/ja058282w>.
- (26) Lögdberg, S.; Yang, J.; Lualdi, M.; Walmsley, J. C.; Järås, S.; Boutonnet, M.; Blekkan, E. A.; Rytter, E.; Holmen, A. Further Insights into Methane and Higher Hydrocarbons Formation over Cobalt-Based Catalysts with γ -Al₂O₃, α -Al₂O₃ and TiO₂ as Support Materials. *J. Catal.* **2017**,

352, 515–531. <https://doi.org/10.1016/j.jcat.2017.06.003>.

- (27) Beitel, G. A.; Laskov, A.; Oosterbeek, H.; Kuipers, E. W. Polarization Modulation Infrared Reflection Absorption Spectroscopy of CO Adsorption on Co(0001) under a High-Pressure Regime. *J. Phys. Chem.* **1996**, *100* (30), 12494–12502. <https://doi.org/10.1021/jp960045f>.
- (28) Chen, W.; Zijlstra, B.; Filot, I. A. W.; Pestman, R.; Hensen, E. J. M. Mechanism of Carbon Monoxide Dissociation on a Cobalt Fischer–Tropsch Catalyst. *ChemCatChem* **2018**, *10* (1), 136–140. <https://doi.org/10.1002/cctc.201701203>.
- (29) Weststrate, C. J.; Loosdrecht, J. Van De; Niemantsverdriet, J. W. Spectroscopic Insights into Cobalt-Catalyzed Fischer–Tropsch Synthesis : A Review of the Carbon Monoxide Interaction with Single Crystalline Surfaces of Cobalt. *J. Catal.* **2016**, *342*, 1–16. <https://doi.org/10.1016/j.jcat.2016.07.010>.
- (30) Zijlstra, B.; Broos, R. J. P.; Chen, W.; Oosterbeek, H.; Filot, I. A. W.; Hensen, E. J. M. Coverage Effects in CO Dissociation on Metallic Cobalt Nanoparticles. *ACS Catal.* **2019**, *9* (8), 7365–7372. <https://doi.org/10.1021/acscatal.9b01967>.
- (31) McNab, A. I.; McCue, A. J.; Dionisi, D.; Anderson, J. A. Combined Quantitative FTIR and Online GC Study of Fischer–Tropsch Catalysts. *J. Catal.* **2017**, *353*, 295–304. <https://doi.org/10.1016/j.jcat.2017.07.028>.
- (32) Parastaev, A.; Muravev, V.; Osta, E. H.; Kimpel, T. F.; Simons, J. F. M.; van Hoof, A. J. F.; Uslamin, E.; Zhang, L.; Struijs, J. J. C.; Burueva, D. B.; Pokochueva, E. V.; Kovtunov, K. V.; Koptug, I. V.; Villar-Garcia, I. J.; Escudero, C.; Altantzis, T.; Liu, P.; Béch  , A.; Bals, S.; Kosinov, N.; Hensen, E. J. M. Breaking Structure Sensitivity in CO₂ Hydrogenation by Tuning Metal–Oxide Interfaces in Supported Cobalt Nanoparticles. *Nat. Catal.* **2022**, *5* (11), 1051–1060. <https://doi.org/10.1038/s41929-022-00874-4>.
- (33) Munnik, P.; de Jongh, P. E.; de Jong, K. P. Recent Developments in the Synthesis of Supported Catalysts. *Chem. Rev.* **2015**, 150619062952001. <https://doi.org/10.1021/cr500486u>.
- (34) Shimura, K.; Miyazawa, T.; Hanaoka, T.; Hirata, S. Factors Influencing the Activity of Co/Ca/TiO₂ Catalyst for Fischer–Tropsch Synthesis. *Catal. Today* **2014**, *232*, 2–10. <https://doi.org/10.1016/j.cattod.2013.10.043>.
- (35) Ralston, W. T.; Li, C.; Alayoglu, S.; An, K. Evidence of Highly Active Cobalt Oxide Catalyst for the Fischer – Tropsch Synthesis and CO₂ Hydrogenation. **2014**, 10–13.
- (36) De La Pe  a O’Shea, V. A.; Consuelo   lvarez Galv  n, M.; Platero Prats, A. E.; Campos-Martin, J. M.; Fierro, J. L. G. Direct Evidence of the SMSI Decoration Effect: The Case of Co/TiO₂ Catalyst. *Chem. Commun.* **2011**, *47* (25), 7131–7133. <https://doi.org/10.1039/c1cc10318k>.
- (37) Beck, A.; Huang, X.; Artiglia, L.; Zabilskiy, M.; Wang, X.; Rzepka, P.; Palagin, D.; Willinger, M. G.; van Bokhoven, J. A. The Dynamics of Overlayer Formation on Catalyst Nanoparticles and Strong Metal-Support Interaction. *Nat. Commun.* **2020**, *11* (1), 1–8. <https://doi.org/10.1038/s41467-020-17070-2>.
- (38) Tauster, S. J.; Fung, S. C.; Garten, R. L. Strong Metal-Support Interactions. Group 8 Noble Metals Supported on TiO₂. *J. Am. Chem. Soc.* **1978**, *100* (1), 170–175. <https://doi.org/10.1021/ja00469a029>.

Appendix C: Chapter 4

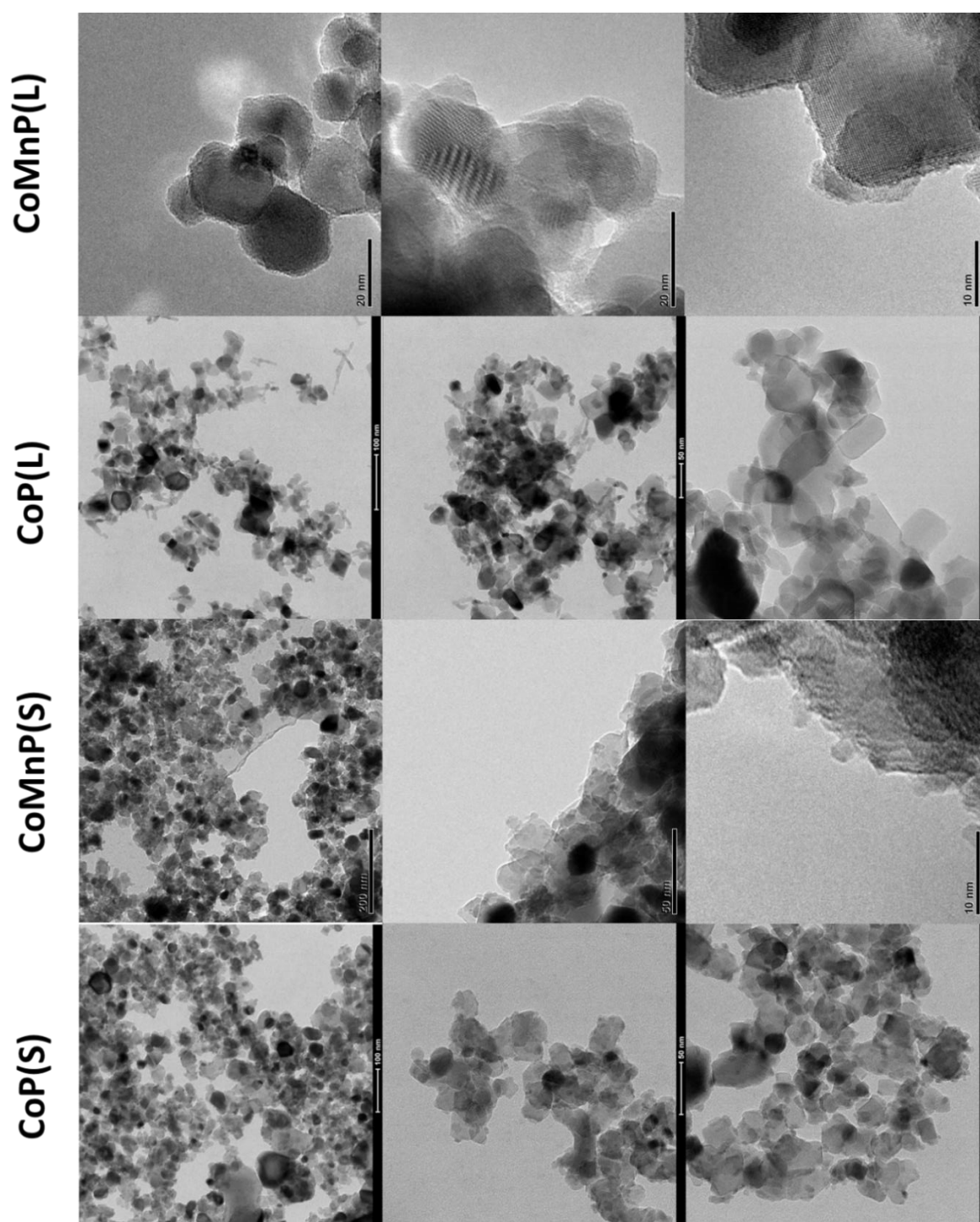


Figure C1. Representative TEM micrographs of the calcined precipitated catalysts.

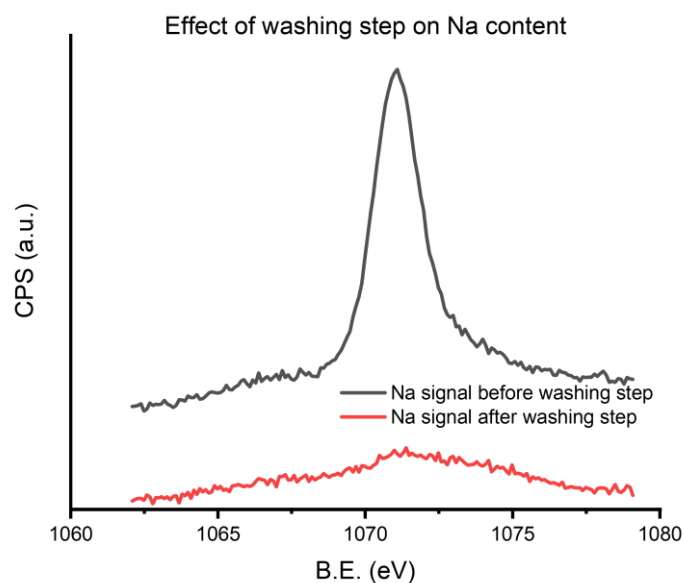


Figure C2. Na 1s XPS spectra of catalyst CoMnP(S) after and before washing the calcined precursor, showing the absence of Na after washing.

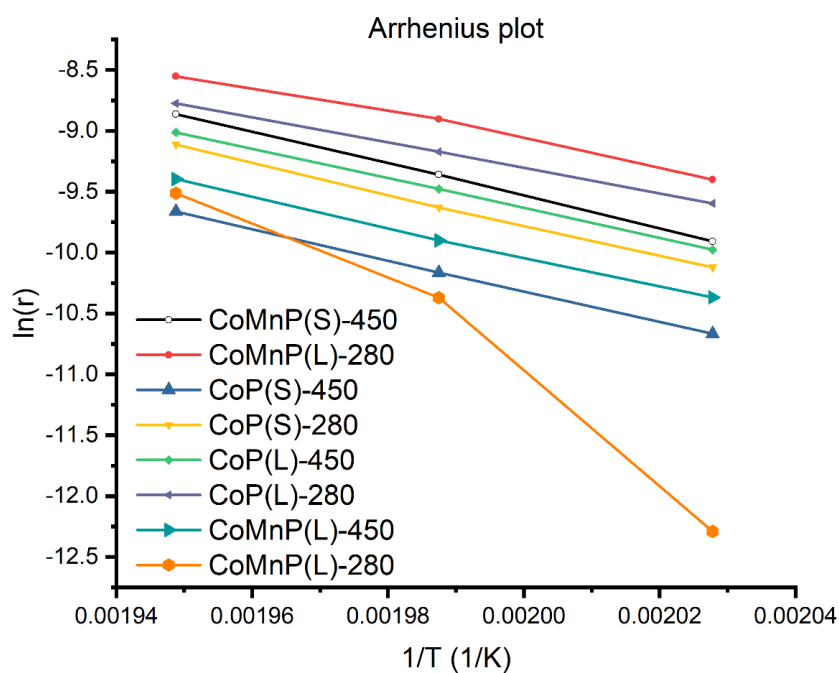


Figure C3. (left) Arrhenius plots for the various catalysts evaluated in the FT reaction at 20 bar, a H_2/CO ratio of 2 at temperatures in the range of 220°C to 240°C.

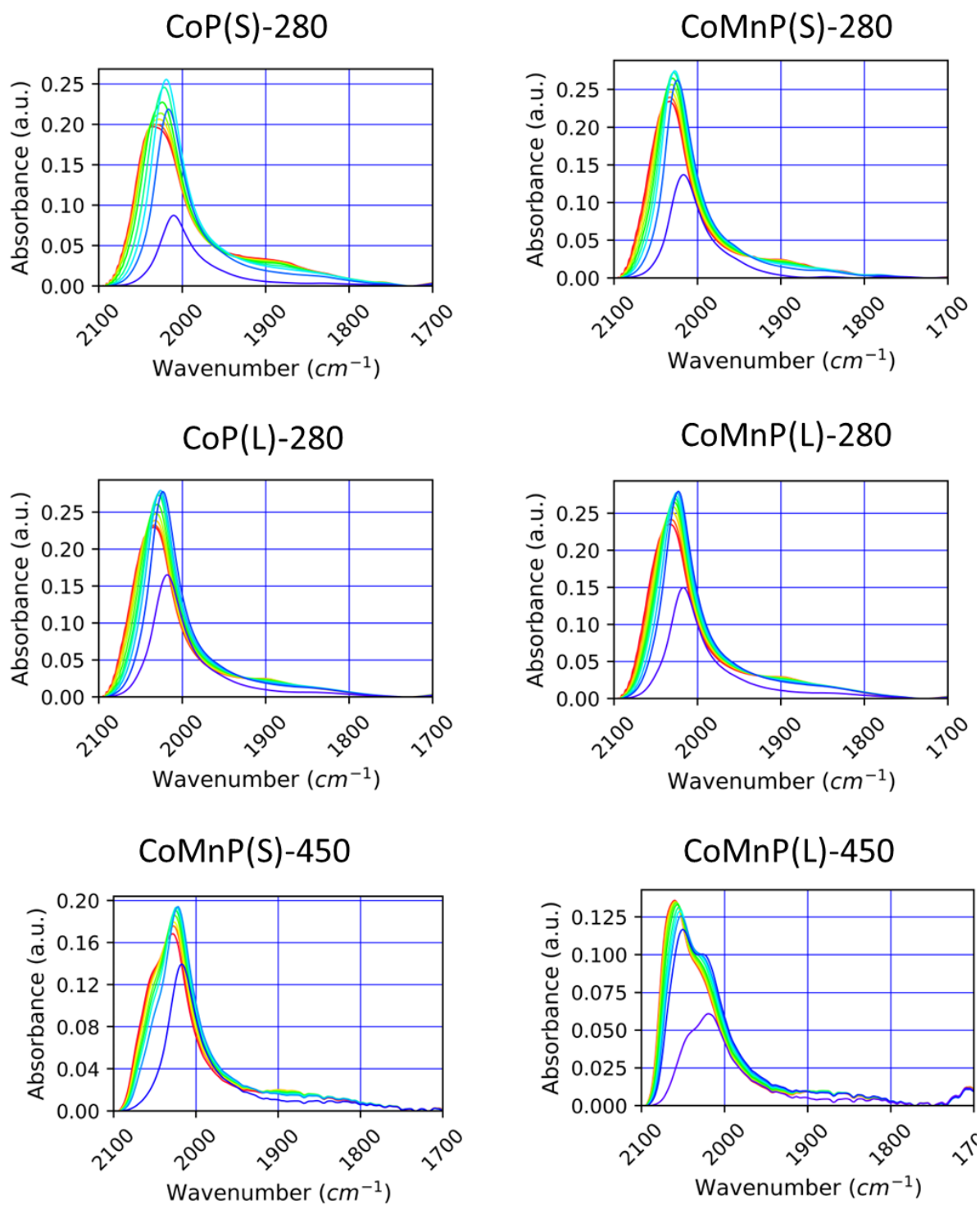


Figure C4. CO IR spectra with increasing CO partial pressure recorded at room temperature. The catalyst notations are followed by the reduction temperature in $^{\circ}\text{C}$.

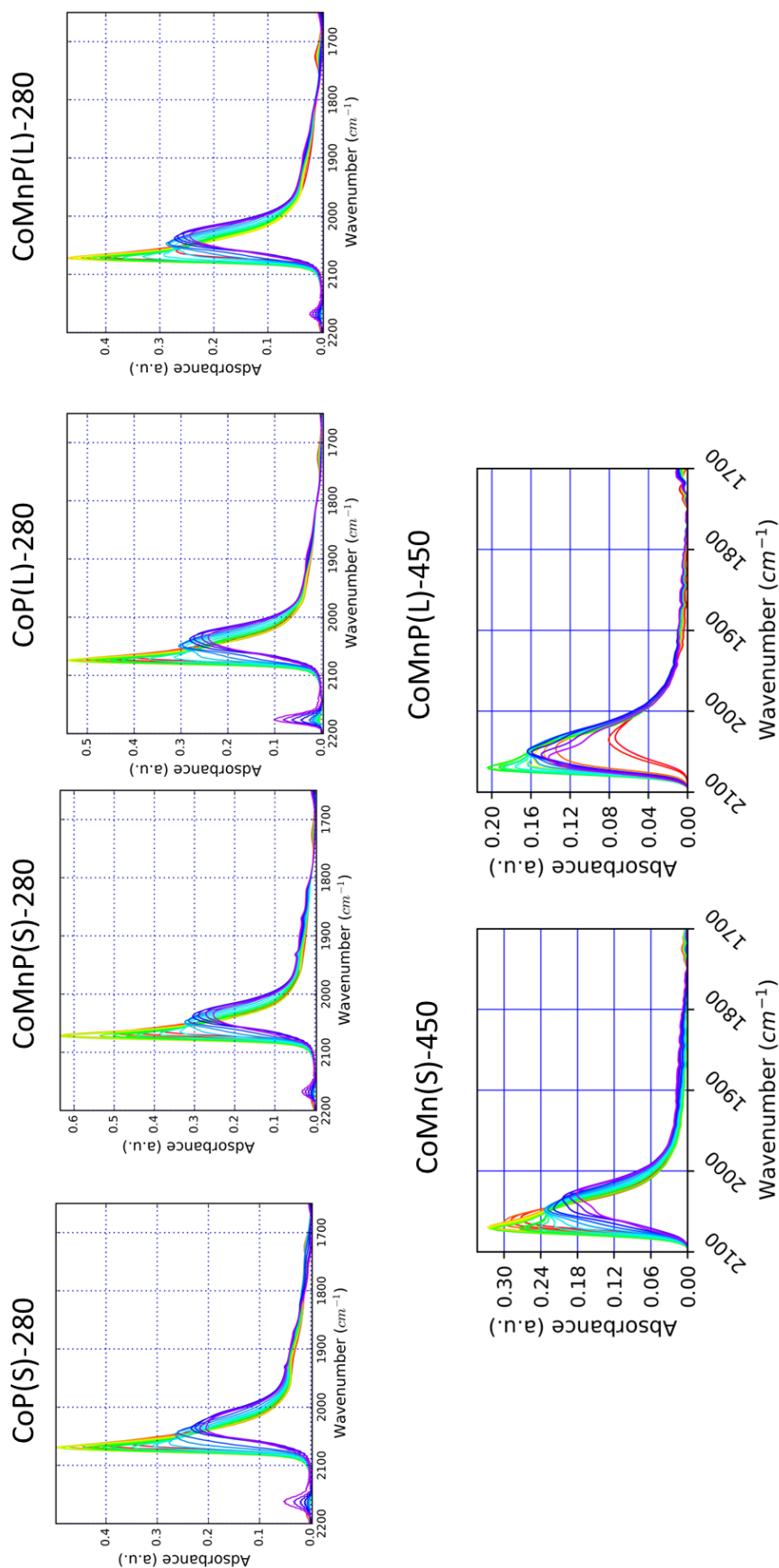


Figure C5. CO TP IR spectra with constant CO partial pressure recorded in a temperature range between 30 – 300 $^{\circ}\text{C}$. The catalyst notations are followed by the reduction temperature in $^{\circ}\text{C}$.

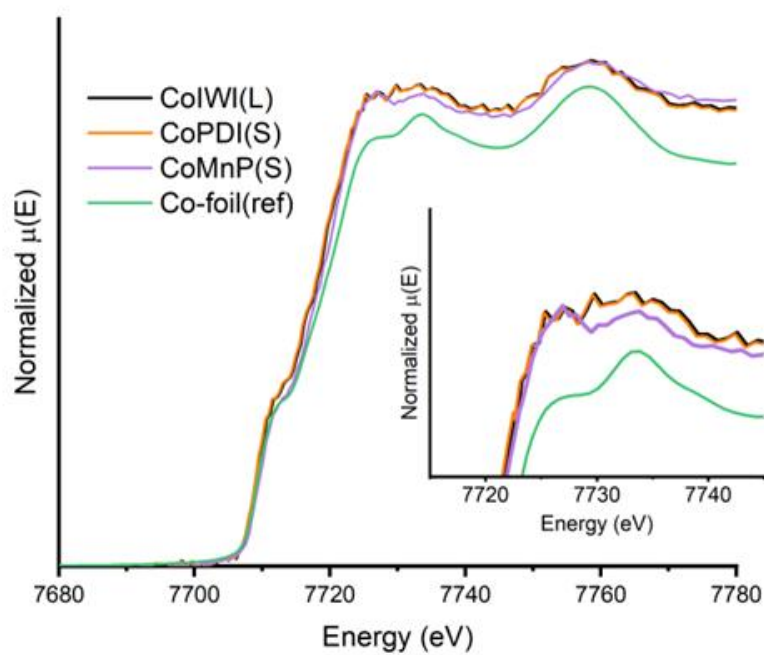


Figure C6. Comparison of XANES spectra after reduction at 450°C. The influence of the preparation methods on the XANES spectra is clearly visible with the CoMnP(S) standing out indicating structural distortions introduced via precipitation.

Summary

Structure Sensitivity of Manganese-Promoted Cobalt Fischer-Tropsch Synthesis Catalysts

Fischer–Tropsch (FT) synthesis is an increasingly important technology to convert various carbon-containing resources, such as natural gas, coal and biomass into clean transportation fuels and other valuable chemicals. Despite its importance, a large number of questions remains unanswered, especially regarding the underlying reaction mechanism in relation to catalyst structure. On top of the complexity of the reaction mechanism, which involves initiation, propagation and termination steps, there are two main aspects that warrant further understanding when the aim is to improve Co-based FT catalysts. First, the strong impact of the size of Co particles on the catalytic performance, often linked to structure sensitivity of CO dissociation, strongly limits the utilization degree of Co as relatively large particles (>6 nm) are preferred over smaller ones. Besides being of fundamental interest, this also is of practical relevance with respect to expanding FT capacity, also in the light of Co use for energy storage solutions. Second, despite the use of a variety of promoters, their role is not very well understood and this especially pertains to the role of Mn promotion for Co. Besides a role as structural promoter, it is clear that Mn affects the product distribution with contradicting results being reported. A typical observation is that the influence of Mn decreases with increasing reaction pressure. The aim of the present work was to study the way Mn promotion impacts the reaction mechanism and the activity and product distribution as a function of the reaction pressure. Moreover, we study the impact of Mn promotion on different supports that either have weak or strong interactions with Co and Mn. A specific aim is how understanding of the role of Mn in improving Co-based FT catalysis can help to overcome the particle size effect.

In **Chapter 2**, the main kinetic aspects of Mn promotion of Co using SiO₂ as a support are examined, which lay a foundation for subsequent studies involving TiO₂ support. SiO₂ was chosen as it is a relatively inert support. This largely suppresses strong metal-support interactions (SMSI), which can interfere with the promoting effect of Mn. The Mn/Co ratio was varied to determine its effect on the performance as well as to study the optimum content. Thorough characterization revealed the incorporation of Mn into the lattice of the Co₃O₄ precursor, which leads to an increase of the reduction temperature compared to the unpromoted catalyst. After reduction, Mn stays close to the reduced Co surface as known from literature, as follows from hydrogen chemisorption measurements. Despite that part of the Co surface is blocked by MnO, the FT activity and turnover frequency (TOF) at a total pressure of 2 bar are higher for the Mn-promoted sample. For the optimum Mn/Co ratio of 0.1, it is furthermore found that Mn increases the C₅₊ selectivity and reduces the methane selectivity. Insights into the effect of Mn on the reaction mechanism were obtained by temperature-programmed CO and CO/H₂ IR measurements. The strong blueshift observed of adsorbed CO with increasing temperature is correlated to CO dissociation. The presence of Mn lowers the onset temperature of CO dissociation. Density functional theory calculations were used to explore the role of MnO in CO dissociation. For this purpose, a Mn₄O₄ cluster on the Co(0001) surface optimized by a genetic algorithm was used as a model to study CO dissociation.

Mechanistically, the oxophilic nature of Mn cation upon O removal from the Mn_4O_4 cluster provides sites that can accept the O atom of CO during its dissociation when bound to the Co surface. Experimentally, we found that Mn promotion was strongly pressure dependent. This insight can explain the discrepancies between various studies about Mn promotion. While in general the activity increased but levelled off when the pressure was increased to 20 bar, it was also found that there was a maximum in methane and C_{5+} selectivity at intermediate pressure. The decrease in methane and C_{5+} selectivity at high pressure goes together with a higher C_{2-4} olefins selectivity. A surface model is proposed for Mn promotion of Co in which MnO domains provide additional CO dissociation sites, which are unlike step-edge sites not active in C-C coupling reactions. Therefore, the C_1 growth monomers generated on MnO sites need to diffuse to chain-growth sites. As with increasing pressure, the Co surface gets crowded with CO, this diffusion is hampered, increasing the residence time of these monomers on the terrace, which lowers the chain-growth probability.

Chapter 3 explores the effect of Mn promotion on small (i.e., <6 nm) as well as large (i.e., > 6 nm) on a TiO_2 support. Small Co particles were obtained using citric acid as a chelating agent in combination with CoCO_3 as a Co precursor that slowly forms Co^{2+} -citrate complexes during preparation. It was found that the addition of Mn to this preparation procedure did not affect the particle size of the final Co-oxide precursor. The formation of small particles was confirmed by XRD, TEM and Mössbauer spectroscopy, despite some sintering occurring at the high temperature of reduction at 450 °C. In line with the known structure sensitivity for Co-based FT, the FT activity of small Co particles was lower than that of large Co particles along with a higher methane and lower C_{5+} selectivity. Nevertheless, reduction at low temperature (280 °C) led to a higher catalytic performance. Especially, small Co particles promoted with Mn reduced at 280 °C a higher activity combined with a similar product distribution as large Co particles. Thus, these findings suggest that the addition of Mn to small Co particles can compensate for the loss of active sites for CO dissociation, following the findings of Chapter 2. This is reflected in the reaction kinetics by a lower apparent activation energy. Temperature-programmed IR spectroscopy of adsorbed CO confirmed the increased activity of the Mn-promoted small particle catalysts in CO bond discussion after low-temperature reduction. Comparison of these catalysts in CO and CO_2 hydrogenation shows that the promotional effect of Mn on CO hydrogenation can also benefit CO_2 hydrogenation.

Chapter 4 further develops the approach to reduce small Co particle catalysts on TiO_2 at low temperature towards improved catalytic performance. For this purpose, a precipitation method that yields homogeneously distributed Co particles with a narrow particle size distribution is used that can be combined with Mn promotion. Citric acid is again used as a chelating agent to lower the size of the Co_3O_4 particles in the precursor to ca. 4 nm. The same precipitation procedure without citric acid yields precursor particles with a size of ca. 9 nm. Reduction at 280 °C leave a significant fraction of Co in the oxidic state, independent of the particle size. The degree of reduction (DOR) sample is typically ca. 10 % as judged by quasi *in situ* XPS, which is lower as compared to the samples in Chapter 3. This is likely due to the absence of Pt reduction promoter in the samples prepared in this chapter. Operation in the FT reaction for 4 h at 260 °C only leads to a marginal increase of the DOR. Furthermore, X-ray absorption spectroscopy indicates for these samples small structural changes, amongst others more stacking faults in the metal particles and a different hcp/fcc ratio. The catalytic

performance of these samples in comparison to those in Chapter 3 show a large impact of the preparation method and the reduction temperature. The main finding is that a co-precipitated catalyst containing small Co particles reduced at 280 °C shows the highest Co-weight-based activity. Similar to the findings in Chapter 3, we find a lower apparent activation energy for the most active catalysts. Besides high activity, the promoted small Co particle catalysts that contain a significant amount of Co-oxide also present beneficial properties in terms of high C₅₊ selectivity and high chain-growth probability.

Overall, this work has provided us with new understanding about the way Mn promotes Co/SiO₂ FT synthesis catalysts. It is clear that MnO covers part of the Co surface, providing new active sites for CO dissociation. The increased activity towards CO dissociation affects the product distribution in a pressure-dependent manner, which is due to differences in the CO coverage. This knowledge is translated to improve the performance of especially small Co particles on TiO₂. The loss of active site for CO dissociation on small Co particles can be compensated by Mn promotion as well as incomplete Co reduction. Although it can be speculated that Co-oxide in contact with metallic Co can provide additional sites for CO dissociation just like MnO, it can also be that the Co particles contain more step-edge sites due to the strong interaction with the TiO₂ support and the low reduction temperatures employed. Future work should focus on resolving the complex chemistry involving CO hydrogenation involving metallic Co, Co- and Mn-oxide and the TiO₂ support.

Acknowledgements

I remember the day in May 2014, when I was sitting in the basement of the Ruprecht Karl University of Heidelberg preparing my application for a PhD position in the Netherlands. And how excited and motivated I was when I eventually received an offer. However, I should have been aware of the following wisdom found on the internet: “Every dead body on Mt. Everest was once a highly motivated person”. In autumn 2023 I am sitting again in a university library finishing the last lines of the thesis. It seems almost surreal that after 5 years of PhD and almost 4 years of “writing and reviewing” my odyssey is supposed to come to an end. However, I don’t want to bemoan the past but instead follow Nietzsche’s *amor fati*.

I would like to thank my first promotor prof. Emiel Hensen for the opportunity to work in a well-equipped lab and to present my results on international conferences. Furthermore, I would like to thank my co-promotor Robert Pestman for his support during the Phd and writing phase. Dear Robert, I enjoyed discussing my results with you as you have always found contradictions, unclarities or other shortcomings of my theories and thus help to improve my work considerably. I would like to thank the committee members prof.dr.ir. J. van der Schaaf, prof.dr. F. Gallucci, prof.dr. G. Rothenberg, dr.ir. L.M.T. Somers and dr.ir. I.A.W. Filot for taking the time to carefully read and assess my thesis.

I would also like to thank my IMC coworkers Adelheid and Brahim for numerous supports during ICP or FTIR measurements. Dear Tiny thanks for your willingness to switch gas bottles on a Friday afternoon. Emma thank you for the organization of the IMC madhouse as well as coffee and snoepjes. I would also like to thank Emma’s successor Sue for her help with the organization of my defense.

During the course of my PhD, I have encountered a multitude of people from all over the world whose personalities ranged from pleasant to “interesting”. As it would be presumptuous to remember and acknowledge every single one, I would like to acknowledge all of you and hope you forgive me for not mentioning everyone separately.

I would also like to thank prof. Martin Dienwiebel for offering me the opportunity to dive into tribology and extend my knowledge of surfaces to a more macroscopic approach.

Ferdinand, vielen Dank für deine langjährige Freundschaft, die im Bunsen-Saal seinen Anfang nahm. Auch für die vielen anregenden Diskussionen über Gott und die Welt. Benedikt, auch dir sei für deine langjährige Freundschaft gedankt, die sogar noch weiter zurückreicht. Ich bin dir überaus dankbar für dein immer offenes Ohr und die ständige Bereitschaft zu helfen.

Zu guter Letzt, möchte ich mich bei denen bedanken, ohne deren langjährigen Rückhalt weder das Studium, noch die Promotion möglich gewesen wären: Meine Mutter Barbara, Michael und Domenika sowie Karl-Heinz und Benny. Ich danke euch aus ganzem Herzen! An die Unterstützung meines Vaters, der die Fertigstellung dieses Textes nicht mehr erleben kann, sei hier ebenso erinnert.

Tobias F. Kimpel September 2023

List of publications

Publications within the scope of this thesis:

Tobias F. Kimpel, Jin-Xun Liu, Wei Chen, Robert Pestman, Emiel J.M. Hensen, Pressure dependence and mechanism of Mn promotion of silica-supported Co catalyst in the Fischer-Tropsch reaction, *Journal of Catalysis* 425 (2023) 181–195

Tobias F. Kimpel, Alexander Parastaev, Wei Chen, Robert Pestman, Emiel J.M. Hensen, The influence of Co reduction degree on the particle size dependence of CoMn/TiO₂ Fischer-Tropsch catalysts, in preparation

Tobias F. Kimpel, Alexander Parastaev, Robert Pestman, Emiel J.M. Hensen, Highly active and selective Co(Mn)/TiO₂ catalysts prepared by precipitation: on the impact of reduction temperature, in preparation

Publications outside the scope of this thesis:

Chen, W.; Kimpel, T. F.; Song, Y.; Chiang, F. K.; Zijlstra, B.; Pestman, R.; Wang, P.; Hensen, E. J. M. Influence of Carbon Deposits on the Cobalt-Catalyzed Fischer-Tropsch Reaction: Evidence of a Two-Site Reaction Model. *ACS Catal.* 2018, 8 (2), 1580–1590.

Parastaev, A.; Muravev, V.; Huertas Osta, E.; van Hoof, A. J. F.; Kimpel, T. F.; Kosinov, N.; Hensen, E. J. M. Boosting CO₂ Hydrogenation via Size-Dependent Metal–Support Interactions in Cobalt/Ceria-Based Catalysts. *Nat. Catal.* 2020, 3 (6), 526–533.

Parastaev, A.; Muravev, V.; Osta, E. H.; Kimpel, T. F.; Simons, J. F. M.; van Hoof, A. J. F.; Uslamin, E.; Zhang, L.; Struijs, J. J. C.; Burueva, D. B.; Pokochueva, E. V.; Kovtunov, K. V.; Koptuyug, I. V.; Villar-Garcia, I. J.; Escudero, C.; Altantzis, T.; Liu, P.; Béché, A.; Bals, S.; Kosinov, N.; Hensen, E. J. M. Breaking Structure Sensitivity in CO₂ Hydrogenation by Tuning Metal–Oxide Interfaces in Supported Cobalt Nanoparticles. *Nat. Catal.* 2022, 5 (11), 1051–1060.

Meng, L.; Vanbutsele, G.; Pestman, R.; Godin, A.; Romero, D. E.; van Hoof, A. J. F.; Gao, L.; Kimpel, T. F.; Chai, J.; Martens, J. A.; Hensen, E. J. M. Mechanistic Aspects of N-Paraffins Hydrocracking: Influence of Zeolite Morphology and Acidity of Pd(Pt)/ZSM-5 Catalysts. *J. Catal.* 2020, 389, 544–555.

König, T.; Kimpel, T.; Kürten, D.; Kailer, A.; Dienwiebel, M. Influence of Atmospheres on the Friction and Wear of Cast Iron against Chromium Plated Steel at High Temperatures. *Wear* 2023, 522

Oral presentations:

NCCC XVII, **March 2016**, Noordwijkerhout, Netherlands

EuropaCat-2017, **August 2017**, Florence, Italy

Prepa12, **July 2018**, Louvain-la-Neuve, Belgium

Poster presentations:

NCCC XVIII, **March 2017**, Noordwijkerhout, Netherlands

Curriculum Vitae

Tobias F. Kimpel was born in Eberbach, Germany on August 29th, 1987. He started his B.Sc. studies at Ruprecht Karl University of Heidelberg in 2007. Subsequently, he moved to KIT to perform his M.Sc. studies after which he worked in industry performing high throughput research in heterogeneous catalysis. In September 2014 he joined the IMC group at TU Eindhoven for his PhD project on the structure sensitivity of Mn-promoted cobalt nanoparticles for Fischer-Tropsch synthesis which he finished in November 2019. In the meantime, he conducted a pre-postdoc in tribology and has accepted an industry position working on the development of “green technologies”.